

ABSTRACT

Title of Document: ADAPTIVE MAGNETORHEOLOGICAL
 SLIDING SEAT SYSTEM FOR GROUND
 VEHICLES

Min Mao, Doctor of Philosophy, 2011

Directed By: Professor Norman M. Wereley
 Department of Aerospace Engineering

Magnetorheological (MR) fluids (MRFs) are smart fluids that have reversible field dependent rheological properties that can change rapidly (typically 5 – 10 ms time constant). Such an MRF can be changed from a free flowing fluid into a semi-solid when exposed to a magnetic field. The rapid, reversible, and continuous field dependent variation in rheological properties can be exploited in an MRF-based damper or energy absorber to provide adaptive vibration and shock mitigation capabilities to varying payloads, vibration spectra, and shock pulses, as well as other environmental factors. Electronically controlled electromagnetic coils are typically used to activate the MR effect and tune the damping force so that feedback control implementation is practical and realizable. MR devices have been demonstrated as successful solutions in semi-active systems combining advantages of both passive and active systems for applications where piston velocities are relatively low (typically <

1 m/s), such as seismic mitigation, or vibration isolation. Recently strong interests have focused on employing magnetorheological energy absorbers (MREAs) for high speed impact loads, such as in helicopter cockpit seats for occupant protection in a vertical crash landing. This work presents another novel application of MREAs in this new trend - an adaptive magnetorheological sliding seat (AMSS) system utilizing controllable MREAs to mitigate impact load imparted to the occupant for a ground vehicle in the event of a low speed frontal impact (up to 15 mph).

To accomplish this, a non-linear analytical MREA model based on the Bingham-plastic model and including minor loss effects (denoted as the BPM model) is developed. A design strategy is proposed for MREAs under impact conditions. Using the BPM model, an MREA is designed, fabricated and drop tested up to piston velocities of 5 m/s. The measured data is used to validate the BPM model and the design strategy. The MREA design is then modified for use in the AMSS system and a prototype is built. The prototype MREA is drop tested and its performance, as well as the dynamic behavior in the time domain, is described by the BPM model. Next, theoretical analysis of the AMSS system with two proposed control algorithms is carried out using two modeling approaches: (1) a single-degree-of-freedom (SDOF) rigid occupant (RO) model treating the seat and the occupant as a single rigid mass, and (2) a multi-degree-of-freedom (MDOF) compliant occupant (CO) model interpreting the occupant as three lumped parts - head, torso and pelvis. A general MREA is assumed and characterized by the Bingham-plastic model in the system model. The two control algorithms, named the constant Bingham number or Bi_c control and the constant stroking force or F_c control, are constructed in such a way

that the control objective – to bring the payload to rest while fully utilizing the available stroke – is achieved. Numerical simulations for both rigid and compliant occupant models with assumed system parameter values and a 20 g rectangular crash pulse for initial impact speeds of up to 7 m/s (15.7 mph) show that overall decelerations of the payload are significantly reduced using the AMSS compared to the case of a traditional fixed seat. To experimentally verify the theoretical analysis, a prototype AMSS system is built. The prototype seat system is sled tested in the passive mode (i.e. without control) for initial impact speeds of up to 5.6 m/s and for the 5th percentile female and the 95th percentile male. Using the test data, the CO model is shown to be able to adequately describe the dynamic behavior of the prototype seat system. Utilizing the CO model, the control algorithms for the prototype seat system are developed and a prototype controller is formulated using the DSPACE and SIMULINK real time control environments. The prototype seat system with controller integrated is sled tested for initial impact speeds of up to 5.6 m/s for the 5th female and 95th male (only the 95th male is tested for the Bi_c control). The results show that the controllers of both control algorithms successfully bring the seat to rest while fully utilizing the available stroke and the decelerations measured at the seat are substantially mitigated. The CO model is shown to be effective and a useful tool to predict the control inputs of the control algorithms. Thus, the feasibility and effectiveness of the proposed adaptive sliding seat system is theoretically and experimentally verified.

ADAPTIVE MAGNETORHEOLOGICAL SLIDING SEAT SYSTEM FOR
GROUND VEHICLES

By

Min Mao

Dissertation submitted to the Faculty of the Graduate School of the
University of Maryland, College Park, in partial fulfillment
of the requirements for the degree of
Doctor of Philosophy
2011

Advisory Committee:
Professor Norman M. Wereley, Chair
Professor Amr Baz (Dean's Representative)
Professor Alison B. Flatau
Professor Sung Lee
Professor Derek A. Paley

© Copyright by
Min Mao
2011

Dedication

To my parents, my grandparents, my sister and brother, and my husband.

Acknowledgements

I would like to give my sincere and deepest gratitude to my advisor, Dr. Norman M. Wereley, for his extraordinary guidance and support throughout my graduate studies. Without his constant patience, encouragement and trust, I would not be where I am today. Also, I would like to thank Professor Amr Baz, Professor Alison Flatau, Professor Sung Lee and Professor Derek Paley for agreeing to serve on my dissertation committee. I feel very lucky to have such a distinguished committee who provided insightful critiques of my work.

I am deeply grateful to Dr. Young-Tai Choi and Dr. Wei Hu. Without their tremendous help, encouragement and guidance, this work would not have been possible. I am also grateful to Dr. Sung-Ryong Hong for his help and work in the early stages of this project. I would like to thank Michael Perna and Howard Grossenbacher who manufactured precise parts for the prototype MREAs in this work, the testing fixtures as well as assembly tools, and offered invaluable suggestions and help in solving the thorny hardware problems in the MREAs. Additionally, I want to thank Dr. Jin-Hyeong Yoo, Dr. Grum Ngatu and Louise (Ami) Ahuré for their help during the measurements of MR fluids and preparation of MREAs.

Many thanks to all the colleagues, those who are here and those who have left, in our group as well as my previous officemates, Lina Castano, Byungseok Yoo and Celestine Wakha, who have made me feel a big family full of love and care. I also want to express my gratitude to Qina Diao, Wei Hu, Gang Wang, Haibing Chen, Xiaomin Dong and Lian Duan for their friendship and support.

Further, I would like to pass my sincere acknowledgement to General Motor's (GM) R&D Center for their continuous financial support for my whole Ph.D. study period. I am especially grateful to Dr. Alan L. Browne and Dr. Nancy Johnson for their invaluable support and guidance throughout the GM-funded projects. I want to thank John Ulicny for his great support and work in preparing all of the MR fluids used in this research. I also wish to extend my gratitude to Scott Webb, Nicholas Pinto, Richard Skurkis and Ruth Gusko for their great help and hard work in preparing and conducting the drop test and sled test at GM R&D Center.

Sincerely thank you all, those who have made this dissertation possible and those who have helped me grow both professionally and personally!

Table of Contents

Dedication	ii
Acknowledgements.....	iii
Table of Contents	v
List of Tables	x
List of Figures.....	xi
Disclaimer	xxi
Chapter 1: Introduction.....	1
1.1 Motivation and Research Objectives	1
1.2 Literature Review of MR Fluids and Applications.....	4
1.2.1 MR Fluids	4
1.2.2 MR Fluid Devices and Applications.....	6
1.3 Literature Review of MR Damper Modeling.....	8
1.4 Literature Review of Control Algorithms in MREA Applications.....	13
1.5 Dissertation Organization	16
Chapter 2: MREA Modeling and MREA Design Under Impact Conditions	23
2.1 Introduction.....	23
2.2 MREA (MR Damper) Models	31
2.2.1 Bingham Plastic Nonlinear Flow Model (BP Model).....	31
2.2.2 Bingham Plastic Nonlinear Flow Model With Minor Losses (BPM Model)	33
2.3 MREA Design Using BPM Model	35
2.3.1 MREA Configuration and Geometric Fluid Circuit	35

2.3.2 Design Analysis and Equations	36
2.3.3 Design Strategy	40
2.3.4 Example Implementation of the Design Strategy	42
2.4 Steady State CFD Simulations.....	44
2.5 High Speed Drop Tower test.....	45
2.5.1 High Speed Drop Tower Test Set-up.....	45
2.5.2 Test Results.....	47
2.6 Unsteady Transient Analysis of MREA Force	49
2.6.1 Governing Equations	49
2.6.2 Results.....	51
2.7 MREA Design for the Adaptive Magnetorheological Sliding Seat (AMSS) System.....	52
2.7.1 MREA Performance Requirement.....	52
2.7.2 MREA Design and Predicted Performance	53
2.7.3 Measured SSMREA Performance	55
2.8 Summary.....	57
Chapter 3: Analysis of the Adaptive Magnetorheological Sliding Seat (AMSS)	
System With Control Algorithms	80
3.1 Introduction.....	80
3.2 Single-Degree-of-Freedom (SDOF) Rigid Occupant (RO) Model	85
3.3 Multi-Degree-of-Freedom (MDOF) Compliant Occupant (CO) Model	87
3.4 Control Objective and Control Algorithms.....	89
3.5 Control Algorithm Implementation in RO Model	89

3.5.1 Constant Bingham Number Control	89
3.5.2 Constant Stroking Load/Force Control	93
3.6 Control Algorithm Implementation in CO Model	94
3.7 Simulation Results and Discussion.....	96
3.7.1 Determined Control Inputs for Each Control Algorithm.....	97
3.7.2 System and MREA Dynamic Responses.....	98
3.7.3 MREA Performance Envelope and SSMREA Capability.....	101
3.7.4 System Performance Evaluation.....	105
3.8 Conclusions.....	107
Chapter 4: Sled Test and System Modeling for the Prototype Seat System.....	127
4.1 Introduction.....	127
4.2 Sled Test.....	128
4.2.1 Sled Test Set-up	128
4.2.2 Sled Test Results.....	130
4.3 Modeling of the Adaptive Sliding Seat System.....	134
4.3.1 Modeling of SSMREA.....	134
4.3.2 Single-Degree-of-freedom (SDOF) Rigid Occupant (RO) Model	136
4.3.3 Multi-Degree-of-Freedom (MDOF) Compliant Occupant (CO) Model	137
4.4 Chapter Summary	141
Chapter 5: Sled Test of the Adaptive Magnetorheological Sliding Seat (AMSS)	
System Under Control Mode	160
5.1 Introduction.....	160
5.2 Reference Control Inputs From the CO Model.....	162

5.3. Sled Test of Prototype Seat System Under Control Mode	166
5.3.1 Experimental Setup.....	166
5.3.2 Tuning Factor and Experimental Control Input.....	168
5.3.3 Sled Test Results and Discussion	171
5.4 Effectiveness of the CO Model in Control Inputs Prediction.....	179
5.5. Conclusions.....	182
Chapter 6: Conclusions and Future Work.....	213
6.1 MREA Modeling and Design Under High Speed Impact Conditions.....	217
6.2 MREA Performance Evaluation for High Reynolds Number Flows Via High Speed Drop Test.....	221
6.3 Modeling and Control Algorithm Design of an Adaptive Magnetorheological Sliding Seat (AMSS) System.....	222
6.4 Experimental Verification of the AMSS System and the CO Model	225
6.5 Future Work	228
6.5.1 MR Yield Stress For High Reynolds Number Flows	228
6.5.2 Compliant Occupant Model Improvement	229
Appendix A: Measured seat deceleration and crash pulse for full stroke cases and zero (or nearly zero) stroke cases.....	230
Appendix B: Effective design strategy for a magnetorheological damper using a nonlinear flow model	239
ABSTRACT.....	239
Keywords	240
B.1 Introduction	240

B.2 Nonlinear MR Damper Model	242
B.3 Computer simulation and Analysis	245
B.4 Effective Design Strategy.....	246
B.5 Experimental Validation	248
B.5.1 Damper Design.....	248
B.5.3 Damper Testing.....	250
B.6 Conclusions	251
Acknowledgment	252
References.....	252
Bibliography	262

List of Tables

Table 3.1: Nomenclature used in the CO model.....	109
Table 3.2: Typical values of the parameters in the CO model.....	110
Table 4.1: Sled test matrix.	142
Table 4.2: Full stroke and zero or nearly zero stroke cases.	142
Table 4.3: Values of system parameters in the CO model.....	143
Table 5.1: Values of system parameters in the CO model.....	185
Table 5.2: Reference control input from numerical simulation for 5 th female.	186
Table 5.3: Reference control input from numerical simulation for 95 th male.	186
Table 5.4: Experimental control inputs and tuning factors satisfying 2'' (or nearly 2'') stroke and "soft-landing".	187
Table 5.5: Transient transmissibility (TT) and energy dissipation ratio (EDR).	188

List of Figures

Figure 1.1: Schematic diagram of a typical MR fluid at field-off and field-on states.	20
Figure 1.2: Passive damping seat slide (Schmitt <i>et al.</i> 2003).	21
Figure 1.3: Schematic diagram of the adaptive magnetorheological sliding seat (AMSS) using MREAs in low speed frontal impact.	22
Figure 2.1: Maximum MREA field-on force versus maximum piston velocity (drop speed reported for some research) for most reported researches on MREAs and MR dampers in the literature.	60
Figure 2.2: Schematic diagram of a typical flow mode MREA.	60
Figure 2.3: Schematic diagram and cross sectional view of a typical double-ended conventional (annular duct) MR valve type MREA.	61
Figure 2.4: Schematic diagrams for flow regions where minor losses coefficients were applied.	62
Figure 2.5: Schematic fluid circuit of one coil for a typical conventional valve type MREA.	62
Figure 2.6: Computational flow chart of the MREA design procedure.	63
Figure 2.7: Z vs. x and y with $d=0.6$ mm.	64
Figure 2.8: Z vs. x and y with $d=0.91$ mm.	65
Figure 2.9: FEA magnetic field strength verification for example MREA design.	66
Figure 2.10: Predicted performance by BPM model for the designed MREA.	66
Figure 2.11: CFD computational domain for the MREA.	67
Figure 2.12: CFD elements convergence test.	67

Figure 2.13: Comparison of zero-field force from CFD simulation and BPM prediction.	67
Figure 2.14: The MREA mounted for drop tower test.....	68
Figure 2.15: Power spectrum of MREA impact forces and velocities at nominal drop speed of 6 m/s.	69
Figure 2.16: Time history of MREA impact force and velocity at nominal drop speed of 2 m/s.	70
Figure 2.17: Time history of MREA impact force and velocity at nominal drop speed of 6 m/s.	71
Figure 2.18: Comparisons of MREA force velocity behavior between experimental results and various model predictions.....	72
Figure 2.19: Unsteady transient results for nominal drop speeds of 2 and 6 m/s as well as comparison with experimental data and prediction from BPM model.....	73
Figure 2.20: Cross-sectional view of the SSMREA.	74
Figure 2.21: Predicted SSMREA performance by BPM model and CFD simulation.	74
Figure 2.22: Physical parts of the fabricated SSMREA.	75
Figure 2.23: The assembled SSMREA.	76
Figure 2.24: Measured SSMREA force versus piston velocity at various current levels.	77
Figure 2.25: Measured and modeled peak force versus piston velocity.	77
Figure 2.26: Measured and modeled peak force versus piston velocity with adjusted coefficients in BPM model prediction.	78

Figure 2.27: Experimental and predicted (by BPM model) SSMREA dynamic force for nominal drop speeds of 2 m/s and 5 m/s at 0A and 4A.....	79
Figure 3.1: Configuration of single-degree-of-freedom (SDOF) rigid occupant (RO) model.....	111
Figure 3.2: Configuration of multi-degree-of-freedom (MDOF) compliant occupant (CO) model.	111
Figure 3.3: Resulted maximum MREA stroke if using the control inputs from RO model as the control inputs in CO model.....	112
Figure 3.4: Numerical procedure to find control input using CO model.....	113
Figure 3.5: Determined control input, Bi_c , for the constant Bingham number control from RO model and CO model.....	114
Figure 3.6: Determined control input, F_c , for the constant force control from RO model and CO model.	115
Figure 3.7: Sample applied current over time for achieving Bi_c and F_c control from RO model and CO model for 50 th male at initial impact speed of 2 m/s and 7 m/s.....	116
Figure 3.8: Seat/occupant deceleration for rigid (RO model) and compliant occupant (CO model) cases. Conditions are for a 50th male at impact speed of 2 m/s and 7 m/s (note that compliant model results in (b) are for seat itself).	116
Figure 3.9: Sample simulated occupant biodynamic responses (magnitudes) from CO model for 50th male at initial impact speed of 2 m/s and 7 m/s.	117

Figure 3.10: Sample resulted transient MREA piston velocity, V_p , piston displacement, X_p , for achieving Bi_c and F_c control from RO model and CO model for 50th male at initial impact speed of 2 m/s and 7 m/s. 118

Figure 3.11: Sample resulted transient MREA field-off force, F_{off} , yield force, F_y , and MREA force, F_{mr} , for achieving Bi_c and F_c control from RO model and CO model for 50th male at initial impact speed of 2 m/s and 7 m/s. 119

Figure 3.12: Resulted peak MREA force for achieving the constant Bingham number control (Bi_c control) from RO model and CO model. 120

Figure 3.13: Resulted peak MREA force for achieving the constant stroking force control (F_c control) from RO model and CO model. 121

Figure 3.14: Corresponding MREA dynamic range, D_n obtained from the peak MREA force for achieving the constant Bingham number control (Bi_c control) from RO model and CO model. 122

Figure 3.15: Corresponding MREA dynamic range obtained from the peak MREA force for achieving the constant stroking force control (F_c control) from RO model and CO model. 122

Figure 3.16: Measured and predicted MREA force as well as required force boundaries for each control algorithm obtained in sliding seat model analysis. 123

Figure 3.17: Comparisons of peak magnitude of seat/occupant deceleration vs. initial impact speed for RO model with different control algorithms and occupant types (Note that in the fixed seat cases, the peak decelerations are 20 g). 124

Figure 3.18: Comparisons of peak deceleration magnitude vs. initial impact speed for individual parts of occupant from CO model with different control algorithms and occupant types: (a) pelvis, (b) upper torso, (c) head.	125
Figure 3.19: Comparisons of energy dissipation ratio vs. initial impact speed with different control algorithms and occupant types for RO model and CO model.	126
Figure 4.1: The adaptive sliding seat system sled test set-up.	144
Figure 4.2: Comparison of sliding seat dynamic response between power seat and manual seat for 5 th female ('Sled' in the legend means crash pulse).	145
Figure 4.3: Power spectrum analysis of sliding seat decelerations and SSMREA piston displacement.	146
Figure 4.4: Seat deceleration and crash pulse at nominal initial impact speed 2.6 m/s with various applied current levels for the 5 th female.	147
Figure 4.5: MREA piston displacement and piston velocity at nominal initial impact speed 2.6 m/s with various applied current levels for the 5 th female.	148
Figure 4.6: Seat deceleration and crash pulse at nominal initial impact speed 2.6 m/s with various applied current levels for the 95 th male.	149
Figure 4.7: MREA piston displacement and piston velocity at nominal initial impact speed 2.6 m/s with various applied current levels for the 95 th male.	150
Figure 4.8: SSMREA force characterization based on BPM model and drop test data.	151
Figure 4.9: SSMREA force characterization from the proposed simple equation. ..	151

Figure 4.10: The single-degree-of-freedom (SDOF) rigid occupant (RO) model for the sliding seat system.	152
Figure 4.11: MATLAB/SIMULINK model of the RO model.....	152
Figure 4.12: Simulated dynamic response of the adaptive sliding seat system from RO model and comparison with measured data.....	153
Figure 4.13: The multi-degree-of-freedom (MDOF) compliant occupant model (CO model) for the sliding seat system.	154
Figure 4.14: MATLAB/SIMULINK model of the CO model.....	155
Figure 4.15: Identified K_{sb} and K_{lb} at each case using the 5 th female data.....	156
Figure 4.16: Identified K_{sb} and K_{lb} versus applied current levels at various nominal initial impact speed.	157
Figure 4.17: Comparison of simulation results using the mean value of K_{sb} and K_{lb} and their respective identified value at each case.	158
Figure 4.18: Simulated seat deceleration from CO model using the mean value of K_{sb} and K_{lb} and comparison with measured data.....	159
Figure 5.1: Numerical procedure to find control input using CO model.....	189
Figure 5.2: SIMULINK model file for constant stroking force control.	190
Figure 5.3: SIMULINK model file for constant current control.	191
Figure 5.4: Reference control inputs versus initial impact speed for each control algorithm and occupant type.....	192
Figure 5.5: Measured MREA force capability and expected MREA peak force and peak piston velocity at each intended initial impact speed during implementation of the control algorithms.	193

Figure 5.6: Schematic diagram of the adaptive sliding seat system with controller.	194
Figure 5.7: Sled test setup of the adaptive sliding seat system with controller.	194
Figure 5.8: The controller model files in SIMULINK.....	196
Figure 5.9: Tuning factor in the controller to find the real control input that enables the prototype AMSS system achieve the control objective.	197
Figure 5.10: Power spectrum analysis of seat deceleration and piston displacement at nominal initial impact speed of 5.6 m/s.	198
Figure 5.11: Seat decelerations under the constant stroking force (F_c) control for 5 th female.....	199
Figure 5.12: Seat decelerations under the constant stroking force (F_c) control for 95 th male.....	200
Figure 5.13: Seat decelerations under the constant Bingham number (Bi_c) control for 95 th male.....	201
Figure 5.14: Comparison of the constant stroking force (F_c) control with the constant Bingham number control (Bi_c) at the same nominal initial impact speed for 95 th male.....	202
Figure 5.15: MREA dynamic response under constant stroking force control at nominal initial impact speed of 2.6 m/s for 95 th male.	203
Figure 5.16: Example of sled and sliding seat impact starting time and ending time.	204
Figure 5.17: Illustration of the influence of the metal-to-metal impact effect on the measured seat deceleration (i.e. large first peak appearing at the beginning	

moment of the seat deceleration) due to loose fit between the pin and rod eye.	204
Figure 5.18: Demonstration of calculation of ATT2 (the first peak in the seat deceleration was cut based on the value of the 2 nd peak and was reassigned the value of the 2 nd peak).	205
Figure 5.19: Peak transient transmissibility PTT1 and PTT2 versus initial impact speed.	206
Figure 5.20: Average transient transmissibility ATT1 and ATT2 versus initial impact speed.	206
Figure 5.21: Energy dissipation ratio versus initial impact speed.	207
Figure 5.22: Comparison of reference control inputs from CO model simulation with experimental control inputs from sled test as well as the tuning factor for constant stroking force or F_c control.	208
Figure 5.23: Comparison of reference control inputs from CO model simulation with experimental control inputs from sled test as well as the tuning factor for constant Bingham number or Bi_c control	209
Figure 5.24: Simulated seat deceleration from CO model and comparison with measured data for 5 th female under F_c control.	210
Figure 5.25: Simulated seat deceleration from CO model and comparison with measured data for 95 th male under F_c control.	211
Figure 5.26: Simulated seat deceleration from CO model and comparison with measured data for 95 th male under Bi_c control.	212

Figure A.1: Measured seat deceleration and crash pulse at nominal initial impact speed 2.6 m/s for 5 th female.....	232
Figure A.2: Measured seat deceleration and crash pulse at nominal initial impact speed 3.5 m/s for 5 th female.....	233
Figure A.3: Measured seat deceleration and crash pulse at initial impact speed 4.5 m/s for 5 th female.....	234
Figure A.4: Measured seat deceleration and crash pulse at initial impact speed 2.6 m/s for 95 th male.....	235
Figure A.5: Measured seat deceleration and crash pulse at initial impact speed 3.5 m/s for 95 th male.....	236
Figure A.6: Measured seat deceleration and crash pulse at initial impact speed 4.5 m/s for 95 th male.....	237
Figure A.7: Illustration of the influence of the metal-to-metal impact effect on the measured seat deceleration (i.e. large first peak appearing at the beginning moment of the seat deceleration) due to a loose fit between the pin and rod eye.	238
Figure B.1: Magnified fluid path in the piston head of a basic MR damper.....	255
Figure B.2: Damping force vs. piston velocity.....	255
Figure B.3: Bingham number vs. Reynolds number.....	256
Figure B.4: Dynamic range vs. Reynolds number.....	256
Figure B.5: Gap thickness d vs. Reynolds number.....	257
Figure B.6: Area ratio \bar{A} vs. Reynolds number.....	257
Figure B.7: Active length L vs. Reynolds number.....	258

Figure B.8: Effective gap diameter d_e vs. Reynolds number	258
Figure B.9: The example bi-fold damper design.	259
Figure B.10: MTS force vs. displacement for sinusoidal input.	260
Figure B.11: MTS force vs. velocity for sinusoidal input.	260
Figure B.12: Predicted damping force (dash-dot lines) vs. MTS measured (solid lines).....	261

Disclaimer

The examples in this study are solely provided for the purpose of scientific discussion of the devices described as they relate to occupant protection efforts in automotive engineering. The work presented here explicitly does not cover all and any engineering design issues around occupant protection efforts; it is not to be construed to being an engineering manual, to provide any specific or ultimate solution nor to represent a certain engineering decision by General Motors LLC, its subsidiaries and affiliates and/or any reasons for such decisions.

Chapter 1: Introduction

1.1 Motivation and Research Objectives

With demonstrated successful vibration and shock load mitigation capabilities in many semi-active systems ranging from earthquake protection civil structures to gun recoil shock load suppression systems in recent years, magnetorheological (MR) fluid based dampers and magnetorheological energy absorbers (MREAs) have attracted strong interest in high speed impact applications (Ahmadian and Norris 2004; Browne *et al.* 2009; Choi *et al.* 2005; Choi and Wereley 2005; Hiemenz *et al.* 2007b; Mao *et al.* 2005, 2007a,b; Wereley and Choi 2008; Singh *et al.* 2009). This research focuses on an adaptive sliding seat system utilizing MREAs to mitigate load imparted to the payload (seat and occupant) in the event of a low speed frontal impact (up to 15 mph) for a general ground transportation vehicle.

Current occupant protection systems in a general ground transportation vehicle, particularly the three point seatbelt and airbag, as well as the seat itself, are typically designed to function well for larger size occupants (50th and 95th percentile male) for initial impact speed (delta v or vehicle approaching speed) of 30 mph or higher in a frontal impact mode. For lower speed frontal impact (typically up to 15 mph), studies (Temming and Zobel 2000; Bois *et al.* 2004; Cappon *et al.* 2003; Tracy 2005) have shown that the impact load imparted to the occupant also needs to be mitigated to improve occupant protection. Using current occupant protection systems (seat belts and air bags), the protection offered to the occupant in low speed impact is very

limited (only seatbelts are typically used). Moreover, these systems are passive and cannot accommodate changes in occupant mass, impact speed, or impact severity, to provide the same or comparable effective protection. Therefore, it may be beneficial to add adaptive stroking elements to existing occupant protection systems to potentially enhance occupant protection in low speed frontal impacts. MREAs are promising candidates for such stroking elements based on their demonstrated capability to adaptively modify the load stroke profile via application of magnetic field.

MR fluids are smart fluids whose rheological properties can be rapidly (typically 5 – 10 ms time constant) and reversibly modified upon exposure to an external magnetic field. A typical MR fluid is a suspension of micrometer-sized magnetic particles randomly distributed in a carrier fluid (Figure 1.1a), usually a non-conducting oil. When subjected to magnetic field, the initially randomly suspended particles align themselves along the lines of the magnetic flux to form chain like structures (Figure 1.1b), so that the MR fluid changes from a free flowing fluid into a soft semi-solid, and vice versa upon removing the magnetic field. Magnetorheological energy absorbers (MREAs) are adaptive energy dissipation (i.e. adaptive load versus stroke) devices using MR fluids as the hydraulic working fluid. Typically, the MR fluid in an MREA operates in flow mode (Rosenfeld and Wereley 2004) because this mode can satisfy the requirements of larger damping forces and relatively larger strokes compared to other working modes, such as squeeze mode or shear mode (Carlson 1999; Brigley *et al.* 2008). In the flow mode, the resulting particle chains, activated by a magnetic field, restrict the movement of the fluid in the direction

perpendicular to magnetic flux and effect an MR yield stress in the damper in addition to the normal passive viscous stress. The MR yield stress can be continuously controlled by varying the intensity of the magnetic field, often realized with an electromagnetic coil by changing its applied current level and thus providing a convenient electro-mechanical interface for feedback control. Therefore, utilizing the rapid, reversible, and continuous field dependent variation in rheological properties of MR fluids, MREAs possess the capability of adapting to varying payloads, vibration spectra, and shock pulses, as well as other environmental factors. A system utilizing MREAs is typically denoted as a semi-active system. Many investigations have shown that semi-active systems using MREAs or other MR devices combines the virtues of passive systems and active systems, but with relatively simple hardware, software implementations and low power consumption, which satisfies many practical application requirements. Therefore, assessing the feasibility of MREAs as the smart damping elements in an adaptive seat suspension may be advantageous for enhancing occupant protections in low speed frontal impact for varying occupant mass and impact speed.

Inspired by the passive damping seat slide (Figures 1.2) presented by Schmitt *et al.* (2003) for rear-end impacts, an adaptive sliding seat utilizing MREAs as the damping elements as shown in Figure 1.3 is proposed in this research to mitigate impact load transmitted to the payload in low speed frontal impacts. To the best knowledge of the author, this research is the first known work that combined both theoretical and experimental efforts to investigate the feasibility of integrating MREAs with properly designed control algorithms into vehicle occupant protection

systems as supplemental and smart elements to provide effective protection for varying occupant weights and impact speeds. Some parts of this research have been presented in conference proceedings (Mao *et al.* 2008, 2009, 2010).

The objectives of this research are: (1) to prove feasibility of an adjustable load-stroke profile using magnetorheological devices (MREAs) via both theoretical analysis and experimental study; (2) develop an MREA model and design strategy for high speed impact (e.g., for piston speeds that exceed the Reynolds number associated with the transition from laminar to turbulent flow); (3) build prototype MREAs and a prototype adaptive magnetorheological sliding seat (AMSS) system and perform sled tests; (4) develop a simple but effective biodynamic model to describe system behavior and develop optimal control algorithms; (5) propose and practically realize optimal control algorithms in the prototype system to maximize crash energy dissipation and minimize impact load transmitted to payload; (6) verify performance of the prototype system integrated with a controller via sled test and assess system performance.

1.2 Literature Review of MR Fluids and Applications

1.2.1 MR Fluids

Magnetorheological (MR) fluids are smart fluids with field dependent rheological properties that can be rapidly (typically 5 – 10 ms time constant) and reversibly be modified from a free flowing fluid into a semi-solid when exposed to a magnetic field. MR fluid was first discovered and developed by Rabinow (1948) at the US National Bureau of Standards in the late 1940s. A typical MR fluid is a suspension of micrometer-sized magnetic particles (often 20%-45% by volume) in a

carrier fluid such as mineral oil, synthetic oil, water or glycol. The magnetic particles are often made from materials with large saturation magnetization. For best performance, available alloys of iron and cobalt with a saturation magnetization of about 2.4 Tesla are preferred. But such alloys are very expensive for most practical applications so that carbonyl iron, having a saturation magnetization of 2.15 Tesla, is often used in practice (Carlson 1999). Typically, a variety of additives are usually added to prevent particle sedimentation and to promote particle suspension stability, provide oxidation resistance, improve lubricity, inhibit wear and enhance magnetic polarization (Carlson 1999; Kciuk and Turczyn 2006).

In the absence of magnetic field, the particles suspended in an MR fluid are randomly distributed (Figure 1.1a) and the fluid behaves like a standard Newtonian fluid. When subjected to an external magnetic field, the particles align with each other in the direction of the magnetic flux to form chain-like structure as shown in Figure 1.1b. These chains restrict fluid flow that is perpendicular to the direction of the magnetic flux, and thus effectively increase its apparent viscosity. A yield stress is developed within the fluid when magnetic field is applied. The yield stress can be continuously tuned by varying the applied magnetic field strength, usually realized by varying applied current levels to an electromagnetic coil. This change in yield stress is rapid (under 10 ms) and reversible. The maximum achievable yield strength ranges from 50 to 100 kPa at magnetic field strength of about 150–250 kA/m for typical MR fluids (Carlson 1999; Kciuk and Turczyn 2006), which satisfies the requirements for many practical applications. In addition, MR fluids are stable and work well over a wide temperature range from -40 to 150 °C with manageable variations in yield

stress. They are insensitive to moisture and contaminants, which is desirable in dirty or contaminated environments, and eases MR device assembly. Also, power supplies required to activate the electromagnetic coils are commercially available, having power requirements typically below or around 50 W with voltages 12-24 V (Carlson 1999; Kciuk and Turczyn 2006). Due to these many favorable properties, MR fluids flourish in many applications in recent decades.

1.2.2 MR Fluid Devices and Applications

Utilizing the rapid, reversible, and continuous field dependence of the rheological properties of MR fluids, MR fluid based devices possess the capability of adapting to varying payloads, vibration spectra, and shock pulses, as well as other environmental factors. MR fluids can be tailored for use in semi-active devices for a variety of applications. A widely explored application area for MR dampers is seismic and wind mitigation in civil infrastructure systems (Dyke *et al.* 1996a,b, 1998; Hiemenz and Wereley 1999; Jansen and Dyke 2000; Spencer *et al.* 1996; Yi and Dyke 2000; Spencer *et al.* 2000; Yang 2001; Yoshioka *et al.* 2002; Hiemenz *et al.* 2003; Yang *et al.* 2002, 2004). Another key application area of MR dampers and devices is in the automotive industry. Various investigations on MR fluid based primary seat suspensions and MR fluid based clutches and brakes for general transportation vehicles have been carried out over the past decade (Lee *et al.* 1999; Kavlicoglu *et al.* 2002; Lampe and Grundmann 2000; Neelakantan and Washington 2005; Farjoud *et al.* 2008; Senkal and Gurocak 2009; Choi *et al.* 2000; Lai and Liao 2002; Ahmadian and Song 2005; Dong *et al.* 2005; Shen *et al.* 2006). Many MR devices are available in commercial systems. Delphi developed a MagneRide semi-active suspension

utilizing MR fluid to provide continuously variable real-time suspension damping control to largely improve driver comfort. It was first used by General Motors in the Chevrolet Corvette and Cadillac Seville STS (2002) and is now widely used in premium primary suspensions or an advanced feature in many vehicle models such as Ferrari 599 and Audi R8. Also, Lord Corporation's MR seat dampers and MR clutches are well known to be successful commercial MR devices. Other MR fluid applications include: gun recoil alleviation (Ahmadian and Poynor 2001; Ahmadian *et al.* 2002), helicopter stability augmentation for lag mode and helicopter crew seat suspension vibration mitigation (Hu and Wereley 2005a,b, 2008; Ngatu *et al.* 2009; Hiemenz *et al.* 2007a), medical therapy (Liu *et al.* 2001; Flores and Liu 2002; Carlson *et al.* 2001; Herr and Wilkenfeld 2003).

Although numerous studies have been conducted on MR fluids and their application to shock and impulsive loadings (Ahmadian and Poynor 2001; Ahmadian *et al.* 2002; Facey *et al.* 2005; Batterbee *et al.* 2007; Nam and Park 2007), most studies have focused on applying MR dampers or MREAs at relatively low piston speeds (typically < 1 m/s). Recently strong interest has emerged in employing MREAs in high speed impact applications. Ahmadian's group (2004) and Browne *et al.* (2009) examined their respective MREA behavior under high speed impact during drop tower tests. Also, in our prior work, (Mao *et al.* 2007b, 2008) we designed and drop tested two MREAs and developed MREA models to predict performance and dynamic behavior. Wereley's group (Hiemenz *et al.* 2007b; Wereley and Choi 2008; Singh *et al.* 2009) first explored control algorithms for crashworthiness enhancement in vertically stroking crew seats via simulation. However, the intensive research on

MREAs and their applications under high speed impact conditions, especially combined theoretical analyses and experimental validations, is still limited. Therefore, this work seek to demonstrate the technology readiness of MREAs for high speed impact applications.

1.3 Literature Review of MR Damper Modeling

With the high increasing interest in the application of various kinds of magnetorheological (MR) dampers, substantial effort has been devoted to the development and discussion of theoretical models and analytical methods. Generally these models are classified into two categories: (1) quasi-static or steady state models, and (2) dynamic models. Quasi-static models are usually based on Bingham plastic models or Hershel-Bulkley models, and do not consider the hysteresis phenomenon in the force-velocity behavior of the MR damper. Phillips (1969) employed the Bingham model of MR/ER (electrorheological) fluids and developed a nondimensional analysis as well as the corresponding equations to determine pressure drop of MR/ER fluid flowing through a rectangular duct. Gavin *et al.* (1996) refined this analysis using an axi-symmetric model to better describe MR/ER damper quasi-static behavior. Wereley's group (Kamath and Wereley 1996; Wereley and Pang 1998; Hu and Wereley 2003) developed similar quasi-steady models with different nondimensional variables: Bingham number and damping coefficient. To include shear thinning and thickening effects, Lee and Wereley (2000), Wereley (2008), Wang and Gordaninejad (2000, 2001) utilized the Hershel-Bulkley model to predict fluid flow in a rectangular duct and a circular pipe respectively. To more precisely describe practical MR/ER damper hysteretic characteristics of force-velocity relations, a variety of dynamic

models were reported in the literature. Peel *et al.* (1996) derived a dynamic model by taking account of ER fluid inertia and compressibility. Spencer *et al.* (1997b) and Yang (2001) proposed a phenomenological model for MR dampers based on the Bouc-Wen hysteresis model. Bitman *et al.* (2005) constructed an Eyring-plastic model on the basis of an Eyring rheological model by combination of simple nonlinear functions. The Eyring-plastic model can capture practical damper responses quite well, particularly in both pre-yield and post-yield states.

The above models are very useful and often adequate for most controllable fluid device design and analysis. Particularly, the Bingham plastic quasi-static model, because of its simplicity, serves as an excellent starting point in the design of MR fluid-based devices. For most applications in the literature, the Reynolds number is small enough and laminar flow prevails so that the viscous Newtonian pressure in these quasi-static Bingham plastic analyses is developed on the basis of a linear (laminar) flow model, namely, the viscous pressure drop down the MR valve is proportional to the flow rate.

However, recently, magnetorheological energy absorbers (MREAs) have been proposed as stroking elements because they possess adaptive force capability needed for systems that require control of impact or shock loads for varying payload masses (Mao *et al.* 2005, 2007a,b, 2008, 2009; Hiemenz *et al.* 2007b). Typically the stroking load is a function that increases as a function of payload mass for a fixed available stroke. The smallest payload can accommodate the smallest stroking load, so that the off-state stroking force is specified to meet the stroking load threshold of this smallest payload. In contrast, the largest payload can accommodate the largest stroking load,

so that the maximum force is tuned to meet the stroking load of this largest payload. MREAs provide a controllable dynamic range, defined as the ratio of MREA stroking force at maximum field to its off-state (zero-field) force, and can meet a specified minimum off-state force level over a relatively high speed range.

To maintain a high dynamic range, a relatively large valve diameter is needed to maintain the Reynolds number, Re , sufficiently low. A large valve diameter requires a large magnetic circuit, so that the MREA may also have a large diameter. However, practical situations impose constraints on the MREA diameter. This trade-off, as well as design variables such as high shaft speed, high dynamic range or tunability, and maximum passive or off-state force levels at high shaft speed, are likely to induce high Reynolds number flows in MR valves.

Therefore, in MREAs subject to impact loads, the Reynolds number is typically much higher than for devices intended for vibration mitigation or isolation applications. The induced high Reynolds number flows in the MR valve can cause significant degradation of dynamic range, as well as undesired high off-state force levels. Ahmadian *et al.* (2004) examined the performance of a double-ended MREA subject to impact velocities of up to 6.6 m/s. They achieved a dynamic range of $D \approx 2.75$ at 2.2 m/s (86 in/s). However, at a speed of 6.6 m/s (260 in/s), the dynamic range reduced nominally to $D \approx 1$. They hypothesized that the transition from controllable ($D > 1$) to uncontrollable behavior ($D \approx 1$) is related to the transition of fluid flow from laminar to turbulent, which is supported by the analysis of Mao *et al.* (2005). Browne *et al.* (2009) conducted impact tests of an MREA at stroking velocities ranging from 1.0 to 10 m/s and showed that the MR damper force could be

tuned by adjusting the magnetic field. However, a similar trend was found in these two studies—the dynamic ranges of the MR dampers were significantly reduced and the increase in field-off forces vary as a quadratic function of velocity suggesting that nonlinear velocity squared damping effects play a key role. From these two pilot studies, valuable insight on MREA behavior under impact loadings was gained, even though models or qualitative analysis were not addressed to explain this MREA force vs. velocity behavior. Later in our own study (Mao *et al.* 2008), a bifold MREA was designed based on the Bingham-plastic model (BP model) for nominal piston velocities of up to 6.75 m/s, and was drop tested up to nominally 6 m/s. The results showed that a dynamic range of $D=2$ can be achieved by keeping the Reynolds number below 850 over the tested speed range. However, the measured field-off forces for piston velocities above 2 m/s were much higher than the predicted force levels. It was recognized that nonlinear viscous losses (i.e. velocity squared effects) played an important role in predicting force levels at higher speeds. This was verified by the substantial agreement of experimental data with modeling results upon adding nonlinear viscous loss components in the off-state force calculation. Thus, it was concluded that such minor losses should be added to the BP model and associated design strategy for MREAs under high speed impact conditions.

Even though pressure drop due to minor losses is well known in fluid piping systems (White 1986), it has been ignored in most MR fluid-based device modeling, analysis and design in the literature reported so far. To some extent, this way of dealing with MR damper models and analysis is reasonable because most prior work focused on relatively low speed vibration isolation problems where shaft speeds were

typically below 1 m/s (low Re laminar flows) and minor losses can be neglected to simplify design and analysis. It is worth noting that, in some studies (Dogruer *et al.* 2008), minor loss factors were included for calculating the total pressure drop during their design analysis. In addition, it was shown that the modeling results agreed well with the experimental data up to a piston velocity of 0.15 m/s (low Reynolds number flow range) for harmonic excitations. Since this study (Dogruer *et al.* 2008) also dealt with low speed application, the importance of minor losses seemed to be buried in the fact that the classical Bingham-plastic model can accurately handle most of the MR devices modeling issues without consideration of minor losses in low speed ranges as most past researches did. Few studies to date in the MR literature have correlated minor losses to off-state forces, as well as reported reductions in dynamic range as impact speed increases. A key reason is that application of MREAs to high speed impact situations has only recently emerged.

Nevertheless, initial studies on MREAs under impact conditions have shown that MREA analysis based on quasi-steady Bingham plastic analysis (Gavin *et al.* 1996; Peel *et al.* 1996; Wereley and Pang 1998) and BP model (Mao *et al.* 2005), which is deemed sufficient for MR devices design and performance characterization, is not adequate to describe MREA behavior when high speed impact loadings take place, such as in the case of the low speed vehicle impacts in this work, and thus are not adequate for MREA design purposes. For this reason, in this study, a nonlinear analytical MREA model taking into account the effects of minor loss factors (i.e., the BPM model) is developed based on the Bingham-plastic nonlinear flow model (BP model) and experimentally validated.

1.4 Literature Review of Control Algorithms in MREA Applications

MR dampers and MREAs provide us with adaptive hardware as well as relatively simple electromechanical interfaces for implementing semi-active systems. To fully take advantage of the adaptive and smart capabilities of MR devices, effective and practically realizable control algorithms are necessary. Bearing this in mind, many researchers have put significant efforts into studying and developing useful control algorithms to fit the requirements of various MR applications. Spencer (1997a), Jansen and Dyke (2000) compared a variety of promising control algorithms through simulation, and discussed the advantages of each algorithm, such as: the Lyapunov controller, decentralized bang-bang controller, modulated homogeneous friction algorithm, clipped optimal controller. Wang and Gordaninejad (2002), and Park and Jeon (2002) developed a Lyapunov-based control algorithm for bridge vibration and seat suspension vibration respectively and evaluated the respective system performance through simulation. Choi and Han (2003) examined a semi-active skyhook controller for the MR seat suspension in a commercial vehicle by adopting a hardware-in-the-loop-simulation (HILS) methodology and assessed the control responses such as acceleration at the driver's seat under both bump and random road conditions. Choi and Wereley (2003) investigated a sliding mode controller in the application of a MR/ER landing gear system and demonstrated the feasibility and effectiveness the controlled MR/ER fluid based landing gear system through simulation. In addition, more complicated control algorithms, such as optimal fuzzy control (Wang and Hu 2005) and neural network control (Wang and Liao 2005), were also studied using simulation.

Despite the demonstrated effectiveness of the above mentioned control algorithms in the vibration reduction, they may not be directly applied to the control in high speed impact applications because these algorithms basically are trying to maintain the systems that are to be controlled in some equilibrium or reference positions under vibration disturbances. However, for MREAs in high speed impact conditions, the goal is dissipate the energy of impact as efficiently as possible over the available stroke of the MREA. The use of MREAs in crashworthiness systems is relatively new research so that not much work has been reported in the literature. Choi and Wereley (2005) first investigated the biodynamic responses of an MR helicopter crew seat suspension to shock loads due to a vertical crash landing of a helicopter as well as to sinusoidal vibration. In their study, a crash pulse due to a high sink rate landing in the form of a half-sine function with duration of 30 ms was assumed. The damping force of the MR damper was described as the summation of the viscous component, which is the product of the constant damping coefficient and the instantaneous piston velocity, with the MR yield force. Rather than using the Bingham-plastic model, the MR yield force is characterized by a nonlinear hysteresis model. They assessed the performance of the seat suspensions in three modes of operation: 1) passive hydraulic seat suspension, 2) passive MR seat suspension with applied constant yield stress, and 3) semi-active MR seat suspension when the yield stress was controlled using a nonlinear optimal control algorithm. For the nonlinear optimal control algorithm, the optimal control input was derived based on Sontag's formula using a robust control Lyapunov function (RCLF) that satisfies the Hamilton-Jacobi-Isaacs (HJI) equation associated with the system and minimizes the cost

function. Choi and Wereley (2005) compared biodynamic responses of an occupant while seated in an MR seat suspension when subjected to a crash pulse at an initial vertical landing velocity of 6.71 m/s (15 mph) for these three modes of operations. Deceleration time histories of the seat, pelvis, upper torso, viscera and head were presented. In addition, they also compared simulated biodynamic response of the occupant in the MR seat with respect to the initial crash landing velocities varying from 6.1 to 12.2 m/s in terms of the peak force of the pelvis, the upper torso, and the viscera, as well as HIC_{15} of the head for the three modes of operation. They showed that: 1) the passive and semi-active MR seat suspensions presented better shock mitigation performance than the passive hydraulic seat suspension, 2) the MR seat suspension with constant yield force demonstrated good shock attenuation performance similar to the MR seat suspension under the nonlinear optimal control algorithm. Later, Hiemenz *et al.* (2007b) studied a constant load-limiting control algorithm for purpose of enhancing crashworthiness of an MR vertical stroking helicopter crew seat system through simulating the derived lumped system model and showed promising practical implementation. Wereley and Choi (2008) conducted a nondimensional analysis for MREAs in drop-induced shock mitigation and developed a critical Bingham number control in order to meet a soft-landing objective, which is to ensure that the seat comes to rest after fully utilizing its available stroke. Through simulation, they demonstrated that this control algorithm is advantageous compared to non-soft-landing cases. Singh *et al.* (2009) presented an optimal control algorithm, which utilized the “soft-landing” idea described in Wereley and Choi (2008) to control a vertical stroking seat to land softly, in the event of a harsh landing. But their

respective systems involved are different. In the case of Wereley and Choi (2008), no spring was included. Singh *et al.* (2009) considered seats with both with and without a recoil spring. However in both cases the “soft landing” criterion led to avoidance of end stop impact.

For the adaptive magnetorheological sliding seat (AMSS) in this research, the system is distinct from the previous MR crashworthy systems in the sense that this system operate in the horizontal direction, we can adapt the “soft landing” idea to implement adaptive control of the AMSS system. Thus, we set the control objective as the soft-end impact, that is, to find some control input or a load-stroke profile over the course of the impact period to bring the payload to a rest while fully utilizing the available stroke (here set to be 2”). In this way, we not only avoid the detrimental effects of end stop impacts, but also maximize the impact energy dissipation in the system because no available stroke would be wasted.

1.5 Dissertation Organization

The dissertation is organized as follows:

- Chapter 2 develops an analytical MREA model using a Bingham-Plastic model augmented with Minor loss factors (i.e. BPM model) for MREAs under high speed impact conditions based on a nonlinear flow Bingham-plastic model in our prior work (i.e. BP model). Using this BPM model, an effective design strategy is proposed for linear stroke type MREA, and an example design is developed. The MREA off-state performance is further examined via CFD (computational fluid dynamics) simulations using commercial ANSYS software with the FLOTRAN

module. It is shown that the forces predicted using the CFD solutions match well with the predictions from the BPM model at various representative piston velocities. An MREA was then fabricated and drop tested up to piston velocities of 5 m/s using the high speed drop tower facility at the GM R&D Center. The BPM model is experimentally validated using data from these drop tests. The prototype MREA is then refined and tailored to the AMSS system. Its performance is characterized using drop tests and the data is used to validate model predictions. In addition, these tests show that the MREA dynamic behavior (force-time histories) can also be obtained using the BPM model by simply substituting the dynamic piston velocity recorded in the drop tests (velocity-time histories) in the equations of the BPM model. This provides the theoretical foundation for the later control algorithm implementation.

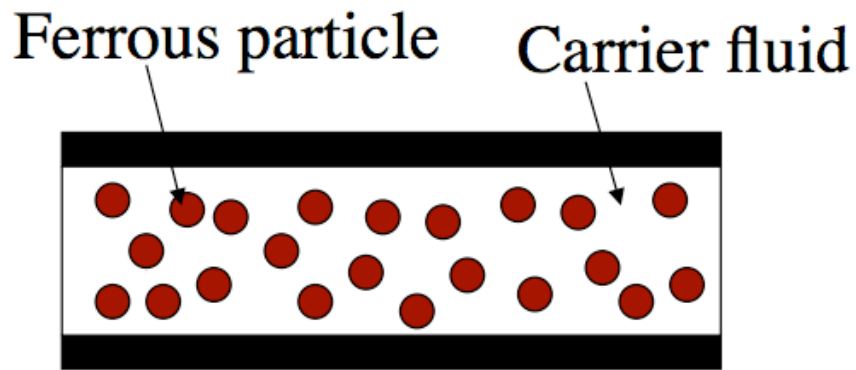
- Chapter 3 theoretically explores the feasibility and potential benefits of the AMSS system using a single-degree-of-freedom (SDOF) rigid occupant (RO) model and a multi-degree-of-freedom (MDOF) compliant occupant (CO) model. In the RO model, the seat/occupant complex is represented by a single mass. In the CO model, the occupant is modeled as three lumped masses – head, torso and pelvis, and the seat itself is treated as a separate mass. In both models, the MREA force is ideally represented using the quasi-static Bingham-plastic model. A rectangular crash pulse with magnitude of 20 g whose duration depends on the initial impact speed is assumed to serve as the impact load to the vehicle floor. Two optimal control algorithms are proposed to achieve the control objective – bring the payload to a rest while fully utilizing the available stroke – depending on

available measurable information. The first is called the constant Bingham number or Bi_c control and is applicable when the instantaneous piston velocity feedback is unavailable. The second is called the constant stroking load or F_c control and is suitable for the situation when the instantaneous piston velocity over the course of the impact period can be measured and fed back. Governing system equations for both models are derived. Closed form analytical solutions including the control input, the payload dynamic response as well as the MREA dynamic responses in the RO model are presented for each control algorithm. For the CO model, a numerical technique is used to find the solutions. With assumed typical system parameter values, simulations are conducted for three types of occupants, the 5th percentile female and the 50th and 95th percentile male for initial impact speeds up to 7 m/s (15.7 mph). The optimal control inputs, the system and MREA responses for sample cases for both models and control algorithms are presented and discussed. The benefits of the AMSS system using either control algorithm are addressed in terms of the peak decelerations transmitted and the energy dissipation ratio (defined as the ratio between the MREA damped energy to the initial payload kinetic energy) as compared to the case of a traditional fixed seat.

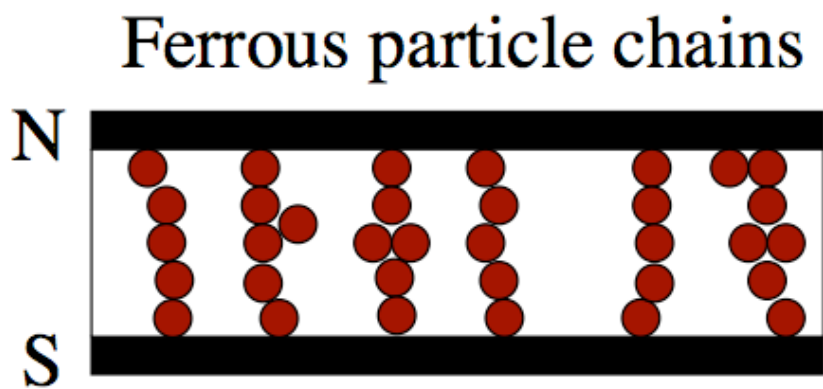
- Chapter 4 deals with the sled test of the prototype AMSS system under passive control, and the validation of the AMSS system model comprising a CO model. The experimental setup and test matrix are presented. Sample testing data are demonstrated and experimental results are discussed. The accuracy of the system

model for describing the dynamic behavior of the prototype AMSS system is addressed.

- In Chapter 5 the experimental verification of the optimal control algorithms for the AMSS system is assessed via sled test. The effectiveness of the CO model in predicting optimal control inputs is also assessed. The control inputs are pre-determined via numerical simulation using the CO model, as well as the crash pulses collected during sled tests under passive control. Prototype controllers for constant Bingham number (Bi_c) control and constant stroking load (F_c) control are implemented using the DSPACE and MATLAB/SIMULINK real-time control environment. Sled tests of the prototype AMSS system using these prototype controllers are performed and the test results are analyzed. The feasibility of the AMSS is successfully demonstrated. The CO model is shown to be effective and a useful tool to predict control inputs for the control algorithms.
- Chapter 6 summarizes original contributions of this research, provides conclusions and offers recommendations for future work.

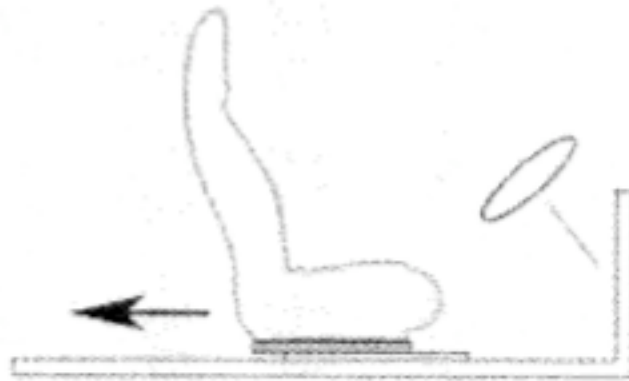


(a) Field-off state

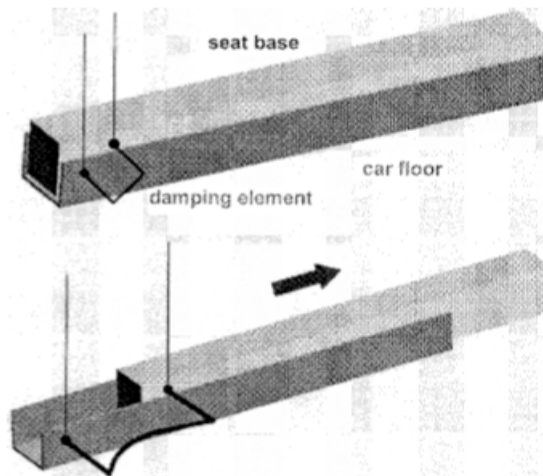


(b) Field-on state

Figure 1.1: Schematic diagram of a typical MR fluid at field-off and field-on states.



(a) Schematic diagram showing principle of the seat slide



(b) Working principle demonstration for the seat slide with the damping elements



(c) The passive damping elements made by steel (before and after deformation)

Figure 1.2: Passive damping seat slide (Schmitt *et al.* 2003).

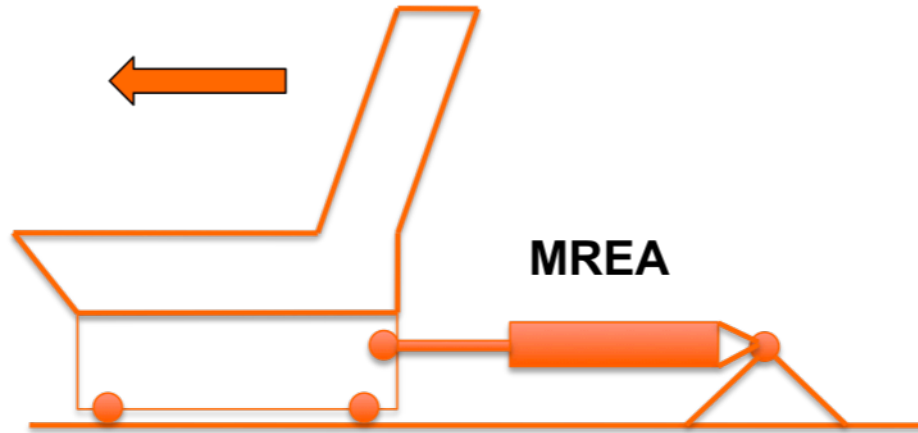


Figure 1.3: Schematic diagram of the adaptive magnetorheological sliding seat (AMSS) using MREAs in low speed frontal impact.

Chapter 2: MREA Modeling and MREA Design Under Impact Conditions

2.1 Introduction

Over the past decades, magnetorheological (MR) dampers have been intensively investigated for civil, aerospace, and automotive applications as well as medical devices mainly for providing adaptive damping. As these applications have been developed, a variety of MR damper models have been developed and discussed. Generally these models can be classified into two categories: (1) quasi-static or steady state models, and (2) dynamic models.

Quasi-static models include Bingham-plastic models, Hershel-Bulkley models and their variations of dimensional and nondimensional analyses. The main features of these models are that they can accurately describe the post-yield behavior of MR fluids but are not sufficient to capture force-velocity hysteresis in the MR dampers. The early study of Bingham-plastic models for MR/ER (electrorheological) fluids can be traced back to Phillips (1969). He developed a group of nondimensional variables and derived the corresponding polynomial equations to determine pressure drop of an MR fluid flowing through a parallel plate duct using the Bingham model of MR fluids. A similar approach was utilized by Gavin *et al.* (1996) to more precisely describe MR damper quasi-static behavior using an axisymmetric model. Wereley's group (Wereley and Pang 1998; Hu and Wereley 2003) developed a set of quasi-static

Bingham flow models and nondimensional analyses for MR dampers under flow, shear and/or mixed modes with different nondimensional variables, such as Bingham number, nondimensional plug thickness, and assumed a constant yield stress. To allow for shear thinning and thickening effects appeared in the measurements reported in the literature, Wereley's group (Lee and Wereley 2000; Wereley 2008), Wang and Gordaninejad (2000, 2001) utilized the Hershel-Bulkley model to predict the fluid flow in a rectangular duct and an annular duct respectively.

The quasi-static models work well when expressing force-displacement and post-yield force-velocity behavior of an MR damper. However, such models cannot precisely describe force-velocity behavior of an MR damper, especially at low speed due to hysteresis manifested by the low speed compression loop. To tackle this problem, a variety of dynamic models were explored and reported in the literature. Peel *et al.* (1996) derived a dynamic model by taking account of ER (MR) fluid inertia and compressibility. Spencer *et al.* (1997b) and Yang (2001) proposed a phenomenological model for MR dampers based on the Bouc-Wen hysteresis model. The Bouc-Wen model is later extensively examined in terms of different ways of finding the model related characteristic parameters and the model based improved forms for better characterizing the hysteresis phenomenon of MR dampers (Dominguez *et al.* 2004, 2006). Wereley's group also did intensive work in MR dampers' dynamic modeling and developed several distinct hysteresis models. Wereley *et al.* (1998) proposed a hysteretic biviscous model composed of several piecewise continuous functions and showed that the model can capture nonlinear hysteresis characteristics of MR dampers accurately. Another two hysteresis models,

the nonlinear viscoelastic-plastic model and the stiffness-viscosity-elasto-slide model, were also investigated for helicopter MR dampers (Wereley *et al.* 1999) and the results demonstrated that both models can capture the damper hysteresis behavior reasonably accurately. To reduce the model complexity and to ease control implementations with hysteresis models, Choi *et al.* (2005) proposed a simple nonlinear model by replacing the signum function in the Bingham plastic model with a hyperbolic-tangent function with two characteristic parameters, which are used to characterize the force-velocity hysteresis loop. They demonstrated the effectiveness of this model by employing it into an MR vibration isolation system with a skyhook control algorithm. For a similar purpose, Bitman *et al.* (2005) constructed an Eyring-plastic model on the basis of an Eyring rheological model by combination of simple nonlinear functions and it showed that the model can capture practical damper responses quite well in both the pre-yield and the post-yield states. Another type of model extensively studied by Wereley's group is the hydromechanical analysis, which considers compliances of MR fluid volumes in the damper, flow resistances through the MR valves, as well as inertia effects (Hong *et al.* 2003, 2006; Mao *et al.* 2007a,b, 2008) to model dynamic behavior of force versus velocity for MR dampers and MREAs. They validated the accuracy of the hydromechanical model for different MREA configurations and loading conditions, including bifold valve, annular valve and bypass valve, under sinusoidal excitations and/or subject to impact loadings.

The above models are very useful and often adequate for most MR fluid device applications. The dynamic models are mostly useful to describe an existing MR dampers' force-velocity behavior for system control purposes because their

parameters can be readily identified from experimental data. But to design a new MR damper or device from the conceptual sketch, the quasi-static models are most convenient and are usually used. Particularly, the Bingham plastic quasi-static model, because of its simplicity, serves as an excellent starting point in the design of MR fluid-based devices. For most applications reported in the literature, the maximum piston velocities of the MR dampers are typically low (as shown in Figure 2.1) and the induced Reynolds numbers are small enough so that laminar flows prevail. In these cases, the passive viscous force of the MR dampers can be well described by the routinely used quasi-static Bingham plastic analysis, which is developed on the basis of a linear (laminar) flow model and the viscous pressure drop of the MR valve is proportional to the flow rate or piston velocity. However, as revealed by recent emerging investigations in employing magnetorheological energy absorbers (MREAs) under high speed impact and shock loadings for varying payload masses (Ahmadian and Norris 2004; Mao *et al.* 2005, 2007a,b, 2008, 2009; Browne *et al.* 2009), it was found that the routinely used Bingham-plastic model considering only laminar flows was not sufficient to describe MREA behaviors due to dominant nonlinear viscous flows. This is because, compared to typical MR damper applications in low speed vibration mitigations, in the high speed impact applications relatively large damping capacity with an appropriate controllable dynamic range, defined as the ratio of the force at maximum field to the off-state force, over a relatively higher MREA operating speed range are usually required in order to account for varying payload mass. Typically the stroking load is a function that increases as a function of payload mass for a fixed available stroke. The off-state

stroking force is specified to meet the stroking load threshold of the smallest payload. And the maximum force is tuned to meet the stroking load of the largest payload. This yields a need for a relatively high dynamic range and high damping capacity.

To accommodate the relatively high performance requirements for MREAs design in high speed impact conditions, we (Mao *et al.* 2005) modified the passive viscous force in a typical MR damper Bingham-plastic model to also include the turbulent flow cases (the modified model is termed as BP model) and proposed an effective design strategy to achieve a desired dynamic range in the way of encouraging flows in an MR valve in laminar status by choosing proper primary MREA design parameters' values. Thus, to maintain a high dynamic range, a relatively large valve diameter is desirable to maintain the Reynolds number, Re , sufficiently low. A large valve diameter would often result in a large magnetic circuit, so that the MREA may also have a large diameter. However, practical situations impose constraints on the MREA diameter. This trade-off, as well as design variables such as high shaft speed, high dynamic range or tunability, and maximum passive or off-state force levels at high shaft speed, are likely to induce high Reynolds number flows in MR valves.

Therefore, in MREAs subject to impact loads, the Reynolds number is typically much higher than for devices intended for vibration mitigation or isolation applications. The induced high Reynolds number flows in the MR valve can cause significant degradation of dynamic range, as well as undesired high off-state force levels. Ahmadian and Norris (2004) examined the performance of a double-ended MREA subject to impact velocities of up to 6.6 m/s. They achieved a dynamic range

of $D \approx 2.75$ at 2.2 m/s (86 in/s). However, at a speed of 6.6 m/s (260 in/s), the dynamic range reduced nominally to $D \approx 1$. They hypothesized that the transition from controllable ($D > 1$) to uncontrollable behavior ($D \approx 1$) is related to the transition of fluid flow from laminar to turbulent, which is supported by the analysis of Mao *et al.* (2005). Browne *et al.* (2009) conducted impact tests of an MREA at stroking velocities ranging from 1.0 to 10 m/s and showed that the MR damper force could be tuned by adjusting the magnetic field. However, a similar trend was found in these two studies—the dynamic ranges of the MR dampers were significantly reduced and the increase in field-off forces as a function of velocity, which was not linear as is typically assumed, was quadratic suggesting that nonlinear velocity squared damping effects play a key role. From these two pilot studies, valuable insight on MREA behavior under impact loadings was gained, even though models or qualitative analysis were not addressed to explain this MREA force vs. velocity behavior. Later in our own study (Mao *et al.* 2008), a bifold MREA was designed based on the Bingham-plastic model (BP model) for nominal piston velocities of up to 6.75 m/s, and was drop tested up to nominally 6 m/s. The results showed that a dynamic range of $D = 2$ can be achieved by keeping the Reynolds number below 850 over the tested speed range. However, the measured field-off forces for piston velocities above 2 m/s were much higher than the predicted force levels. It was recognized that minor losses factors (velocity squared effects) played an important role in predicting force levels at higher speeds. This was verified by the substantial agreement of experimental data with modeling results upon adding the minor losses components in the off-state force

calculation. Thus, it was concluded that minor losses should be added in the BP model and associated design strategy for MREAs under high speed impact conditions.

Even though pressure drop due to minor losses is well known in fluid piping systems (White 1986), it has been ignored in most MR fluid-based device modeling, analysis and design in the literature reported so far. To some extent, this way of dealing with MR damper models and analysis is reasonable because most prior work focused on relatively low speed vibration isolation problems where shaft speeds were typically below 1 m/s (low Re laminar flows) and minor losses can be neglected to simplify design and analysis. It is worth noting that, in some studies (Dogruer *et al.* 2008), minor loss factors were included for calculating the total pressure drop during their design analysis. In addition, it was shown that the modeling results agreed well with the experimental data up to a piston velocity of 0.15 m/s (low Reynolds number flow range) for harmonic excitations. Since this study (Dogruer *et al.* 2008) also dealt with low speed application, the importance of minor losses seemed to be buried in the fact that the classical Bingham-plastic model can accurately handling most of the MR devices modeling issues without consideration of minor losses in low speed ranges as most past researches did. Few studies to date in the MR literature have correlated minor losses to off-state forces, as well as reported reductions in dynamic range as impact speed increases. A key reason is that application of MREAs to high speed impact situations has only recently emerged.

Nevertheless, the pilot studies on MREAs under impact conditions have shown that MREA analysis based on quasi-steady Bingham plastic analysis (Gavin *et al.* 1996; Peel *et al.* 1996; Wereley and Pang 1998) and BP model (Mao *et al.* 2005),

which is deemed sufficient for MR devices design and performance characterization, is not adequate to describe MREA behavior when high speed impact loadings take place, such as in the low speed vehicle collisions in this work, and thus exhibited poor quality for MREA design purpose. Therefore, in this work, a nonlinear analytical MREA model, taking into account the effects of minor losses factors (called the BPM model), is developed based on the Bingham-plastic (BP) model. Using this BPM model, an effective design strategy is proposed for an MREA, and a candidate design is developed. Before its actual manufacture, the MREA off-state performance was further examined using CFD (computational fluid dynamics) simulations using commercial software ANSYS with the FLOTRAN module. It will be shown that forces predicted using the CFD solutions match well with the predictions from the BPM model at various representative piston velocities. An MREA was then fabricated and tested up to an effective piston velocity of 5 m/s using the high speed drop tower facility at the GM R&D Center. The good agreement of the modeling results with the experimental data shows that the BPM model accurately predicts the off-state performance of the MREA, which was designed based on the BPM model, for these drop test impact conditions. The key conclusion of this study is that the BPM model is capable (where the BP model is not) of predicting the MREA passive force vs. velocity performance and provides an effective MREA design tool for the entire speed range of impact conditions in this study. Note that, some contents of this chapter have already been published in our conference paper (Mao *et al.* 2009).

2.2 MREA (MR Damper) Models

2.2.1 Bingham Plastic Nonlinear Flow Model (BP Model)

A schematic diagram of annular duct type MR valve in a typical flow-mode MREA (or interchangeably called MR damper in this study) is presented in Figure 2.2. According to the Bingham-plastic nonlinear flow model (BP model), which considers laminar and turbulent flows (White 1986; Franzini and Finnemore 1997; Mao *et al.* 2005), the damping force, F , of the MR damper is given by:

$$F = \Delta P_\eta \cdot A_p + (\Delta P_{MR} \cdot A_p + F_f) \cdot \text{sgn}(V_p) \quad (2.1)$$

where

$$\Delta P_\eta = \rho g h_f = f \frac{\rho L V_d^2}{2 D_h} \quad (2.2)$$

and

$$\Delta P_{MR} = \frac{4 L \tau_y}{D_h}. \quad (2.3)$$

Here, ΔP_η and ΔP_{MR} are the viscous pressure drop and the pressure drop due to MR yield stress respectively, F_f is the friction force. A_p is the effective piston area, V_p , V_d are the piston velocity and the average fluid velocity in the MR gap, respectively. ρ and τ_y are the MR fluid density and yield stress respectively. L (here $L = L_1 + L_2 + L_3$) is the total active MR valve length and D_h is the hydraulic diameter. h_f stands for the viscous resistance head and g is the acceleration due to gravity. f represents the Darcy friction factor and is piecewise determined by the Reynolds number, Re , as follows (White 1986; Franzini and Finnemore 1997):

$$f = \frac{96}{\text{Re}} \quad \text{if } \text{Re} \leq 2000 \quad (2.4)$$

$$f = (1 - \alpha) \frac{96}{2000} + \alpha \frac{1}{\left[1.8 \log_{10} \left[\left(\frac{\varepsilon / D_h}{3.7} \right)^{1.11} + \frac{6.9}{4000} \right] \right]^2} \quad \text{if } 2000 < \text{Re} \leq 4000 \quad (2.5)$$

$$\frac{1}{f^{1/2}} \approx 1.8 \log_{10} \left[\left(\frac{\varepsilon / D_h}{3.7} \right)^{1.11} + \frac{6.9}{\text{Re}} \right] \quad \text{if } \text{Re} \geq 4000 \quad (2.6)$$

where

$$\alpha = \frac{\text{Re} - 2000}{4000 - 2000} \quad (2.7)$$

and the Reynolds number is defined by:

$$\text{Re} = \frac{\rho V_d D_h}{\eta} \quad (2.8)$$

Note that here the critical Reynolds number is taken to be 2000 to more favorably ensure a laminar flow range for $\text{Re} < 2000$ (Spurk and Aksel 2008). ε is the average pipe wall roughness and is about to 0.0016 mm for the MREA in this study. η is the viscosity of the MR fluid. The average fluid velocity, V_d , in the MR gap is given by:

$$V_d = \frac{A_p V_p}{A_d} = \bar{A} V_p \quad (2.9)$$

where $\bar{A} \equiv A_p / A_d$ denotes the area ratio between the effective piston area, A_p , and the cross-sectional area of the MR gap, A_d .

By approximating the annular duct of the MR valve by a rectangular duct, the hydraulic diameter, D_h , is given by (White 1986):

$$D_h = 2d \quad (2.10)$$

where d is the effective MR valve gap width. And the MR gap cross-sectional area, A_d , can be expressed as:

$$A_d = \pi D_b d \quad (2.11)$$

where D_b is the effective MR valve diameter and here $D_b = D_p + d$. Then the viscous pressure, ΔP_η , for a laminar flow is reduced to the most familiar form in the literature as follows:

$$\Delta P_\eta = \frac{12\eta L A_p V_p}{b d^3} \quad (2.12)$$

where b is the circumference of the MR valve and here $b = \pi D_b$.

2.2.2 Bingham Plastic Nonlinear Flow Model With Minor Losses (BPM Model)

In this section, minor losses will be incorporated into the BP model. For any pipe system, in addition to the Darcy-friction loss (or Moody-type friction loss), there are additional so-called minor losses due to pipe entrance or exit flows, sudden/gradual contractions or expansions, bends, valves, fittings, and so on. These losses represent additional energy dissipation in the flow, usually caused by secondary flows such as flow separation, eddies, and wakes that are generated by changes in flow direction, cross-section or other pipeline geometry.

Minor losses typically play a minor role in long pipelines, and are often neglected. However, minor losses play an important role in MREAs (Dixon 1999), especially in the case of high piston velocity such as under impact loading, because flow passages in MREAs are relatively short and geometrically complicated.

Because flow patterns associated with minor losses are quite complex, the theory is semi-analytical. The losses are usually measured experimentally and

correlated with pipe-flow parameters. Measured minor losses are generally expressed as a ratio of the head loss, $h_m = \Delta P / (\rho g)$, through the device to the velocity head $V^2 / (2g)$ of the associated pipe flow, that is, the minor losses coefficient, K_m , is given by:

$$K_m = \frac{h_m}{V^2 / (2g)} \quad (2.13)$$

Here V is the mean velocity of the associated fluid flow. Factors affecting the value of K_m include the exact geometry of the component in question, the Reynolds number and proximity to other fittings, etc. A number of minor loss coefficients for different fittings, components, and flow passages, can be found in the literature (White 1986; Idelchik 1994).

A single flow system may have many minor losses. The total minor loss, h_{m_tot} , is a linear combination of the component loss factors:

$$h_{m_tot} = \sum_i K_{m_i} \frac{V_i^2}{2g} \quad (2.14)$$

Here, g is the gravity acceleration, K_{m_i} stands for the i^{th} minor loss coefficient in the flow system and V_i is the corresponding mean fluid velocity associated with this minor loss coefficient. Then the pressure drop resulting from these minor losses, ΔP_{ml} , is:

$$\Delta P_{ml} = \rho g h_{m_tot} = \rho \sum_i K_{m_i} \frac{V_i^2}{2} \quad (2.15)$$

Adding the pressure drop from minor losses into the Bingham-plastic nonlinear flow model, the MREA force is given by:

$$F = (\Delta P_\eta + \Delta P_{ml}) \cdot A_p + (\Delta P_{MR} \cdot A_p + F_f) \cdot \text{sgn}(V_p) \quad (2.16)$$

Note that the minor loss pressure drop is strongly dependent on the exact geometrical profile of the fluid circuit in the MREA. In a later section, an MREA configuration is examined to demonstrate the usage of the BPM model for purposes of MREA design and performance prediction.

2.3 MREA Design Using BPM Model

2.3.1 MREA Configuration and Geometric Fluid Circuit

An MREA was designed using the BPM model. A schematic of the MREA is depicted in Figure 2.3. This MREA is double-ended (a rod on either side of the piston), and a 3-stage electromagnetic coil was placed inside the piston head, which moves together with the piston rod assembly. The two piston rods have the same diameter and protrude through the hydraulic cylinder caps on either side of the MREA. Because no change in volume is induced as the piston rod moves, an accumulator is not required.

The corresponding schematic diagram of the geometric fluid circuit with minor loss regions is presented in Figure 2.4. In Figure 2.4, the numbers from 0 to 10 denote flow regions and the blue arrows indicate the flow directions. In addition to the Darcy-friction type viscous force in MR valve segments 2, 4, 6 and 8, other minor loss coefficients include:

- (1) Entrance effect, K_{entry} , for flow from region 1 to 2;
- (2) Sudden expansion, K_{SE} , for flow from region 2 to 3, region 4 to 5, and region 6 to 7;

- (3) Sudden contraction, K_{SC} , for flow from region 3 to 4, region 5 to 6, and region 7 to 8;
- (4) Exit effect, K_{exit} , for flow from region 8 to 9;
- (5) Viscous Darcy-friction loss, in passages 3, 5 and 7.

Note that for flow from region 0 to region 1 and from region 9 to region 10, minor losses arise from changes in flow direction. Compared to other minor losses in regions 2 to 8, however, these are relatively small and are neglected to simplify the analysis. The radii for the sudden expansion pairs 2 to 3, 4 to 6 and 6 to 7 are typically identical, so that the sudden expansion coefficient, K_{SE} , for these three regions is the same. Similarly, sudden contraction regions 3 to 4, 5 to 6 and 7 to 8, all share the same values of the sudden contraction coefficient, K_{SC} .

To generalize the design method using the BPM model for an MREA with multiple stage (n -stage) coils, the design analysis is formulated for a single stage coil and then extended to n -stage coils via the principle of superposition.

2.3.2 Design Analysis and Equations

Figure 2.5 is a schematic of the fluid flow geometry for a one coil conventional MREA. When fluid flows from region I to region III, the total minor losses pressure drop has 3 components:

- (1) Sudden expansion, for flow from region I to II;
- (2) Sudden contraction, for flow from region II to III;
- (3) Viscous Darcy-friction loss in the annular gap between the inner surface of the outer cylinder and the outer surface of the coil (region II, referred to as the coil gap).

In Figure 2.5, the symbols represent the geometrical dimensions of the components of the flow system and their respective meanings are:

L_a : the active length of the MR valve (regions I and III) associated with one coil

L_c : the length of the coil

d : the MR valve thickness

d_c : the coil gap thickness

D_{in} : the inner diameter of the outer cylinder (or flux return)

D_b : the effective MR valve diameter ($D_b = D_{in} - d$)

D_p : the piston diameter ($D_p = D_{in} - 2d$).

The pressure drop due to the MR yield stress associated with this coil can be expressed as:

$$\Delta P_{MR_1} = \frac{2L_a \tau_y}{d} \quad (2.17)$$

The passive pressure drop, ΔP_{off_1} , is given by:

$$\Delta P_{off_1} = \Delta P_{\eta_1} + \Delta P_{ml_1} + \Delta P_{coil_1} \quad (2.18)$$

where ΔP_{η_1} is the passive viscous pressure drop along the MR gap, ΔP_{ml_1} and ΔP_{coil_1} are the minor loss pressure drops and passive viscous pressure drop induced by the coil gap, respectively. By correlating with the specific geometric dimensions shown in Figure 2.5, they are derived as:

$$\Delta P_{\eta_1} = \frac{\rho}{2} V_d^2 \cdot \frac{f L_a}{2d} \quad (2.19)$$

$$\Delta P_{ml_1} = \frac{\rho}{2} V_d^2 \cdot (K_{SC} + K_{SE}) \quad (2.20)$$

$$\Delta P_{coil_1} = \frac{\rho}{2} V_c^2 \cdot \frac{f_c L_c}{2d_c} \quad (2.21)$$

Here, V_c is the average fluid velocity in the coil gap and can be computed from the following equation:

$$V_c = \frac{A_p V_p}{A_c} \quad (2.22)$$

where A_p is the effective piston area and A_c is the effective coil gap cross-sectional area, and are related to the geometric parameters in Figure 2.5 as given below:

$$A_p = \frac{\pi}{4} (D_p^2 - D_r^2) \quad (2.23)$$

$$A_c = \pi (r_o^2 - r_i^2) \quad (2.24)$$

$$r_o = D_{in}, \quad r_i = D_{in} - d_c \quad (2.25)$$

Note that D_r is the rod diameter (that is shown in Figure 2.3a). K_{SC} and K_{SE} are the sudden expansion and sudden contraction coefficients, respectively. They are determined using empirical formulae (White 1986):

$$K_{SE} = \left(1 - \frac{A_d}{A_c}\right)^2 \quad (2.26)$$

$$K_{SC} = 0.42 \left(1 - \frac{A_d}{A_c}\right) \quad (2.27)$$

Note that alternative semi-empirical formulae for these two minor loss coefficients are available in Idelchik (1994). In this study, Eqs. (2.26) and (2.27) are chosen for simplicity without loss of accuracy. Here, f and f_c are the Darcy-friction factors of the MR gap and the coil gap, respectively. For the Darcy-friction factor of the coil gap, an annular duct model is used because the coil gap is generally designed to be at

least two or three times larger than the MR gap. According to White (1986), f_c can also be calculated from Eqs. (2.5) and (2.6) by replacing Re and D_h with the following Re_{eff} and D_{eff} for $Re_{eff} > 2000$:

$$Re_{eff} = \frac{\rho V_c D_{eff}}{\eta} \quad (2.28)$$

$$D_{eff} = \frac{1}{\zeta} D_{hc} = \frac{1}{\zeta} 2(r_o - r_i) \quad (2.29)$$

$$\zeta = \frac{(r_o - r_i)^2 (r_o^2 - r_i^2)}{r_o^4 - r_i^4 - (r_o^2 - r_i^2)^2 / \ln(r_o / r_i)} \quad (2.30)$$

When $Re_{eff} \leq 2000$, it is given by:

$$f_c = \frac{64}{Re_{eff}} \quad (2.31)$$

For simplicity, we define:

$$\Delta P_{TML_{-1}} = \Delta P_{ml_{-1}} + \Delta P_{coil_{-1}} \quad (2.32)$$

Then for an MREA with n -stage coil (where n is a positive integer), and neglecting the friction force F_f , the relationship between the passive pressure drop per coil, $\Delta P_{off_{-1}}$, and the field-off force, F_{off} , is:

$$F_{off} = (n \cdot \Delta P_{off_{-1}} + \Delta P_{EE}) \cdot A_p = [n \cdot (\Delta P_{\eta_{-1}} + \Delta P_{TML_{-1}}) + \Delta P_{EE}] \cdot A_p \quad (2.33)$$

Here, ΔP_{EE} is the minor loss pressure drop due to sharp entrance and exit effects and is empirically estimated by (White 1986):

$$\Delta P_{EE} = \frac{\rho}{2} V_d^2 \cdot (K_{entry} + K_{exit}) \quad (2.34)$$

In this analysis, K_{entry} takes the typical constant value of 0.5 and $K_{exit} = 1$.

Similarly, the MR effect pressure drop per coil, ΔP_{MR_1} , is related to the MR yield force of the n -stage coil, F_{MR} , by:

$$F_{MR} = n \cdot \Delta P_{MR_1} \cdot A_p = n \cdot \frac{2L_a \tau_y}{d} A_p \quad (2.35)$$

2.3.3 Design Strategy

Although the equations involved in the design analysis of the MREA appear to be complicated, there are only two characteristic equations for designing the valve geometry, namely, Eqs. (2.33) and (2.35). In the design stage, usually the fluid properties ρ, η, τ_y and the MREA performance requirements F_{off}, F_{MR} at the maximum piston velocity, V_p , are specified. The unknown variables in Eqs. (2.33) and (2.35) are $D_{in}, D_r, d, d_c, L_a, L_c$, all of which are explicit when fully expanding these two equations. However, there are six unknowns with only two equations. Mathematically, the design solution is not unique. Thus, we transform the design problem to be an optimization problem by minimizing the following cost function with these 6 unknowns:

$$Z = \min \left| \frac{F_{off_obj} - \hat{F}_{off}(D_{in}, D_r, d, d_c, L_a, L_c)}{F_{off_obj}} \right| \quad (2.36)$$

where $|\cdot|$ is the absolute value operator, F_{off_obj} is the specified off-state objective force and \hat{F}_{off} denotes the analytical off-state force estimated from Eq. (2.33). The feasible solutions lie in the subspace satisfying $Z \approx 0$. We can pick the most reasonable solutions from the subspace for further electromagnetic coil design and magnetic field strength verification using finite element analysis (FEA). Final solutions would be those achieving the desired magnetic field strength.

Since it is impractical to have an explicit closed-form analytical solution for the optimization problem of Eq. (2.36), we must resort to numerical techniques. Various numerical techniques for solving optimization problems can be adopted to solve the design problem here. For simplicity, we used a rather intuitive and straightforward way to solve the design problem by gradually reducing the number of unknown variables via logical means. To do so, we developed a strategy to determine design variables numerically. Unlike the strategy in our prior work (Mao *et al.* 2005), this strategy applies to MREA designs with loss factors due to velocity squared effects for both laminar and turbulent flows. The procedure that was used follows:

- (1) Specify the numerical values of ρ, η and desired τ_y and design specifications of F_{off}, F_{MR}, V_p ,
- (2) Empirically assume the proper sizes of D_{in} and D_r based on imposed practical MREA space constraints, material strength requirements, size charts of standard sealing parts involved, etc. Unknown design variables have been reduced to four.
- (3) Assume the number of coil stages, n , with the help of the required maximum MR yield force, F_{MR} , and achievable τ_y . Usually, the integer number n varies from 1 to 4.
- (4) Initially guess an empirical value for the MR valve gap d . Typically, it is assumed to be in the range of 0.5 mm to 2 mm. Thus far, the numerical value of L_a can be determined from Eq. (2.35), and the left side of Eq. (2.33) can be derived. Thus, only two additional design variables are unresolved.

- (5) Define $x = d_c/d$ (or $y = L_c/L_a$), list a reasonable range of x (or y) as a vector. Then substitute $d_c = x \cdot d$ (or $L_c = y \cdot L_a$) into Eq. (2.33) and solve the equation to obtain a corresponding value of L_c (or d_c).
- (6) Calculate Z with previously obtained values of the related variables. The solutions are those satisfying $Z \approx 0$. Pick one or more sets of the most reasonable solution pairs of (d_c, L_c) with the values of (d, L_a) to design the magnetic circuit and verify the magnetic field for the desired MR yield stress (usually, FEA is used). If the solution pair meets the desired magnetic field, then the design is done. If not, either repeat to choose remaining pair of (d_c, L_c) , or repeat steps (4) to (6), or steps (3) to (6), or steps (2) to (6), as necessary.

For clarity, the design procedure is also summarized as a computational flow chart shown in Figure 2.6. Note that the proposed design strategy is particularly tailored to the MREA shown in Figure 2.4 with the MR valve shown. If the MREA uses a different valve configuration, the designer must examine the geometric profile of the flow system and determine key minor loss components. System equations must be developed for the desired valve geometry, similarly to what was done here in the design analysis using the BPM model. Then, a similar design procedure can be adopted to solve the design parameters with the help of numerical computational software.

2.3.4 Example Implementation of the Design Strategy

An MREA was designed using the proposed design strategy. The design objective is: field-off force should be no more than nominally 15 kN and maximum

field-on force should be no less than nominally 21 kN at a peak piston velocity of 4.5 m/s.

Considering friction from seals, the design specification for the MREA was adjusted to be: $F_{off_obj}=14.85$ kN and $F_{MR_obj}=6.15$ kN at $V_p=4.5$ m/s. The MR fluid properties were: $\rho = 3522$ kg/m³, $\eta = 0.072$ Pa-s, $\tau_y = 60$ kPa at $H=172$ kA/m (corresponding to a magnetic field strength of 0.7 Tesla in the MR valve gap). These values completed step (1).

For step (2), based on the design constraints imposed on the MREA total size and the size chart for standard sealing parts (such as piston ring, U-cap), $D_{in} = 1.625''$ and $D_r = 0.625''$. The number of coil stages, n , was chosen to be 3.

For steps (4) to (6), we used the following technique with the help of the commercial computation software MATLAB to facilitate and visualize the numerical design procedure:

Given the initial guess of d , then L_a can be obtained. Let $x = linspace(1,5,401)$ and $y = linspace(0.5,4.5,61)$, then Z can be derived by substituting the vectors $d_c = x \cdot d$ and $L_c = y \cdot L_a$ into the related equations. Exploiting MATLAB graphical capabilities, the plot of Z versus x and y can be visualized. Then the pairs of (x,y) satisfying $Z \approx 0$ (within acceptable tolerances) are solutions satisfying the design specifications.

For the design problem here, firstly, we initially guess $d=0.6$ mm, but no solution exists for $Z \approx 0$, as can be seen in Figures 2.7. Then we repeat steps (4)-(6) with several different initial guesses of d and finally chose $d = 0.91$ mm as shown in Figures 2.8. It can be seen that many pairs of (x,y) can satisfy the relationship $Z \approx 0$,

and two example points of (x,y) are explicitly indicated in Figure 2.8b. Note that in Figures 2.7 and 2.8, values of Z are not shown as absolute values, but the signed values.

We chose the pair of (4.03, 1.22) corresponding to $d_c=3.67$ mm and $L_c=18.5$ mm for further magnetic circuit design, which has a shorter electromagnetic coil, and thus a shorter MREA. After magnetic field verification via analysis and FEA simulation, the final refined parameter values are: $D_{in}=1.625''$, $D_r=0.625''$, $d=0.91$ mm, $d_c=3.67$ mm, $L_c=18.6$ mm, $L_a=15.2$ mm (total MR active length would be 45.6 mm); the maximum achievable magnetic field is 0.7 Tesla corresponding to an MR fluid yield stress of 60 kPa with applied current of 3.25 A for 24 AWG magnetic wires. The FEA result for the magnetic field verification is shown in Figure 2.9. The predicted MREA performance using the BPM model with these geometric values and fluid properties is presented in Figure 2.10. As seen in this figure, the predicted off-state and maximum field forces of the MREA are: $F_{off}=14.83$ kN and $F_{on}=20.99\approx 21$ kN at the piston velocity of $V_p=4.5$ m/s.

2.4 Steady State CFD Simulations

In the above MREA design using the BPM model, the minor loss coefficients are semi-analytical estimates based on formulae from White (1986), and are determined by approximating the gap/duct geometry by equivalent pipe systems. Thus, there is a degree of uncertainty in these values. To further verify the performance of the MREA design, CFD simulation using the commercial software

package ANSYS (particularly, FLOTTRAN) was carried out to derive the field-off force to compare with the analytical prediction from the BPM model.

MREA is axis-symmetric about its shaft axis, so that 2D axisymmetric analysis was used to represent flow in the MREA. The CFD computational domain with its meshed elements is displayed in Figure 2.11. A finite element mesh is required for this CFD analysis. The fluid in the computational domain is assumed to be incompressible and adiabatic. No-slip boundary conditions are applied at the lines representing the interaction surface between the fluid and solid structure.

Figure 2.12 presents convergence of CFD simulation results versus the number of element meshes. As seen in this figure, the simulation results converge when the number of elements in the mesh was more than about 10,000 elements. Thus, in this study, 10,230 elements were used.

Figure 2.13 compares off-state (zero-field) forces of the MREA predicted by the BPM model and CFD simulation. As seen in this figure, the off-state force from FEA simulation substantially agrees with off-state BPM model result.

The MREA design was validated using CFD simulation. The MREA was then manufactured using the geometric dimensions determined using the design procedure.

2.5 High Speed Drop Tower test

2.5.1 High Speed Drop Tower Test Set-up

The MREA was tested using the high speed drop tower facility at the GM R&D Center (see Figure 2.14). The MREA was attached firmly to the top surface of the mounting plate and aligned with its central axis perpendicular to the ground plane. A small block of aluminum honeycomb was attached using double sided tape to the

small flat plate that had been mounted to the upper end of the MREA rod. This honeycomb cube served to eliminate the ringing in the load cells due to metal-to-metal impact which would have otherwise occurred and also helped to diminish the inertial spike associated with the impact of the drop mass upon the piston/rod. The large blocks of aluminum honeycomb positioned to the side of the test device as seen in Figure 2.14 were used to arrest the drop platform after approximately 7.5 cm of stroke in those cases in which the drop energy exceeded the energy absorbing capability of the MREA. Instrumentation included an accelerometer mounted to the drop platform, four load cells positioned beneath the mounting plate and a linear variable displacement transducer (LVDT) mounted to the MREA that provided the amount of stroke as a function of time.

To conduct a test, the MREA rod was fully extended, the drop tower raised to the drop height corresponding to a pre-selected impact velocity, a pre-selected amount of current applied to the MREA, and the drop platform released to fall freely under the action of gravity until striking the MREA test assembly. Data from each of four load cells plus the LVDT and accelerometer were recorded. The sampling rate was 10 kHz. A high speed digital video record was made of each impact test. More complete descriptions of the theory behind the testing protocols and the practical aspects of impact testing using a free-flight drop tower facility are given in Browne and Johnson (2001), Johnson and Browne (2001) respectively.

2.5.2 Test Results

Drop tests were conducted for nominal drop speeds ranging from 1 m/s to 6 m/s with 1 m/s increments. The applied current varied discretely from 0 A, 1.0 A, 2.0 A to 3.25 A for each nominal drop speed.

In the data acquisition system, signals from each of four load cells and the LVDT were sampled at a rate of 10 kHz and pre-filtered with an SAE (Society of Automotive Engineers) CFC (channel frequency class) 1000 filter (i.e., cutoff frequency of 1650 Hz). The LVDT signal was also differentiated to calculate the piston velocity. Based on the SAE J211 in Huang (2002), it is reasonable to choose CFC 60 (i.e., cutoff frequency of 100 Hz) to filter the recorded load cell data for MREA force evaluation and CFC 180 (i.e., cutoff frequency of 300 Hz) to filter LVDT data for MREA stroking and velocity evaluation. The filter selection was further justified by the power spectra analysis of force and velocity signals for sample data at a nominal drop speed of 6 m/s as in Figure 2.15. As seen in this figure, power in the force signals was concentrated below 100 Hz, and in the velocity signals below 125 Hz. Therefore, it is appropriate to filter the wideband data by CFC 60 for impact forces and by CFC 180 for impact velocities.

Samples of test data are plotted in Figures 2.16 and 2.17. For nominal drop speeds of 2 m/s, the peak piston velocity rises to more than 2 m/s at 0A and decreases as applied current increases (refer to Figure 2.16b). It is also observed that, the peak piston velocity at a nominal drop speed of 6 m/s only reaches 5 m/s for various current levels. Therefore, in this study, the peak piston velocity rather than the nominal drop speed will be used to characterize the MREA force vs. velocity

behavior. In addition, the MREA peak force and peak velocity pair are of key interest because they indicate the upper limit of MREA capability. Therefore, in this study, the peak force and peak piston velocity in the drop impact test are used as the key metrics to characterize MREA post-yield behavior.

The measured value pairs of MREA peak force and peak piston velocity at 0 A and 3.25 A are presented in Figure 2.18. Predictions are compared for all analyses: BPM, BP and FEA (off-state only) analyses. It can be seen that the two lines representing predicted off-state force from the BPM model and FEA simulation almost coincide with the experimental data points for applied current of 0A. While the predictions from the BP model (the cyan dash-dot line) underpredict the experimental results to a large degree for higher piston velocities, the BP results converge to the BPM predictions at piston velocities below 0.8 m/s.

For the maximum field-on case at 3.25 A, both BP and BPM models cannot fully capture MREA behavior. The BPM model overpredicts the experimental force above roughly 2.5 m/s, whereas the BP model underpredicts above 1 m/s. Although the BPM model predicts the measured field-on behavior of the MREA much better than the BP model, this being largely due to the accuracy of the BPM model in the off-state. This suggests that the MR yield force predicted by using Eq. (2.3) is not adequate for the high speed range. This deficiency may result from turbulent and recirculation flows induced at high Reynolds number when the MR fluid passing through the MR valve into the coil gap and back into the MR valve for high piston velocity. In this design, a piston velocity of 2.5 m/s corresponds to a Reynolds number of $Re \approx 2000$, which is the laminar flow upper bound. Further efforts are

needed to understand the correlation between the MR yield stress and the high Reynolds number flows to improve the accuracy of these predictions.

Nevertheless, this study demonstrates a noticeable improvement to the widely used BP model and a relatively comprehensive understanding of the MREA behavior under high speed impact conditions. The BP model was sufficient to characterize the MREA force velocity relationship for speeds below 0.8 m/s. However, for speeds above 0.8 m/s, the BP model fails to sustain its accuracy. On the other hand, the results show that the BPM model can more accurately capture the MREA field-off force velocity behavior for both low speed excitations and high speed impact loadings. In addition, the BPM model can be also effectively used for an MREA design for impact load conditions.

Thus far, the effectiveness of the BPM model for MREA design and performance prediction (especially in off-state) under high speed impact conditions is experimentally validated.

2.6 Unsteady Transient Analysis of MREA Force

2.6.1 Governing Equations

The above drop test results analysis and validation of BPM model are performed in terms of the peak force and peak piston velocity extracted from the transient drop test data with an implicit assumption that the MR fluid flow in the MREA system is of steady state regardless laminar or non-laminar flow status. We also need to find a way to describe the MREA dynamic (transient) behavior. To do so, an inertia term will be added in the equation for MREA dynamic behavior prediction. Based on the Bernoulli's equation for unsteady frictionless flow along a streamline from section 1

to section 2 (White 1986), the modified equation to account for Darcy-friction loss and minor losses for incompressible flow is as follows:

$$\int_1^2 \frac{\partial V}{\partial t} ds + \int_1^2 \frac{dP}{\rho} + \frac{1}{2}(V_2^2 - V_1^2) + g(z_2 - z_1) + gh_f + gh_{m_tot} = 0 \quad (2.37)$$

where V is the fluid velocity along the stream line, P is the pressure. V_2 and V_1 are fluid velocity at section 1 and section 2 respectively, z_2 and z_1 are elevation height at section 1 and section 2 to the reference point. Other symbols hold the same meanings as before.

Considering a 1-dimensional parallel plate approximation to the MR valve for simplicity, and multiplying ρ on both sides, Eq. (2.37) is reduced to be:

$$\rho \frac{dV}{dt} \cdot L + P_2 - P_1 + \frac{\rho}{2}(V_2^2 - V_1^2) + \rho g(z_2 - z_1) + \rho gh_f + \rho gh_{m_tot} = 0 \quad (2.38)$$

Rearranging Eq. (2.38), we get the following form of passive pressure drop, ΔP_{pass} , between the entrance (for variables with subscript of 1) and exit (for variables with subscript of 2) of the MR valve:

$$\Delta P_{pass} = P_2 - P_1 = - \left[\rho \frac{dV}{dt} L + \frac{\rho}{2}(V_2^2 - V_1^2) + \rho g(z_2 - z_1) + \rho gh_f + \rho gh_{m_tot} \right] \quad (2.39)$$

According to the law of conservation of mass, for the MR valve here, $V_2 = V_1$. Neglecting the elevation difference between z_2 and z_1 to simplify the analysis, Eq. (2.39) is now further reduced to be:

$$\Delta P_{pass} = P_2 - P_1 = - \rho \left[\frac{dV}{dt} L + gh_f + gh_{m_tot} \right] \quad (2.40)$$

Here dV/dt would be the instantaneous average acceleration of the fluid flow in the MR gap since V is the instantaneous average flow velocity in the MR gap. It can be

approximately derived from the time history data of V_p using Eq. (2.9). L, ρ, g and h_f, h_{m_tot} hold the same meanings as before. Here h_f and h_{m_tot} are obtained by directly applying the associated instantaneous fluid velocity data derived from measured V_p . Then the instantaneous or dynamic MREA passive force, F_{off_t} can be obtained by:

$$F_{off_t} = \Delta P_{pass} \cdot A_p \quad (2.41)$$

Assuming the MR yield stress is kept unchanged, then the total dynamic force at field-on case, F_t , is given by:

$$F_t = F_{off_t} + (\Delta P_{MR} \cdot A_p + F_f) \cdot \text{sgn}(V_p) \quad (2.42)$$

2.6.2 Results

Using Eqs. (2.40)-(2.42) and applying the measured piston velocity from the drop test for each nominal drop speed, the dynamic MREA passive force at field-off case (0A) as well as the dynamic MREA force at field-on case can be obtained. Some sample results are shown in Figure 2.19 and compared with the measured MREA dynamic force in the drop test. To understand how important the inertia force is in the total dynamic force, we neglect the inertia force and compute the dynamic force by directly applying the instantaneous time history of (or measured) piston velocity in the BPM model. The results are also presented in Figure 2.19 and compared with dynamic force including inertia force as well as experimental data. Note that all of the force data (modeling results and experimental results) presented in the figure are filtered with a CFC 60 (i.e., cutoff frequency 100 Hz) filter.

As observed from the figure, for all representative nominal drop speeds, the MREA dynamic force predicted by the unsteady transient analysis including inertia force shows little difference from the dynamic force predicted by the BPM model. In addition, the modeling results at 0A for both drop speeds and 3.25 A for nominal drop speed of 2 m/s agreed very well with the measured data. But for 3.25A and nominal drop speed of 6 m/s, similar to what was demonstrated in Figure 2.18 at 3.25A and piston velocity of 5 m/s, the modeling forces were over-predicted compared to the experimental results. However, all of these results have shown that even though the magnitude of the acceleration of the MR fluid in the MR gap may be very large, its relative small mass makes the inertia force only account for a very small fraction in the total passive dynamic force and can be reasonably neglected. It is concluded that for the MREA and the drop test data presented here, the BPM model can also be directly used to predict the dynamic MREA force.

2.7 MREA Design for the Adaptive Magnetorheological Sliding Seat (AMSS) System

2.7.1 MREA Performance Requirement

To specify a suitable performance requirement for the MREA design for the adaptive sliding seat system, a simple analysis is conducted here. In this project, a maximum deceleration threshold of 20 g is specified for occupants from the 5th female to 95th male under initial impact speed (ΔV) of up to 4.5 m/s. For simplicity, assuming that the occupant and the seat act as a single rigid mass, the maximum force the single rigid mass is allowed would be:

- 5th female: $F = m \cdot a = (49 + 20) \times 20 \times 9.81 = 13.5 \text{ kN}$

- 95th male: $F = m \cdot a = (101 + 20) \times 20 \times 9.81 = 23.7 \text{ kN}$

In the above equations, m represents the total mass of the occupant and the seat. A 5th female's mass is 49 kg and a 95th male's mass is 101 kg. The seat mass is assumed to be 20 kg. Therefore, the maximum allowable off-state force provided by the MREA(s) would be 13.5 kN and the minimum required controllable force would be 10.2 kN (=23.7-13.5). Because in the practical adaptive sliding seat system two identical MREA units would be mounted on each side of the sliding seat in a parallel connection, the maximum off-state force for one MREA design would be 13.5/2=6.75 kN and the controllable MR yield force would be 5.1 kN. These two forces requirements should be met at the maximum MREA piston velocity corresponding to an initial vehicle impact speed (ΔV) of 4.5 m/s. The maximum MREA piston velocities for initial impact speeds up to 4.5 m/s for both 5th female and 95th male are estimated to be below 3 m/s (which will be well demonstrated in the later chapter). Thus, any MREA that is capable to provide an off-state force less than 6.75 kN and a controllable MR yield force of 5.1 kN for piston velocity up to 3 m/s would be sufficient to function in the adaptive sliding seat system.

2.7.2 MREA Design and Predicted Performance

To save time and cost, the example MREA design used to validate the BPM model in the previous section was modified to achieve the MREA performance requirements for the sliding seat system. The cross-sectional view of the modified MREA (later it would be called as SSMREA to specify that it is the MREA particularly for the sliding seat system) is shown in Figure 2.20. As seen in the figure, the double-rod configuration was changed to be a single-rod and a gas accumulator

configuration to meet the imposed space constraints. In addition, the MR gap thickness was increased to be 1.21 mm in order to lower the off-state force. The maximum MR yield stress was kept at 60 kPa by increasing wire turns of each coil and the applied current level from 3.25A to 4.0A. In a summary, the values of the primary parameters of the SSMREA are: $D_{in}=1.625''$, $D_r=0.625''$, $d=1.21$ mm, $d_c=2.67$ mm, $L_c=17.8$ mm, and total MR active length $L=48.8$ mm; the maximum achievable magnetic field is 0.7 Tesla corresponding to an MR yield stress of 60 kPa with applied current of 4.0A for 24 AWG magnetic wires.

To predict the MREA force, the BPM model was used. The empirical estimation of coefficients of K_{SE} and K_{SC} are shown in Eqs. (2.26) and (2.27). K_{entry} and K_{exit} take the typical value of 0.5 and 1.0 respectively. In addition, CFD simulation using ANSYS was also carried out to predict the off-state force and compared with estimations from the BPM model. The predicted SSMREA performance is demonstrated in Figure 2.21. As seen in the figure, the predicted off-state force by CFD analysis appears somewhat discrepancy with the prediction from the BPM model. Since the empirical estimations of minor loss coefficients used in the BPM model have some uncertainties, it is believed that the off-state force by the CFD simulation would be more accurate. Note that in the figure, the force curve indicated by “CFD 4A” is obtained by summation of the off-state force of “CFD 0A” with the MR yield force calculated from Eq. (2.3). To the best knowledge of the author, it is very difficult if not impossible to use ANSYS to simulate the field-on cases due to significant interactions between the MR fluid dynamics and the electromagnetic fields. Thus, we used the FLOTTRAN module in ANSYS to simulate off-state cases to

derive off-state forces. For the on-state, a separate electromagnetic analysis was carried out using ANSYS to predict the magnetic field strength in the MR gap and calculate the MR yield force using Eq. (2.3), in which the MR yield stress is obtained by mapping the FEA magnetic field strength to the corresponding MR yield stress via given or experimentally measured MR fluid property charts. This way of dealing with MR fluid field-on cases is also widely adopted in the literature. Thus, the off-state force is 4.1 kN at piston velocity of 3 m/s and the achievable controllable MR yield force is 4.8 kN. Though the MR yield force is about 6% less than the desired 5.1 kN, it is determined to be acceptable for this project. The fabricated physical parts and the assembled unit of the SSMREA are shown in Figures 2.22 and 2.23 respectively.

2.7.3 Measured SSMREA Performance

The SSMREA was tested using the high speed drop tower facility at the GM R&D center. The experimental set-up was the same as described in section 2.5. Drop tests were conducted for nominal drop speeds ranging from 1 m/s to 5 m/s with 1 m/s increments. The applied current varied discretely from 0A, 2.0A to 4.0A for each nominal drop speed. Figure 2.24 shows the measured peak force versus peak piston velocity at 0A, 2.0A and 4.0A. Figure 2.25 compares the measured peak forces at 0A and 4.0A with the predictions from the BPM model and CFD simulations. As seen in the figure, the experimental forces at 0A and 4.0A better match the predictions from CFD simulations. Hence, it shows that CFD analysis would be more accurate in predicting MREA performance in design stage than the BPM model since the empirical estimations of minor loss coefficients sometimes may not be sufficiently accurate. Nevertheless, the BPM model plays a critical role in an MREA's initial

design stage because it provides a baseline MREA design with specific geometrical dimensions, which is necessary for setting up the CFD geometrical model for simulations in order to predict the MREA performance or refine the geometrical dimensions.

On the other hand, as observed in Figure 2.25, the predictions from BPM model at 0A and 4A using empirical formulas in White (1986) slightly under-estimate the forces. This implies that some of the empirical minor loss coefficients need to be adjusted to more accurately describe the MREA performance. Using the experimental data and parameter identification techniques (least square error), the adjusted sudden contraction and sudden expansion coefficients are: $K_{sc} = 0.48758$ (originally 0.22246) and $K_{se} = 0.5441$ (originally 0.28056).

The results predicted by the BPM model using the adjusted sudden contraction and sudden expansion coefficients are presented in Figure 2.26. It is seen that with the adjusted coefficients, the BPM model can accurately describe the MREA performance at 0A and 4A. However, for the measured MREA force at 4A, though it is overall well described by the BPM model with the adjusted coefficients, the controllable MR yield force still appears a slightly decreasing trend above piston velocity of about 3 m/s (this is more obvious in Figure 2.24), at which the Reynolds number is 2281. This is similar as what we observed in the results analysis of the previous MREA. Thus it indicates the following two aspects for MREA design and MREA modeling:

(1) To avoid significant MR yield force degradation or dynamic range reduction at high Reynolds numbers ($Re > 2000$), whenever possible the MREA should be designed to operate in laminar ($Re < 2000$) flow for all piston speeds of interest.

(2) To make the BPM model more accurate at field-on state when high Reynolds numbers flows ($Re > 2000$) induced, it is essential to understand the effect of the high Reynolds number flows on the post-yield yield stress of an MR fluid. Further theoretical and experimental studies are needed in future work to address this issue.

Furthermore, the MREA dynamic force (force-time history) is also simulated using the BPM model with the adjusted coefficients and some sample results are presented in Figures 2.27. It is shown that the modeling results agree well with the experimental dynamic force. Thus, the BPM model is also valid in describing the transient MREA force as time evolving during the impact period. In other words, given an instantaneous piston velocity, the MREA force at that time instant can be obtained via BPM model. This forms the foundation of the adaptive control of the MREA for the sliding seat system during the impact period. Otherwise, the command current at any time instants to be applied in the MREA during the impact period can by no means be obtained in the controller to implement a control algorithm.

2.8 Summary

In this chapter, a nonlinear analytical model of magnetorheological energy absorbers (MREAs) taking into account effects of minor loss factors (BPM model) was developed based on a simpler Bingham-plastic nonlinear flow model (BP model). An effective design strategy was proposed for a double-ended annular valve type MREA and an example MREA was designed. Before the MREA was actually

manufactured, the MREA performance was further verified using CFD analysis. Then the MREA was fabricated and tested for piston velocities up to 5 m/s using the high speed drop tower facility at the GM R&D Center. Test results showed that the predictions from the BPM model and the CFD analysis agreed well with the experimental data over the tested piston velocity range in the off-state, while the BP model demonstrated large discrepancy for higher piston velocities above 0.8 m/s.

Moreover, to describe the MREA dynamic force (force-time history) under drop impact, an unsteady transient analysis was conducted. The results showed that inertia force only accounts for a small fraction of the total force. The dynamic forces simulated by the BPM model match well with the measured dynamic forces.

Then an SSMREA was designed by modifying the example MREA in order to satisfy the requirements for application in the adaptive sliding seat system. Similarly, the SSMREA was drop tested for piston velocities up to 5 m/s and the experimental results compared well with the modeling results of the BPM model and the CFD simulations at 0A and 4.0A.

In addition, it is shown that the SSMREA dynamic forces predicted by the BPM model also agree well with the measured forces using the adjusted minor loss coefficients. Therefore, the BPM model is proved to be also valid in predicting MREA transient force under impact conditions. This conclusion provides a foundation for the feasibility of the MREA control during impact period because given a measured piston velocity at any time points, the corresponding command current can be determined using the BPM model.

The key conclusions are:

(1) The BPM model can accurately predict the passive MREA force (field-off) for both low speed excitations and high speed impact conditions and is a useful tool for an effective MREA design. It can also well predict the field-on force for flow conditions where Reynolds numbers is up to 2000. For higher Reynolds number flows (particularly $Re > 2000$), further study is needed in future work.

(2) Whenever possible the MREA should be designed to function in laminar flows for all interested piston speed range to avoid significant MR yield force degradation or dynamic range reduction when high Reynolds number flows induced ($Re > 2000$).

(3) The BPM model can be directly used to predict MREA dynamic force under impact conditions so that control of MREA during impact period is feasible.

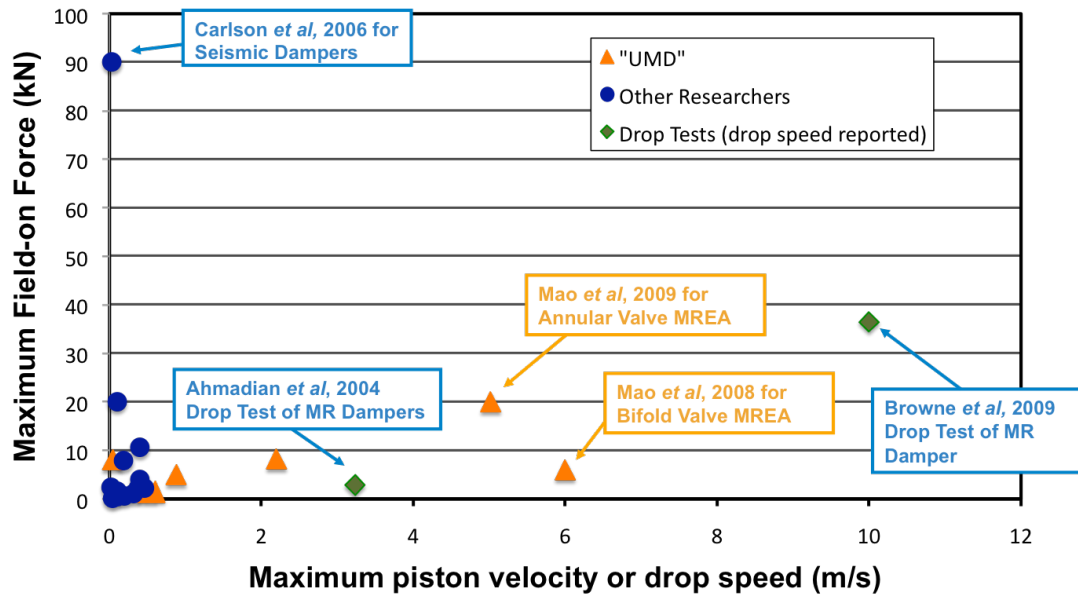


Figure 2.1: Maximum MREA field-on force versus maximum piston velocity (drop speed reported for some research) for most reported researches on MREAs and MR dampers in the literature.

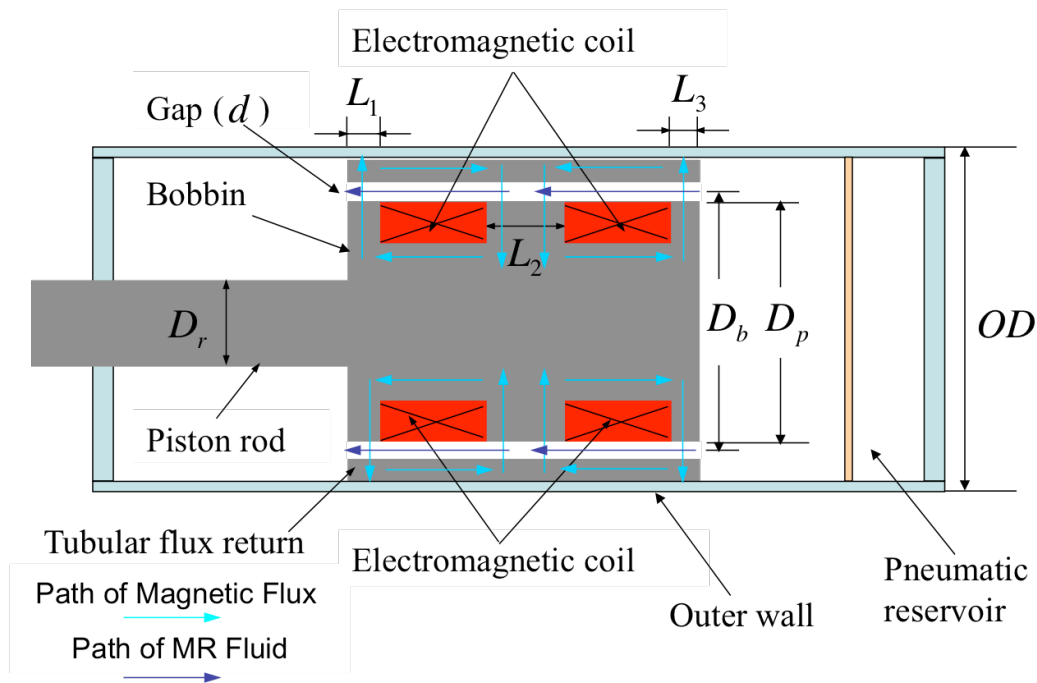
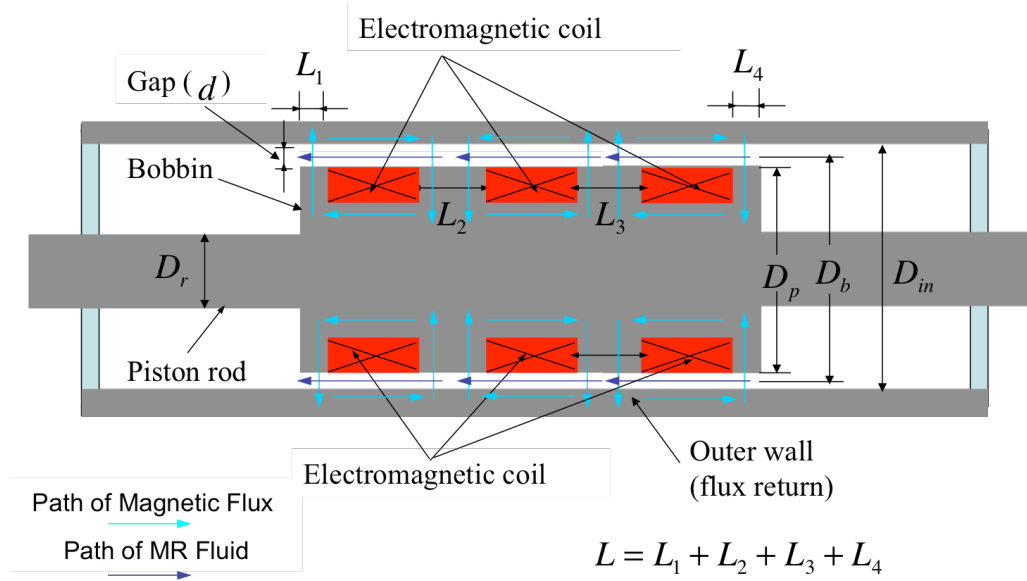
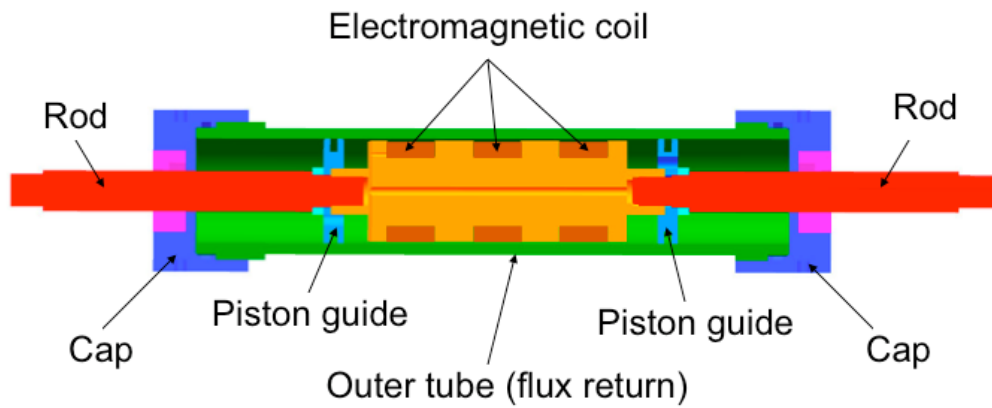


Figure 2.2: Schematic diagram of a typical flow mode MREA.



(a) Schematic diagram



(b) Cross sectional view

Figure 2.3: Schematic diagram and cross sectional view of a typical double-ended conventional (annular duct) MR valve type MREA.

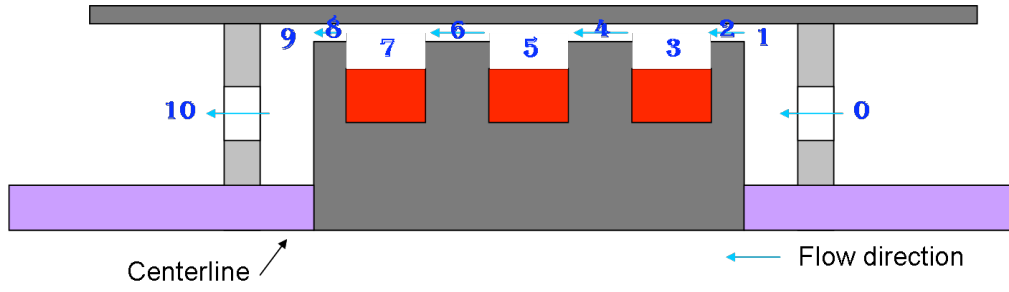


Figure 2.4: Schematic diagrams for flow regions where minor losses coefficients were applied.

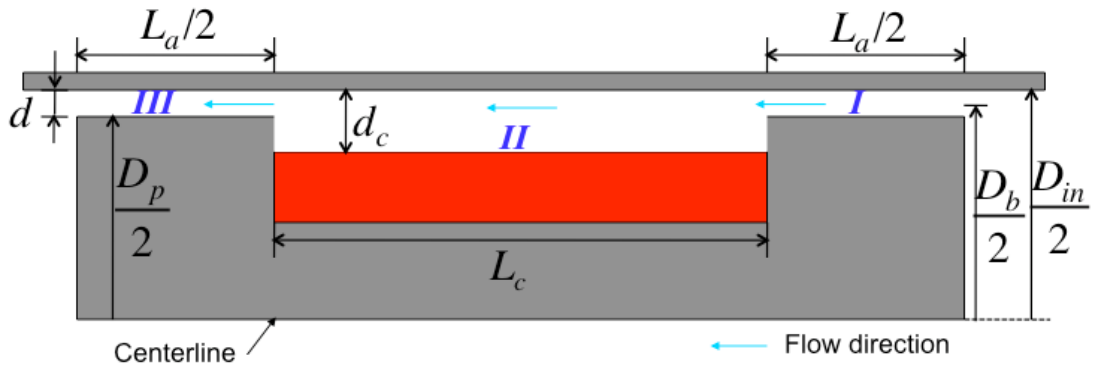


Figure 2.5: Schematic fluid circuit of one coil for a typical conventional valve type MREA.

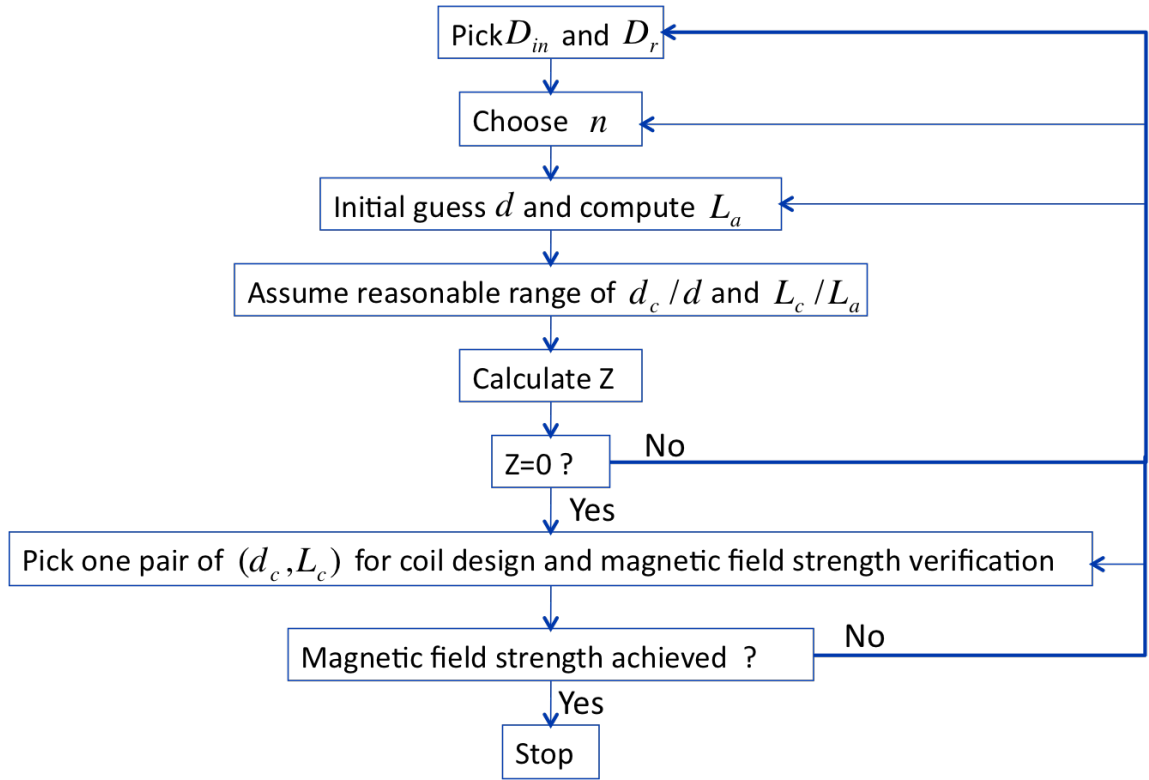
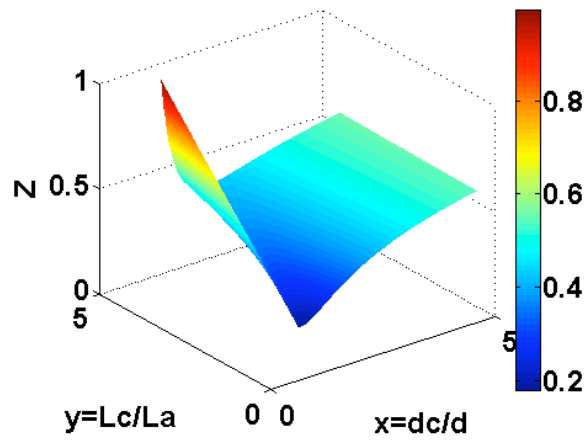
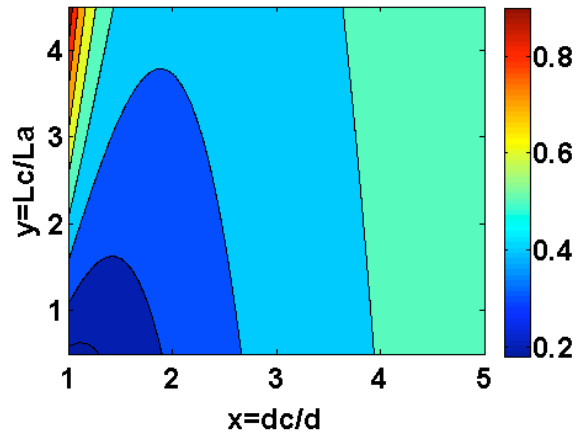


Figure 2.6: Computational flow chart of the MREA design procedure.

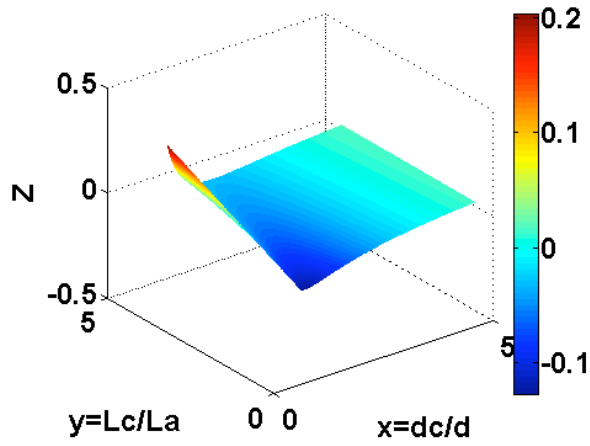


(a) 3-D plot of Z vs. x and y

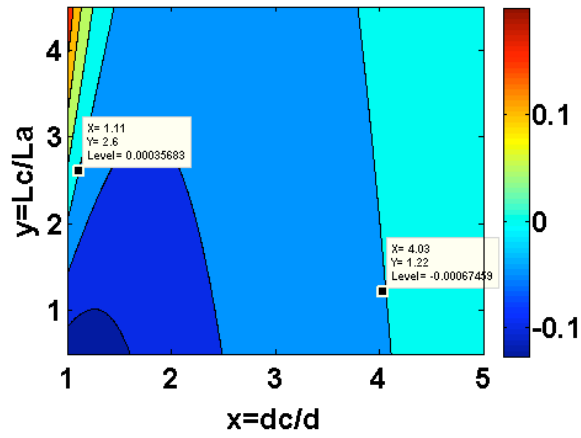


(b) Contour plot of Z

Figure 2.7: Z vs. x and y with $d=0.6$ mm.



(a) 3-D plot of Z vs. x and y



(b) Contour plot of Z

Figure 2.8: Z vs. x and y with $d=0.91$ mm.

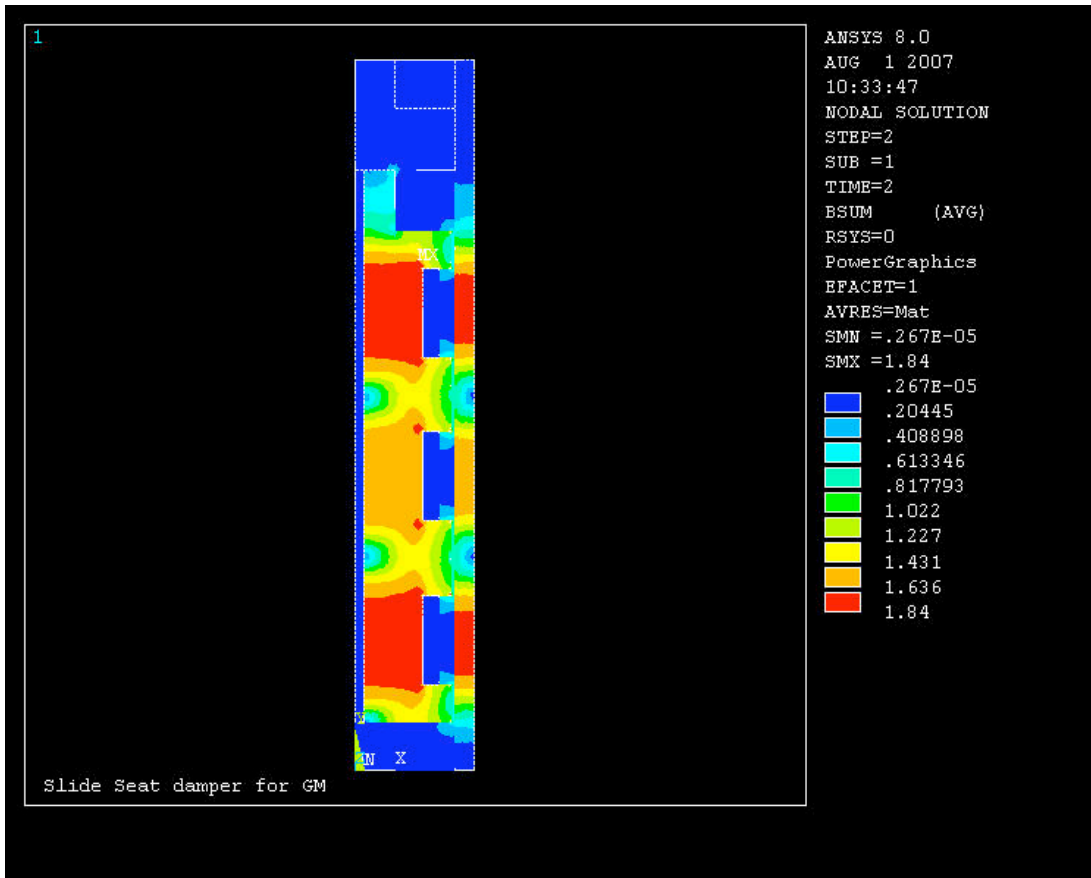


Figure 2.9: FEA magnetic field strength verification for example MREA design.

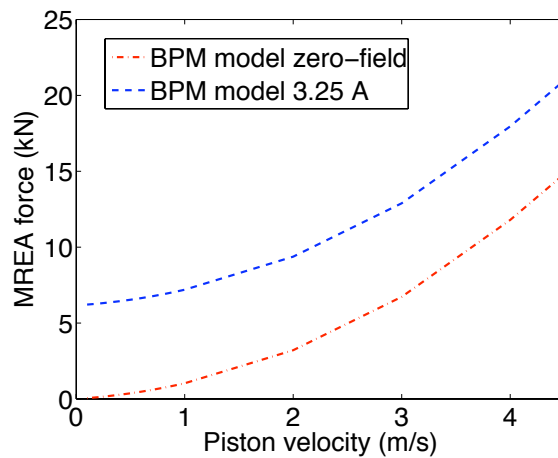


Figure 2.10: Predicted performance by BPM model for the designed MREA.



Figure 2.11: CFD computational domain for the MREA.

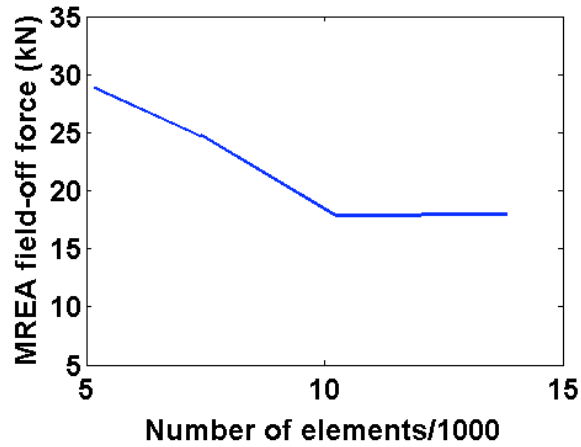


Figure 2.12: CFD elements convergence test.

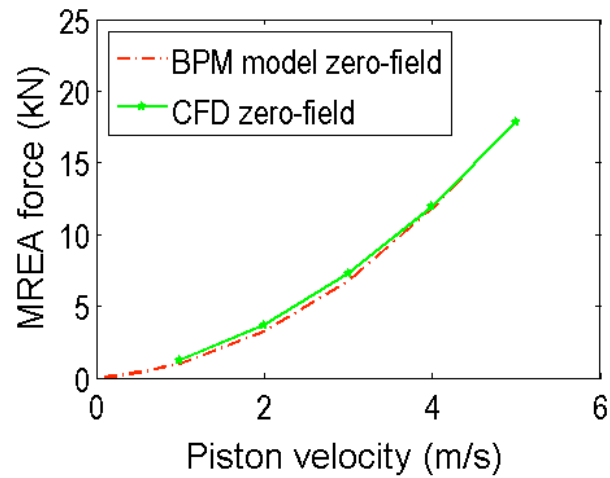
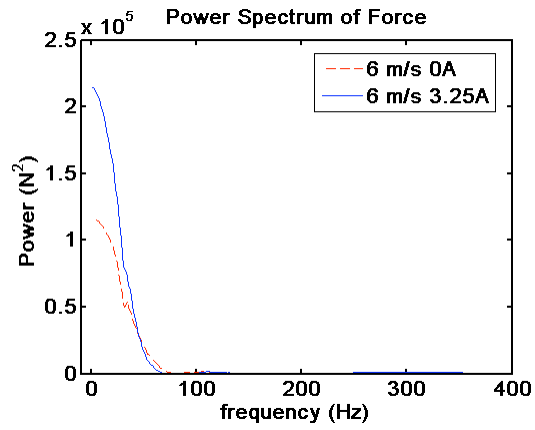


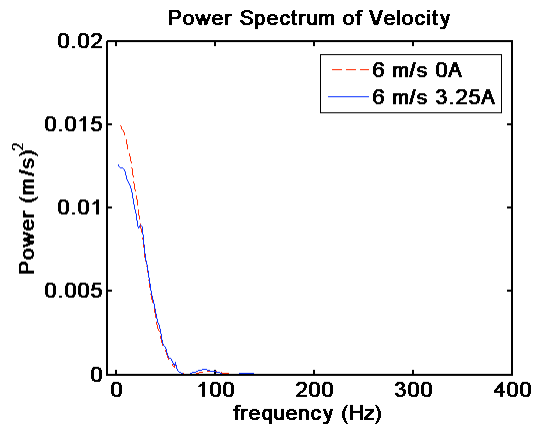
Figure 2.13: Comparison of zero-field force from CFD simulation and BPM prediction.



Figure 2.14: The MREA mounted for drop tower test.

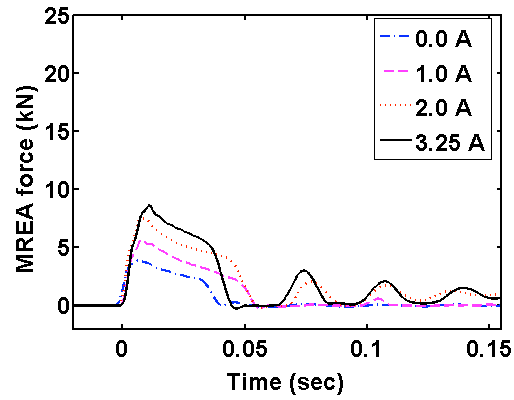


(a) power spectrum of impact forces

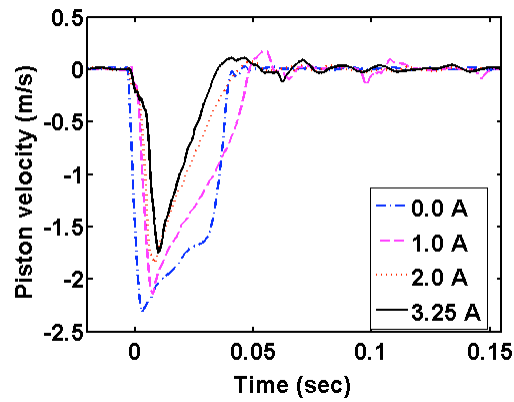


(b) power spectrum of impact velocities

Figure 2.15: Power spectrum of MREA impact forces and velocities at nominal drop speed of 6 m/s.

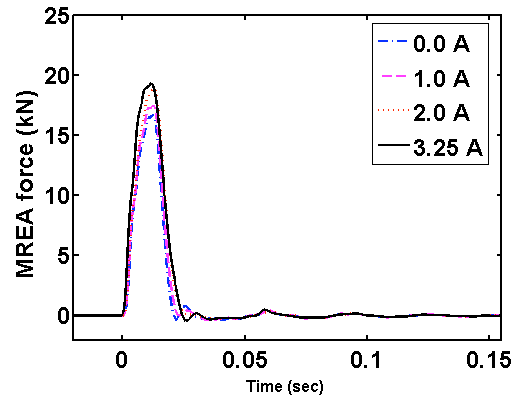


(a) MREA force

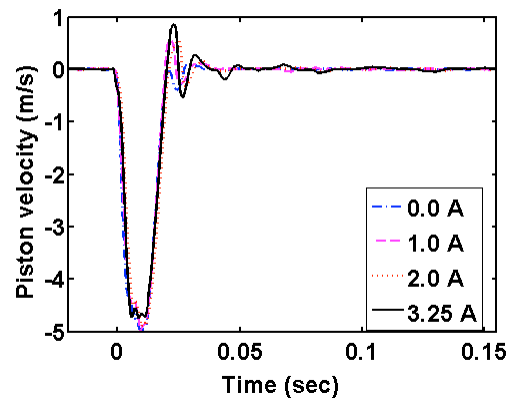


(b) MREA piston velocity

Figure 2.16: Time history of MREA impact force and velocity at nominal drop speed of 2 m/s.



(a) MREA force



(b) MREA piston velocity

Figure 2.17: Time history of MREA impact force and velocity at nominal drop speed of 6 m/s.

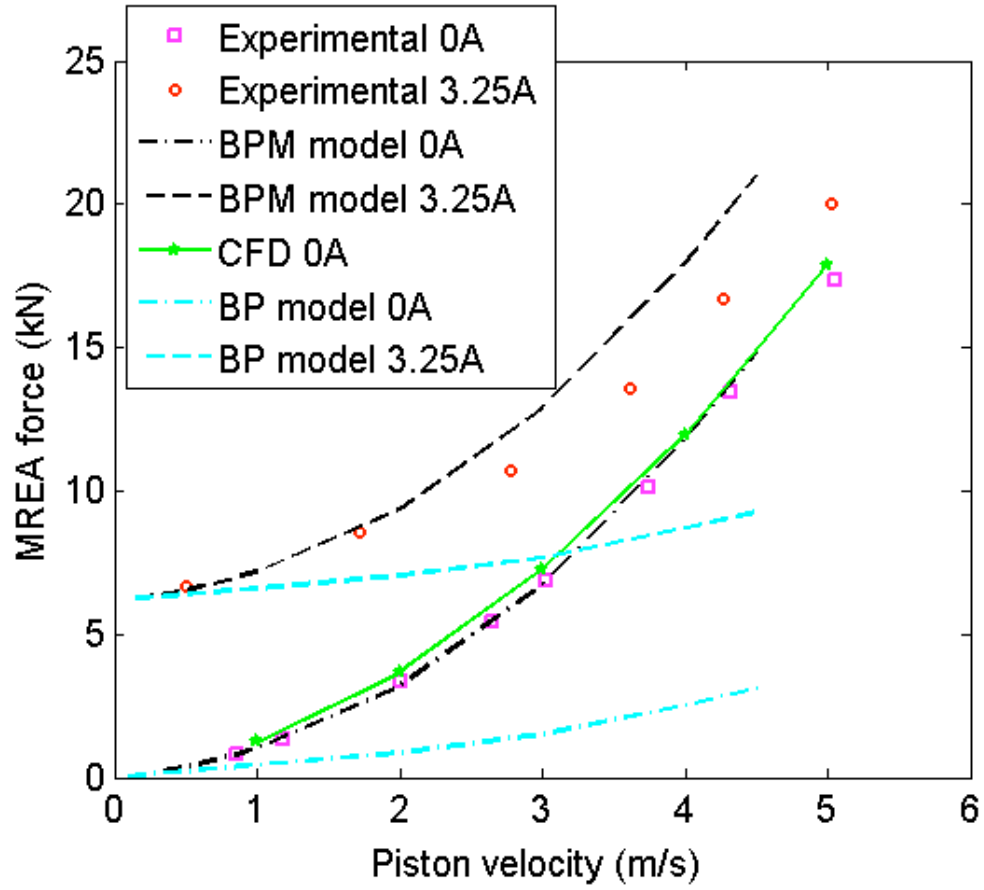
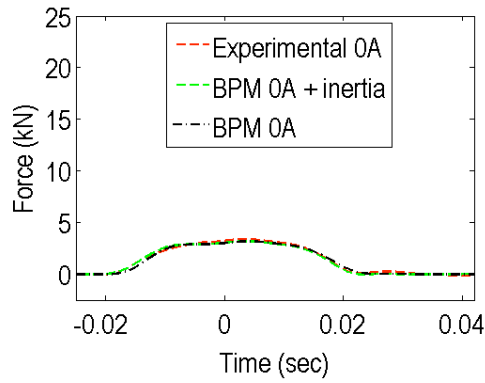
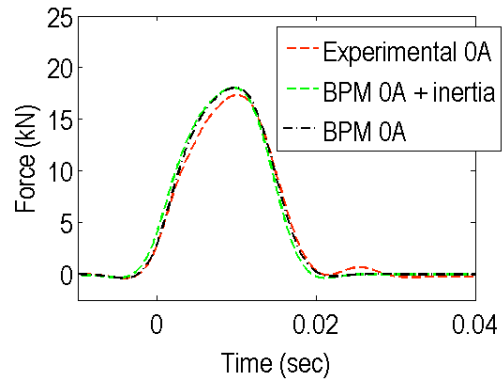


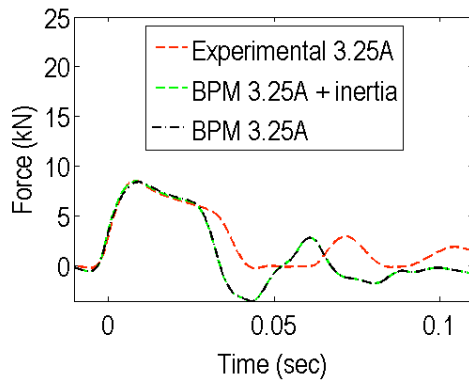
Figure 2.18: Comparisons of MREA force velocity behavior between experimental results and various model predictions.



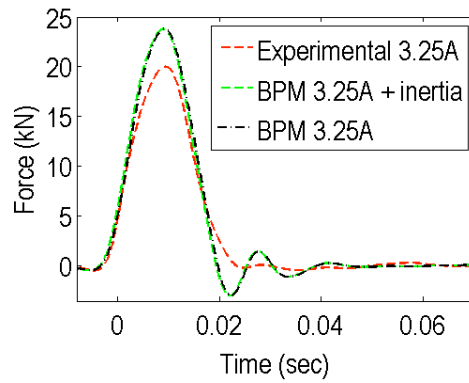
(a) nominal drop speed 2 m/s and 0A.



(b) nominal drop speed 6 m/s and 0A.



(c) nominal drop speed 2 m/s and 3.25A.



(d) nominal drop speed 6 m/s and 3.25A.

Figure 2.19: Unsteady transient results for nominal drop speeds of 2 and 6 m/s as well as comparison with experimental data and prediction from BPM model.

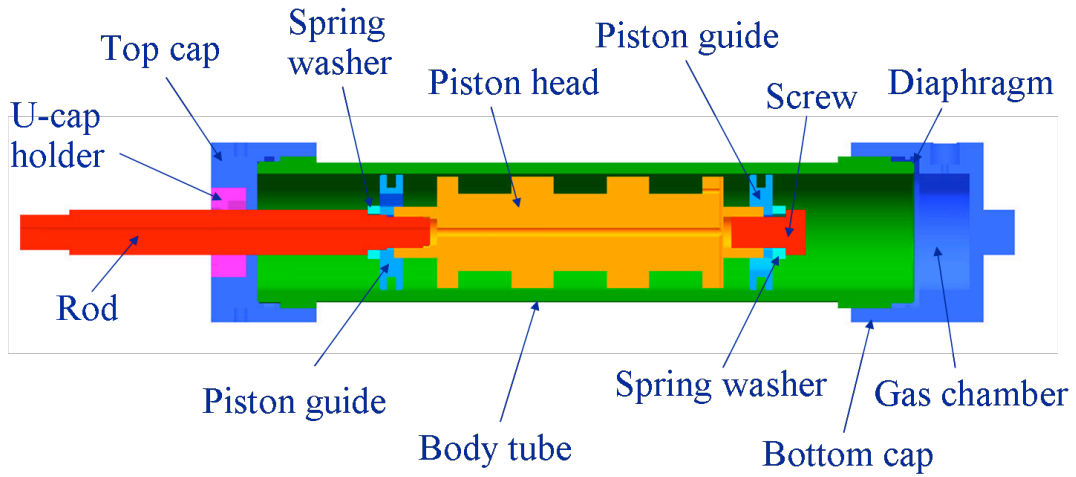


Figure 2.20: Cross-sectional view of the SSMREA.

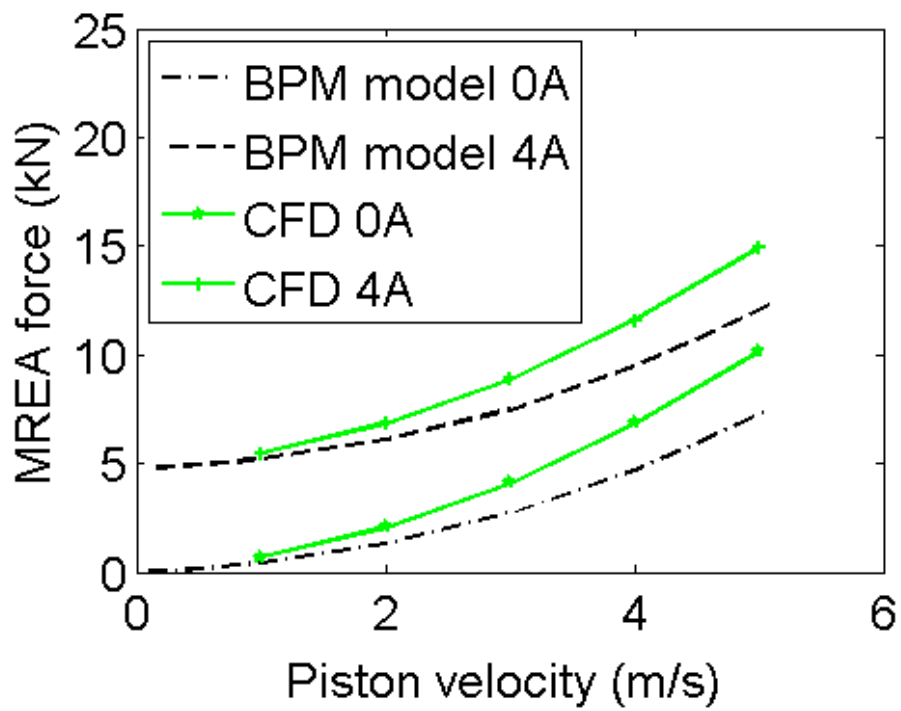


Figure 2.21: Predicted SSMREA performance by BPM model and CFD simulation.



Figure 2.22: Physical parts of the fabricated SSMREA.

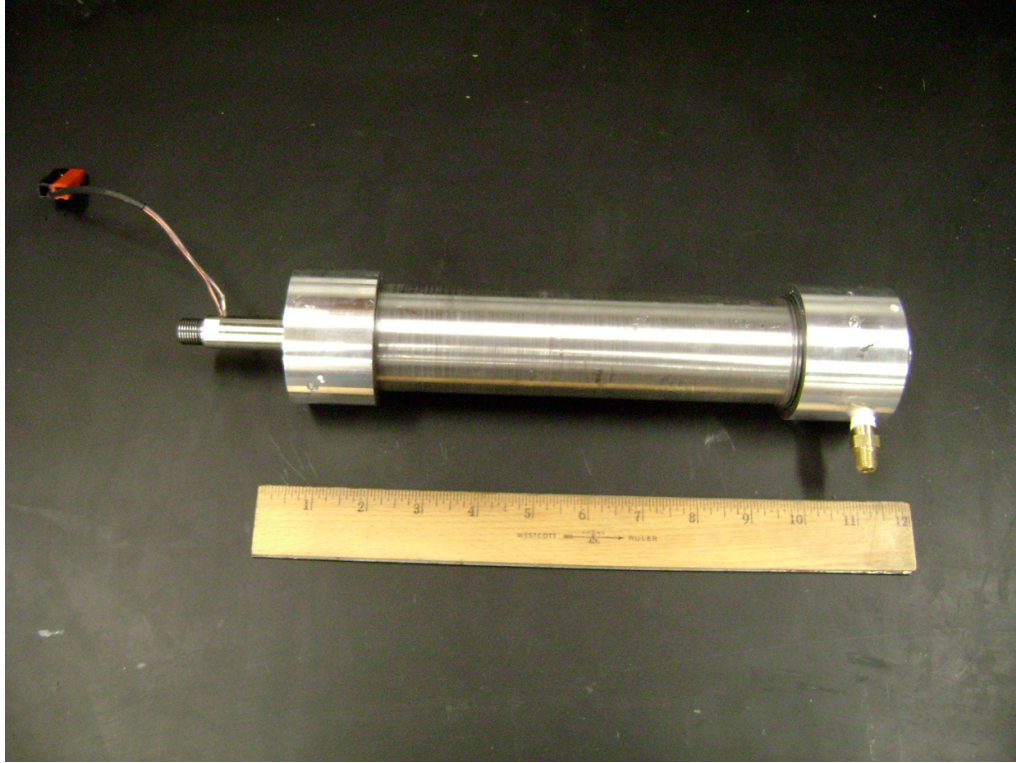


Figure 2.23: The assembled SSMREA.

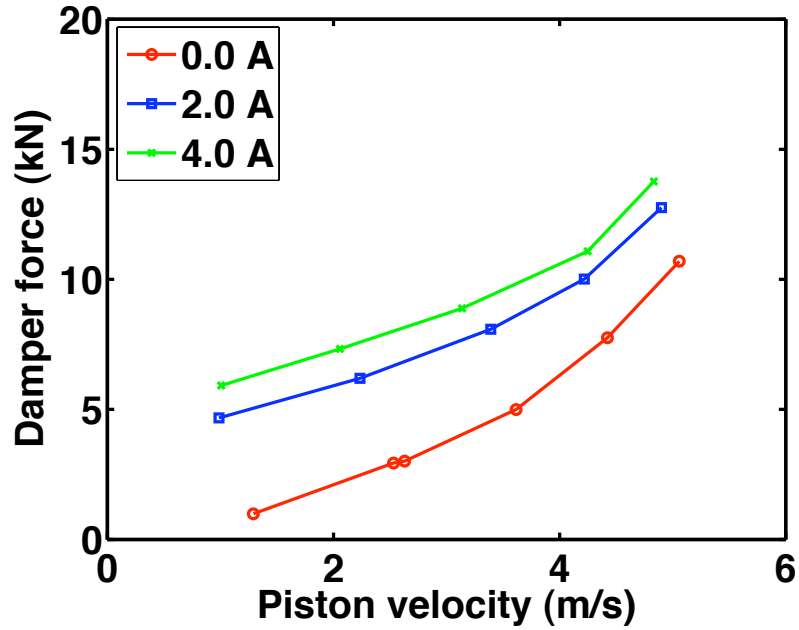


Figure 2.24: Measured SSMREA force versus piston velocity at various current levels.

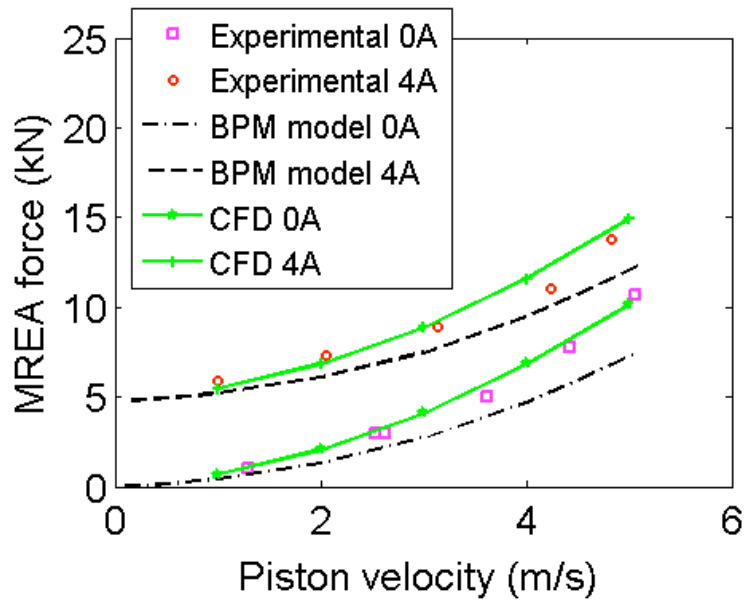


Figure 2.25: Measured and modeled peak force versus piston velocity.

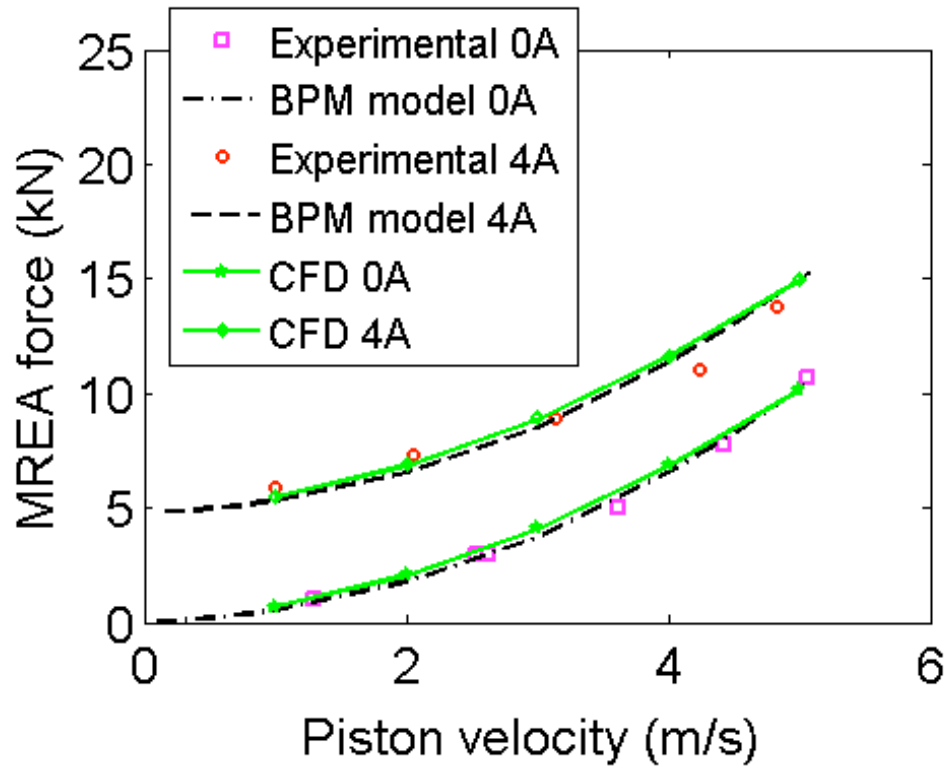
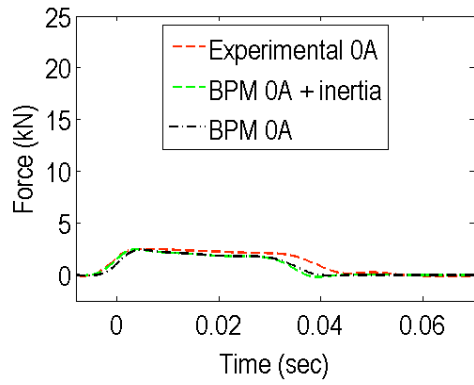
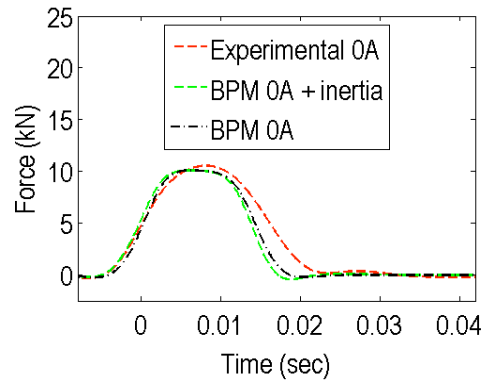


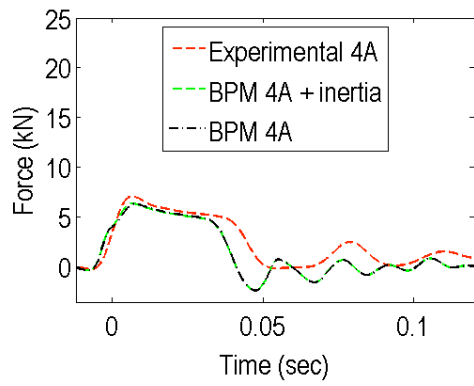
Figure 2.26: Measured and modeled peak force versus piston velocity with adjusted coefficients in BPM model prediction.



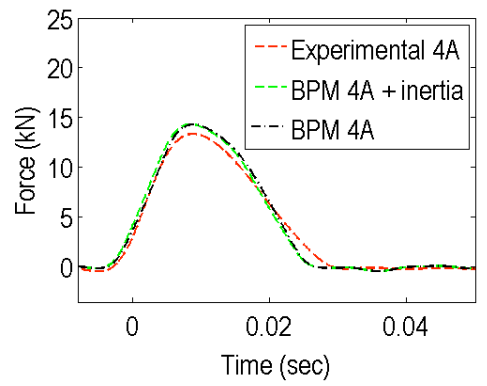
(a) nominal drop speed 2 m/s and 0A.



(b) nominal drop speed 5 m/s and 0A.



(c) nominal drop speed 2 m/s and 4A.



(d) nominal drop speed 5 m/s and 4A.

Figure 2.27: Experimental and predicted (by BPM model) SSMREA dynamic force for nominal drop speeds of 2 m/s and 5 m/s at 0A and 4A.

Chapter 3: Analysis of the Adaptive Magnetorheological Sliding Seat (AMSS) System With Control Algorithms

3.1 Introduction

As recent studies showing successful usage of magnetorheological (MR) energy absorbers (MREAs) as semi-active systems into various applications, MREAs have attracted attentions as tunable energy absorbing devices in high speed impact conditions to reduce shock load imparted to the payload mass, such as the adaptive sliding seat using MREAs we are to examine in this study.

Magnetorheological energy absorbers (MREAs) are adaptive energy dissipation devices using magnetorheological (MR) fluids as the hydraulic working fluids. MR fluids are smart fluids of which the rheological properties can be rapidly (typically 5 – 10 ms time constant) and reversibly modified upon exposure to an external magnetic field. A typical MR fluid is a suspension of micrometer-sized magnetic particles in a carrier fluid, usually a type of non-conducting oil. When subjected to a magnetic field, the particles randomly distributed in the carrier oil align themselves along the lines of the magnetic flux to form chain like structures and in a macro-view the MR fluid changes from a free flowing fluid into a semi-solid, and vice versa upon removing the magnetic field. When this kind of properties is exploited in a flow mode MR energy absorber or MR damper, the resulting particle chains restrict the movement of the fluid in the direction of perpendicular to the direction of magnetic flux and effect an MR yield stress in the damper. The MR yield stress can be

continuously controlled by varying the intensity of the magnetic field, often realized with an electromagnetic coil by changing its applied current level and thus providing a convenient electro-mechanical interface for fast feedback control in practical use.

Utilizing the rapid, reversible, and continuous field dependent variation in rheological properties of MR fluids, MREAs or MR dampers possess the capability of adapting to varying payloads, vibration spectra, and shock pulses, as well as other environmental factors and have been investigated for a variety of applications including: seismic mitigation (Dyke *et al.* 1996b; Yang *et al.* 2004), operator seat/cab vibration damping in general transportation vehicles (Park and Jeon 2002), gun recoil alleviation (Ahmadian and Poyner 2001), helicopter stability augmentation (Hu and Wereley 2005b), and so on. Although MR devices have been widely investigated, most past studies have been focused on relatively low speed operational situations (typically < 1 m/s). Recently, strong interests have emerged in employing MREAs in high speed impact applications for shock load mitigations. Pilot studies have investigated MREAs performance under impact conditions (Mao *et al.* 2007b; Browne *et al.* 2009), typically via drop tests and have demonstrated controllability of impact forces. Application specific investigations are ongoing for automotive applications (Browne *et al.* 2007), and for helicopter crew seats to mitigate vertical crash loads (Hiemenz *et al.* 2007b; Singh *et al.* 2009).

Though the generic concept of a sliding seat using smart devices has already been presented in the patent by Browne *et al.* (2007), no analysis concerning the system's dynamics and performance as well as controlling issue has been addressed. In this study, we conduct a theoretical feasibility analysis of a sliding seat employing

an MREA monitored by an adaptive control algorithm intended to mitigate impact loads imparted to a payload mass in a ground vehicle in the event of a low speed frontal impact (up to 7 m/s or 15.7 mph).

For control algorithms associated with semi-active systems utilizing MR fluid based devices, most researches that have been done are mainly for vibration mitigation purposes and the control algorithms proposed are not suitable for the problem in this study, namely, for MREA control under impact conditions. After all, vibration suppression is much different from impact load mitigation in many ways, such as the excitation frequency and amplitude, the involved system dynamics, the control objective and so on. Our group did valuable pioneer endeavors in exploring useful control algorithms in shock load mitigation systems utilizing MR dampers and MR energy absorbers. Our prior work (Choi and Wereley 2005) first investigated Lyapunov-based nonlinear optimal feedback control in an MR helicopter crew seat suspension subject to simultaneous control of vibration (during steady and maneuvering flight) and shock loads (due to a vertical high sink rate landing). Such a nonlinear control algorithm proved to be a compromise between vibration and shock mitigation performance, so that specialized control strategies for shock mitigation were explored. We simulated the biodynamic response (lumped parameter model) of an occupant in a vertically stroking helicopter crew seat system employing an MREA, and we subsequently developed a constant stroking load (14.5 g) control algorithm (Hiemenz *et al.* 2007b). Simulation results for a sink rate of 42 ft/s showed that the load-limiting control successfully maintained the total force imparted into the seat below its threshold values for all occupant weights under consideration and for a

range of sink rates (< 42 ft/s). This approach worked well provided that sufficient stroke were available (12" in this case). In some cases, the available stroke may be limited, so that Wereley and Choi (2008) developed a control algorithm to reduce drop-induced shock. In this study, a payload mass was dropped with a prescribed initial velocity onto an MREA that was used to protect the payload from the drop-induced impact. To minimize the peak load transmitted to the payload mass, as well as to prevent end stop impact, they developed an algorithm to achieve a soft landing, that is, bring the payload mass to a stop using the available stroke. This control algorithm was simple, in that given the initial impact velocity, the pre-calculated yield force of the MREA could be selected based on the payload mass to achieve the soft landing. This control strategy was modified and applied to a vertically stroking helicopter crew seat employing an MREA to accomplish a soft landing (i.e., no end stop impact) during a high sink rate landing (Singh *et al.* 2009) for a range of sink rates and occupant weights.

In the present study, the soft landing criterion is adapted in this context to achieve adaptive control of a sliding seat system employing an MREA to reduce load imparted to the occupant for varying initial impact speed and occupant weights. Two approaches were taken in the analysis. In the first approach, the seat-occupant system was described as a simple single-degree-of-freedom (SDOF) rigid occupant (RO) model and the seat-occupant payload was lumped in a single mass. Such a rigid occupant model greatly simplifies the analysis and provides insights into efficient control of load during impact. In the second approach, a compliant occupant is seated and constrained via seats belts (modeled as stiffnesses) to travel with the seat. The

occupant was represented as a lumped parameter model, so that a minimal number of biodynamic degrees of freedom were introduced. In both analyses, MREA force was modeled using the Bingham-plastic model. A rectangular pulse with a prescribed magnitude (20 g) and duration associated with a prescribed initial impact speed (up to 7 m/s), was assumed to emulate the crash pulse in the low speed frontal impact. Two control algorithms were explored to bring payload mass to rest: (1) constant Bingham number control, where the yield force is set at the initial impact solely on the basis of impact speed and occupant weight, and (2) constant force control, where the yield force varies as a function of stroking velocity to maintain stroking load constant. For each modeling approach, governing equations of the system were developed. For the rigid occupant model, it was possible to derive a closed-form analytical solution of the load-stroke profile to achieve the soft-landing criterion. However, the compliant occupant model was not amenable to analytical solutions for the load stroke profiles, so that an iterative numerical technique was used. Three occupant types were investigated for both models: the 5th percentile female, and the 50th and 95th percentile males. Sample transient results including seat/occupant dynamic responses as well as associated MREA responses for the 50th male were presented for each control algorithm and compared with their counterparts in the case of a fixed seat. It was shown that the controlled seat system was brought to a stop in the available stroke and the payload decelerations were significantly reduced. In addition, extensive coupling between the seat structures and occupant biodynamic response was demonstrated.

3.2 Single-Degree-of-Freedom (SDOF) Rigid Occupant (RO) Model

To simplify analysis, a single-degree-of-freedom (SDOF) rigid occupant (RO) model was used to describe a sliding seat system where an MREA is used to decelerate the payload (seat plus occupant mass). In this case, it is assumed that the occupant is rigid, and that seat and occupant motions are equivalent. Figure 3.1 depicts the RO model with an MREA. Here, the payload mass comprises the seat mass, m_s and occupant or body mass, m_b . Also, x_s is displacement of the payload, x_v is the vehicle floor displacement and F_{mr} is the MREA damping force. The governing equation of the RO model is

$$(m_b + m_s)\ddot{x}_s + F_{mr} = 0 \quad (3.1)$$

where F_{mr} is expressed as:

$$F_{mr} = c \cdot (\dot{x}_s - \dot{x}_v) + F_y \cdot \text{sign}(\dot{x}_s - \dot{x}_v) \quad (3.2)$$

Here c is the damping constant of the MREA, and F_y is the yield force of the MREA due to an MR fluid and $\dot{x}_s - \dot{x}_v$ denotes the MREA piston/rod velocity. The MR yield force, F_y , is typically modeled as a function of the current applied to the MREA, I :

$$F_y = \alpha \cdot I^\beta \quad (3.3)$$

where α and β are parameters to characterize the relationship between the MREA yield force and the applied current level. These two parameters are determined from experimental data and are assumed to be $\alpha = 5000$ and $\beta = 0.5$ in this study.

The relative velocity, $\dot{x}_s - \dot{x}_v$, denotes the piston velocity of the MREA so that we can define the MREA piston velocity, V_p , as follows:

$$V_p = \dot{x}_s - \dot{x}_v \quad (3.4)$$

Then the MREA damping force can be rewritten as:

$$F_{mr} = c \cdot V_p + F_y \cdot \text{sign}(V_p) \quad (3.5)$$

The first term is called the field-off force and usually expressed as:

$$F_{off} = c \cdot V_p \quad (3.6)$$

Differentiating Eq. (3.4) and rearranging the terms yields:

$$\dot{V}_p + \ddot{x}_v = \ddot{x}_s \quad (3.7)$$

Here the seat/occupant complex deceleration, \ddot{x}_s , can be deduced from Eq. (3.1) as follows with $m = m_b + m_s$:

$$\ddot{x}_s = -\frac{F_{mr}}{m} = -\frac{F_y}{m} \text{sign}(V_p) - \frac{c}{m} V_p \quad (3.8)$$

The vehicle floor deceleration (crash pulse), \ddot{x}_v , is assumed to be a rectangular pulse as follows:

$$\ddot{x}_v = \begin{cases} 0 & t \leq t_0 \\ -A_v & t_0 < t < t_v \\ 0 & t \geq t_v \end{cases} \quad (3.9)$$

where A_v is the magnitude of the crash pulse, t_0 denotes the leading edge of the pulse and t_v denotes the trailing edge of the crash pulse. For simplicity, we assume that $t_0 = 0$. Therefore, t_v also denotes crash pulse duration. Based on the kinetic relationship between deceleration and velocity, the relation of the vehicle initial impact speed, v_0 (\dot{x}_v at $t = 0$), the crash pulse magnitude, A_v , and duration, t_v , can be expressed as:

$$t_v = \frac{v_0}{A_v} \quad (3.10)$$

3.3 Multi-Degree-of-Freedom (MDOF) Compliant Occupant (CO) Model

In the RO model, the occupant and the seat were lumped into a single mass so that dynamic behavior of the seat and occupant were the same. To address biodynamic response, an MDOF compliant occupant (CO) model comprising pelvis, torso and head motions, was developed.

The schematic of the sliding seat with a simplistic compliant biodynamic occupant model is shown in Figure 3.2. In the figure, the definitions of each symbol are listed in Table 3.1. Typical parameter values are listed for each type of occupant (e.g. Hybrid III ATD) in Table 3.2. Because the effect of the length, l_b , in the calculation of the relative displacement of the lap belt is relatively small, it is neglected and values are not listed. Also note that here the numerical value of head mass, m_h , does not include the neck mass. Similarly, the upper torso mass, m_t , and the pelvis mass, m_p , do not include arm mass and leg mass, respectively. The reason is that the arms and legs will not rigidly bundle and move uniformly together with the upper torso and pelvis, respectively. They have essentially different and complex dynamic responses from those of the upper torso and pelvis during the impact. To more accurately predict their dynamics, neck, arms and legs are usually modeled as distinct degree of freedom (such as MADYMO human model or FEM human model) and connected with each other and with the torso by complex model mechanisms. In this feasibility study of the adaptive sliding seat, we just simply neglect their participation in the CO model. As a result, the occupant mass m_b in the RO model simulation will be assumed equal to that of the occupant mass in CO model, $m_b = m_h + m_t + m_p$, that is, limb masses are neglected in both cases.

In addition, to simplify the theoretical analysis of the CO model, the following assumptions were made:

(1) The seat belt (including shoulder belt and lap belt) ties occupant to seat with no slack.

(2) A load-limiter is not considered.

(3) Effective spring rate of seat belt is constant.

(4) Seat belt stretches in horizontal direction. It implies that rotation angle of upper torso is assumed to be small.

(5) Seat is assumed to be rigid.

Resorting to the approach of using Lagrangian equations to derive system dynamics, the governing equations of the CO model of the sliding seat with MREA and these limited biodynamic degrees of freedom are given by:

$$m_s \ddot{x}_s = k_{sb}(x_{pl} + l_{sb} \sin(\theta_t) - l_{sb} \sin(\theta_{t0}) - x_s) + k_{lb}(x_{pl} - x_s) - F_{mr} \quad (3.11)$$

$$\begin{aligned} & (m_p + m_t + m_h) \ddot{x}_{pl} + (m_t l_c + m_h l_t) \cos(\theta_t) \ddot{\theta}_t + m_h l_h \cos(\theta_h) \ddot{\theta}_h \\ & = (m_t l_c + m_h l_t) \dot{\theta}_t^2 \sin(\theta_t) + m_h l_h \dot{\theta}_h^2 \sin(\theta_h) \\ & - k_{sb}(x_{pl} + l_{sb} \sin(\theta_t) - l_{sb} \sin(\theta_{t0}) - x_s) - k_{lb}(x_{pl} - x_s) \end{aligned} \quad (3.12)$$

$$\begin{aligned} & (m_t l_c + m_h l_t) \cos(\theta_t) \ddot{x}_{pl} + (m_t l_c^2 + m_h l_t^2) \ddot{\theta}_t + m_h l_h l_t \cos(\theta_t - \theta_h) \ddot{\theta}_h \\ & = -m_h l_h l_t \dot{\theta}_h^2 \sin(\theta_t - \theta_h) - k_{sb}(x_{pl} + l_{sb} \sin(\theta_t) - l_{sb} \sin(\theta_{t0}) - x_s) l_{sb} \cos(\theta_t) \end{aligned} \quad (3.13)$$

$$\begin{aligned} & m_h l_h \cos(\theta_h) \ddot{x}_{pl} + m_h l_t l_h \cos(\theta_t - \theta_h) \ddot{\theta}_t + m_h l_h^2 \ddot{\theta}_h \\ & = m_h l_t l_h \dot{\theta}_t^2 \sin(\theta_t - \theta_h) - m_h l_h \dot{x}_{pl} \dot{\theta}_h \sin \theta_h \end{aligned} \quad (3.14)$$

Here, \ddot{x}_v does not explicitly appear in the above equations, but is introduced when F_{mr} is substituted from in Eq. (3.2).

3.4 Control Objective and Control Algorithms

Wereley and Choi (2008) proposed a soft landing criterion to maximize shock mitigation of the payload mass that ensures that the payload comes to rest at the end of its available stroke. Thus, the control objective here is to find an appropriate control input, $U_c(t)$ ($U_l \leq U_c(t) \leq U_u$), so that for $t \in (t_0, t_f)$ the following terminal conditions are satisfied at the final time:

$$\begin{cases} V_p(t = t_f) = 0 \\ X_p(t = t_f) = S_m \end{cases} \quad (3.15)$$

where t_0 is the time of initial impact and t_f is the time when the sliding seat comes to rest. Here, X_p ($X_p = x_s - x_v$) is the MREA displacement and S_m is the maximum allowable MREA stroke (here set to be 2 inches). U_l, U_u are the lower bound and upper bound of the control input, but in this study it will be assumed that the control input always lies in this bounded range.

There may be a variety of control inputs, either time variant or time invariant that satisfy the boundary conditions of Eq. (15). To simplify the analysis as well as to realize practical control strategies, we propose two control algorithms: (1) the constant Bingham number or Bi_c control, and (2) the constant stroking load/force or F_c control.

3.5 Control Algorithm Implementation in RO Model

3.5.1 Constant Bingham Number Control

For this control strategy, the goal is to determine a constant current control input that satisfies the optimal terminal conditions from Eq. (3.15). In essence, because the

current is held constant, we are setting the initial value of the Bingham number (to be defined below) to a value satisfying the soft landing terminal conditions. To do this, the time domain solution of the MREA piston velocity, V_p , and the MREA piston displacement, X_p (here $X_p = x_s - x_v$) are needed. Before proceeding to derive V_p and X_p , the crash pulse \ddot{x}_v is expressed more conveniently as:

$$\ddot{x}_v = -A_v \cdot [u(t) - u(t - t_v)] \quad (3.16)$$

where $u(t)$ and $u(t - t_v)$ are the time domain unit step functions. Substituting Eqs. (3.8) and (3.16) into Eq. (3.7) and rearranging yields:

$$\dot{V}_p + \frac{F_y}{m} \text{sign}(V_p) + \frac{c}{m} V_p = A_v \cdot [u(t) - u(t - t_v)] \quad (3.17)$$

Integrating the ordinary differential equation Eq. (3.17) once with the initial condition of $V_p(0) = 0$, the time domain MREA piston velocity $V_p(t)$ can be obtained and is expressed as follows:

$$V_p(t) = \frac{m}{c} \left[A_v - \frac{F_y}{m} \text{sign}(V_p) \right] \cdot \left(1 - e^{-\frac{c}{m}t} \right) - A_v \cdot \frac{m}{c} \left[1 - e^{-\frac{c}{m}(t-t_v)} \right] \cdot u(t - t_v) \quad (3.18)$$

The Bingham number is the ratio of the MR yield force to the passive viscous damping force, as follows:

$$Bi = \frac{F_y}{c v_0} \text{sign}(V_p) \quad (3.19)$$

Also, define the time constant for the sliding seat system as:

$$\tau_v = \frac{m}{c} \quad (3.20)$$

Thus, Eq. (3.18) can be rewritten as:

$$V_p(t) = v_0 \left[\frac{\tau_v}{t_v} - Bi \right] \cdot (1 - e^{-t/\tau_v}) - \frac{v_0 \tau_v}{t_v} [1 - e^{-(t-t_v)/\tau_v}] \cdot u(t-t_v) \quad (3.21)$$

Note that in the above equation A_v is replaced by v_0/t_v based on Eq. (3.10).

Similarly, integrating Eq. (3.21) using the initial condition of $X_p(0) = 0$ yields:

$$X_p(t) = v_0 \left[\frac{\tau_v}{t_v} - Bi \right] \cdot [t + \tau_v \cdot (e^{-t/\tau_v} - 1)] - \frac{v_0 \tau_v}{t_v} [(t-t_v) + \tau_v \cdot (e^{-(t-t_v)/\tau_v} - u(t-t_v))] \cdot u(t-t_v) \quad (3.22)$$

For the constant Bingham number control, the conditions in Eq. (15) should be satisfied, namely:

$$V_p(t_f) = v_0 \left[\frac{\tau_v}{t_v} - Bi \right] \cdot (1 - e^{-t_f/\tau_v}) - \frac{v_0 \tau_v}{t_v} [1 - e^{-(t_f-t_v)/\tau_v}] \cdot u(t_f-t_v) = 0 \quad (3.23)$$

$$X_p(t_f) = S_m = v_0 \left[\frac{\tau_v}{t_v} - Bi \right] \cdot [t_f + \tau_v \cdot (e^{-t_f/\tau_v} - 1)] - \frac{v_0 \tau_v}{t_v} [(t_f-t_v) + \tau_v \cdot (e^{-(t_f-t_v)/\tau_v} - u(t_f-t_v))] \cdot u(t_f-t_v) \quad (3.24)$$

Here $t_f \geq t_v$ in both equations, so that $u(t_f-t_v) = 1$. From Eq. (3.23) we obtain the constant Bingham number, $Bi_{c,v}$, for the MREA satisfying the terminal condition that the piston velocity is zero:

$$Bi_{c,v} = \frac{\frac{\tau_v}{t_v} [e^{t_v/\tau_v} - 1]}{e^{t_f/\tau_v} - 1} \quad (3.25)$$

Similarly, the Bingham number, $Bi_{c,x}$, for the MREA satisfying the terminal condition that all available stroke has been used is:

$$Bi_{c,x} = \frac{\tau_v - \frac{S_m}{v_0} - \frac{\tau_v^2}{t_v} e^{-t_f/\tau_v} (e^{t_v/\tau_v} - 1)}{t_f + \tau_v (e^{-t_f/\tau_v} - 1)} \quad (3.26)$$

Because at $t = t_f$ both terminal conditions, Eq. (3.23) and Eq. (3.24), must be satisfied simultaneously:

$$Bi_{c,v} = Bi_{c,x} \quad (3.27)$$

Solving Eq. (3.27), we can obtain the payload mass rest time, t_f , as follows:

$$t_f = \tau_v \cdot \left\{ \frac{\frac{\frac{S_m - \tau_v}{v_0} - W \left[\frac{\frac{S_m - \tau_v}{v_0} - \frac{\tau_v^2}{t_v(1 - e^{t_f/\tau_v})}}{\frac{\tau_v^2}{t_v(1 - e^{t_f/\tau_v})}} \right]}{\frac{\tau_v^2}{t_v(1 - e^{t_f/\tau_v})}}}{\frac{S_m - \tau_v}{v_0}} \right\} \quad (3.28)$$

where $W[\cdot]$ is the Lambert W function or also called product log (Corless *et al.*, 1996) and will be used hereafter to represent the $W[\cdot]$ expression in Eq. (3.28) for simplicity. Substituting Eq. (3.28) into either Eq. (3.25) or Eq.(3.26), we can obtain the constant Bingham number, Bi_c , for this control algorithm as:

$$Bi_c = \frac{\frac{\tau_v}{t_v}(1 - e^{t_f/\tau_v})}{\frac{\frac{S_m - \tau_v}{v_0} - W[\cdot]}{\frac{\tau_v^2}{t_v(1 - e^{t_f/\tau_v})}} - 1} \quad (3.29)$$

Once Bi_c is obtained, the constant MR yield force is determined via Eq. (19) and the constant current that should be applied via Eq. (3). The payload mass deceleration, \ddot{x}_s , is:

$$\ddot{x}_s(t) = -Bi_c - \frac{c}{m}V_p(t) \quad (3.30)$$

3.5.2 Constant Stroking Load/Force Control

For this control strategy, the goal is to select a constant MREA force, F_c , that satisfies the soft landing terminal conditions from Eq. (3.15). Unlike in the previous algorithm, the MREA force is held constant, or $F_{mr} = F_c$. From Eqs. (3.7-3.8) and (3.16), the governing equation for the piston velocity is :

$$\dot{V}_p + \frac{F_c}{m} = A_v \cdot [u(t) - u(t - t_v)] \quad (3.31)$$

The MREA piston velocity can be determined by solving the ODE, Eq. (3.31), with the initial condition of $V_p(0) = 0$. The MREA piston velocity $V_p(t)$ is:

$$V_p(t) = \left(\frac{v_o}{t_v} - \frac{F_c}{m}\right) \cdot t - \frac{v_o}{t_v}(t - t_v) \cdot u(t - t_v) \quad (3.32)$$

Integrating Eq. (3.32) with the initial condition, $X_p(0) = 0$, yields the MREA piston displacement, $X_p(t)$:

$$X_p(t) = \left(\frac{v_o}{t_v} - \frac{F_c}{m}\right) \cdot \frac{t^2}{2} - \frac{v_o}{2t_v}(t - t_v)^2 \cdot u(t - t_v) \quad (3.33)$$

The constant stroking load, F_c , must be selected so that the terminal conditions in Eq. (3.15) are satisfied:

$$V_p(t_f) = \left(\frac{v_o}{t_v} - \frac{F_c}{m}\right) \cdot t_f - \frac{v_o}{t_v}(t_f - t_v) \cdot u(t_f - t_v) = 0 \quad (3.34)$$

$$X_p(t_f) = S_m = \left(\frac{v_o}{t_v} - \frac{F_c}{m}\right) \cdot \frac{t_f^2}{2} - \frac{v_o}{2t_v}(t_f - t_v)^2 \cdot u(t_f - t_v) \quad (3.35)$$

As before, $u(t_f - t_v) = 1$ in both Eqs. (3.34) and (3.35). Thus, from Eq. (3.34) we can easily compute the terminal time at which the payload mass, t_f , achieves the soft landing:

$$t_f = \frac{mv_0}{F_c} \quad (3.36)$$

Substituting Eq. (3.36) into Eq. (3.35), the required constant stroking load F_c can be obtained:

$$F_c = \frac{\frac{1}{2}mv_0^2}{\frac{1}{2}v_0t_v + S_m} \quad (3.37)$$

Given the constant stroking load, the MREA yield force can be determined from Eq. (3.2) given the instantaneous piston velocity. Once the yield force time history is determined, then the corresponding current time history, for the MREA to satisfy the constant total MREA force can be determined from Eq. (3.3).

By substituting Eq. (3.37) into (3.36), the terminal time, t_f , at which the payload mass achieves the soft landing, is:

$$t_f = t_v + \frac{2S_m}{v_0} \quad (3.38)$$

As a result, the instantaneous payload deceleration, \ddot{x}_s , is:

$$\ddot{x}_s(t) = -\frac{F_c}{m} = -\frac{\frac{1}{2}v_0^2}{\frac{1}{2}v_0t_v + S_m} \quad (3.39)$$

As can be seen from Eq. (3.39), \ddot{x}_s is constant, therefore, constant MREA force control has been achieved.

3.6 Control Algorithm Implementation in CO Model

When biodynamic degrees of freedom (incorporating passive restraints as stiffness terms) are introduced into the simulation, the MREA cannot control these

degrees of freedom, but can only exert control force on the seat. The pelvis, upper torso, and head, are essentially treated as transient responses that occur after the MREA control strategy has been applied. In a practical situation, it is neither practical to place actuators to directly effect motions of these biodynamic degrees of freedom (DOFs), nor is it practical to directly measure these same DOFs. The rigid payload mass control strategies, developed above, could be used to control the seat with an occupant represented as a simple three DOF lumped parameter model. However, the rigid payload mass solution tends to generally overpredict (underpredict at initial impact speed of 7 m/s) the required stroking load. This is well revealed by the resulted maximum stroke as shown in Figure 3.3 if we take the control inputs of F_c and Bi_c determined from the RO model directly as the control inputs for the CO model and perform the simulation with the help of MATLAB/SIMULINK for each control algorithm. As seen in Figure 3.3, at initial impact speeds below 7 m/s, for all occupant types and for both F_c and Bi_c control, the resulted maximum MREA strokes are substantially less than 2 inches. This implies that the required stroking loads are overpredicted by the rigid payload mass solution (RO model control inputs) so that the MREA only utilizes a portion of the full 2 inches stroke. On the other hand, at initial impact speed of 7 m/s, except for 5th female with Bi_c control, for all other cases, the resulted maximum MREA strokes are greater than 2 inches. This indicates that the rigid payload mass solution underpredicts the required stroking load and the MREA demands more stroke than the 2 inches full stroke in order to come to a rest. It will cause a more or less severe end-stop impact and not the desired “soft-landing”. Therefore, if we directly use the control inputs determined analytically from

the RO model as the control inputs for the MDOF compliant occupant (CO) model, we cannot achieve the control objective.

To correct this problem, we also need to obtain the control strategy (control inputs) for the CO model. Due to the complexity of the system equations in the CO model, analytical solutions as those presented in the RO model, such as the control inputs, F_c and Bi_c , the sliding ending time, t_f , as well as the dynamic responses of the seat and individual parts of the occupant, are very difficult to obtain. Therefore, here we resorted to numerical techniques to find these solutions. Again, MATLAB/SIMULINK was used to simulate the CO model subject to each control algorithm, and the shooting method was utilized to obtain the control inputs. The numerical procedure for each control algorithm is essentially the same and illustrated in Figure 3.4. Once the numerical solutions for the control algorithms are found, the dynamic responses of the seat and each individual part of the occupant can be obtained by applying the proper control input to the SIMULINK model file.

3.7 Simulation Results and Discussion

Three types of occupants, the 5th percentile female, the 50th percentile male and the 95th percentile male, were simulated for each control algorithm for initial impact speeds up to 7 m/s (15.7 mph). The crash pulse for each case is a 20 g rectangular pulse, whose duration is dependent on the prescribed initial impact speed, v_0 .

3.7.1 Determined Control Inputs for Each Control Algorithm

For the RO model, the numerical values of the control inputs F_c , Bi_c and t_f associated with each control algorithm can be directly obtained using analytical solutions developed above.

For the CO model, a numerical method was used to determine time histories of the seat and biodynamic DOFs based on applying the control inputs F_c or Bi_c for the respective t_f . The results are plotted versus initial impact speed, v_0 , (up to 7 m/s) and occupant body mass, m_b , for both RO model and CO model in Figures 3.5-3.6. The seat mass m_s is assumed to be 20 kg and the MREA damping constant c is assumed to be 800 Ns/m.

In the case of the constant Bingham number control strategy, the optimal Bi_c varies with both the occupant body mass m_b and initial impact speed v_0 for both a rigid SDOF payload and a biodynamic MDOF payload. The optimal Bingham number for the biodynamic MDOF payload is slightly lower than that of the rigid SDOF case in general (except for the 50th and 95th male at 7 m/s), indicating that the biodynamic transient response tends to reduce the required stroking load of the seat.

In the case of constant stroking load control, the constant stroking force, F_c , varies with the occupant body mass m_b and initial impact speed v_0 . And for the RO model and CO model, the resulted F_c holds very similar numerical values at various initial impact speeds for each occupant type. In contrast to Bi_c , F_c increases substantially with the initial impact speed for the whole speed range. The relationship between F_c and m_b given the same initial impact speed shows a linear manner for

both models. Though lacking an analytical solution for CO model, from the analytical solution of F_c in Eq. (3.37) it is seen that F_c is related to m_b ($m = m_b + m_s$) linearly.

Based on the above discussion, it indicates that in terms of determining the control inputs for each control algorithm, the RO model yields similar results to the CO model. However, the RO model has the advantage of much simpler model and closed-form analytical solutions. The simulation results of RO vs. CO model on dynamic response are quite different.

3.7.2 System and MREA Dynamic Responses

Once the required control inputs for each control algorithm are determined, the MREA dynamics and the system dynamics including seat and occupant decelerations in both models can be obtained. Figures 3.7-3.9 present sample results of a 50th male at initial impact speeds of 2 m/s and 7 m/s and compare with their counterparts in the case of a conventional fixed seat.

As seen in Figures 3.7, for Bi_c control, the applied current to the MREA is constant because the control algorithm sets the current at the time of impact based on occupant mass and impact velocity. Furthermore, current levels are very similar for both rigid and compliant occupant cases at either initial impact speeds, but the time durations are slightly different. At 7 m/s, the duration of the control current for the compliant occupant case is about 10 ms longer than that for the rigid occupant case. At 2 m/s, the durations are nearly identical. In contrast, for F_c control, the applied current varies over time to compensate for the variation of viscous force as the piston velocity varies during impact. Nevertheless, the current levels for both rigid and compliant occupants are very similar. The addition of biodynamic degrees of freedom

in the compliant occupant case changes the commanded current to be piecewise smooth, as opposed to piecewise linear for the rigid occupant case. For both control strategies, the current levels at an impact speed of 7 m/s are much higher than those at 2 m/s, because the required stroking force is higher at 7 m/s than 2 m/s, and higher stroking load is commanded by the controller.

Despite the similarity of the applied current time histories for both the rigid and compliant occupant cases, the dynamic responses of the seat are very different in each model for both control algorithms as shown in Figures 3.8. For the rigid occupant case, the seat and occupant are lumped in a single mass and the resulting payload deceleration is significantly reduced compared to the crash pulse (namely, in the case of the fixed seat) even at 7 m/s. For the compliant occupant case, the seat is distinct from the occupant. However, the strong dynamic and mechanical (i.e. seat belts) coupling between the seat and the biodynamic degrees of freedom (i.e., occupant) leads to significantly different seat decelerations. As observed in the figures, for both control algorithms and both initial impact speeds in the compliant occupant case, secondary peaks arise whose magnitudes are comparable or even larger (F_c control at 7 m/s) than the initial deceleration peaks. In the RO model case, only the initial peaks (or constant levels) show up. The magnitudes of the initial peaks in the compliant occupant case are much larger than those for the rigid occupant case. In addition, at initial impact speed of 7 m/s, the magnitudes of the seat decelerations for both control algorithms seem to be at the same level of the crash pulse and even higher than the crash pulse at the secondary peak for F_c control. Also, seat decelerations under Bi_c

and F_c control are comparable except for the aforementioned secondary peaks at impact speed of 7 m/s.

For the rigid body occupant, seat deceleration represents the deceleration of the entire payload mass comprising both seat and occupant masses. In the case of the compliant occupant, the seat, which is coupled to the occupant via seatbelts, does not provide adequate biodynamic response information. Figure 3.9 presents the biodynamic response for each individual body part (pelvis, upper torso, head) using the compliant occupant model. Decelerations of the occupant's pelvis, upper torso and head are each significantly reduced using either the Bi_c or F_c control strategy. In addition, both control strategies, i.e., Bi_c and F_c control, induce very similar biodynamic response. Thus, the two control algorithms provide the occupant with almost the same level of impact load mitigation, even though the Bi_c control uses only the initial impact speed, unlike the F_c control that uses velocity feedback.

MREA responses such as the instantaneous MREA piston velocity, piston displacement and the associated MREA field-off force, MR yield force and total force are also illustrated in Figures 3.10-3.11. The piston velocity and displacement time histories for the compliant occupant model are quite different from those of the rigid occupant model. However, under the influence of control, they are quite similar. Also, with the initial impact speed increasing from 2 m/s to 7 m/s, the peak piston velocity also increases. The increase is about 0.4 m/s and 1 m/s, respectively, for the rigid and compliant occupant models. Nevertheless the peak field-off forces increments are small since the assumed damping constant c here is relatively small. Moreover, the fraction that the field-off force accounts for in the total force is seen to

greatly drop down as the initial impact speed rises from 2 m/s to 7 m/s while the fraction of the MR yield force in the total force varies in a reverse manner to the field-off force. In addition, the MR yield force behaves quite differently according to the control algorithm. For the F_c control, the MR yield force evolves over time accordingly with the evolving of the field-off force and be consistent with the applied current (in Figures 3.7(a) –(b)). As a result, the F_c control is implemented and a constant total force level is achieved. While for Bi_c control, the MR yield force keeps constant since the applied current is constant over the impact period according to what the control algorithm is meant to. As a result, the total MREA force appears a shape consistent with the field-off force and the piston velocity. Therefore, the MREA behaves as it is expected and provides the force required for implementing each control algorithm.

3.7.3 MREA Performance Envelope and SSMREA Capability

To gain insight into the capacity range an MREA is expected to bear in order to successfully implement the control algorithms, the resulting MREA performance envelope including the peak field-off force, F_{off} , peak MR yield force, F_y , peak MREA total force, F_{mr} , and the dynamic range, D_n , at various initial impact speeds and for various occupant types are assessed. Here, the dynamic range of the MREA is defined as the ratio of the peak MREA total force to the peak MREA field-off force at the peak piston velocity that are obtained from the MREA dynamic response at a particular initial impact speed.

The respective results versus initial impact speed are presented in Figures 3.12-3.15 for each control algorithm and each model. Figures 3.11-3.12 are the various

peak MREA forces, namely F_{off} , F_y and F_{mr} , for the Bi_c control and F_c control, respectively. Based on the results, it is found that:

(1) The results from the RO model are very similar to those from the CO model for each control algorithm.

(2) Despite the general similarity of the results for both control algorithms, slight differences are also observed. The peak field-off forces, F_{off} , are almost the same at various initial impact speeds. However, the peak MR yield-force, F_y and peak MREA total force, F_{mr} , for the Bi_c control are a bit higher in the range of about 0.4 ~0.9 kN than those of the F_c control as the initial impact speed varies. Therefore, the derived peak dynamic ranges, D_n , from F_{off} and F_{mr} in the case of Bi_c control are also a bit larger than those of the F_c control in the range of about 0.3~1 over the initial impact speed range.

(3) For each control algorithm, the peak field-off force, F_{off} , shows little changes with variations of occupant mass and very small increment as initial impact speed increases from 1 m/s to 7 m/s.

(4) For each control algorithm, the peak MR yield-force, F_y and peak MREA total force, F_{mr} , largely increases as initial impact speed increases and occupant body mass increases. The increasing rates with respect to both, namely v_0 and m_b , are approximately linear.

(5) As a result of the facts described in the above (2) and (3), the dynamic range, D_n , increases as initial impact speed increases from 1 m/s to 7 m/s at an approximate

rate of the linear order except for the cases of 5th female above initial impact speed of 4 m/s.

Therefore, we may expect that the Bi_c control demands a little higher MREA capacity than the F_c control. Another thing is that both modeling approaches seem to provide similar information about the MREA performance envelope. Thus at the initial stage, RO model would be a simple and useful tool to provide valuable insight to analyze the MREA performance requirement for the AMSS system since analytical solutions are easily attainable.

Utilizing the MREA performance envelope extracted from the simulation results, the performance requirements for the MREA in the AMSS system to implement the two control algorithms (F_c control and Bi_c control) can be visualized for the assumed MREA and the AMSS system. Theoretically, if an MREA can provide the corresponding total MREA force at any particular initial impact speed for each control algorithm and for any occupant types from the 5th female to the 95th male, the adaptive control of the AMSS system would be realizable and the system would response as expected for the examined initial impact speed range and the occupant types. In this research, our goal is to experimentally prove that the controller is feasible for occupant types ranging from the 5th female to the 95th male and for initial impact speed ranging from 2 m/s up to 4.5 m/s. In this analysis, the initial impact speed ranging from 1 m/s to 7 m/s is examined in simulation. Therefore, for each modeling approach, the MREA total force corresponding to the 5th female over the initial impact speeds from 2 m/s to 6 m/s whichever is lower in the two control algorithms would consist of the lower force boundary that the MREA for the system

needs to provide over the associated piston velocity range, that is, the MREA field-off force requirement over the piston velocity range. Similarly, the MREA total force corresponding to the 95th male over the initial impact speeds from 2 m/s to 6 m/s whichever is higher in the two control algorithms would form the upper force boundary that the MREA needs to offer for the system, which corresponds to the MREA full field-on force requirements over the associated piston velocity range.

However, as observed in Figures 3.13 though the results from the RO model and the CO model are rather similar, they are still different. Moreover, at this point we are not sure which model describes the system to the most accurate degree. Therefore, in the MREA performance requirement specification, for safety we would consider the lower one of the lower force boundaries from the two models as the lower boundary and the higher one of the upper force boundaries from the two models as the upper boundary. On the other hand, as we illustrated previously, in the MREA design, we usually take the highest interested piston velocity (not the initial impact speed) as the performance specification for the design process and assumes that the forces at lower piston velocity would automatically satisfy the boundary, which is usually the case in many MREAs. Also, in the later physical prototype AMSS system, two identical units of MREA will be used in a parallel connection with one at each side of the seat. Thus, the MREA forces in the simulation results need to be divided by 2 to get the right force level for one MREA. The division results per MREA are shown in Figure 3.16. To preliminarily verify if the SSMREA can provide the required MREA force for the AMSS system in the analysis, the measured SSMREA force at field-off (0A) and full field-on (4A) are also presented in the figure and compare with the various analysis

force boundaries showing the required MREA forces to implement the two control algorithms.

As observed in Figures 3.16, for initial impact speeds above 4 m/s, the 4 force curves obtained from RO model each shows a reverse turning due to a slight decreasing of the piston velocity. But for the results from the CO model, the four force curves demonstrate normal increasing trend as initial impact speed increases. It can be seen that, except for the analysis forces from the RO model for F_c control and the 5th female at initial impact speed of 2 and 3 m/s, the measured SSMREA force range between 0A and 4A almost covers all the analysis force boundaries. Therefore, it is believed that the developed SSMREA would be capable to serve as the MREA in the AMSS system for this feasibility study.

3.7.4 System Performance Evaluation

To compare the performance of the AMSS system between the two control algorithms and between the AMSS system and the traditional fixed seat for all occupant types, the peak deceleration (in magnitude) and the energy dissipation ratio obtained from the RO model and the CO model are assessed.

Here the energy dissipation ratio is defined as ratio of the energy dissipated by the MREA during the impact period, namely $t \in (t_0, t_f)$, to the initial kinetic energy the payload (including the occupant body mass and the seat) possesses. The mathematic formula of the energy dissipation ratio (EDR), E_d , is given below:

$$E_d = \frac{\int_{x_p(t_0)}^{x_p(t_f)} F_{mr} \cdot dX_p}{\frac{1}{2}mv_0^2} = \frac{\int_{t_0}^{t_f} F_{mr} \cdot V_p dt}{\frac{1}{2}mv_0^2} \quad (3.40)$$

Peak payload decelerations (i.e. combined occupant and seat mass) in the rigid occupant (RO) model, and biodynamic responses for the compliant occupant (CO) model are shown in Figure 3.17 and Figures 3.18, respectively. Note that for the RO case, the peak decelerations at all initial impact speeds for the case of the traditional fixed seat are equal to the crash pulse magnitude (20 g) and are not presented in the figure. It is shown that, for either modeling approaches, at various initial impact speeds and for various occupant types, the respective peak deceleration levels are all significantly reduced using the controlled AMSS compared to their counterparts in the case of a traditional fixed seat. Based on the results, though in the RO model the peak decelerations with Bi_c control are about 1 g or 2 g higher than those with the F_c control, the two control algorithms generally provide comparable impact load mitigations to the occupants with only slight differences, especially for the peak decelerations of the individual body parts in the CO model. In addition, it is also seen that for various peak decelerations presented either in the RO model or in the CO model they are mostly reduced at lower initial impact speeds and less reduced as initial impact speed increases. We can easily find the reason for this from the energy dissipation ratio shown in Figures 3.19.

As seen in Figures 3.19, for the results in both models, the energy dissipation ratio (EDR) significantly drops as initial impact speed increases from 1 m/s to 7 m/s for all occupant types and both control algorithms. For instance, the EDR reduces from about 95% to 30% in the RO model and about 86% to 30% in the CO model for each control algorithm as the initial impact speed increases from 1 m/s to 7 m/s. Nevertheless, the favorable result is that by using the AMSS system, the initial kinetic

energy at all initial impact speeds examined was significantly dissipated even at 7 m/s. Similar to the observations in the peak deceleration, the two control algorithms provide comparable performance regarding the dissipated impact energy for the examined initial impact speed range. Also, the results from RO model and CO model are quite similar, especially for higher initial impact speeds above 4 m/s.

Thus, based on the simulation results, it is concluded that the impact loads imparted to the occupant are significantly reduced via dissipating the impact energy using the AMSS system with either control algorithm compared to the case of a traditional fixed seat.

3.8 Conclusions

A sliding seat utilizing adaptive control of an MREA was analyzed to accomplish a “soft-landing” in order to reduce impact loads imparted to a payload mass in a ground vehicle in the event of a low speed frontal impact (up to 7 m/s or 15.7 mph). Two occupant models were examined. First approach, a rigid occupant (RO) model assumed that the payload mass comprised of the seat and occupant mass. Second, to assess the coupling effects of a compliant occupant, the system was represented as a multi-degree-of-freedom (MDOF) compliant occupant (CO) model by incorporating a simplistic biodynamic model into the analysis, consisting of lumped mass and stiffness corresponding to pelvis, torso, and head (Note that leg and arm masses were neglected). Two control algorithms were formulated to bring the payload (occupant plus seat) mass to a stop using the available stroke: (1) the constant Bingham number or Bi_c control where the only measurement needed is the initial impact speed, and (2) the constant force or F_c control where both initial impact speed

and velocity feedback are required. Governing system equations were developed for both models. For the rigid occupant (RO) case, analytical solutions of the control inputs, dynamic responses and MREA responses were obtained. For the CO model, an iterative numerical technique was used to obtain the control trajectories or control gains, and these were implemented in order to ascertain the seat, biodynamic and MREA responses.

For both rigid and compliant occupant models, numerical simulations were conducted for three occupant types, namely, the 5th percentile female and the 50th and 95th percentile males, with respect to initial impact speeds of up to 7 m/s under a rectangular crash pulse of 20 g. Simulation results predicted that the impact loads imparted to the occupant are significantly reduced via dissipating the impact energy using the AMSS system using either control algorithm compared to a traditional fixed seat. Both control strategies provided comparable mitigations for various occupant types for the initial impact speed range examined. Both control algorithms are relatively easy to implement, although the constant Bingham number or Bi_c control is much simpler because it only requires sensing of the initial impact speed and the occupant weight, whereas F_c control requires the addition of velocity feedback in order to vary the current to maintain constant stroking force.

Table 3.1: Nomenclature used in the CO model.

Symbols	Descriptions
m_h	Head mass
m_t	Upper torso mass
m_p	Pelvis mass
m_s	Seat mass
k_{lb}	Lap belt spring rate
k_{sb}	Shoulder belt spring rate
l_h	Length from neck joint to head
l_c	Length from pelvis to upper torso
l_t	Length from pelvis to neck joint
l_{sb}	Length from pelvis to shoulder belt
l_{lb}	Length from pelvis to lap belt
x_{pl}	Pelvis displacement
x_s	Sliding seat displacement
\ddot{x}_v	Vehicle floor deceleration (crash pulse)
F_{mr}	MREA force
θ_h	Head rotation angle
θ_t	Upper torso rotation angle

Table 3.2: Typical values of the parameters in the CO model.

Symbols	5 th percentile female	50 th percentile male	95 th percentile male
$m_h (kg)$	3.65	4.54	4.94
$m_t (kg)$	11.90	17.2	22.60
$m_p (kg)$	13.70	23.0	30.30
$m_s (kg)$	20.0	20.0	20.0
$k_{sb} (kN/m)$	80	80	80
$k_{lb} (kN/m)$	80	80	80
$l_h (mm)$	200	220	230
$l_c (mm)$	270	300	320
$l_t (mm)$	450	500	530
$l_{sb} (mm)$	400	450	480
$\theta_h (\text{deg}) @ t = 0ms$	-10	-10	-10
$\theta_t (\text{deg}) @ t = 0ms$	-20	-20	-20

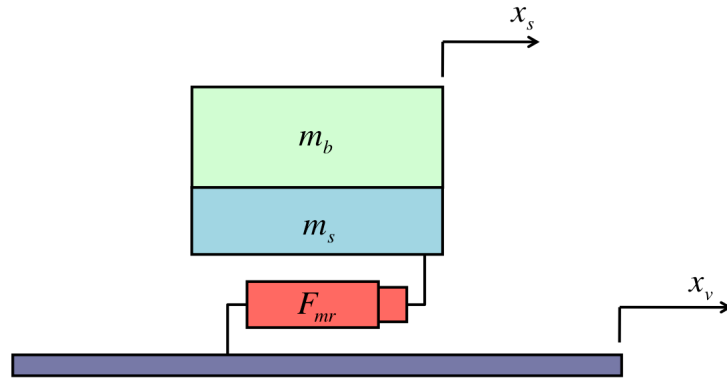


Figure 3.1: Configuration of single-degree-of-freedom (SDOF) rigid occupant (RO) model.

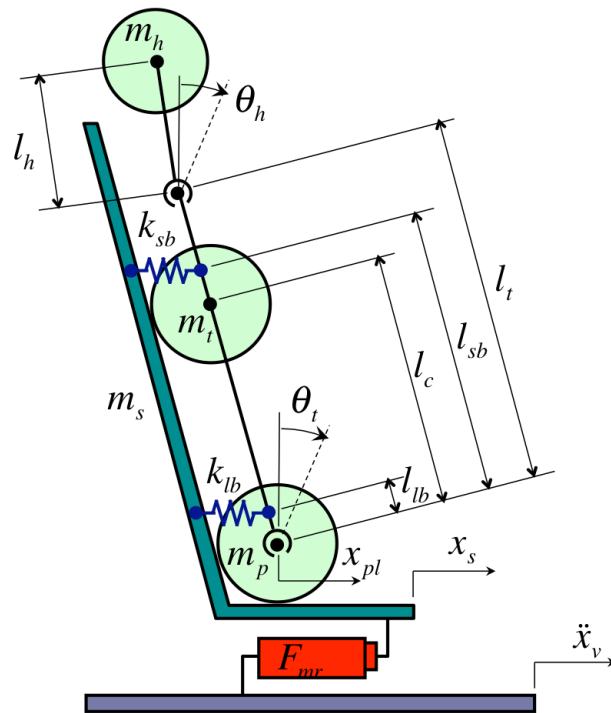


Figure 3.2: Configuration of multi-degree-of-freedom (MDOF) compliant occupant (CO) model.

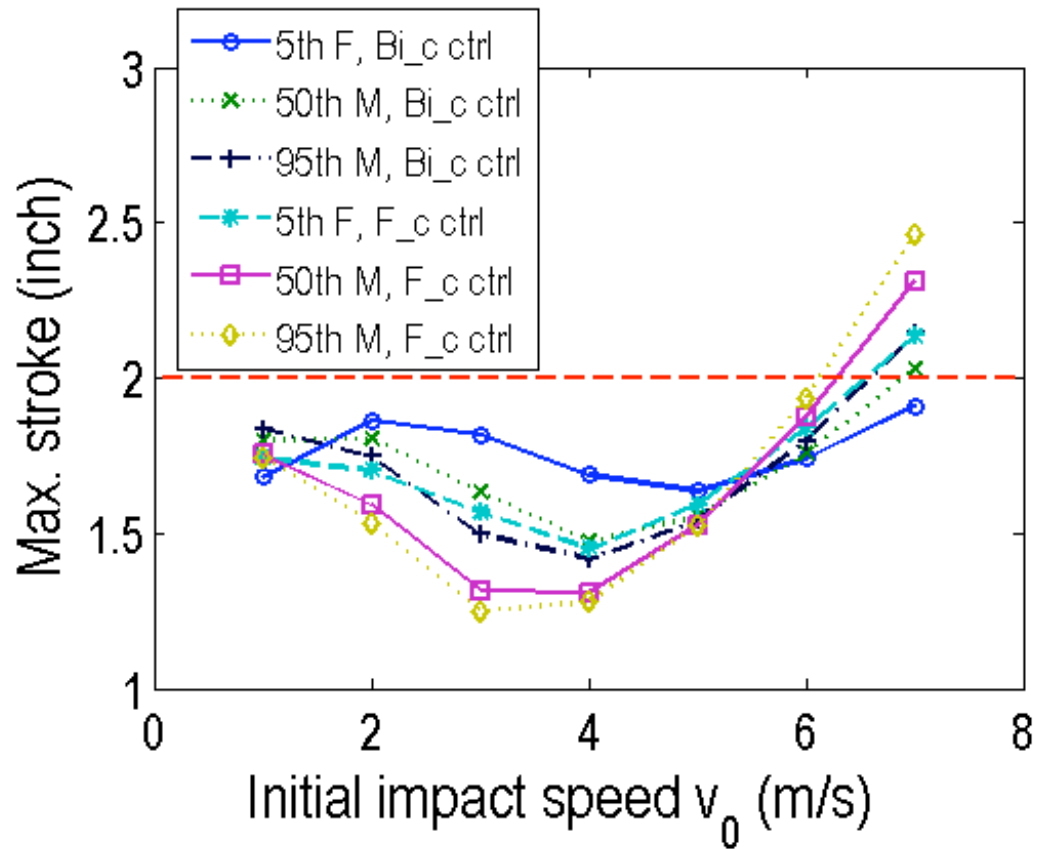


Figure 3.3: Resulted maximum MREA stroke if using the control inputs from RO model as the control inputs in CO model.

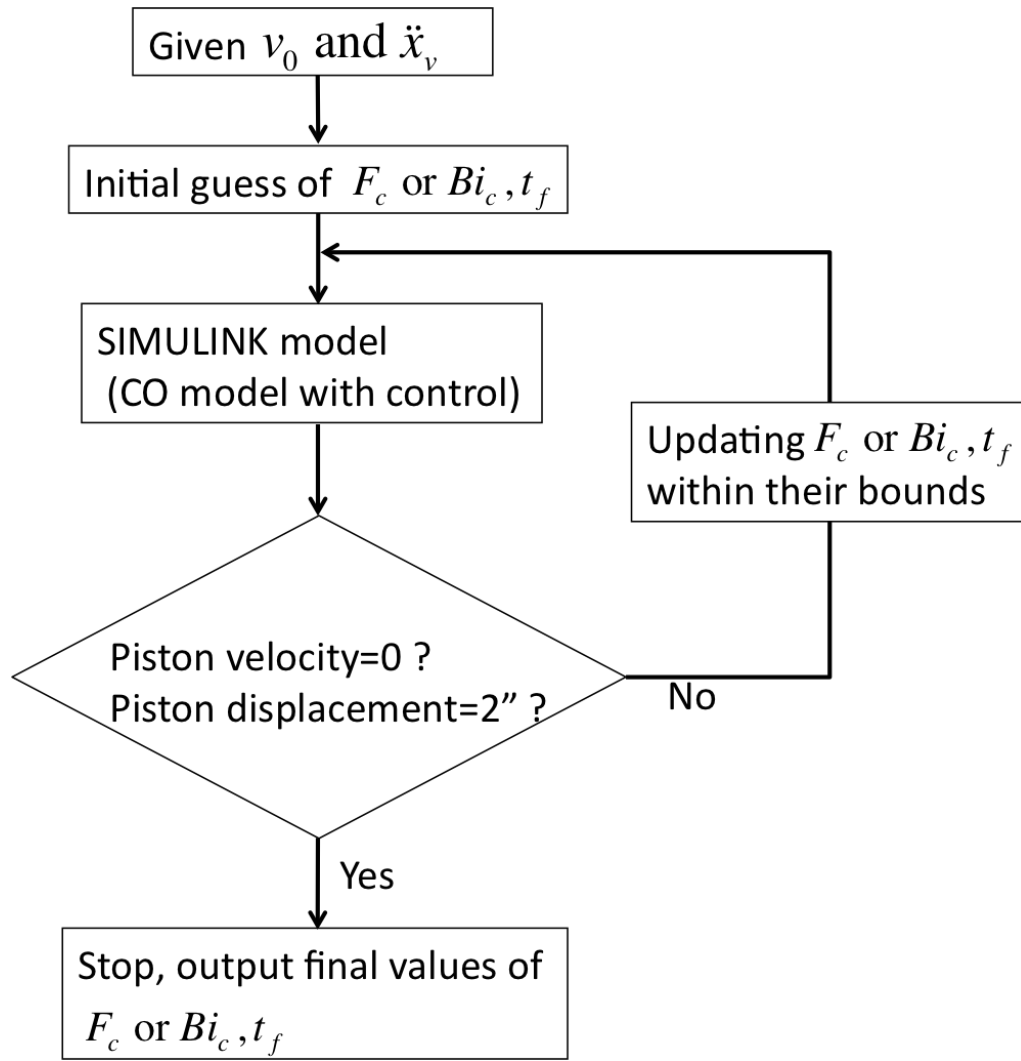
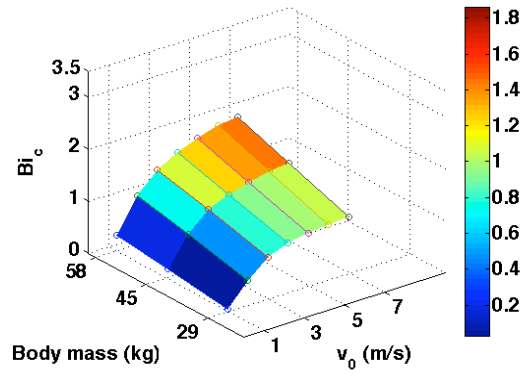
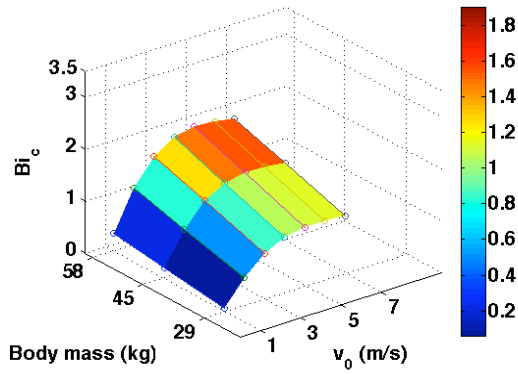
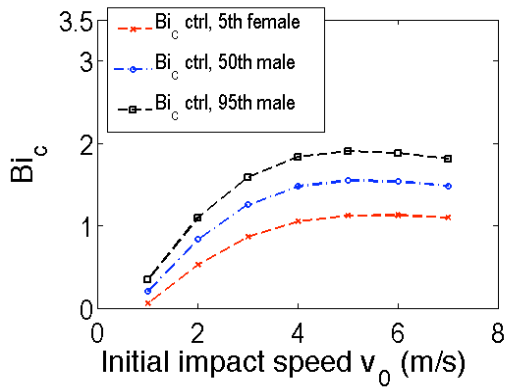


Figure 3.4: Numerical procedure to find control input using CO model.

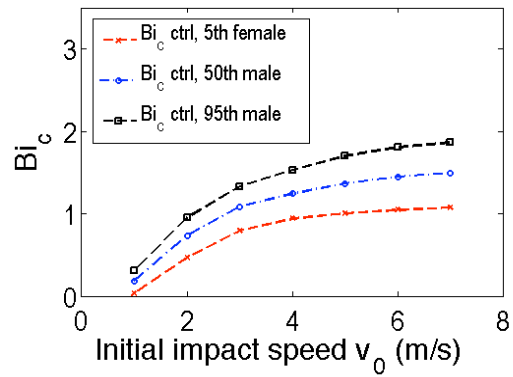


(a1) Bi_c vs. m_o and v_o for RO model

(a2) Bi_c vs. m_o and v_o for CO model

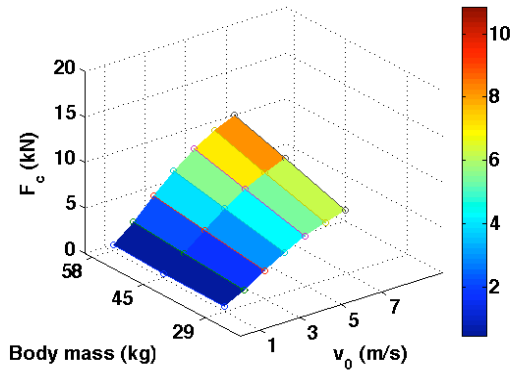


(b1) Bi_c vs. v_o for RO model

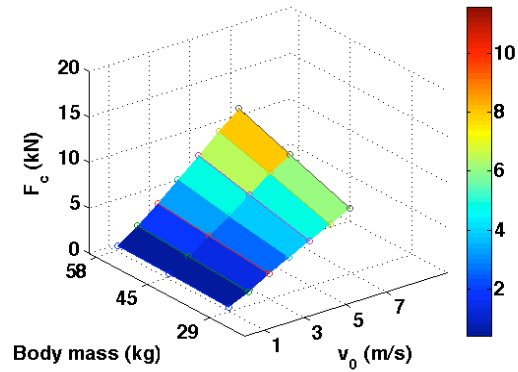


(b2) Bi_c vs. v_o for CO model

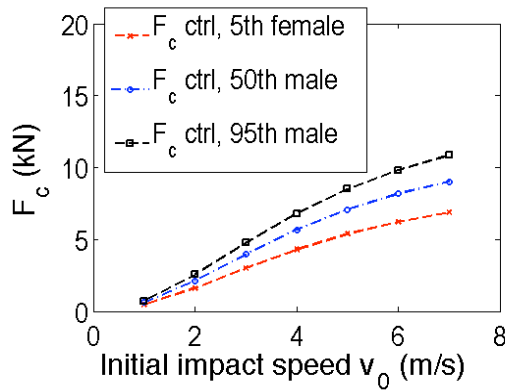
Figure 3.5: Determined control input, Bi_c , for the constant Bingham number control from RO model and CO model.



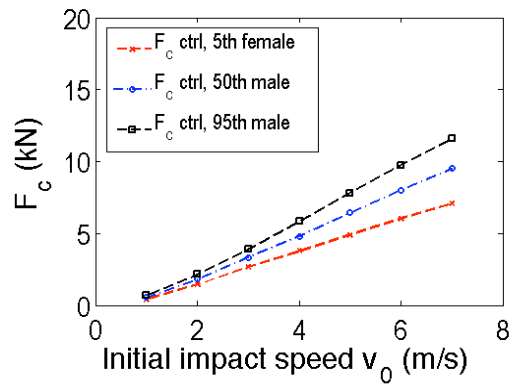
(a1) F_c vs. m_b and v_0 for RO model



(a2) F_c vs. m_b and v_0 for CO model

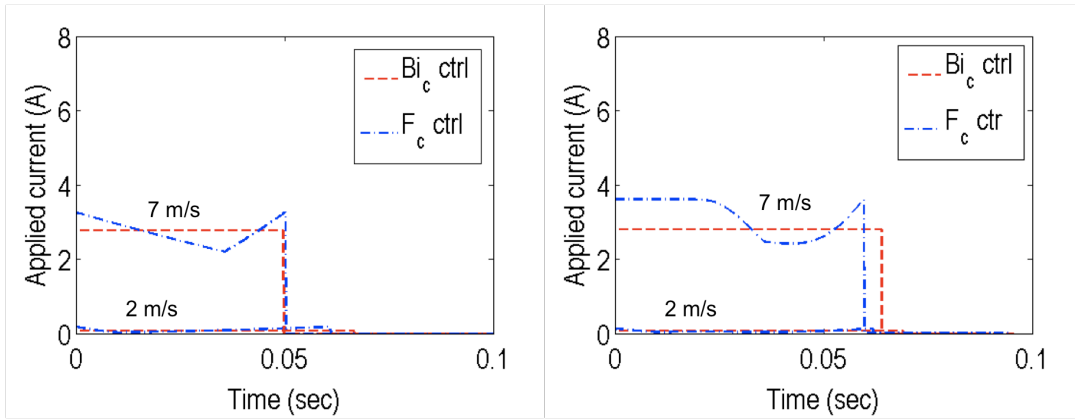


(b1) F_c vs. v_0 for RO model



(b2) F_c vs. v_0 for CO model

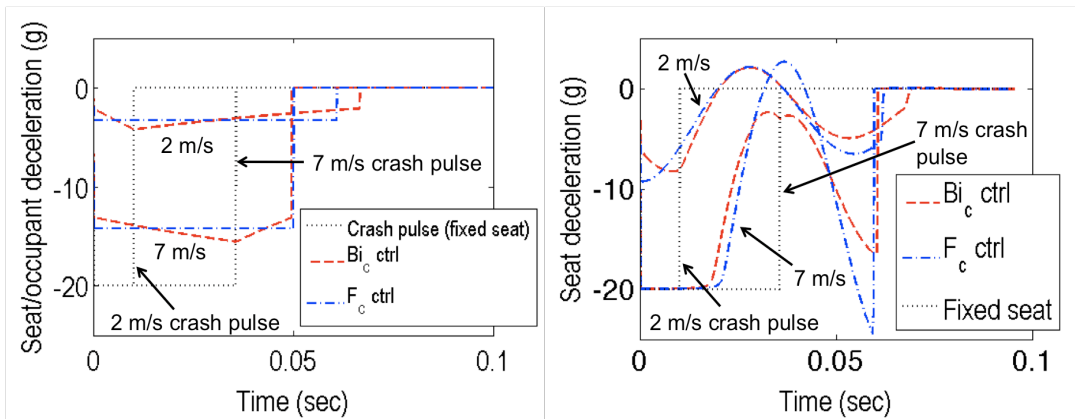
Figure 3.6: Determined control input, F_c , for the constant force control from RO model and CO model.



(a) Applied current, I (RO model)

(b) Applied current, I (CO model)

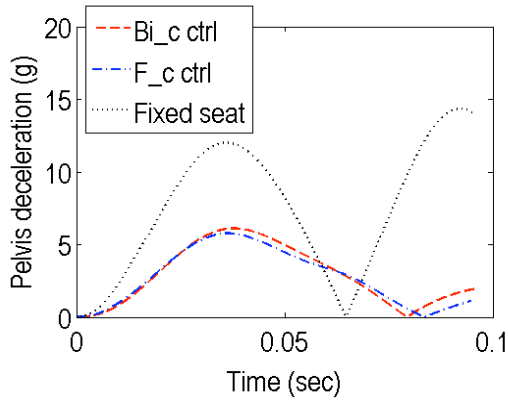
Figure 3.7: Sample applied current over time for achieving Bi_c and F_c control from RO model and CO model for 50th male at initial impact speed of 2 m/s and 7 m/s.



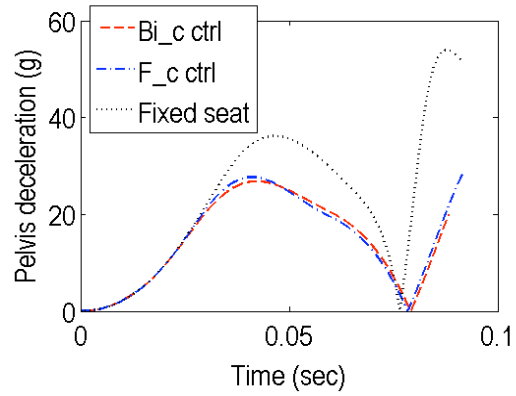
(a) Seat/occupant deceleration, \ddot{x}_s (RO)

(b) Seat deceleration, \ddot{x}_s (CO)

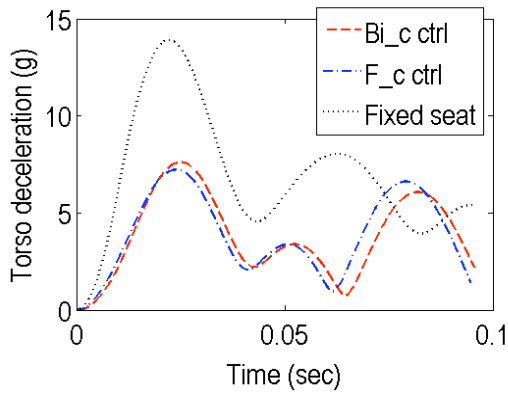
Figure 3.8: Seat/occupant deceleration for rigid (RO model) and compliant occupant (CO model) cases. Conditions are for a 50th male at impact speed of 2 m/s and 7 m/s (note that compliant model results in (b) are for seat itself).



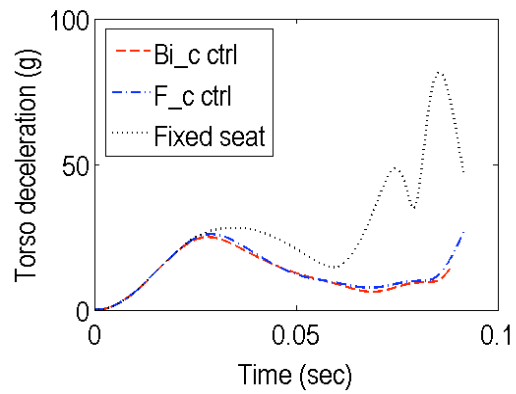
(a1) Pelvis deceleration, \ddot{x}_{pl} , at $v_0=2$ m/s



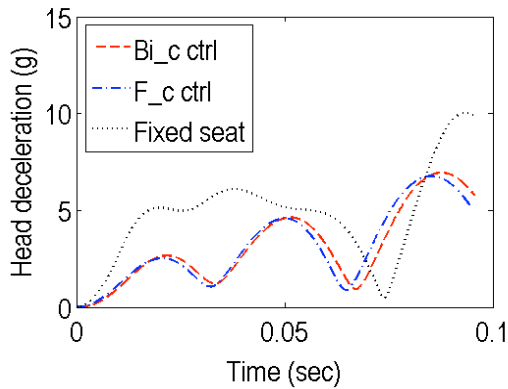
(a2) pelvis deceleration, \ddot{x}_{pl} , at $v_0=7$ m/s



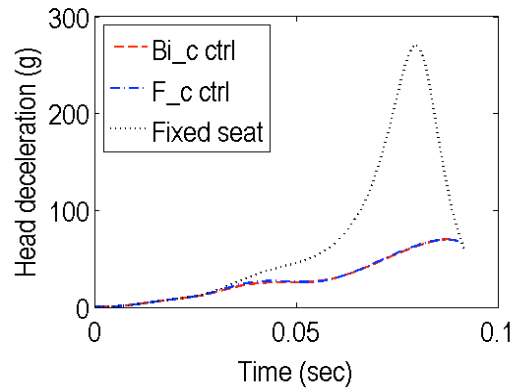
(b1) Torso deceleration, \ddot{x}_t , at $v_0=2$ m/s



(b2) Torso deceleration, \ddot{x}_t , at $v_0=7$ m/s

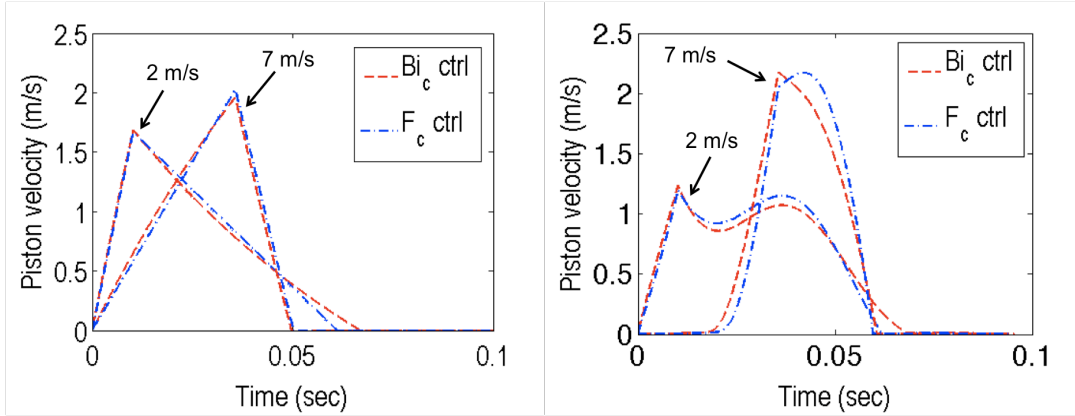


(c1) Head deceleration, \ddot{x}_h , at $v_0=2$ m/s



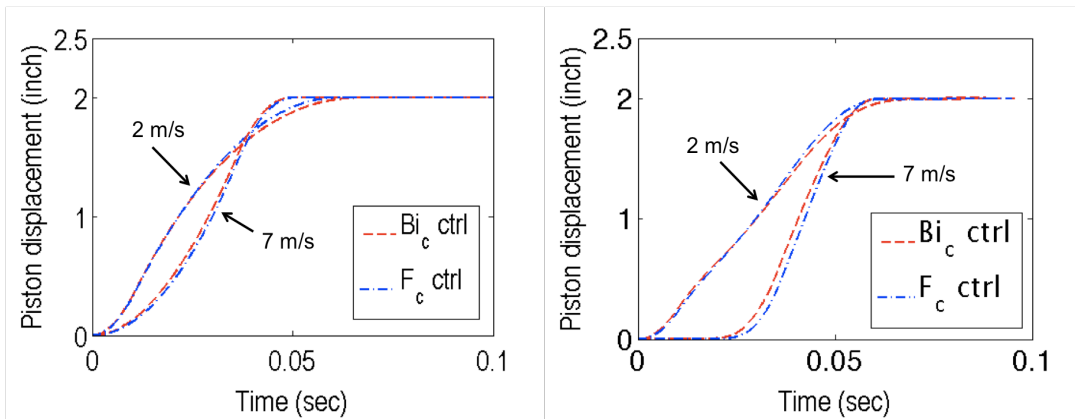
(c2) Head deceleration, \ddot{x}_h , at $v_0=7$ m/s

Figure 3.9: Sample simulated occupant biodynamic responses (magnitudes) from CO model for 50th male at initial impact speed of 2 m/s and 7 m/s.



(a1) Piston velocity, V_p (RO model)

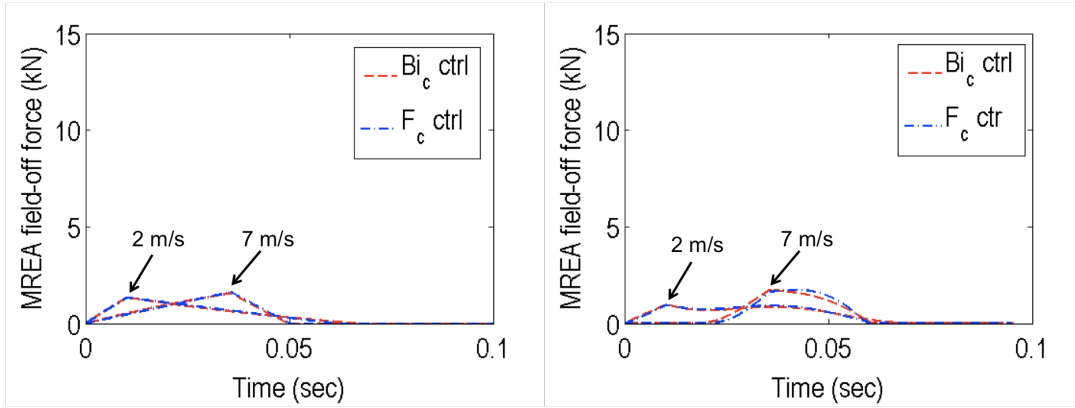
(a2) Piston velocity, V_p (CO model)



(b1) Piston displacement, X_p (RO)

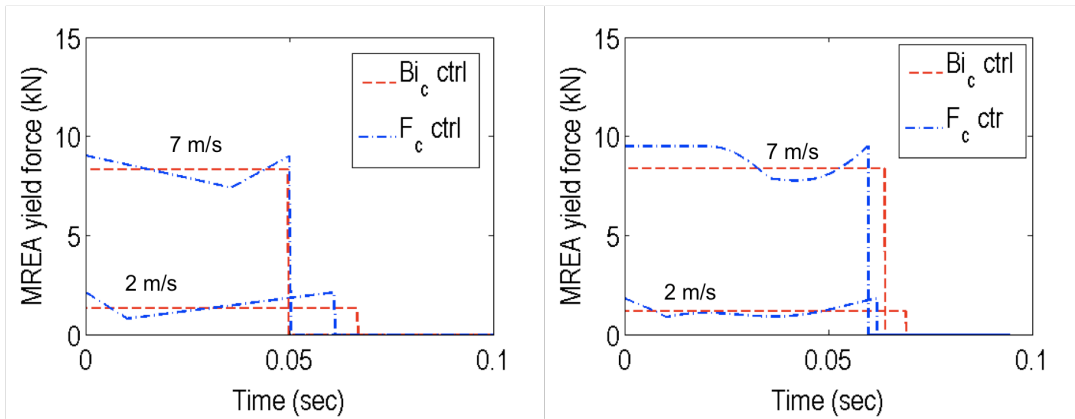
(b2) Piston displacement, X_p (CO)

Figure 3.10: Sample resulted transient MREA piston velocity, V_p , piston displacement, X_p , for achieving Bi_c and F_c control from RO model and CO model for 50th male at initial impact speed of 2 m/s and 7 m/s.



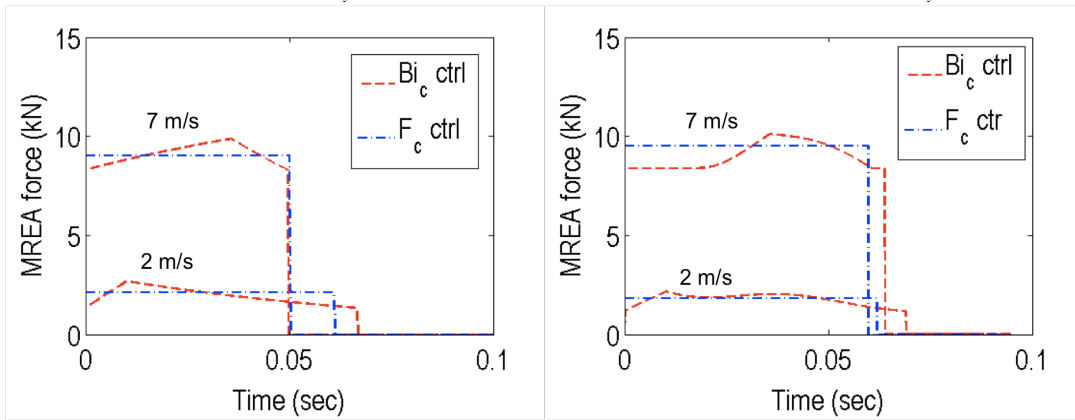
(a1) MREA field-off force, F_{off} (RO)

(a2) MREA field-off force, F_{off} (CO)



(b1) MREA yield force, F_y (RO)

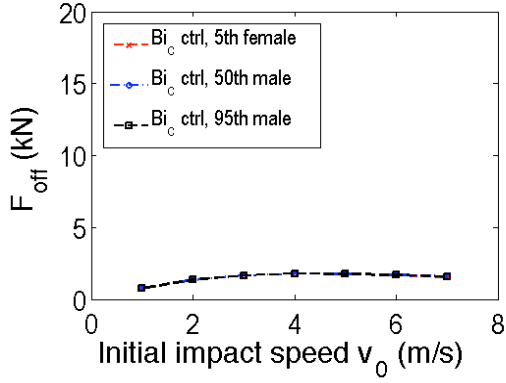
(b2) MREA yield force, F_y (CO)



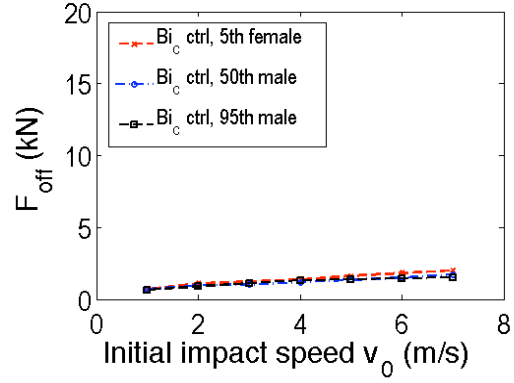
(c1) Total MREA force, F_{mr} (RO)

(c2) Total MREA force, F_{mr} (CO)

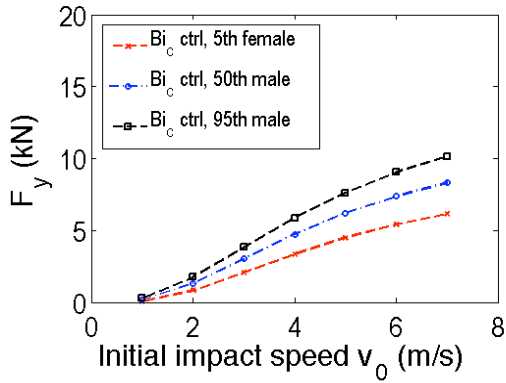
Figure 3.11: Sample resulted transient MREA field-off force, F_{off} , yield force, F_y , and MREA force, F_{mr} , for achieving Bi_c and F_c control from RO model and CO model for 50th male at initial impact speed of 2 m/s and 7 m/s.



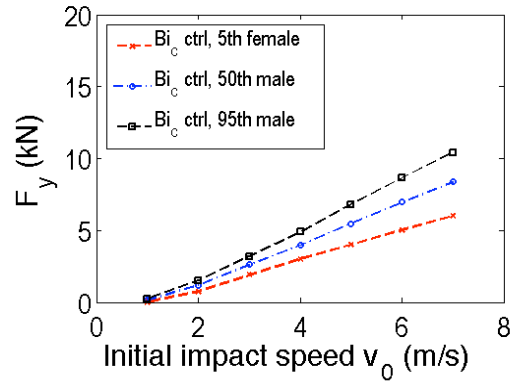
(a1) MREA field-off force, F_{off} (RO)



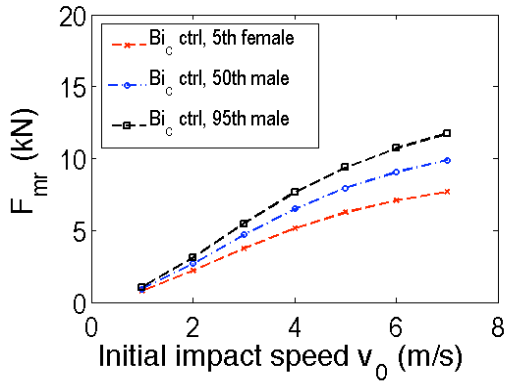
(a2) MREA field-off force, F_{off} (CO)



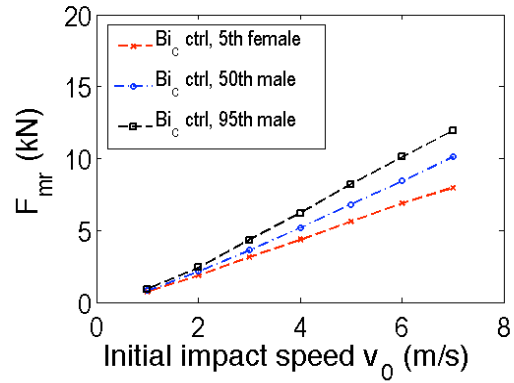
(b1) MREA yield force, F_y (RO)



(b2) MREA yield force, F_y (CO)

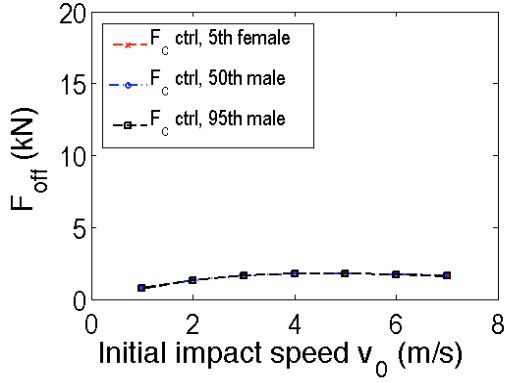


(c1) Total MREA force, F_{mr} (RO)

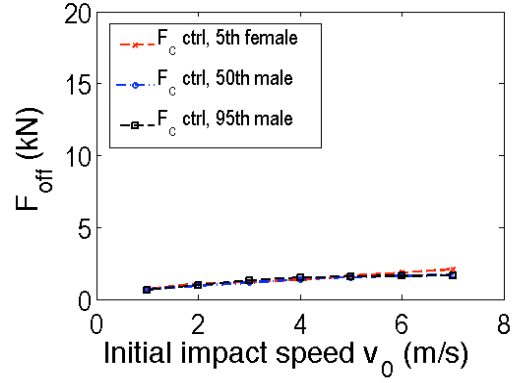


(c2) Total MREA force, F_{mr} (CO)

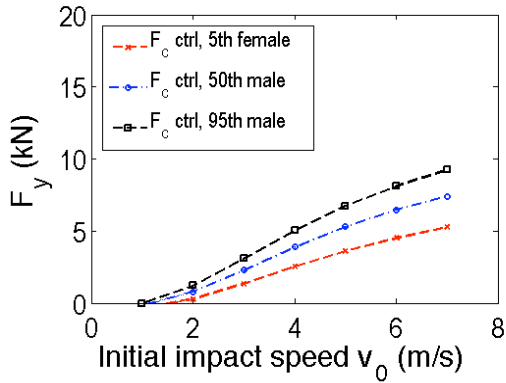
Figure 3.12: Resulted peak MREA force for achieving the constant Bingham number control (Bi_c control) from RO model and CO model.



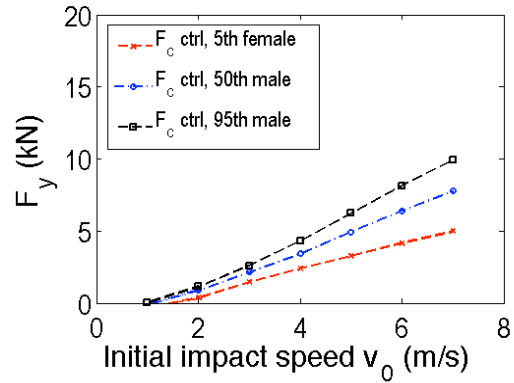
(a1) MREA field-off force, F_{off} (RO)



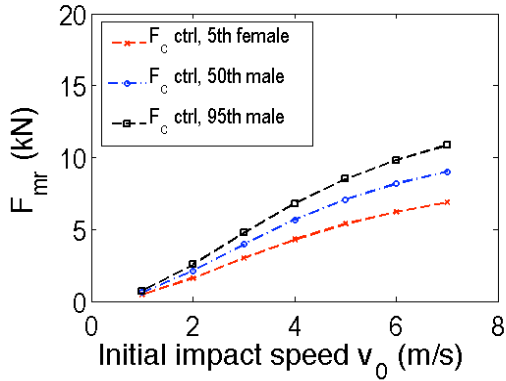
(a2) MREA field-off force, F_{off} (CO)



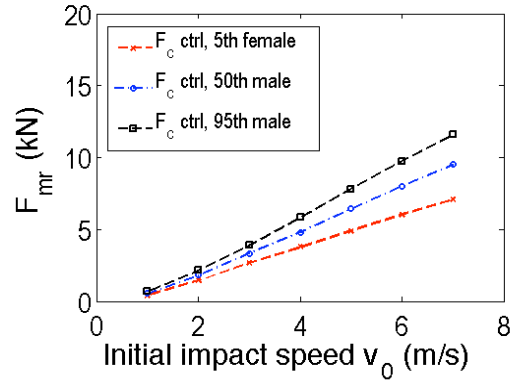
(b1) MREA yield force, F_y (RO)



(b2) MREA yield force, F_y (CO)

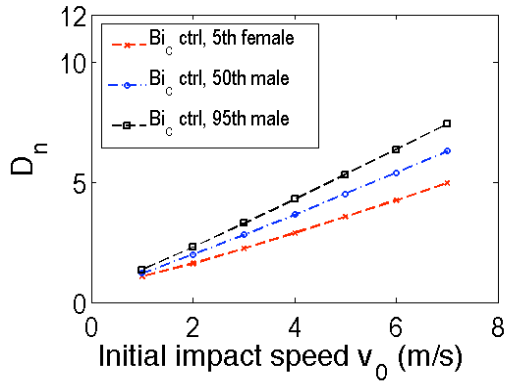


(c1) Total MREA force, F_{mr} (RO)

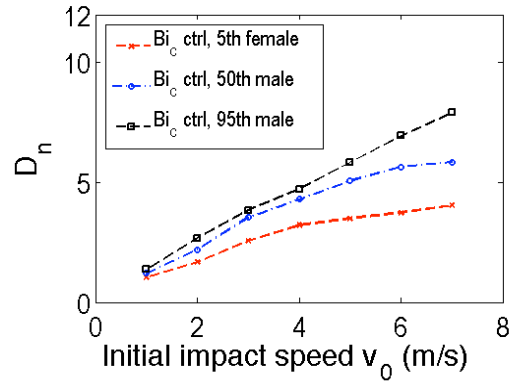


(c2) Total MREA force, F_{mr} (CO)

Figure 3.13: Resulted peak MREA force for achieving the constant stroking force control (F_c control) from RO model and CO model.

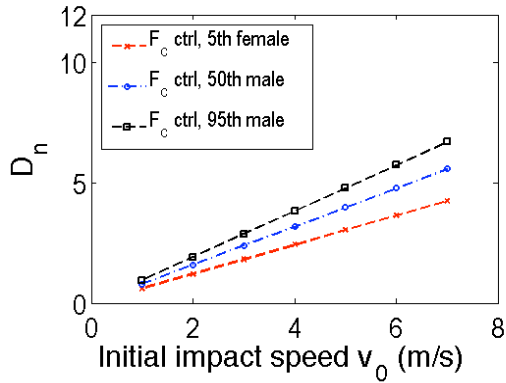


(a) MREA dynamic range, D_n (RO)

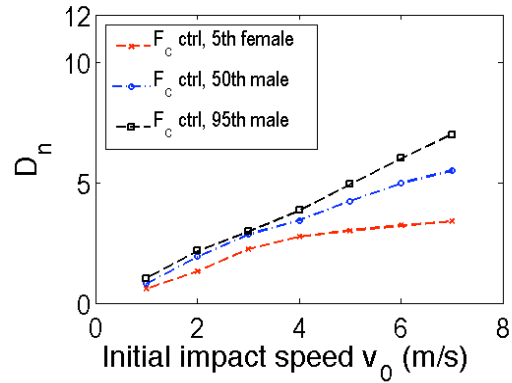


(b) MREA dynamic range, D_n (CO)

Figure 3.14: Corresponding MREA dynamic range, D_n obtained from the peak MREA force for achieving the constant Bingham number control (Bi_c control) from RO model and CO model.



(a) MREA dynamic range, D_n (RO)



(b) MREA dynamic range, D_n (CO)

Figure 3.15: Corresponding MREA dynamic range obtained from the peak MREA force for achieving the constant stroking force control (F_c control) from RO model and CO model.

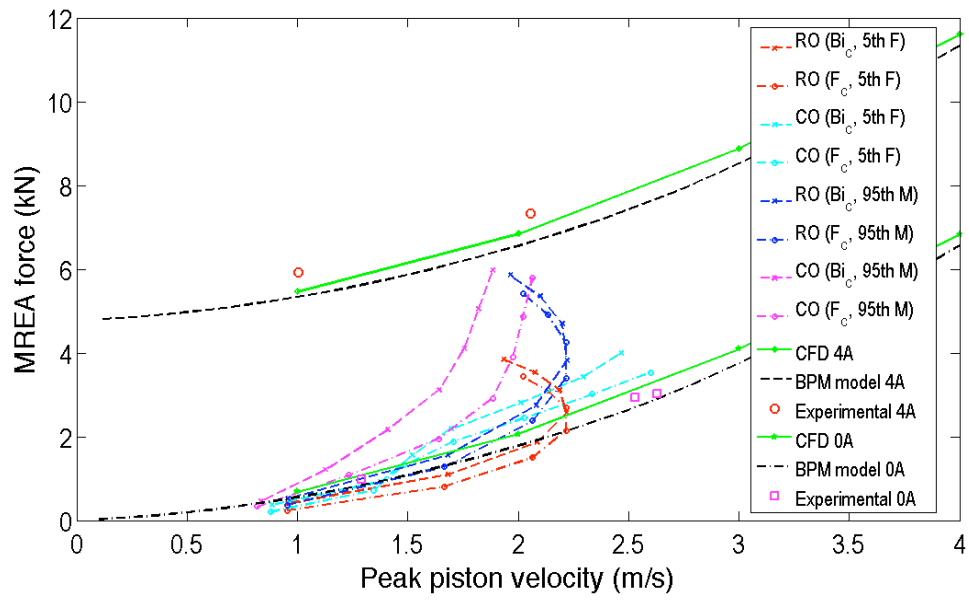


Figure 3.16: Measured and predicted MREA force as well as required force boundaries for each control algorithm obtained in sliding seat model analysis.

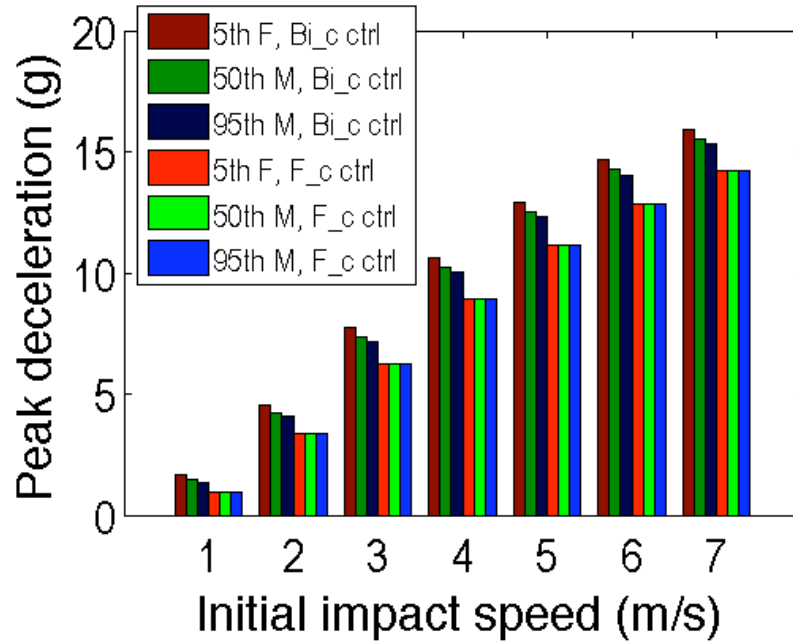


Figure 3.17: Comparisons of peak magnitude of seat/occupant deceleration vs. initial impact speed for RO model with different control algorithms and occupant types (Note that in the fixed seat cases, the peak decelerations are 20 g).

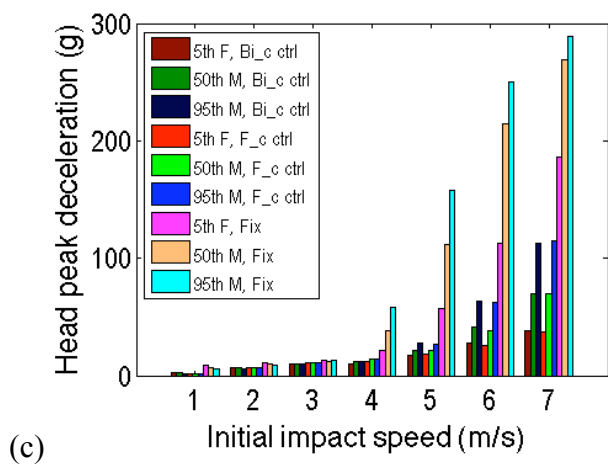
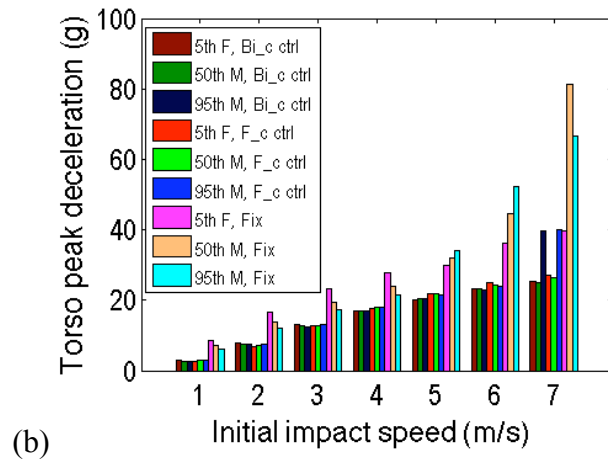
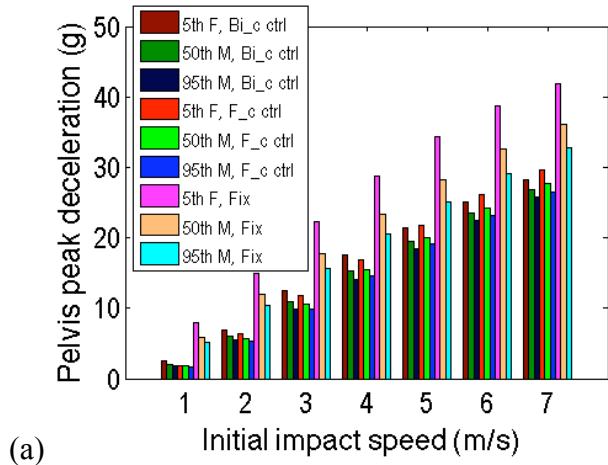
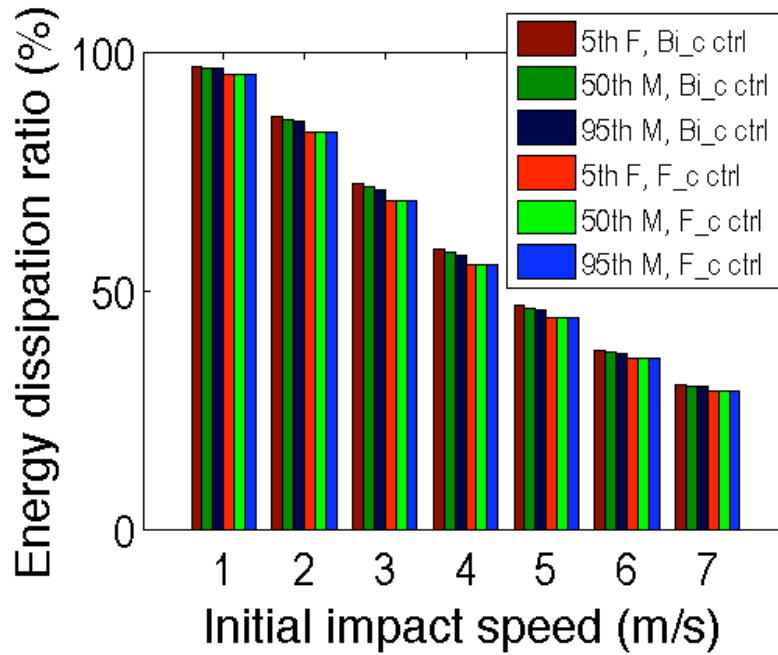
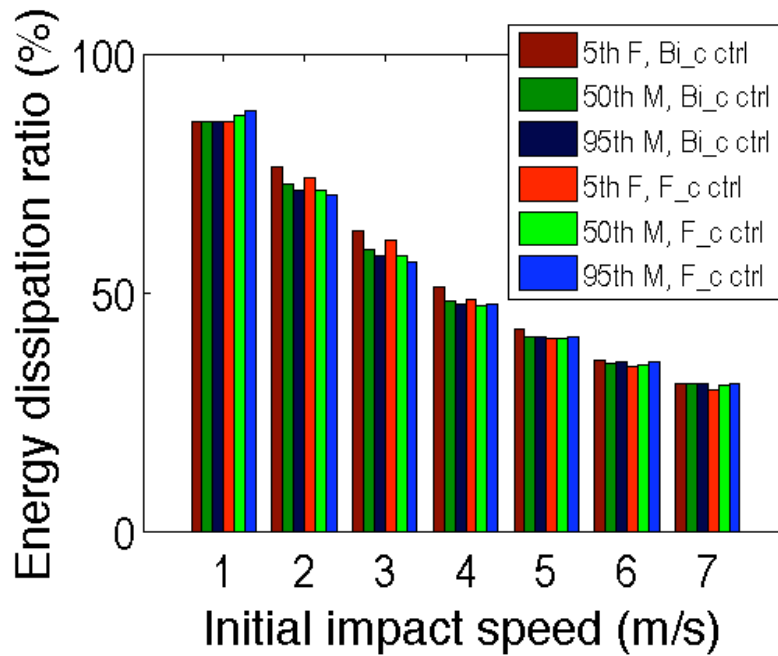


Figure 3.18: Comparisons of peak deceleration magnitude vs. initial impact speed for individual parts of occupant from CO model with different control algorithms and occupant types: (a) pelvis, (b) upper torso, (c) head.



(a) RO model



(b) CO model

Figure 3.19: Comparisons of energy dissipation ratio vs. initial impact speed with different control algorithms and occupant types for RO model and CO model.

Chapter 4: Sled Test and System Modeling for the Prototype Seat System

4.1 Introduction

In previous chapter, we conceptually proposed and analyzed two control algorithms, the constant Bingham number control and constant stroking force control, to make the adaptive sliding seat system achieve “soft-landing” while taking full advantage of the available MREA stroke. The analysis was carried out using two modeling approaches - a single-degree-of-freedom (SDOF) rigid occupant (RO) model and a multi-degree-of-freedom (MDOF) compliant occupant (CO) model. Simulation results of both models showed that the controlled seat system was brought to a stop in the available stroke and the payload decelerations were significantly reduced compared to the counterparts in a traditional fixed seat.

In this section, we will build a prototype sliding seat system using the developed SSMREA and describe its dynamic behavior using the above two system models, namely, the RO model and the CO model. Therefore, test of the prototype seat system will be first conducted under passive mode with no controller integrated, that is, the MREA will work under arbitrarily or empirically pre-selected constant current mode for each test.

Thus, in this chapter, following the introduction of the experimental setup of the sled test, the test results for some sample cases were presented and discussed. Using the collected data, the two system models were re-visited, in which the assumed

MREA behavior is replaced with the experimentally characterized behavior of the particular SSMREA. By comparing the simulation results from the two system models with the measured data, their respective adequacy for capturing the dynamic behavior of the prototype seat system will be addressed.

4.2 Sled Test

4.2.1 Sled Test Set-up

The prototype sliding seat system was built at the GMC R&D Center and directly attached to the sled test facility as shown in Figure 4.1. Two identical units of the SSMREA were installed in the seat system, one at each slide rail of the seat in a symmetric parallel manner. For each SSMREA, the shaft/rod end was connected to the rear of the slide rail and another end (at which the gas chamber was located) was attached to the mounting structure that was rigidly fixed to the sled platform. Upon each test, the shaft of each SSMREA was fully pushed into the MREA body by pushing the seat to slide to its zero stroke position so that the extension stroke of the SSMREA can be used during the impact. In the middle position of each slide rail (we'll refer them as left rail and right rail later), an accelerometer was mounted to measure the transient deceleration of the seat. In addition, a string-pot (cable extension transducer) was attached to one of the rack like structures at the bottom rear part of the seat pan to measure the instantaneous SSMREA piston displacement. Also, a stroke restriction mechanism was applied to one of the sliding rail of the seat to limit the maximal stroke of the SSMREA to be 2". Then an anthropomorphic test dummy (ATD) was placed in the seat to play the role of an occupant and was

restrained to the seat by a lap belt as well as a chest belt (to emulate shoulder belt) without slack.

The whole set of the prototype sliding seat system plus the dummy was attached to the sled platform of a Hyge (Hydraulically controlled, gas energized) sled test facility at the GM R&D Center. The combined entity of sliding seat system including the dummy plus the sled platform will be referred to as sled ballast thereafter. To conduct the sled test, the sled ballast is made to run from an initial rest position till its translating velocity approaching a prescribed speed (initial impact speed) via speed trap, then it continues moving over a very short distance at this speed and impacts with an aluminum block set, which is attached to a snubber residing in the wall block and consists of a 8” thickness hexcel and 2” thickness crown (nominally 1000 psi crush strength), to produce a deceleration load, namely the crash pulse, imparted to the adaptive sliding seat system. The deceleration load or crash pulse is generated in such a way that its nominal strength (magnitude) is 20 g and its nominal shape is a rectangular. In this study, we will refer to this deceleration load as sled deceleration or crash pulse. As well, sometimes in the figure legend, we use “sled” or the like to denote the crash pulse. The crash pulse was measured by an accelerometer and its time history was recorded by the data acquisition system.

As mentioned earlier, the main purpose of the sled test at this moment is to simulate a low speed frontal impact event in the laboratory scale to study and model the behavior of the prototype sliding seat system with MREA integrated. So no controller is presented in the system set-up. Two types of occupant were investigated: 1) the 5th percentile female or simply 5th female, and 2) the 95th percentile male or

simply 95th male. Due to the unavailability of the 95th male dummy at the time of test, the 5th female dummy was used to represent the 95th male dummy by adding extra blocks of mass in the body parts of upper torso and the pelvis. For the 5th female, four initial impact speeds, 2.6, 3.5, 4.5 to 5.6 m/s, with a few pre-selected current levels for each speed were tested. For the 95th male, three initial impact speeds - 2.6, 3.5 and 4.5 m/s - with multiple pre-selected current levels for each speed were tested.

For clarity, the test matrix is outlined in Table 4.1. Also, Table 4.2 summarizes the test cases with full stroke and zero (or nearly zero) stroke for the 5th female and 95th male, respectively. For all tests of the 5th female, the sliding seat used a power seat (71 lbs); for all tests of the 95th male, a manual seat (51 lbs) was used due to large degree of deformation of the power seat after tests of the 5th female. However, it was found that change of seat did not impose significant difference in the dynamic response (deceleration time history) of the sliding seat to the imparted crash pulse as demonstrated in Figure 4.2. It is observed that, from case to case, the nominal crash pulses were actually not identical and exhibited minor differences. Therefore, later whenever the results are presented, the measured seat deceleration time history is always accompanied with its particular associated crash pulse (sled deceleration).

4.2.2 Sled Test Results

In the data acquisition system, the crash pulse was measured with a sampling rate of 10 kHz and pre-filtered with a built-in SAE (Society of Automotive Engineers) CFC (channel frequency class) 60 (i.e., cutoff frequency 100 Hz) filter. Thus, the recorded crash pulses in the data system are clean data and ready for direct usage in result analysis. In contrast, the seat decelerations measured at the two

locations, the middle part of the left rail and the right rail, were recorded separately as two signals in the data system with the same sampling rate of 10 kHz. And a built-in SAE CFC 600 (i.e., cutoff frequency 1000 Hz) filter was used to pre-filter the two signals. Therefore, these two data sets are not deemed as clean enough for direct usage for results analysis. To make the recorded seat deceleration data suitable for analysis, a CFC 60 filter was used to filter them based on three considerations: 1) the power spectrum analysis results for typical cases, 2) reference information in Huang (2002), and 3) to be consistent with the built-in crash pulse filter in the data acquisition system. Figures 4.3 present some sample power spectrum results for two typical cases, i.e., 4.5 m/s and 0.5A for the 5th female and 4.5 m/s and 3.0A for the 95th male. As seen in the figures, most power of the seat deceleration signal measured at both locations is distributed below 100 Hz, which justifies the filter class selection for it. In addition, power spectrum analysis for the SSMREA piston displacement measured by the string-pot was also performed to support a proper selection of the filter class for it. It can be seen that all power of the string-pot signal (piston displacement) is distributed far below 20 Hz for both sample cases. However, to be consistent with the deceleration filtering, the piston displacement was filtered with cut-off frequency of 100 Hz. The piston velocity was obtained by differentiating the filtered piston displacement and then filtered again by a second-order butterworth filter with cutoff frequency of 30 Hz.

Figures 4.4-4.7 demonstrate sample measured seat system dynamic response (seat deceleration time histories) and the associated MREA dynamic behavior at nominal initial impact speed 2.6 m/s with various applied current levels for the 5th

female and 95th male, respectively. Other cases with full stroke and zero (or nearly zero) stroke as listed in Table 4.2 are displayed in appendix A. Since the seat decelerations measured at the two seat sites (left rail and right rail) appeared to be slightly different from each other, we simply averaged these two data sets at each time instant to represent the overall seat deceleration at that time point, which is denoted by “Average” in the legends of the figures. As observed in the figures, for cases when the lowest current level was applied under the same initial impact speed (for instance, 0A for 5th female and 0.5A for 95th male at 2.6 m/s) and the SSMREA full stroke was sufficiently utilized (refer to Table 4.2), the deceleration transmitted to the seat during the impact period is largely reduced compared to the crash pulse. As the applied MREA current level increases, the degree of deceleration reduction to the seat decreases. For the cases with the highest applied current level at each initial impact speed for both 5th female and 95th male, for example, the cases of 2.0A for 5th female and 3.0A for 95th male at 2.6 m/s, the seat deceleration is nearly the same as the crash pulse. The reason is quite apparent based on the used MREA stroke shown in Figures 4.5 and 4.7. For sufficiently high current, the MREA force may cause the MREA to lock up, so that the MREA does not stroke, so that no energy can be dissipated. For example, for the 5th female, at 0A and 2.6 m/s, 2” stroke was used, at 2A and 2.6 m/s, almost no stroke was used, because the MREA stroking load is greater than the load generated during the impact event. Also, the associated piston velocity is also different when applied current level changes. Generally, the peak piston velocity largely decreases as applied current level increases. For the lower current levels (0A and 0.5A for 5th female and 0.5A and 1.0A for 95th male at 2.6

m/s), two obvious peaks were observed. The first peak is higher than the second one for the 5th female while the first peak is lower than the second one for the 95th male. But as applied current level increases, the smaller peak seems less pronounced and becomes less obvious.

It is also noted that at the lowest current level, i.e. 0A for 5th female and 0.5A for 95th male, another secondary peak in the seat deceleration showed up after the first primary peak diminishing to zero. This secondary peak was induced due to the metal-to-metal impact between the seat and the 2” full stroke restriction mechanism because the MREA force is relatively small and the seat requires more than 2” stroke to come to a stop. Namely, there was an end impact between the seat and the stroke restriction mechanism for these current levels. Also, the secondary peak at the left rail is higher than that of the right rail because the stroke restriction mechanism was located on the left rail. As seen in Figures 4.5 and 4.7, the measured MREA strokes at 0A for 5th female and 0.5A for 95th male are both far exceeded the 2” stroke restriction. In these cases, the seat kept sliding after 2” stroke and impacted with the full stroke restriction mechanism and broke through it until it finally came to a stop. The secondary peak is thus induced by the seat end-stop impact because the SSMREA piston velocity is not approaching zero when running out of the maximal allowable stroke (here is 2”) as observed in Figures 4.5(b) and 4.7(b) – the piston velocity at 2” stroke is about 0.72 m/s and 1.23 m/s for the 5th female and 95th male respectively. Also, as seen in Figure 4.6(a) the secondary peak for the 95th male at 2.6 m/s is even much larger than the primary peak. It is reasonable to believe that strong end-stop impact like this may cause extra harmful impact load to impart to the occupant and thus degrade the

overall effectiveness of the adaptive sliding seat system. This indicates that, in an experimental way, setting the “soft-landing” criterion as the control objective of the adaptive sliding seat system is appropriate and beneficial.

In all, the results as demonstrated in the figures and in Table 4.2 reveal a fact that: there would be at least a proper current level that could fully utilize the available stroke and avoid an end-stop impact. Thus, it implies that at least the constant current control is practically feasible for the adaptive sliding seat system. In order to systematically determine a right constant current level or force level (control input) for the prototype seat system to achieve the “soft-landing” objective at each initial impact speed and for each occupant type, the mathematical model of the prototype seat system must be established. So in the following section, we will take advantage of the system models proposed in Chapter 3 to assess if they are adequate to describe the prototype seat system behavior.

4.3 Modeling of the Adaptive Sliding Seat System

4.3.1 Modeling of SSMREA

As discussed in Chapter 2, the SSMREA force-velocity characteristics and the transient behavior under high speed impact loadings can be adequately described by the BPM model. Figure 4.8 shows the MREA force predicted by BPM model with the adjusted coefficients for K_{SC} and K_{SE} (namely, $K_{SC} = 0.48758$ and $K_{SE} = 0.5441$) at various tested current levels as well as the experimental data. It is seen that the SSMREA force-velocity behavior is well described by the BPM model at various current levels.

However, as indicated in Chapter 2, using the BPM model to calculate the SSMREA force after the instant piston velocity was measured and fed into the controller is relatively complicated because many parameters are functions of piston velocity. In practice, the impact period is relatively very short (roughly less than 50 ms in our case). Thus the computing time for a command current according to the measured piston velocity in a real-time controller (say for the constant force control) is essentially important for a successful control algorithm implementation and must be made as short as possible. Therefore, there is a need to simplify the MREA force computing process in the real-time controller. By inspecting the force calculation in the BPM model, we found that the SSMREA force can be characterized by the following simple equation without sacrifice of accuracy:

$$F_{mr} = \alpha \cdot I^\beta \cdot \text{sign}(V_p) + C_2 \cdot V_p^2 + C_1 \cdot V_p \quad (4.1)$$

Here the definition of the variables is listed below:

F_{mr} : MREA force (kN)

I : applied current to MREA (Ampere)

α, β : parameters for relationship between MREA force and current (here $\alpha=2.4715$, $\beta=0.4754$)

V_p : rod/piston velocity (m/s)

C_2, C_1 : parameters for relationship between field-off force and piston velocity (here identified as $C_2 = 0.3852$, $C_1 = 0.1036$)

The SSMREA force-velocity behavior computed from Eq. (4.1) is presented in Figure 4.9 and compares with the experimental data as well as the BPM prediction. It is seen that the force-velocity behavior obtained from Eq. (4.1) and from BPM model

coincides with each other and both agree well with the experimental data at various current levels. Therefore, this simple MREA force equation is shown to be as accurate as the BPM model in characterizing the SSMREA force-velocity behavior. It thereby will be used in the prototype sliding seat system model to replace the previously assumed MREA force characterization using Bingham-plastic model. Also it will be used in the later controller implementation.

4.3.2 Single-Degree-of-freedom (SDOF) Rigid Occupant (RO) Model

First, we will study the adequacy of the single-degree-of-freedom (SDOF) rigid occupant (RO) model introduced in Chapter 3 (also shown in Figure 4.10). Recall the governing equation of the RO model:

$$(m_b + m_s)\ddot{x}_s + F_{mr} = 0 \quad (4.2)$$

Here F_{mr} is the SSMREA force and now it is expressed as:

$$F_{mr} = 2000 \left[2.4715I^{0.4754} \text{sign}(\dot{x}_s - \dot{x}_v) + 0.3852(\dot{x}_s - \dot{x}_v)^2 + 0.1036(\dot{x}_s - \dot{x}_v) \right] \quad (4.3)$$

Note that since there are two identical units of SSMREA connected in parallel in the prototype sliding seat system, the force needs to time 2 and then time 1000 to change the force unit from kN to Newton when included in the seat system model to be consistent with the SI units of other variables in the system model.

We will simulate the seat deceleration using this model and compare it with the measured seat deceleration. In the simulation, the crash pulse, \ddot{x}_v , will be the measured crash pulse in the sled test in stead of the assumed ideal rectangular crash pulse. Also, the seat mass, m_s , will be the corresponding seat mass in the real sled

test, that is, 32.2 kg (71 lbs) for the 5th female and 23.1 kg (51 lbs) for the 95th male.

The occupant body mass, m_b , is the same as before.

SIMULINK module in MATLAB was used to obtain the seat deceleration in Eq. (4.2) and the SIMULINK model of the RO model is shown in Figure 4.11. The simulated seat deceleration for sample cases are presented in Figures 4.12. It is seen that the simulation results demonstrate large discrepancy with the measured data. Thus, the RO model cannot adequately capture the dynamic behavior of the prototype seat system.

4.3.3 Multi-Degree-of-Freedom (MDOF) Compliant Occupant (CO) Model

Similarly, we will address the adequacy of the MDOF compliant occupant (CO) model (shown again in Figure 4.13) using the sled test data. Recall that the governing equations of the CO model are then given by:

$$m_s \ddot{x}_s = k_{sb}(x_p + l_{sb} \sin(\theta_t) - l_{sb} \sin(\theta_{t0}) - x_s) + k_{lb}(x_p - x_s) - F_{mr} \quad (4.4)$$

$$\begin{aligned} & (m_p + m_t + m_h) \ddot{x}_p + (m_t l_c + m_h l_t) \cos(\theta_t) \ddot{\theta}_t + m_h l_h \cos(\theta_h) \ddot{\theta}_h \\ &= (m_t l_c + m_h l_t) \dot{\theta}_t^2 \sin(\theta_t) + m_h l_h \dot{\theta}_h^2 \sin(\theta_h) \\ & \quad - k_{sb}(x_p + l_{sb} \sin(\theta_t) - l_{sb} \sin(\theta_{t0}) - x_s) - k_{lb}(x_p - x_s) \end{aligned} \quad (4.5)$$

$$\begin{aligned} & (m_t l_c + m_h l_t) \cos(\theta_t) \ddot{x}_p + (m_t l_c^2 + m_h l_t^2) \ddot{\theta}_t + m_h l_h l_t \cos(\theta_t - \theta_h) \ddot{\theta}_h \\ &= -m_h l_h l_t \dot{\theta}_h^2 \sin(\theta_t - \theta_h) - k_{sb}(x_p + l_{sb} \sin(\theta_t) - l_{sb} \sin(\theta_{t0}) - x_s) l_{sb} \cos(\theta_t) \end{aligned} \quad (4.6)$$

$$\begin{aligned} & m_h l_h \cos(\theta_h) \ddot{x}_p + m_h l_t l_h \cos(\theta_t - \theta_h) \ddot{\theta}_t + m_h l_h^2 \ddot{\theta}_h \\ &= m_h l_t l_h \dot{\theta}_t^2 \sin(\theta_t - \theta_h) - m_h l_h \dot{x}_p \dot{\theta}_h \sin \theta_h \end{aligned} \quad (4.7)$$

Like in RO model, in this model F_{mr} takes the form in Eq. (4.1) and \ddot{x}_v is the measured crash pulse in the sled test. Values of the other parameters in the CO model for purposes of simulation are listed again in Table 4.3. Note that in the table, the

stiffness of the seat belt and lap belt are not presented because their real values in the prototype seat system are not known yet and will be estimated by minimizing the error between the model prediction and the experimental data, which will be discussed next.

MATLAB/SIMULINK was also resorted to obtain the seat deceleration from the CO model. Since experimental data for the deceleration of the occupant body parts is not available, we will focus our attention to the seat deceleration only. The SIMULINK model of the CO model is exhibited in Figure 4.14. The simulation was conducted in such a way that first the stiffness of the seat belt and lap belt were identified, and then the identified values were used for producing the simulation results to compare with test data.

In the estimation of the shoulder belt and lap belt stiffness, the following cost function is to be minimized:

$$J(K_{sb}, K_{lb}) = w \cdot \sum_{k=1}^N [\ddot{x}_s(t_k) - \hat{\ddot{x}}_s(t_k)]^2 + (1-w) \cdot \left| \max_{k=1,2,\dots,N}(\ddot{x}_s(t_k)) - \max_{k=1,2,\dots,N}(\hat{\ddot{x}}_s(t_k)) \right| \quad (4.8)$$

where $\hat{\ddot{x}}_s(t_k)$ is the predicted or simulated seat deceleration from the CO model, $\ddot{x}_s(t_k)$ is the measured seat deceleration, and t_k is the time instant corresponding to the k^{th} sample. w is the weighting factor and here $w = 0.5$, which implies equal weights for both components of the cost function.

The estimated K_{sb} and K_{lb} for each case are shown in Figure 4.15. In addition, Figures 4.16 presents the stiffness of K_{sb} and K_{lb} versus applied current level at each nominal initial impact speed. Note that only test data for the 5th female was used for the estimation since the 95th male was converted from the 5th female. According to

Figure 4.15, it seems that the values of the identified stiffness for both K_{sb} and K_{lb} are rather scattered and vary with the initial impact speeds and applied current levels, especially for test cases of 2.6 m/s with 0A, 3.5 m/s with 0A and 4.5 m/s with 0.5A. For 2.6 m/s and 3.5 m/s, K_{sb} decreases as current level increases until some value and then increases as current level keep increasing. For 4.5 m/s, K_{sb} increases a little as current level increases and then drops down as current goes up. For 5.6 m/s, it decreases largely when current level increases from 1A to 2A. On the other hand, K_{lb} does not show typical variation pattern with respect to current variation at 2.6 m/s and 3.5 m/s. It decreases as current level increases at 4.5 m/s and 5.6 m/s.

However, if try to make the values of K_{sb} and K_{lb} as a function of applied current level and/or initial impact speed, it would make the controller implementation for the constant force control extremely difficult if it is not impossible. Besides, the variation pattern of K_{sb} and K_{lb} is not so clear since the sample space are rather limited. Therefore, we try to keep their values as constant values in order to make the controller implementation easier and practically feasible. It's reasonable to take their mean values of each case as their respective representative constant values in the system model. As demonstrated in Figures 4.17, it is shown that using the mean value as the constant stiffness is acceptable even for the cases of 2.6 m/s with 0A, 3.5 m/s with 0A and 4.5 m/s with 0.5A. It can be seen that the results using the mean value of K_{sb} and K_{lb} almost coincide with the results using their respective identified values of K_{sb} and K_{lb} during the impact period. The only noticeable discrepancy happens after the impact period and is during the occupant bounce back period for every demonstrated case. In this study, we focus our efforts mainly in the impact period and

the attempt to control MREA also in the occupant bounce back period may be carried out in future work. Further more, both simulation results, either using the mean value or using the respective identified value, agree well with the experimental data though the mean value and the respective identified value of either K_{sb} or K_{lb} are very different from each other for these three cases. This indicates that the numerical values of K_{sb} and K_{lb} do not substantially affect the dynamic response of the seat during the impact period. They primarily influence the occupant bounce back behavior, which is not the focus of this study and will not be intensively investigated.

Figures 4.18 also illustrate two other sample cases, 2A at 2.6 m/s and 5.6 m/s. It is seen that the simulated seat decelerations using the mean values of K_{sb} and K_{lb} compare well with the measured data. Therefore, it is reasonable to use the mean values of K_{sb} and K_{lb} , namely, $K_{sb} = 33.87$ and $K_{lb} = 43.86$, as their constant representative values in the prototype seat system model.

In all, the simulated seat decelerations from the CO model agree much better with the measured ones than those from the RO model. Though simple enough compared to other much more complicated FEM models or multi-body occupant biodynamic models with a few tens of degrees that are usually used in biomechanics, the CO model here is shown to be able to adequately capture the dynamic behavior of the prototype sliding seat system during the impact period based on available test data. Hence, the CO model will be used to determine the control input for the prototype seat system for each control algorithm, which will be addressed in next chapter.

4.4 Chapter Summary

In this chapter, sled test of the developed prototype sliding seat system under pre-selected constant applied current levels without controller integrated were carried out and the testing results were analyzed. The two seat system models proposed in Chapter 3, namely, the SDOF rigid occupant (RO) model and the MDOF compliant occupant (CO) model, were used to describe the prototype seat system behavior. It is found that the stiffness of K_{sb} and K_{lb} does not substantially affect the dynamic behavior of the seat system while it influences the seat behavior during the occupant bouncing back period. Also, taking the mean values of K_{sb} and K_{lb} from all identified values of all cases as the constant representative parameter values for the seat belts in the system model was proven to be reasonable and acceptable. Comparison of the simulation results from the RO model and the CO model with the experimental data showed that the CO model is able to adequately capture the dynamic behavior of the seat system during the impact period using the mean values of identified K_{sb} and K_{lb} , while the RO model failed to do so. Therefore, the CO model along with the identified constant stiffness for K_{sb} and K_{lb} will be used for controller implementation in next chapter.

Table 4.1: Sled test matrix.

Test No.	Initial impact speed (m/s)	Applied current (A)	Dummy type	Measured max. stroke (inch)
2282	2.66	1.0	5th female	0.16
2283	2.62	0.5	5th female	1.33
2284	2.59	0.0	5th female	2.22
2285	2.57	2.0	5th female	0.00
2286	3.49	2.0	5th female	0.00
2287	3.44	1.0	5th female	0.30
2288	3.49	0.5	5th female	1.75
2289	3.53	0.0	5th female	2.07
2290	4.57	2.0	5th female	0.01
2293	4.57	1.0	5th female	1.15
2295	4.52	0.5	5th female	2.26
2296	5.50	2.0	5th female	0.31
2297	5.53	1.0	5th female	1.54
2301	2.57	1.0	95th male	0.74
2302	2.61	2.0	95th male	0.11
2303	2.57	0.5	95th male	2.72
2304	2.59	3.0	95th male	0.02
2305	3.50	2.0	95th male	0.16
2306	3.50	1.0	95th male	1.30
2307	3.47	0.8	95th male	1.99
2308	3.54	3.0	95th male	0.07
2309	4.59	2.0	95th male	0.75
2310	4.59	1.5	95th male	1.32
2311	4.58	1.0	95th male	2.13
2313	4.55	3.0	95th male	0.38

Table 4.2: Full stroke and zero or nearly zero stroke cases.

Full stroke (nominally 2") cases		Almost zero stroke cases	
5th female	95th male	5th female	95th male
2.6m/s 0A	2.6m/s 0.5A	2.6m/s 2.0A	2.6m/s 3.0A
3.5m/s 0.5A	3.5m/s 0.8A	3.5m/s 2.0A	3.5m/s 3.0A (0.07" stroke)
4.5m/s 0.5A	4.5m/s 1.0A	4.5m/s 2.0A	4.5m/s 3.0A (0.38" stroke)

Table 4.3: Values of system parameters in the CO model.

	5 th percentile female	95 th percentile male*
$m_h(kg)$	3.65	3.65
$m_t(kg)$	11.90	40.48
$m_p(kg)$	13.70	36.38
$m_s(kg)$	32.2	23.1
$l_h(mm)$	200	200
$l_c(mm)$	270	270
$l_t(mm)$	450	450
$l_{sb}(mm)$	400	400
$\theta_h(\text{deg})@t = 0ms$	-10	-10
$\theta_t(\text{deg})@t = 0ms$	-20	-20

* The parameter values listed are not the nominal parameters for 95th percentile male dummy. Rather they are the parameter values in the actual sled test because the 95th male dummy is actually converted from the 5th female dummy by adding makeup mass to the 5th female dummy due to the unavailability of the 95th male dummy at the time of test. 63 lbs mass was added at the upper torso and 50 lbs mass was added to the pelvis of the 5th female dummy. Thus except m_t and m_p , other parameters' values are kept the same as the 5th female in the simulation.

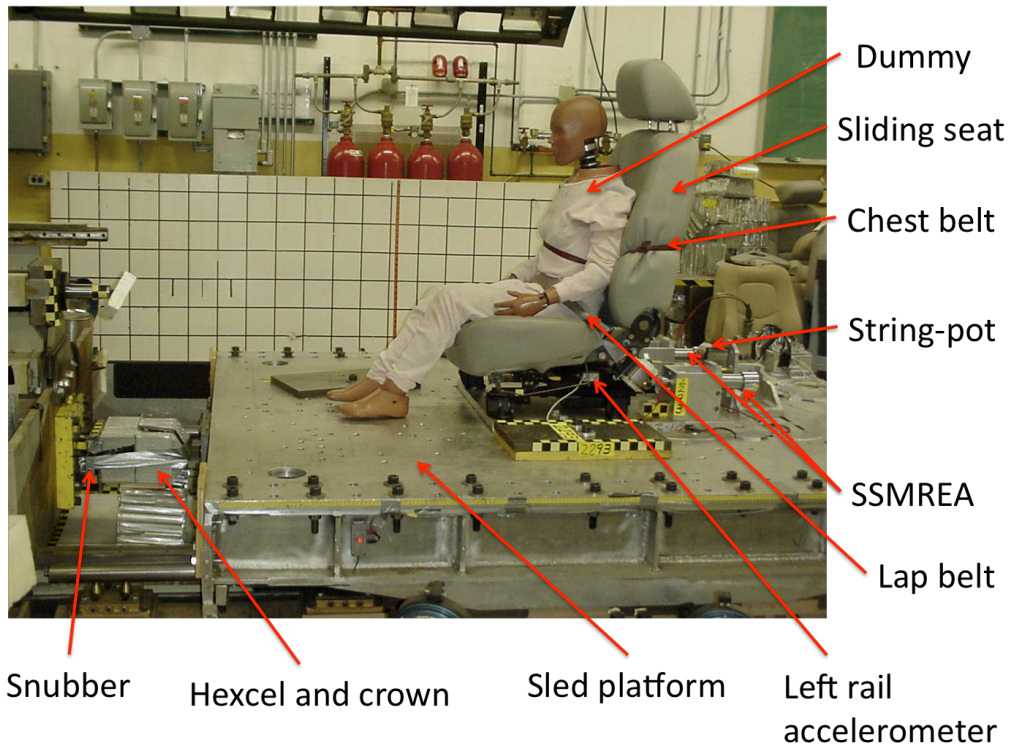
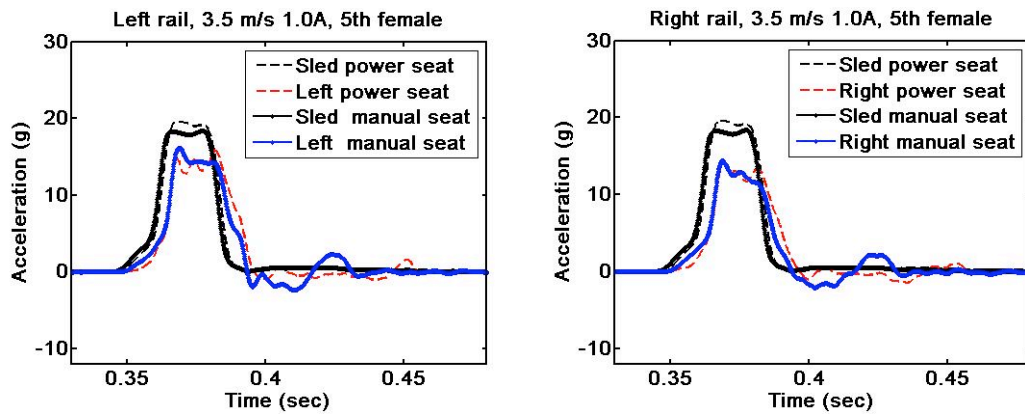
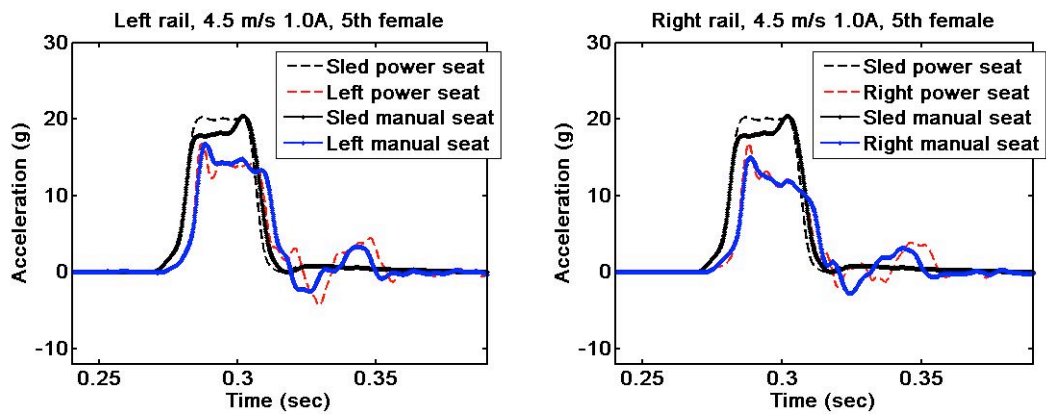


Figure 4.1: The adaptive sliding seat system sled test set-up.

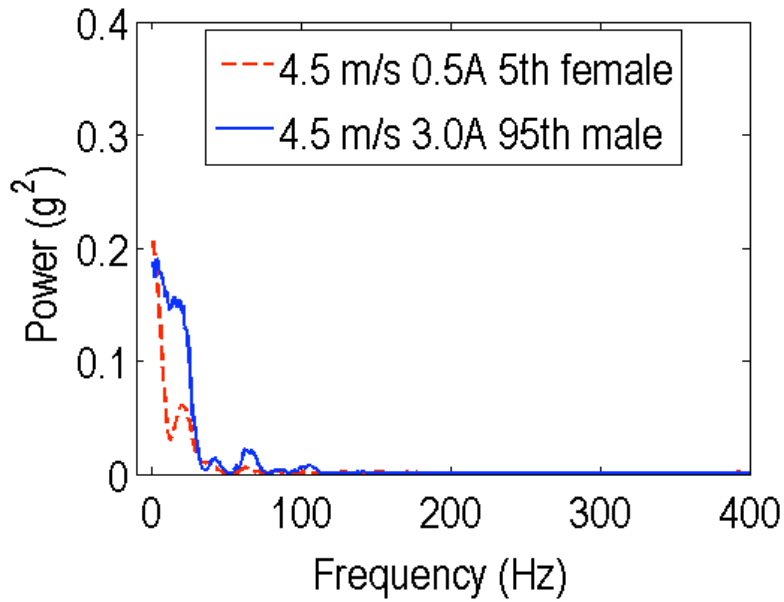


(a) initial impact speed of 3.5 m/s and applied current of 1.0A for 5th female

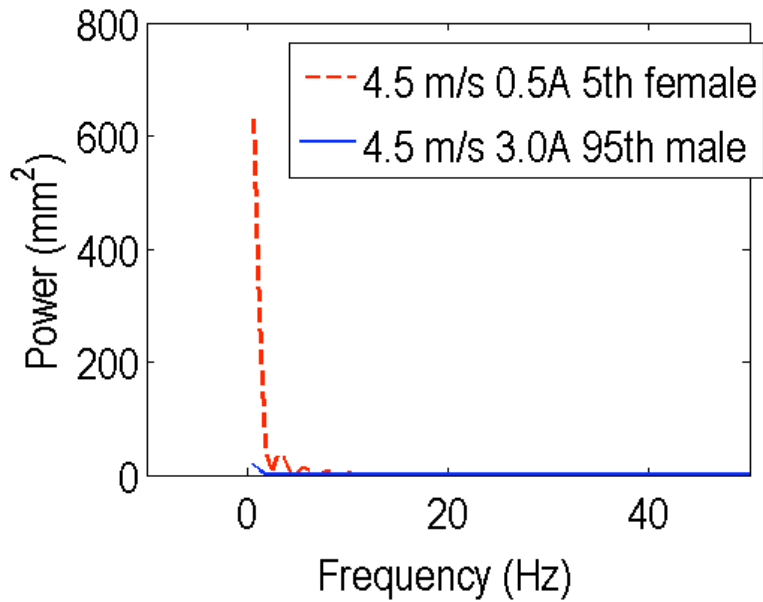


(b) initial impact speed of 4.5 m/s and applied current of 1.0A for 5th female

Figure 4.2: Comparison of sliding seat dynamic response between power seat and manual seat for 5th female ('Sled' in the legend means crash pulse).

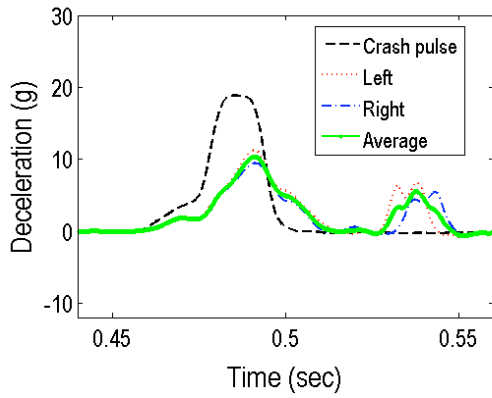


(a) power spectrum of seat deceleration

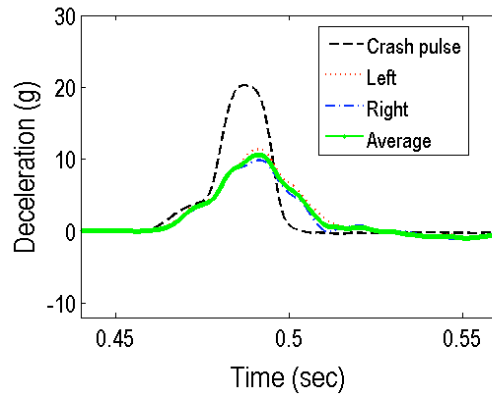


(b) power spectrum of piston displacement

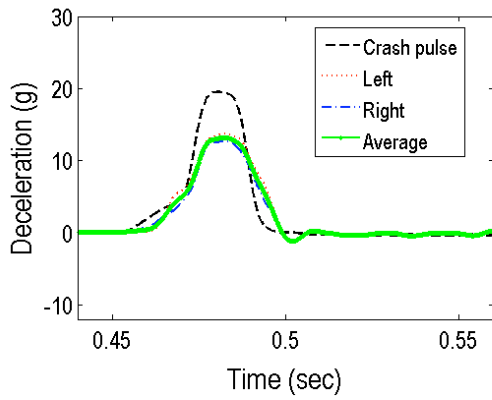
Figure 4.3: Power spectrum analysis of sliding seat decelerations and SSMREA piston displacement.



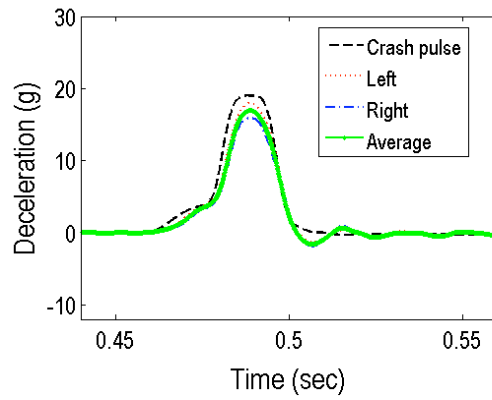
(a) 2.6 m/s and 0.0 A for 5th female



(b) 2.6 m/s and 0.5 A for 5th female

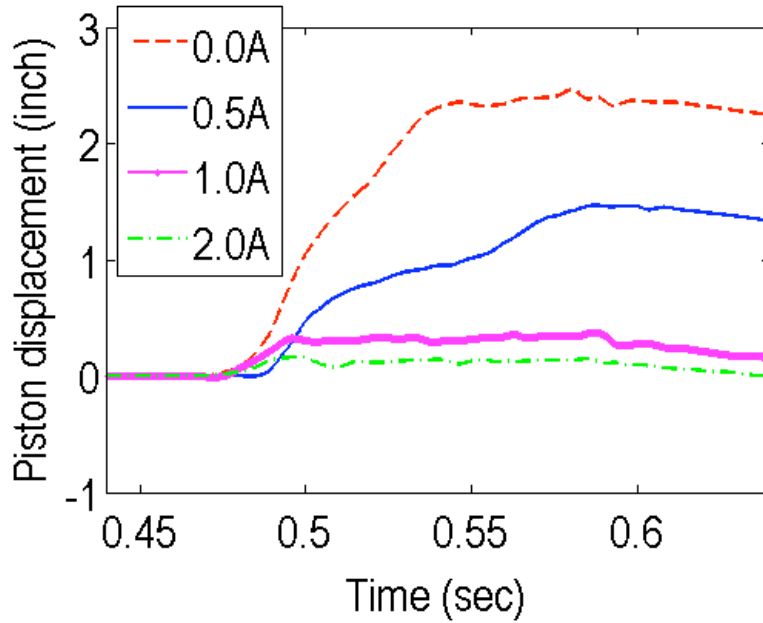


(c) 2.6 m/s and 1.0 A for 5th female

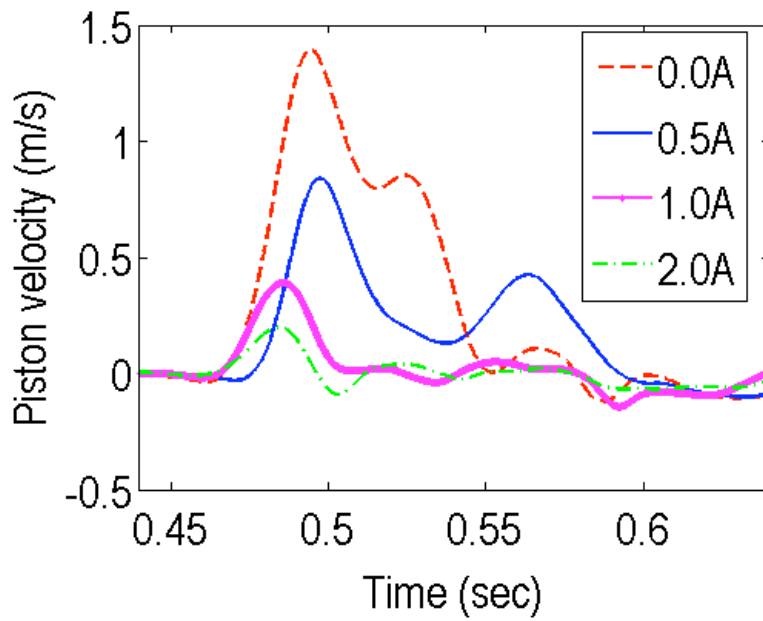


(d) 2.6 m/s and 2.0 A for 5th female

Figure 4.4: Seat deceleration and crash pulse at nominal initial impact speed 2.6 m/s with various applied current levels for the 5th female.

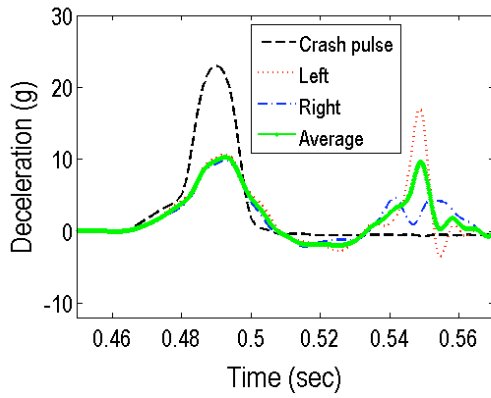


(a) MREA piston displacement

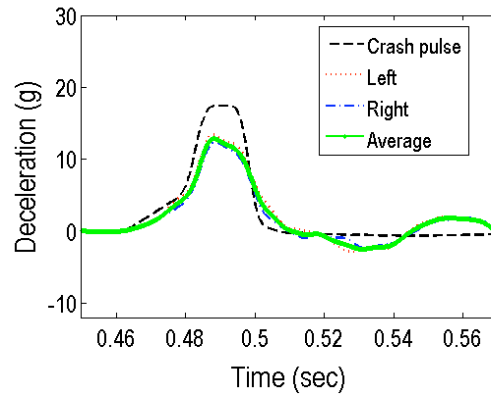


(b) MREA piston velocity

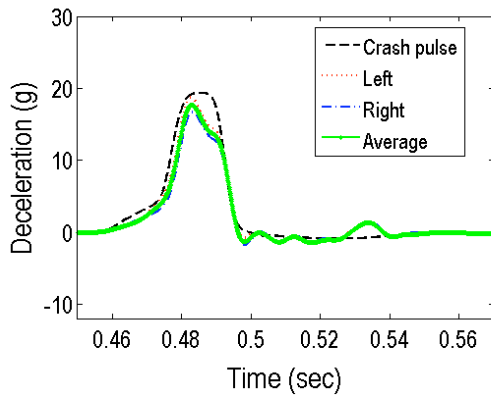
Figure 4.5: MREA piston displacement and piston velocity at nominal initial impact speed 2.6 m/s with various applied current levels for the 5th female.



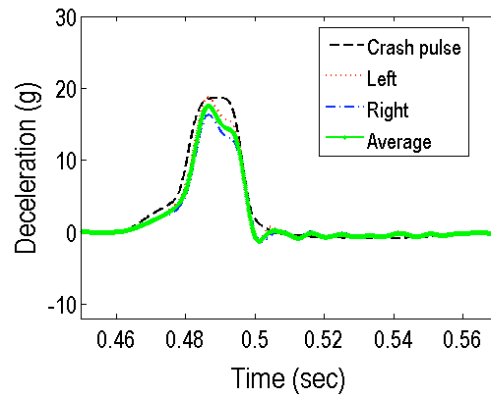
(a) 2.6 m/s and 0.5 A for 95th male



(b) 2.6 m/s and 1.0 A for 95th male

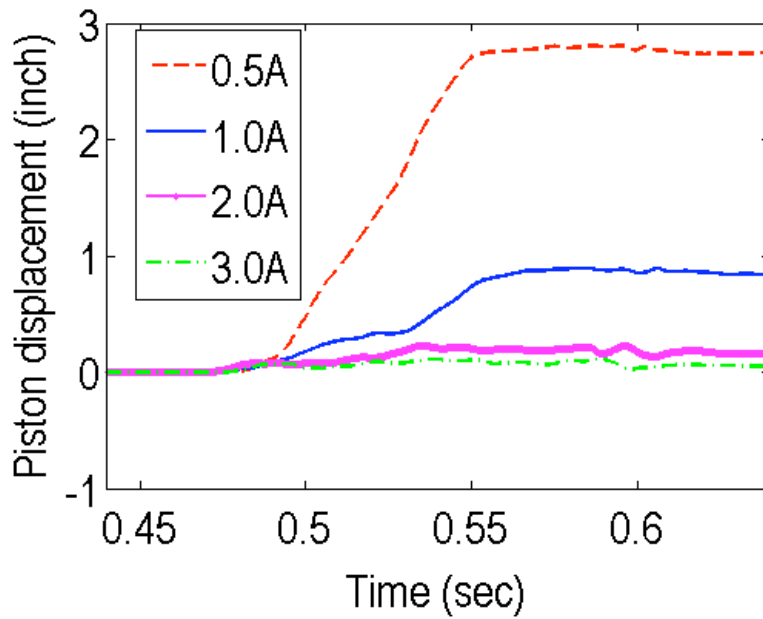


(c) 2.6 m/s and 2.0 A for 95th male

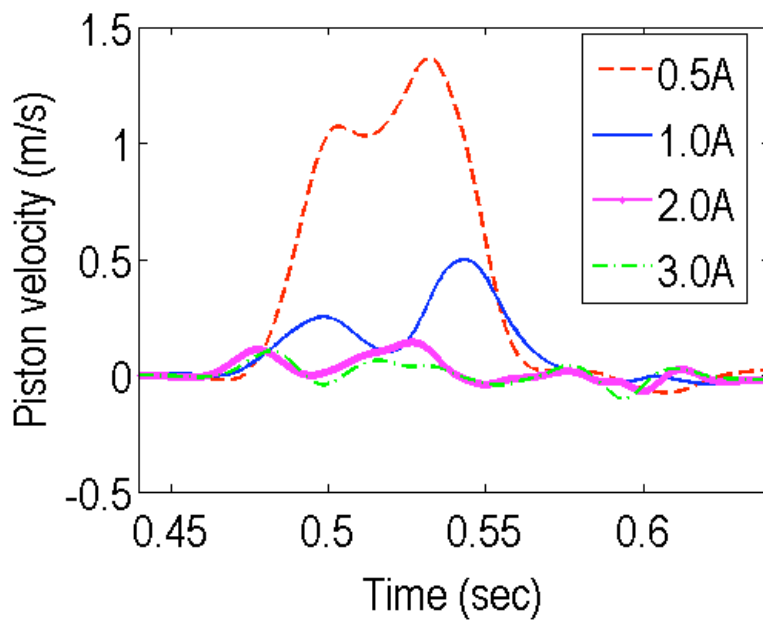


(d) 2.6 m/s and 3.0 A for 95th male

Figure 4.6: Seat deceleration and crash pulse at nominal initial impact speed 2.6 m/s with various applied current levels for the 95th male.



(a) MREA piston displacement



(b) MREA piston velocity

Figure 4.7: MREA piston displacement and piston velocity at nominal initial impact speed 2.6 m/s with various applied current levels for the 95th male.

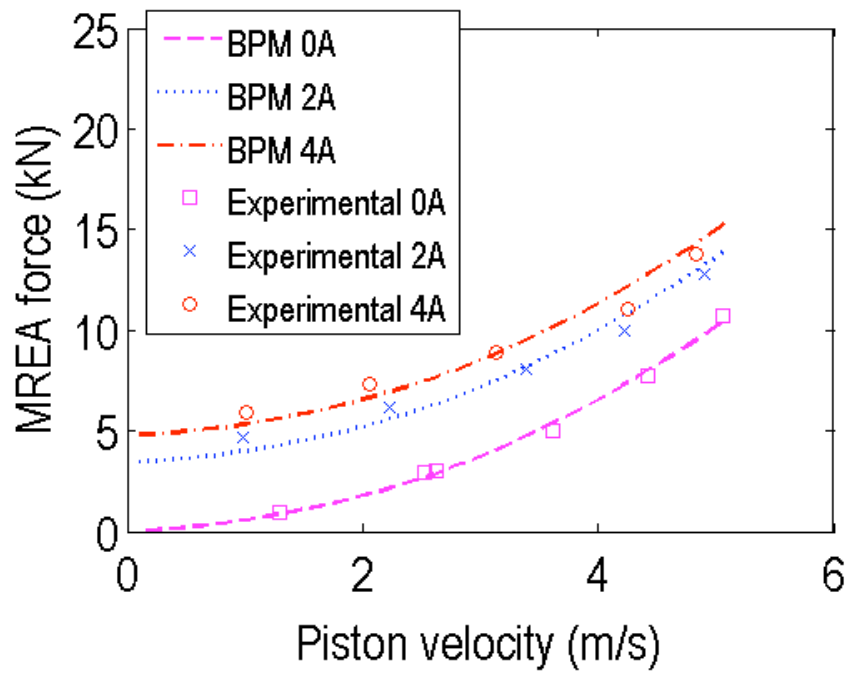


Figure 4.8: SSMREA force characterization based on BPM model and drop test data.

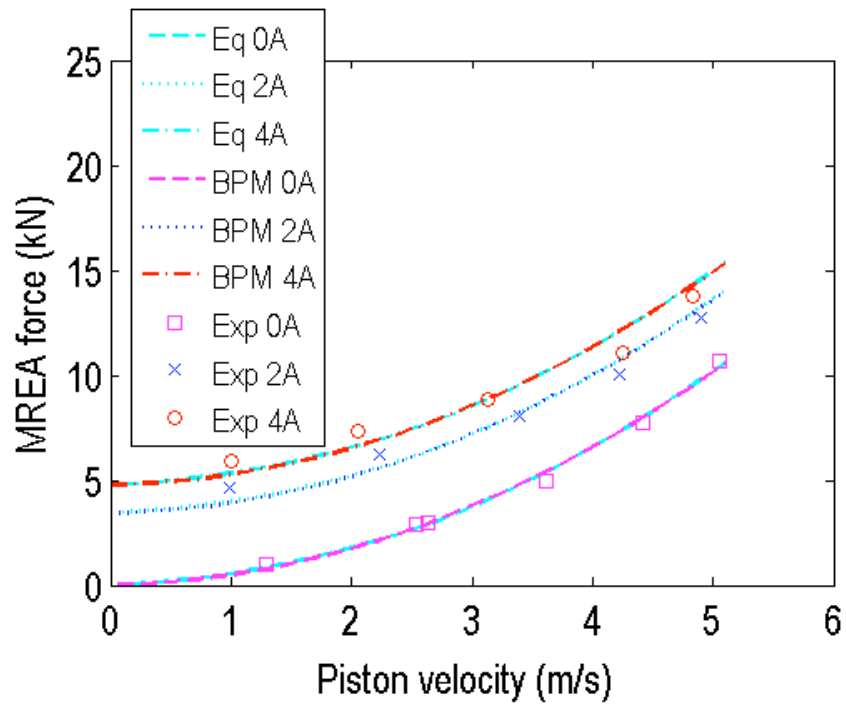


Figure 4.9: SSMREA force characterization from the proposed simple equation.

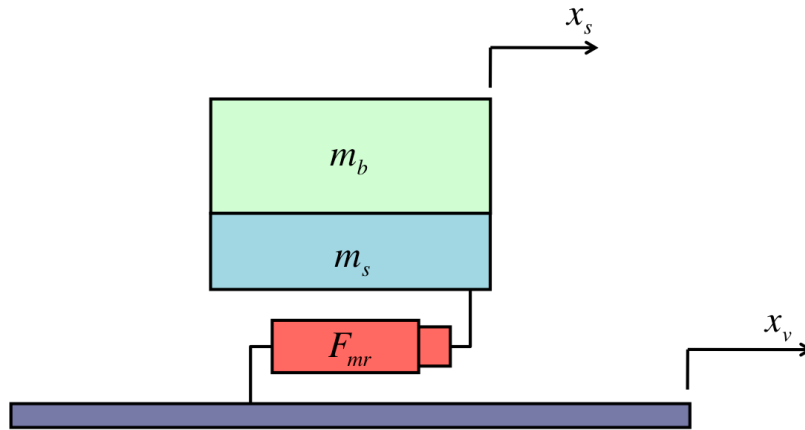


Figure 4.10: The single-degree-of-freedom (SDOF) rigid occupant (RO) model for the sliding seat system.

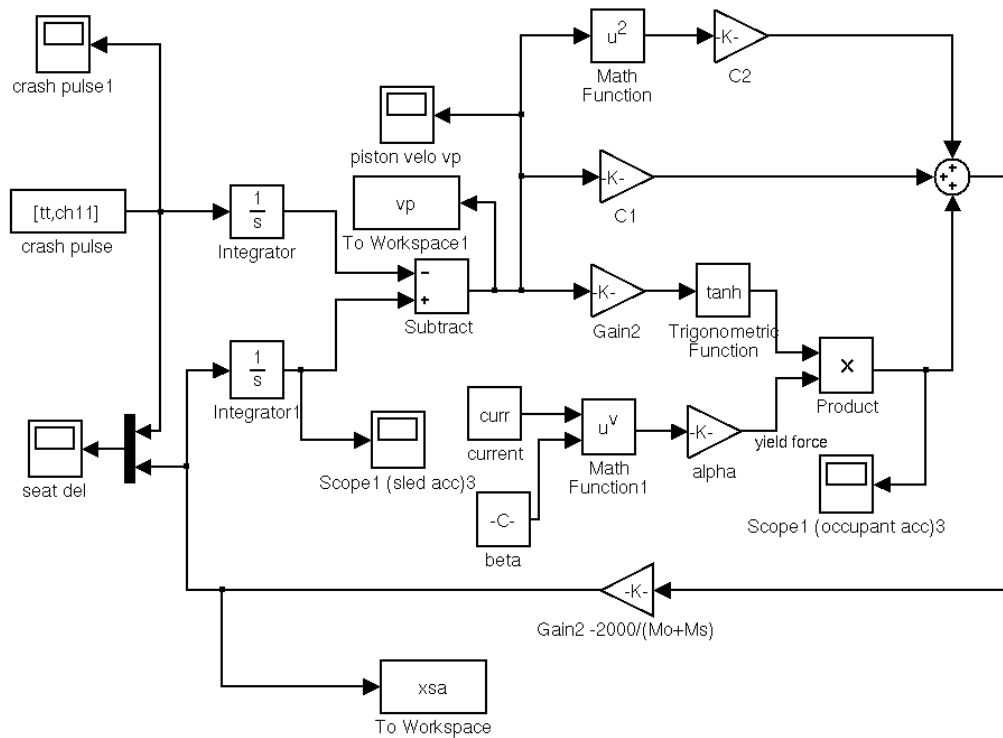
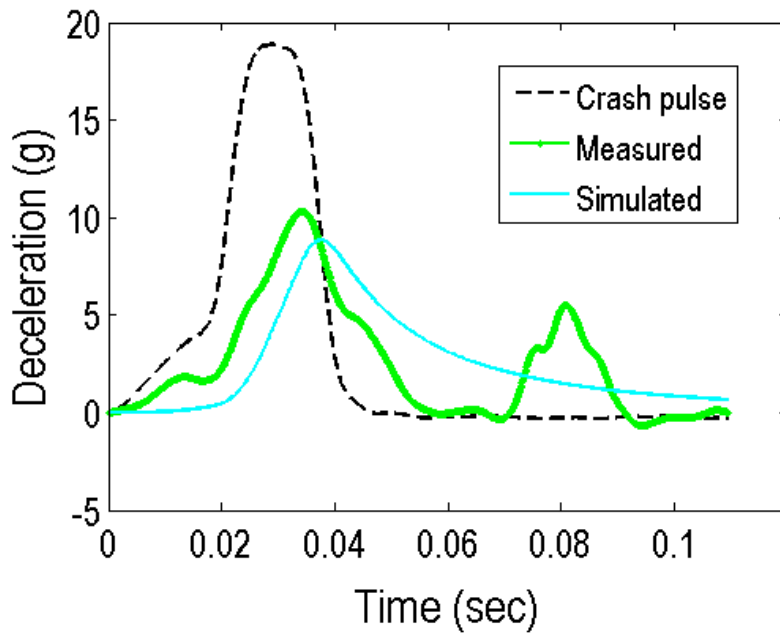
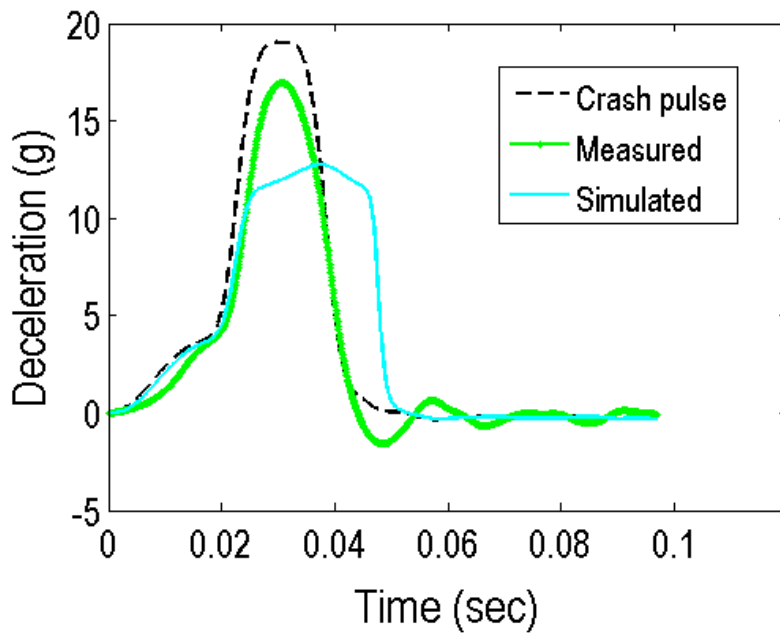


Figure 4.11: MATLAB/SIMULINK model of the RO model.



(a) 2.6 m/s and 0 A for 5th female



(b) 2.6 m/s and 2.0 A for 5th female

Figure 4.12: Simulated dynamic response of the adaptive sliding seat system from RO model and comparison with measured data.

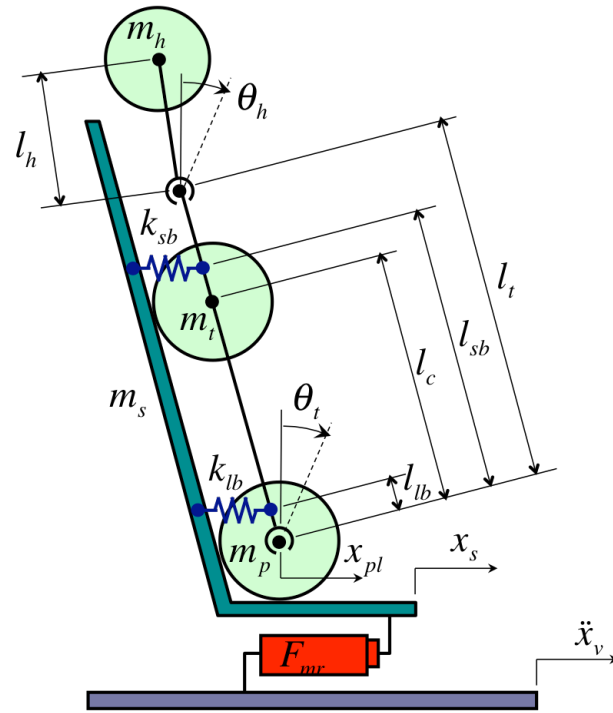


Figure 4.13: The multi-degree-of-freedom (MDOF) compliant occupant model (CO model) for the sliding seat system.

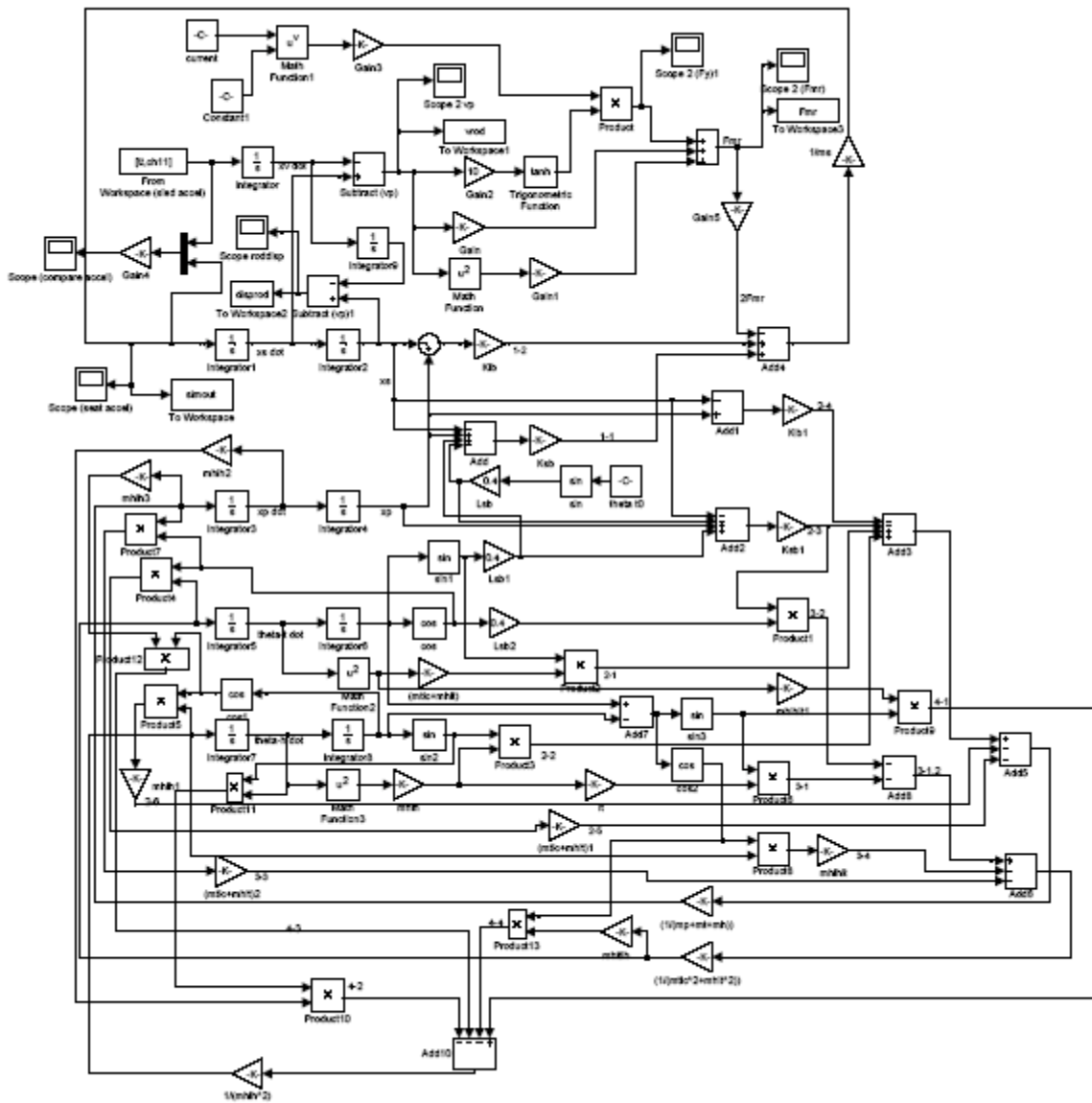


Figure 4.14: MATLAB/SIMULINK model of the CO model.

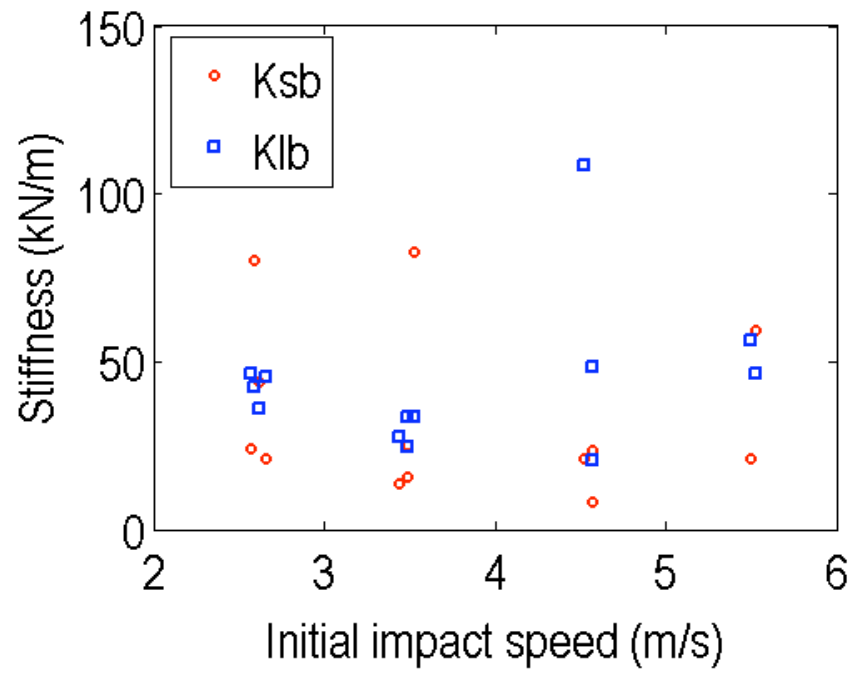
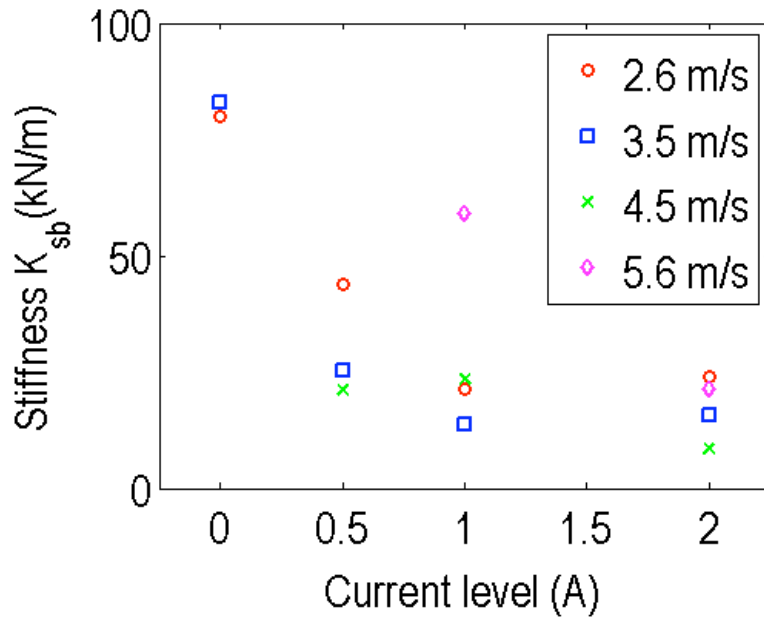
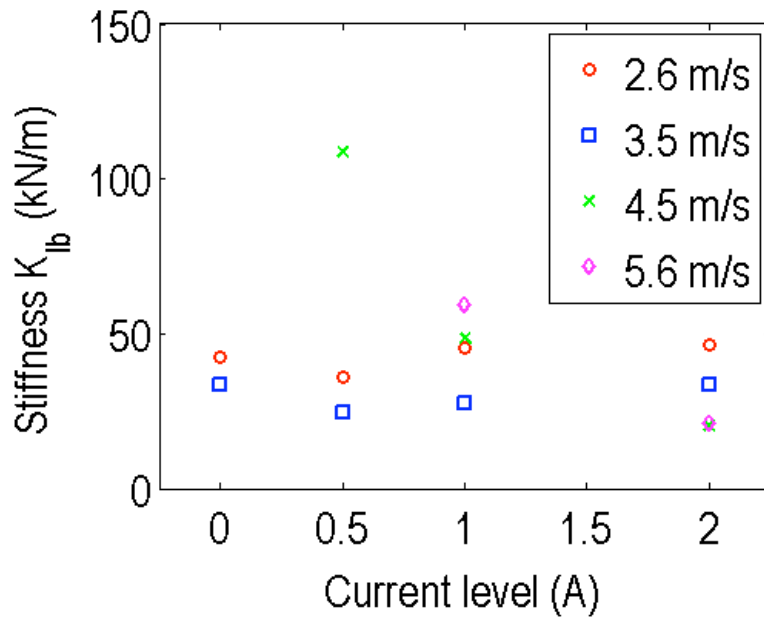


Figure 4.15: Identified K_{sb} and K_{lb} at each case using the 5th female data.

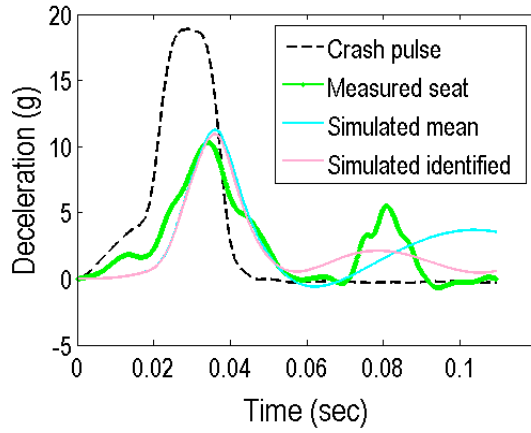


(a) K_{sb} versus current level

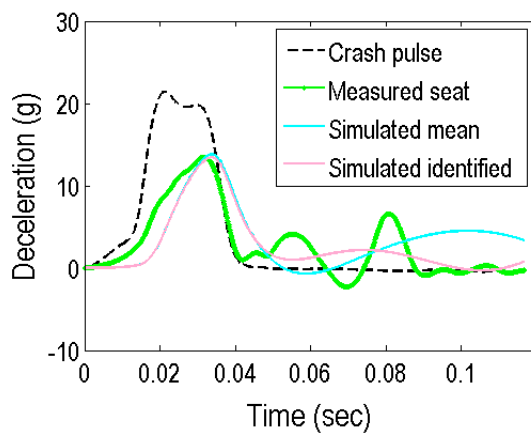


(a) K_{lb} versus current level

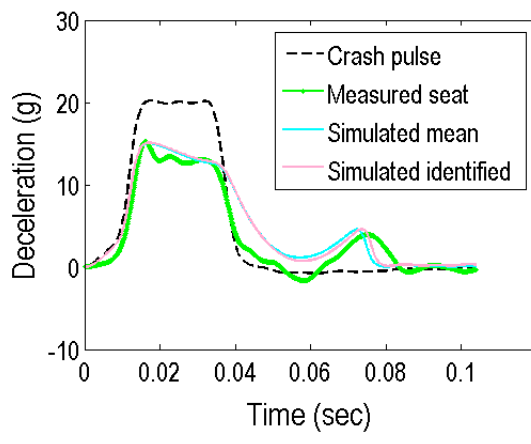
Figure 4.16: Identified K_{sb} and K_{lb} versus applied current levels at various nominal initial impact speed.



(a) 2.6 m/s and 0A

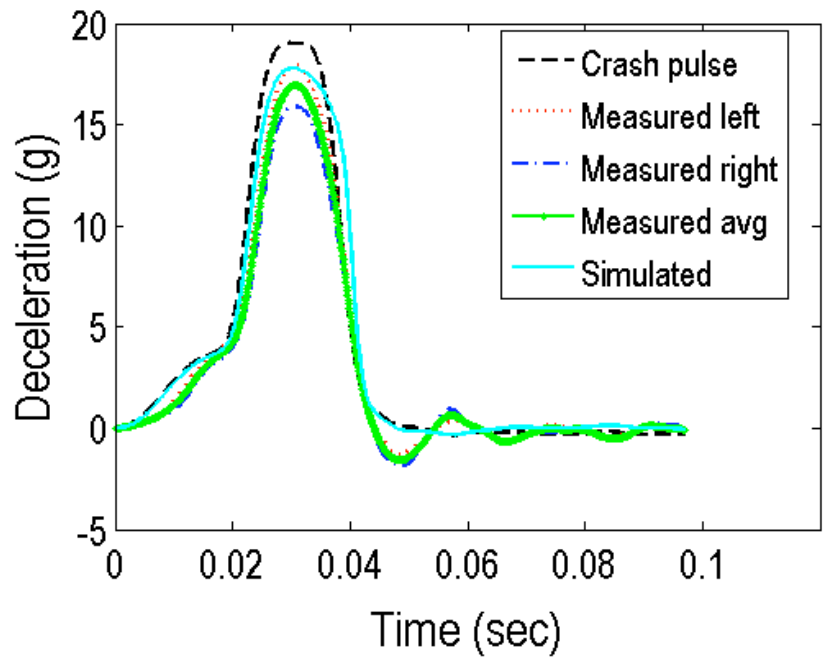


(b) 3.5 m/s and 0A

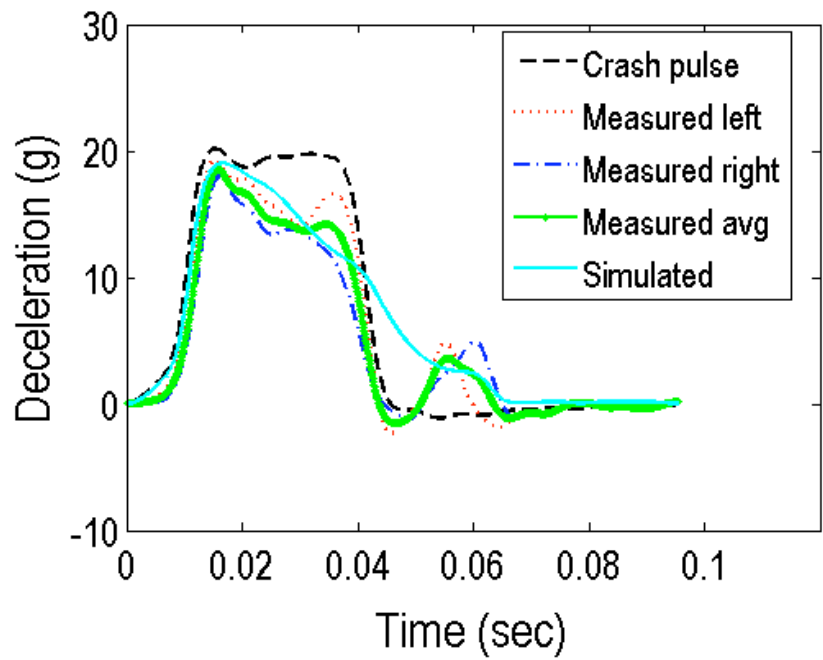


(c) 4.5 m/s and 1A

Figure 4.17: Comparison of simulation results using the mean value of K_{sb} and K_{lb} and their respective identified value at each case.



(a) 2.6 m/s and 2A



(b) 5.6 m/s and 2A

Figure 4.18: Simulated seat deceleration from CO model using the mean value of K_{sb} and K_{lb} and comparison with measured data.

Chapter 5: Sled Test of the Adaptive Magnetorheological Sliding Seat (AMSS) System Under Control Mode

5.1 Introduction

In the previous chapter, a multi-degree-of-freedom (MDOF) compliant occupant (CO) model of the sliding seat system was able to adequately describe the experimental dynamic system behavior of the prototype sliding seat without an integrated controller (passive mode sled test). In this chapter, we will utilize the experimentally validated CO model to realize the two control algorithms in the prototype seat system, i.e., the constant Bingham number or Bi_c control, and the constant stroking force or F_c control.

To do so, the control inputs for each control algorithm at each intended initial impact speed for the 5th female and 95th male were determined using the CO model via numerical simulation in a way very similar to the procedure used in Chapter 3 with the help of MATLAB and SIMULINK module. In the simulation, the experimental crash pulses collected at each initial impact speed in previous sled test, nominally 2.6, 3.5, 4.5 and 5.6 m/s, were used as the crash pulse inputs into the CO model. Also the system parameter values and the MREA model in the simulation were consistent to the physical prototype sliding seat system, namely the experimentally identified values and characteristics. For convenience, we call the control input determined this way the *reference control input*.

The execution of the two control algorithms (the prototype controller) was realized using the DSPACE and SIMULINK real time control environments. The determined reference control input was stored in the controller as a function of initial impact speed and occupant mass. Therefore, the controller will automatically pick the appropriate reference control input, according to the initial impact speed and the occupant mass, and issue the corresponding command current level to be applied to the MREA so that the MREA behavior is controlled as desired. Ideally, the adaptive sliding seat system monitored under the reference control input can achieve the control objective, that is, bringing the seat to a stop at the maximal stroke (2" here) without any end-stop impact. However, because the crash pulse as well as the true initial impact speed may vary from the ones when the reference control input was obtained, a tuning factor (an empirical coefficient used to multiply the reference control input to obtain the tuned control input for the current test based on the resulted MREA strokes in tests conducted prior to the current one) was adopted empirically and iteratively in the test to tune the reference control input so that the seat comes to rest at exactly 2" of stroke. The ultimate tuned control input that can achieve the "soft-landing" at exactly 2" stroke in the test is called the *experimental control input* to distinguish it from the *reference control input*.

The transient test results will be presented and analyzed. The performance of the adaptive seat system under controlled mode in terms of transient transmissibility (a metric used to assess the ability of the adaptive sliding seat system to transfer the crash pulse to the occupant/seat complex and will be discussed later in detail) and the energy dissipation ratio will be addressed. In addition, the effectiveness of the CO

model in predicting the control inputs for the two control algorithms will be also examined.

5.2 Reference Control Inputs From the CO Model

In Chapter 3, we have discussed the CO model and the simulated response of the adaptive sliding seat system controlled by the two control algorithms - the constant Bingham number or Bi_c control and the constant stroking force or F_c control – using assumed typical values for system parameters and MREA behavior. Here, we will apply the control algorithms in the physical prototype seat system and investigate their feasibility and benefits in the practical application environment.

In order to implement the control algorithms in the prototype system, the control input particularly tailored to the prototype seat system for each control algorithm is required. Given that the crash pulse at each nominal initial impact speed for each occupant type are nominally the same, we will utilize the crash pulses collected in previous non-controlled mode sled test to replace the assumed rectangular crash pulses, and utilize the validated CO model with experimentally identified system parameter values and MREA characteristics to derive the control inputs using the similar numerical procedure as before (Figure 3.4).

For clarity, the CO model is presented here again as follows:

$$m_s \ddot{x}_s = k_{sb}(x_{pl} + l_{sb} \sin(\theta_t) - l_{sb} \sin(\theta_{t0}) - x_s) + k_{lb}(x_{pl} - x_s) - F_{mr} \quad (5.1)$$

$$\begin{aligned} & (m_p + m_t + m_h) \ddot{x}_{pl} + (m_t l_c + m_h l_t) \cos(\theta_t) \ddot{\theta}_t + m_h l_h \cos(\theta_h) \ddot{\theta}_h \\ & = (m_t l_c + m_h l_t) \dot{\theta}_t^2 \sin(\theta_t) + m_h l_h \dot{\theta}_h^2 \sin(\theta_h) \\ & \quad - k_{sb}(x_{pl} + l_{sb} \sin(\theta_t) - l_{sb} \sin(\theta_{t0}) - x_s) - k_{lb}(x_{pl} - x_s) \end{aligned} \quad (5.2)$$

$$\begin{aligned}
& (m_t l_c + m_h l_t) \cos(\theta_t) \ddot{x}_{pl} + (m_t l_c^2 + m_h l_t^2) \ddot{\theta}_t + m_h l_h l_t \cos(\theta_t - \theta_h) \ddot{\theta}_h \\
& = -m_h l_h l_t \dot{\theta}_h^2 \sin(\theta_t - \theta_h) - k_{sb} (x_{pl} + l_{sb} \sin(\theta_t) - l_{sb} \sin(\theta_{t0}) - x_s) l_{sb} \cos(\theta_t)
\end{aligned} \tag{5.3}$$

$$\begin{aligned}
& m_h l_h \cos(\theta_h) \ddot{x}_{pl} + m_h l_t l_h \cos(\theta_t - \theta_h) \ddot{\theta}_t + m_h l_h^2 \ddot{\theta}_h \\
& = m_h l_t l_h \dot{\theta}_t^2 \sin(\theta_t - \theta_h) - m_h l_h \dot{x}_{pl} \dot{\theta}_h \sin \theta_h
\end{aligned} \tag{5.4}$$

Like before, F_{mr} denotes the MREA force. It takes two different forms for the two different control algorithms:

(1). For the constant stroking load (force) control, $F_{mr} = F_c$.

(2). For the constant Bingham number control, we will take a slightly different approach to facilitate the practical controller implementation. Since the control algorithm is essentially a constant current control and the only thing we can control in the system is the current level to be applied to the MREA, it would be more convenient and more straightforward to take the constant current level, I_c , instead of Bi_c as the control input to achieve the control objective in the controller execution.

Therefore, the MREA force under this control algorithm will take the form of:

$$F_{mr} = 2.4715 I_c^{0.4754} \text{sign}(V_p) + 0.3852 V_p^2 + 0.1036 V_p \tag{5.5}$$

Using the CO model with the particular system parameters for the prototype system (as shown in Table 5.1) and the crash pulses collected in previous sled test as the vehicle floor acceleration, \ddot{x}_v , the respective control inputs for both control algorithms were obtained via the numerical procedure shown in Figure 5.1. Note that in Figure 5.1, as mentioned we used I_c instead of Bi_c to facilitate practical Bi_c control implementation (Bi_c control is essentially a constant current control). Figures 5.2-5.3 present the corresponding SIMULINK model files of the CO model used in the simulation procedure for each control algorithm. Another thing is, the crash pulses

collected at each nominal initial impact speed in previous sled test varied more or less from case to case with different applied current levels. In addition, the actual measured initial impact speed also slightly deviated from the nominal initial impact speed at each test case. Therefore, we took the mean value of the control inputs determined for each individual case for each nominal initial impact speed set and the mean actual initial impact speed as the pair of reference control input at that initial impact speed. For example, for the nominal initial impact speed of 2.6 m/s, we have a total of four data sets corresponding to applied current levels of 0.0, 0.5, 1.0 and 2.0A and actual initial impact speeds of 2.59, 2.62, 2.66 and 2.57 m/s. For each individual data set, we determined the control input for each control algorithm using the numerical procedure shown in Figure 5.1. They are 1.43, 1.45, 1.47 and 1.44 kN respectively for the constant stroking force or F_c control and 0.17, 0.17, 0.16 and 0.17A respectively for the constant Bingham number or Bi_c control. Then the ultimate mean control inputs for these 4 data sets at the mean initial impact speed are: 1.45 kN at 2.61 m/s for F_c control and 0.17A at 2.61 m/s for Bi_c control. In this way, the reference control inputs for various initial impact speeds were determined and the results are presented in Tables 5.2-5.3 and Figures 5.4. To facilitate the later controller implementation, the reference control inputs were expressed as functions of initial impact speed via curve fitting and also listed in Tables 5.2-5.3. The controller will be programmed to choose the appropriate function to obtain the control inputs based on the input occupant mass. It is seen that the values of F_c and I_c increase as the initial impact speed increases and the occupant mass increases, which are reasonable and consistent with experimental results observed in the passive mode sled

test. Another interesting observation is that F_c for the 95th male and I_c for the 5th female seem to increase linearly with the increasing of initial impact speed though we used quadratic functions to describe them for accuracy. While for the other two combinations - F_c for the 5th female and I_c for the 95th male, they show obvious nonlinear relationship with the initial impact speed.

Also, through the simulation, the MREA peak force and peak piston velocity for each individual data set corresponding to its required F_c and I_c at each initial impact speed were obtained. Similar to the way that the reference control inputs were deduced, the mean peak force and mean peak piston velocity from the data sets with the same nominal initial impact speed were used to represent the expected MREA peak force and peak piston velocity corresponding to the reference control input at that initial impact speed. The resulting peak MREA force versus peak piston velocity was presented in Figure 5.5. To successfully implement the control algorithms, the SSMREA should be able to provide these expected forces at the corresponding piston velocity. As seen in Figure 5.5, the four lines denoting the expected peak MREA force versus peak piston velocity for each control algorithm and each occupant type lie well within the measured force-velocity capacity of the SSMREA. It implies that the SSMREA is able to provide the right force level as required for implementing the control algorithms.

In all, based on the above simulation results, it is believed that these two control algorithms are practically realizable and are to be verified by sled testing the prototype sliding seat system under the control of the two control algorithms.

5.3. Sled Test of Prototype Seat System Under Control Mode

5.3.1 Experimental Setup

Sled test of the prototype adaptive sliding seat system with the two control algorithms implemented was carried out at the GMC R&D Center. The prototype controller for the two control algorithms was developed in SIMULINK (a module in MATLAB) and implemented using the DSPACE real time control system (DSPACE ControlDesk software plus the Autobox with DS1103 board integrated as well as peripheral ADC/DAC board). Figure 5.6 shows the schematic architecture of the adaptive seat system with controller and Figure 5.7 presents the corresponding experimental setup. The controller model files in SIMULINK are presented in Figures 5.8.

The hardware part of the adaptive seat system including the attached sensors and their positions, the crash pulse producing mechanism, and the crash pulse nominal magnitude and shape were the same as the setup for the passive mode sled test and will not be repeated here. The only difference is that two signals in this control mode setup were fed into the ADC channels of the DSPACE system rather than simply recorded by the GM data acquisition system as was done in the passive mode sled test. As shown in Figure 5.7, one of these two signals is the MREA instantaneous piston/rod displacement measured by the string-pot (cable extension transducer), which is also used to obtain the instantaneous MREA piston velocity needed in the constant stroking force control. The other one is the signal pair used to determine the initial impact speed. Using this signal pair, the initial impact speed was measured about 200 ms before the seat system impacted. An occupant weight sensor was not

implemented in our setup, so that the occupant mass was a manual *a priori* input to the prototype controller before each test was conducted. Once the initial impact speed is determined, it is used together with the prescribed occupant mass in the controller to select the appropriate reference control input according to the pre-selected control algorithm. The controller would immediately produce the right command current level based on the selected reference control input and pass this command current to the DAC channel where the current supply is connected. The current supply then instantaneously outputs the right current level to the MREA. In this way, the current level corresponding to the selected control input (the constant current level identical to I_c or the initial current level mapping the constant stroking force F_c) is pre-applied almost 200 ms before the impact event occurs to the MREA and thus it reduces the apparent response time of the MREA, which was experimentally determined to be around 12 ms. Therefore, the MREA was “warmed up”, i.e., required field was applied long before the impact event. It was found that this effectively minimized the time response of the MREA and the MREA responded immediately to the variation of the current level during the impact period (for the constant stroking force control) after the long period “warm up”. Here, 5th female and a 95th male test dummies were utilized in the sled test, unlike in the previous test where the 95th male dummy was actually a 5th female dummy with dead mass added. Also, a manual seat (51 lbs) was used as the basic seat structure in the adaptive seat system for all tests. A quarter inch extra stroke was reserved for safety, that is, the actual total allowable maximum stroke that the seat can slide is 2.25”.

Like before, four nominal initial impact speeds were tested – 2.6, 3.5, 4.5 and 5.6 m/s for each control algorithm. The final completed tests are: the constant stroking force control at the 4 nominal initial impact speeds for both 5th female and 95th male; the constant Bingham number control at the 4 nominal initial impact speeds for 95th male only.

5.3.2 Tuning Factor and Experimental Control Input

Ideally and theoretically, if the pair of initial impact speed and the crash pulse in the real testing at each case was identical to the pair used in the simulation when the reference control input was obtained and everything else in the system was kept unchanged, then the control objective (fully utilized stroke plus completely “soft landing”) should be achieved one time by directly applying the reference control input to the prototype adaptive seat system in the real sled test. However, in practice this usually would not happen. We tried to apply the reference control input firstly starting from the lower nominal initial impact speed and found that the seat was always not stop at 2” stroke with the reference control input. Note that here we treat the measured peak stroke between 1.95” and 2.1” as satisfying the condition of stopping at 2” stroke because the string of the string-pot was observed to be stretched slightly longer due to the minor upward bending at the rear part of the seat where the string-pot was attached. Thus, the measured stroke from the string-pot would be always a little bit larger than the actual stroke.

Key reasons that the reference control input usually cannot achieve the control objective are as follows. First of all, from how the reference control input was obtained for each initial impact speed as well as the results in the passive mode sled

test presented in previous chapter, it can be seen that for each nominal impact speed, the actual initial impact speed always was shown to deviate more or less from the nominal one. And the crash pulse time history was also shown to vary from case to case and non-repeated in an exact means. Thus, we took the mean control input and mean initial impact speed from all the data sets under the same nominal initial impact speed as the reference control input at that initial impact speed. This means the reference control input was determined in a statistical way, because each sled test was not exactly reproducible due to variations in test conditions such as sled speed etc. In addition, modeling error between the CO model and the physical prototype seat system, the MREA model and the real transient force, was present although the error was deemed acceptable. Since the reference control input was obtained based on the simulation results of the CO model, it is inevitable that the reference control input may not enable the prototype system to precisely achieve the control objective in testing.

Therefore, as shown in Figure 5.9 we decided to multiply the reference control input with an empirical tuning factor, whose numerical value was manually set based on the measured strokes in previous tests before each test was conducted, as the control input passed to the MREA control module in the controller. This value was iterated until the measured stroke satisfied 2” of stroke with “soft-landing”.

The obtained control input to truly achieve the control objective in the real test is called the experimental control input and the corresponding numerical value of the tuning factor is the tuning factor needed to adjust the reference control input. The intermediate values of tuning factors in the iteration will be ignored and will not be

addressed here. Table 5.4 lists the results of the experimental control input, the tuning factor and the corresponding measured stroke at each nominal initial impact speed for each control algorithm. As seen in the table, for most cases, we found the correct experimental control input to achieve the control objective for each control algorithm and each occupant type. But for some cases such as the constant stroking force control at nominal initial impact speed of 4.5 and 5.6 m/s for 5th female and the constant Bingham number control at nominal initial impact speed of 4.5 m/s and 5.6 m/s for 95th male (denoted as red and bold numbers in the table), the measured strokes at the listed control inputs were only around 1.7 or 1.8”. For these 4 cases, we took the following approach to deduce the experimental control input and tuning factor:

1. Using the measured crash pulse as the crash pulse input to the CO model and set the stroke termination condition to be the measured stroke instead of 2” in the numerical simulation procedure in Figure 5.1, we’ll get one value of F_c for this setting stroke, say F_{c_1} ,

2. Dividing F_{c_1} by the actual applied control input in the real test, we’ll get a coefficient, say c_t ,

3. Similar to step 1 but setting the stroke termination condition to be 2” stroke, then we’ll get another value of F_c for this 2” stroke, say F_{c_2} ,

4. Assuming the same coefficient would apply to the case of 2” stroke with “soft-landing” in the real test, thus the experimental control input F_{c_exp} for 2” stroke would be $F_{c_exp} = c_t \times F_{c_2}$.

Using the above approach, the experimental control inputs for the special 4 cases at 2” full stroke were obtained and listed in Table 5.4 in bold italic black numbers. Correspondingly, the tuning factor was computed as the ratio of the 2” experimental control input to the reference control input determined in Tables 5.2-5.3 and also listed in Table 5.4 in bold italic black numbers.

5.3.3 Sled Test Results and Discussion

5.3.3.1 Seat and MREA Transient Responses

As before, the crash pulse was recorded with sampling rate of 10 kHz and pre-filtered with an SAE (Society of Automotive Engineers) CFC (channel frequency class) 60 filter (i.e., cutoff frequency 100 Hz) in the data acquisition system. For the seat deceleration (measured at left rail and right rail), the signals were recorded with the same sampling rate of 10 kHz but pre-filtered by an SAE CFC 600 filter (i.e., cutoff frequency 1000 Hz). As before, the crash pulse does not need to be filtered again in the data analysis. For the seat deceleration, we used a CFC 60 filter to eliminate noise in the recorded data for the same reasons addressed in previous passive mode sled test. Figures 5.10 presents the power spectrum analysis of three sample data sets at nominal initial impact speed of 5.6 m/s for F_c control and Bi_c control respectively including the measured seat deceleration (time domain average of decelerations measured at left and right rails) and the piston displacement. As shown in the figures, for each data set, power of the seat decelerations is distributed mostly below 100 Hz and that of the piston displacement is distributed far below 20 Hz. Therefore, this justifies the appropriateness of the CFC 60 filter for the seat deceleration. For the piston displacement, based on the power spectrum analysis and

to keep consistent with the deceleration filtering, in the controller we used a second-order butterworth filter with cut-off frequency of 100 Hz. In addition to obtain the stroke, the filtered piston displacement was also used to produce the piston velocity and this derived piston velocity was filtered again by a second-order butterworth filter with cut-off frequency of 30 Hz before it functions as the velocity feedback for the F_c control.

Figures 5.11-5.13 demonstrate the measured seat deceleration at each nominal initial impact speed for each control algorithm. The average seat deceleration is taken as the average of the time domain deceleration measured at the left and right seat rails. It is seen that the seat deceleration are significantly reduced using either the Bi_c or F_c control strategy for lower impact speeds – below 5.6 m/s for 5th female and below 4.5 m/s for 95th male. For higher impact speeds (5.6 m/s for 5th female and 4.5 and 5.6 m/s for 95th male), the apparent peak seat deceleration appears even higher than the peak of the crash pulse due to the large spike at the beginning of the impact period. As discussed in previous chapters, such a large spike originated from the metal-to-metal impact between the MREA rod eye and the pin that were used to connect the MREA with the sled platform. It is noted that the magnitude of the spike largely increases as the initial impact speeds increases. In addition, there are two relatively smaller peaks after the primary peak diminishing to zero. The one immediately after the primary peak is in the opposite direction to the primary one and the second after the first one is in the same direction to the primary one. Alike the spike in the primary peak, their magnitudes were largely pronounced as the initial

impact speed increases. These two smaller after peaks come from the couplings between the seat and the occupant after the impact period.

In addition, Figures 5.14 also compare the seat deceleration for the two control algorithms at the same nominal initial impact speed. It is seen that at all tested initial impact speeds, the seat deceleration under both control algorithms are almost comparable despite the fact that at nominal initial impact speed of 4.5 m/s and 5.6 m/s under Bi_c control the measured strokes are about a quarter inch less than the 2" full stroke. It indicates that both control strategies, i.e., Bi_c and F_c control, induce very similar biodynamic response, which have been demonstrated in the simulation results of the CO model in Chapter 3. Therefore, it is concluded that the two control algorithms provide the occupant with almost the same level of impact load mitigation based on both the simulation results and the experimental data. Hence Bi_c control is superior because it uses only the initial impact speed and it is very simple to implement in practice, which only gives a one-time command current before the commencement of the impact and does not need any velocity feedback during the impact. On the other hand, the F_c control is more complicated because it requires real time piston velocity feedback to issue the real time current command, which imposes high performance and time-response requirement for the controller in practice.

Figure 5.15 presents one sample case of the MREA transient response and the applied current time history under the constant stroking force control at nominal initial impact speeds of 2.6 m/s for 95th male to demonstrated how this control algorithm was actually realized in the real test (since the constant Bingham number control is rather simple, it is not shown here). Note that, the expected MREA force

(red solid line and denoted as “Expected” in the legend) was computed from the MREA force equation in Eq. (5.5) using the measured piston velocity and the recorded applied current. The real MREA force was not available due to unavailability of force measurement instrument in the experimental setup. As shown in the figure, the MREA force was kept constant and closely followed the control input force by instantaneously varying the applied current level according to the feedback piston velocity. And the MREA comes to a stop at the 2” stroke, which implies the successful achievement of the control objective.

5.3.3.2 Transient Transmissibility

To assess the effectiveness of the adaptive sliding seat system in mitigating the impact load imparted to the payload under the two control algorithms, one way is to evaluate how much the load was transmitted from the crash pulse to the payload. For this purposes, here we introduce the transient transmissibility (TT) in terms of the deceleration. In Huang (2002), the transient transmissibility is defined as the ability of a body mount to transfer the frame impulse to the body. Extending this definition to our problem here, the transient transmissibility in this study is defined as the ability of the adaptive sliding seat system to transfer the crash pulse to the payload (occupant/seat). Since only seat deceleration data is available here, the seat deceleration is presumed to represent the deceleration of the occupant/seat together. Considering the abnormal large spikes appeared in the measured seat decelerations due to metal-to-metal impact, we will formulate two forms of transient transmissibility. One is termed as the peak transient transmissibility (PTT) and the other is termed as the average transient transmissibility (ATT).

Interpreting the transient transmissibility mathematically, the numerical value of PTT expressed as mathematical symbol, A_{PTT} , is equal to the ratio of the peak seat deceleration to the peak crash pulse during the impact period, and is given by:

$$A_{PTT} = \frac{\max_{t \in (t_2, t_3)} |a_{seat}(t)|}{\max_{t \in (t_0, t_1)} |a_{crash}(t)|} \quad (5.6)$$

Similarly, the numerical value of ATT denoted by the mathematical symbol, A_{ATT} , is the ratio of the time averaged seat deceleration to that of the crash pulse during the impact period and is computed as:

$$A_{ATT} = \frac{\frac{\int_{t_2}^{t_3} a_{seat}(t) \cdot dt}{t_3 - t_2}}{\frac{\int_{t_0}^{t_1} a_{crash}(t) \cdot dt}{t_1 - t_0}} = \frac{\bar{a}_{seat}}{\bar{a}_{crash}} \quad (5.7)$$

Here, $a_{seat}(t)$ is the measured time history of seat deceleration and $a_{crash}(t)$ is the measured time history of the crash pulse. \bar{a}_{seat} and \bar{a}_{crash} are the time averaged deceleration of seat and the crash pulse respectively over the impact period. t_0 is the crash pulse starting time and is defined as the time where the crash pulse changes from negative value to positive value and continues being positive before reaching the peak of the sled acceleration wave; t_1 is the crash pulse ending time and is defined as the time where the crash pulse changes from positive value to negative value after falling from the peak. Similarly, t_2 is the seat impact starting time and is defined as the time where deceleration of the seat changes from negative value to positive value and continues being positive before approaching the peak of deceleration curve; t_3 is the seat impact ending time and is defined as the time where deceleration of the seat

changes from positive value to negative value after falling from the peak. Figures 5.16 gives an example showing the starting time and ending time of the crash pulse and the seat deceleration. Then the impact period here means as the time interval between the impact starting time and ending time, such as $t \in (t_0, t_1)$ for crash pulse and $t \in (t_2, t_3)$ for the seat.

The average transient transmissibility (ATT) is introduced because as was pointed out before (also shown again in Figure 5.17) there were pronounced large spikes (first peaks) in the measured seat decelerations at the beginning of the impact period for those higher initial impact speeds due to metal-to-metal impact effect between the rod eye and pin through which the MREA was connected to the fixture of the sled platform. As demonstrated in Figure 5.17, the induced first peak was even much larger than the peak of the crash pulse. It is believed that the first peak does not reflect the genuine peak seat deceleration. Rather, the second peak (as shown in Figure 5.17a) is seen to be more close to the actual peak seat deceleration. For this reason, in the following analysis, we compute the average transient transmissibility (ATT) to minimize the misleading first peaks but also the PTT and ATT metrics that ignore the first peaks and use the second peaks in the seat decelerations at higher speeds. To distinguish these two classes of metrics, we call the PTT and ATT metrics that include the first peaks as PTT1 and ATT1, and the PTT and ATT metrics that ignore the first peaks as PTT2 and ATT2.

Using the Eqs. (5.6) and (5.7), PTT1 and ATT1 can be computed directly. For PTT2, the second peak was taken as the peak of the seat deceleration, that is, the numerator in Eq (5.6). For ATT2, during the calculation of the time averaged seat

deceleration, \bar{a}_{seat} , any instantaneous decelerations whose magnitude was larger than the second peak were cut and given the same values as the second peak as demonstrated in Figure 5.18. The results for all sorts of PPT and ATT were summarized in Table 5.5. And Figures 5.19- 5.20 present the PTT1, PTT2, ATT1 and ATT2 versus the initial impact speed for each control algorithm.

It is shown that PTT1 at higher impact speeds was even greater than 1. This is abnormal because the maximum PTT value can be only equal to 1 and thus we introduced PTT2 to correct the abnormal results by ignoring the first peak. As observed in Figure 5.19b, PTT2 was much lower than 1 even at the highest impact speed (roughly 0.7 at 5.6 m/s). Therefore, in terms of PTT2, the AMSS system can reduce the seat peak deceleration by roughly 55 percent to 30 percent using either control algorithm for various occupant types and initial impact speeds. In addition, generally both PTT1 and PTT2 increase as the initial impact speed increases for either control algorithm and for either occupant type, which implies a better load mitigation for lower initial impact speeds, except for PTT2 of 95th male at initial impact speed of 2.6 m/s. This is because as shown in Figures 5.12a and 5.13a, at 2.6 m/s, for the 95th male, the only peak in the seat deceleration was also seen to be affected by the metal-to-metal impact though no obvious second peak can be identified. Thus, PTT1 and PTT2 have the same values since only one peak was identified and PTT2 appear to be larger than those at the initial impact speed of 3.5 m/s. Also, Bi_c control seems to offer better load mitigations for initial impact speeds up to 5 m/s.

For the ATT, it is seen that both ATT1 and ATT2 are all lower than 1 (roughly below 0.8 at 5.6 m/s) and ATT2 is generally smaller than ATT1 at each single case

but the difference is not substantial. This indicates that the error induced by the first peak due to metal-to-metal impact was minimized by time averaging the transient deceleration. It on the other hand shows that ignoring the first peak in the seat deceleration is reasonable and is a better way to reflect the true AMSS system performance. Thus, regarding ATT1 and ATT2, the seat deceleration in the AMSS system was reduced by roughly 35 percent to 20 percent using either control algorithm for various initial impact speeds and occupant types. Both control algorithms offer comparable load mitigating capabilities to the seat but Bi_c control generally shows slightly better performance. Also, frankly speaking, regarding ATT, the AMSS system is seen to offer better mitigations to 5th female than to 95th male and to lower initial impact speeds than to higher initial impact speeds.

Consequently, it can be concluded that the AMSS system significantly reduced the impact load transmitted to the payload using both control algorithms for various occupant types and initial impact speeds. Generally, the AMSS system provides better load reductions for lower initial impact speeds and the 5th female receives better mitigations than the 95th male at the same initial impact speed. Also, Bi_c control seems to offer better load mitigating capability than F_c control.

5.3.3.3 Energy Dissipation Ratio (EDR)

Recall that the energy dissipation ratio (EDR) is defined as the ratio of the dissipated energy by the MREA to the initial kinetic energy of the payload and is given by:

$$E_d = \frac{\int_{t_2}^{t_3} 2 \cdot F_{mr} \cdot ds}{\frac{1}{2} m v_0^2} \times 100\% \quad (5.8)$$

Here F_{mr} is the instantaneous force of one MREA during the impact period, which can be obtained from Eq. (5.5) using the measured piston velocity and applied current. For F_c control, F_{mr} is approximately equal to the product of the experimental control input of F_c (the black numbers in Table 5.4) and the measured peak stroke. For Bi_c control, F_{mr} is derived from Eq. (5.5) using the measured piston velocity and applied current. ds is the measured instantaneous piston displacement, v_0 is the initial impact speed and m is the payload (seat/occupant) mass (here, it is 161 lbs for 5th female and 274 lbs for 95th male).

The calculated EDR for each case is listed in Table 5.5. Figure 5.21 presents the EDR versus initial impact speed for the two control algorithms. As can be seen that the EDR dramatically decreases as initial impact speed increases from 2.6 m/s to 5.6 m/s for either control algorithm and occupant type. For example, for the 5th female and F_c control, the EDR reduces from 76% to 22% when the initial impact speed increases from 2.6 m/s to 5.6 m/s. Also, the EDR for both control algorithms and both occupant types tends to converge to a similar quantity at initial impact speed of 5.6 m/s. But for initial impact speeds below 5.6 m/s, the EDR for the 5th female is much higher than that for the 95th male at the same initial impact speed. For instance, for 2.6 m/s and F_c control, the EDR are 76% and 53% for the 5th female and 95th male, respectively. Additionally, in terms of the energy dissipation ratio, F_c control and Bi_c control exhibit similar performance.

5.4 Effectiveness of the CO Model in Control Inputs Prediction

As mentioned before, the reference control input determined from the numerical simulation of the CO model was multiplied by a tuning factor to account for modeling

error and uncertainties of small variations of initial impact speed and crash pulse. The tuned control inputs that successfully achieved the control objective in the real tests are termed as the experimental control inputs (listed in black number in Table 5.4 for each case). By inspecting how close the reference control inputs are to the experimental control inputs, the effectiveness of the CO model in predicting the right control input for the two control algorithms can be assessed.

Figures 5.22-5.23 compare the reference control inputs and the experimental control inputs for both control algorithms, as well as the tuning factors at various initial impact speeds. It is seen that generally the reference control inputs obtained from the CO model simulation agree well with the experimental control inputs in the real test at almost all examined initial impact speeds for each control algorithm and each occupant type. Based on the tuning factors, the error between the reference control inputs predicted by CO model simulation and the experimental control inputs are almost within 20 percent at various initial impact speeds for both control algorithms except for the case of Bi_c control at 2.6 m/s (about 60 percent). Though the error for the case of Bi_c control at 2.6 m/s is large, it is deemed acceptable because the impact energy would be relatively small at 2.6 m/s and the impact load transmitted to the payload would still be effectively mitigated even if the applied current level for Bi_c control is 60 percent larger than the current level achieving the 2" stroke and "soft-landing".

Figures 5.24-5.26 present the simulated seat deceleration from the CO model using the experimental crash pulse and compare with the measured data at nominal initial impact speeds of 2.6 and 5.6 m/s for each occupant and each control algorithm.

Generally speaking, during the impact period, the modeling seat deceleration from the CO model compares fairly well with the measured one. However, there's always more or less discrepancy between the modeling results and the measurements. This answers why the reference control input predicted from the CO model always needs to be adjusted by a tuning factor to achieve the “soft-landing” in the real test.

Another thing is, recall the seat deceleration comparison between the two control algorithms shown in Figure 5.14, at impact speeds of 4.5 and 5.6 m/s for B_i control, even though the utilized strokes are about a quarter inch less than the 2” full stroke, it still provides the seat with similar mitigation to the impact load compared to the F_c control at these 2 speeds who utilized the 2” full stroke. This implies that even without the tuning factor, the two control algorithms can still offer effective impact load mitigations to the payload even if the 2” stroke may not be fully utilized by the reference control input pre-determined from the CO model simulation using prior test data. This is extremely useful in practice because a suitable tuning factor is usually not known prior to the impact event. The tuning factors listed here were obtained iteratively by trial-and-error test. If this kind of test to find the right tuning factors is not available in practice or if there are some uncertainties in the actual initial impact speed or crash pulse variations, the two control algorithms would still be applicable with only minor performance degradation if the reference control inputs from the CO model simulation based on the results presented in this study are used.

In all, the CO model is shown to be a relatively simple yet effective analytical model to predict the reference control inputs for both control algorithms.

5.5. Conclusions

In this chapter, the two control algorithms and the CO model studied in Chapter 3 were examined experimentally by sled test of the prototype adaptive sliding seat system under control mode. The reference control inputs for each control algorithm at various initial impact speeds were determined in a statistic means via numerical simulation of the CO model using the crash pulses collected in previous passive mode sled test. Then sled test was conducted to check the feasibility of the two control algorithms in the prototype seat system under control mode and to verify the effectiveness the CO model in predicting the reference control inputs. In the test, the reference control input at each initial impact speed was used together with an empirical tuning factor, which was resorted to account for modeling error and small variations of initial impact speed and crash pulse in each test, to achieve the control objective – “soft-landing” the seat at 2” stroke. The tuned control inputs that successfully achieved the control objective were identified for each control algorithm and each occupant type at the tested initial impact speeds and referred to as the experimental control inputs.

The measured transient response of the seat (time history of the seat deceleration) at each case was presented and the data showed that the impact load imparted to the seat was significantly reduced for lower initial impact speeds -- below 5.6 m/s for 5th female and below 4.5 m/s for 95th male – with either control algorithms. At higher impact speeds (5.6 m/s for 5th female and 4.5 and 5.6 m/s for 95th male), the apparent peak seat deceleration appears even higher than the peak of the crash pulse due to the metal-to-metal impact of the connection fixture (rod eye

and pin) between MREA and the sled platform at the beginning of the impact period. To quantitatively assess the impact load mitigation capability of the AMSS system, transient transmissibility (TT) in terms of the deceleration and energy dissipation ratio were introduced. The transient transmissibility was interpreted in two forms - the peak transient transmissibility (PTT) and the average transient transmissibility (ATT). To reflect the influence of the metal-to-metal impact effect in the measured seat decelerations, results of PTT and ATT considering the first peak (PTT1 and ATT1) and ignoring the first peak (PTT2 and ATT2) were obtained. The results in terms of the transient transmissibility (PTT2, ATT1 and ATT2) and the energy dissipation ratio showed that the AMSS seat system controlled by the two control algorithms can effectively reduce the impact load imparted to the seat for the tested speed range. The 5th female was shown to receive better impact load mitigations than the 95th male at the same initial impact speed. Also, the two control algorithms are turned out to be comparable in mitigating the impact load imparted to the seat, while Bi_c control is much simpler to implement because it uses only the initial impact speed, unlike the F_c control requiring piston velocity feedback. In all, the test results showed that the AMSS system with F_c control and Bi_c control is feasible, effective and relatively simple to implement in practice.

Finally, the effectiveness of the CO model in predicting the reference control input was examined. The agreeable comparison between the reference control inputs and the experimental control inputs indicated that the CO model is a relatively simple yet effective analytical model to predict the reference control inputs for both control algorithms. Also, it is found that the two control algorithms are robust to uncertainties

in the variations of actual initial impact speed and crash pulse and are believed to be still applicable with only minor performance degradation if just simply using the reference control inputs from the CO model simulation as the control inputs even without introducing the tuning factors.

Table 5.1: Values of system parameters in the CO model.

Parameters	5 th percentile female	95 th percentile male*
$m_h (kg)$	3.65	4.94
$m_t (kg)$	11.90	22.60
$m_p (kg)$	13.70	30.30
$m_s (kg)$	32.2	23.1
$k_{sb} (kN / m)$	33.87	33.87
$k_{lb} (kN / m)$	43.86	43.86
$l_h (mm)$	200	230
$l_c (mm)$	270	320
$l_t (mm)$	450	530
$l_{sb} (mm)$	400	480
$\theta_h (\text{deg}) @ t = 0ms$	-10	-10
$\theta_t (\text{deg}) @ t = 0ms$	-20	-20

* The parameter values here are nominal parameters for 95th percentile male dummy.

Table 5.2: Reference control input from numerical simulation for 5th female.

Initial impact speed v_0 (m/s)	5 th female	
	F_c (kN)	I_c (A)
2.61 m/s	1.45	0.17
3.49 m/s	1.92	0.36
4.55 m/s	2.38	0.61
5.52 m/s	2.75	0.85
	$F_c = -0.0388 v_0^2 + 0.7608 v_0 - 0.2699$	$I_c = 0.0079 v_0^2 + 0.1702 v_0 - 0.3282$

Table 5.3: Reference control input from numerical simulation for 95th male.

Initial impact speed v_0 (m/s)	95 th male	
	F_c (kN)	I_c (A)
2.59 m/s	1.93	0.41
3.50 m/s	2.56	0.80
4.58 m/s	3.31	1.41
5.60 m/s	4.03 (extrapolated)	2.14 (extrapolated)
	$F_c = 0.0042 v_0^2 + 0.6640 v_0 + 0.1832$	$I_c = 0.0703 v_0^2 - 0.0028 v_0 - 0.0499$

Table 5.4: Experimental control inputs and tuning factors satisfying 2” (or nearly 2”) stroke and “soft-landing”.

Nominal initial impact speed (m/s)	Actual initial impact speed (m/s)	Occupant type	Control algorithm	Measured stroke (inch)	Reference control input	Experimental control input	Tuning factor
2.6	2.41	5th F	F_c	2.08	1.34 kN	1.65 kN	1.23
3.5	3.38	5th F	F_c	2.02	1.86 kN	2.13 kN	1.14
4.5	4.51	5th F	F_c	1.83	2.37 kN	2.40 kN (2.46 kN)	1.01 (1.04)
5.6	5.59	5th F	F_c	1.73	2.77 kN	2.67 kN (2.77 kN)	0.96 (1.00)
2.6	2.6	95th M	F_c	2.03	1.94 kN	2.21 kN	1.14
3.5	3.54	95th M	F_c	2.06	2.59 kN	2.48 kN	0.96
4.5	4.64	95th M	F_c	2.00	3.35 kN	3.00 kN	0.90
5.6	5.6	95th M	F_c	2.04	4.03 kN	3.54 kN	0.88
2.6	2.61	95th M	$Bi_c(I_c)$	2.04	0.42 A	0.68 A	1.62
3.5	3.64	95th M	$Bi_c(I_c)$	2.03	0.87 A	0.96 A	1.10
4.5	4.56	95th M	$Bi_c(I_c)$	1.78	1.40 A	1.45 A (1.58 A)	1.04 (1.13)
5.6	5.68	95th M	$Bi_c(I_c)$	1.76	2.20 A	2.14 A (2.34 A)	0.97 (1.06)

Table 5.5: Transient transmissibility (TT) and energy dissipation ratio (EDR).

Nominal initial impact speed (m/s)	Occupant type	Control algorithm	Peak crash pulse (g)	PTT1	PTT2	ATT1	ATT2	EDR (%)
2.6	5 th F	F_c	17.55	0.55	0.55	0.66	0.66	76.23
3.5	5 th F	F_c	17.75	0.74	0.59	0.69	0.66	51.17
4.5	5 th F	F_c	19.45	0.86	0.64	0.82	0.77	31.04
5.6	5 th F	F_c	18.68	1.05	0.69	0.77	0.71	22.11
2.6	95 th M	F_c	19.07	0.68	0.68	0.72	0.72	53.27
3.5	95 th M	F_c	19.38	0.86	0.55	0.83	0.71	33.60
4.5	95 th M	F_c	18.46	1.09	0.64	0.85	0.73	23.85
5.6	95 th M	F_c	19.20	1.16	0.72	0.86	0.77	20.42
2.6	95 th M	Bi_c	17.96	0.63	0.63	0.69	0.69	54.55
3.5	95 th M	Bi_c	22.35	0.80	0.45	0.85	0.68	34.25
4.5	95 th M	Bi_c	20.73	1.04	0.60	0.84	0.69	22.91
5.6	95 th M	Bi_c	19.56	1.16	0.74	0.77	0.69	18.12

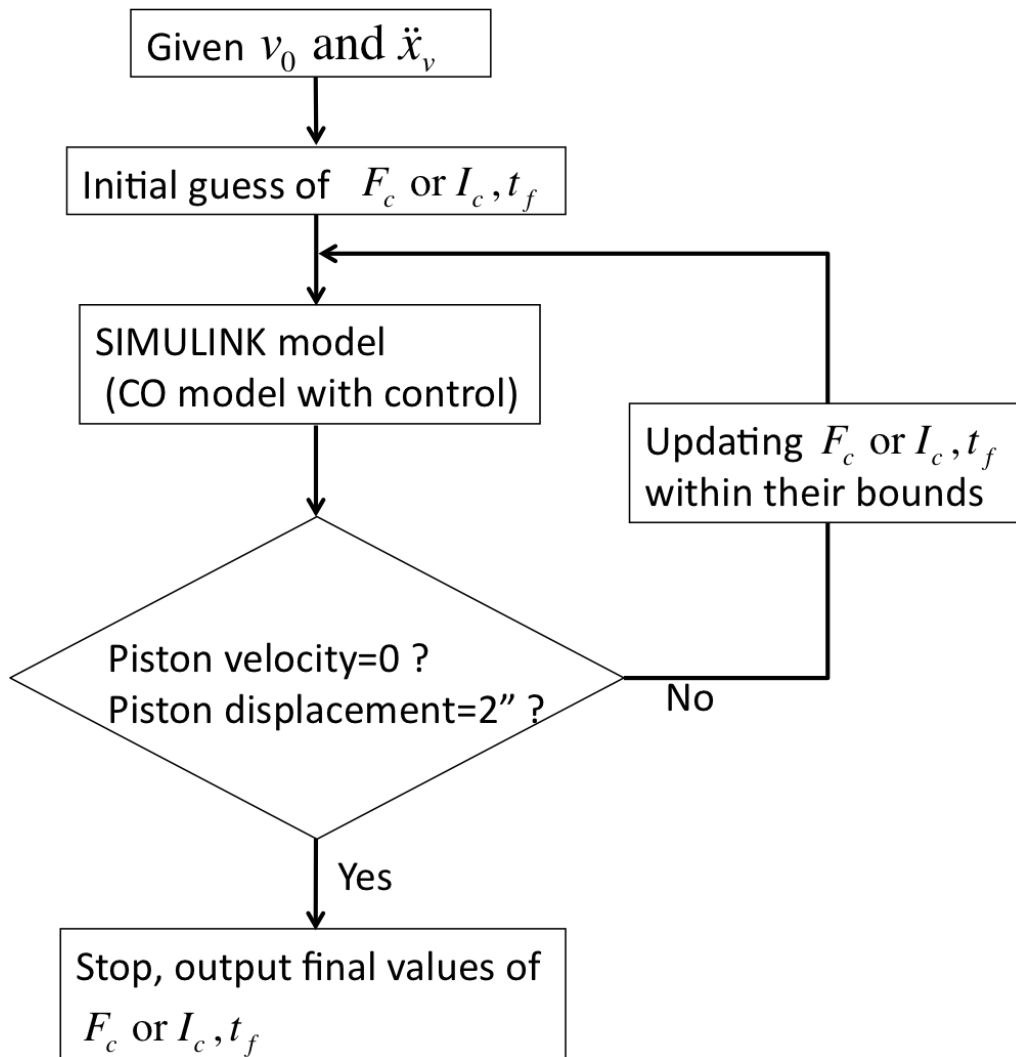


Figure 5.1: Numerical procedure to find control input using CO model.

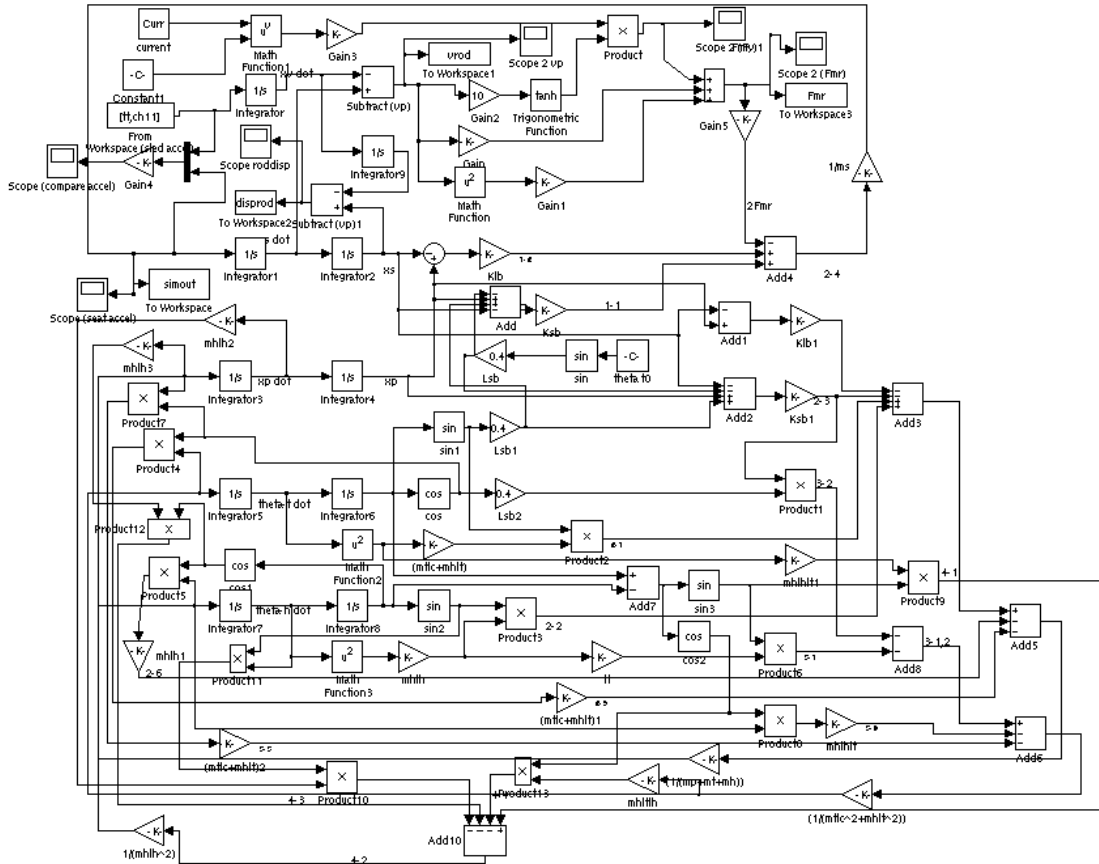
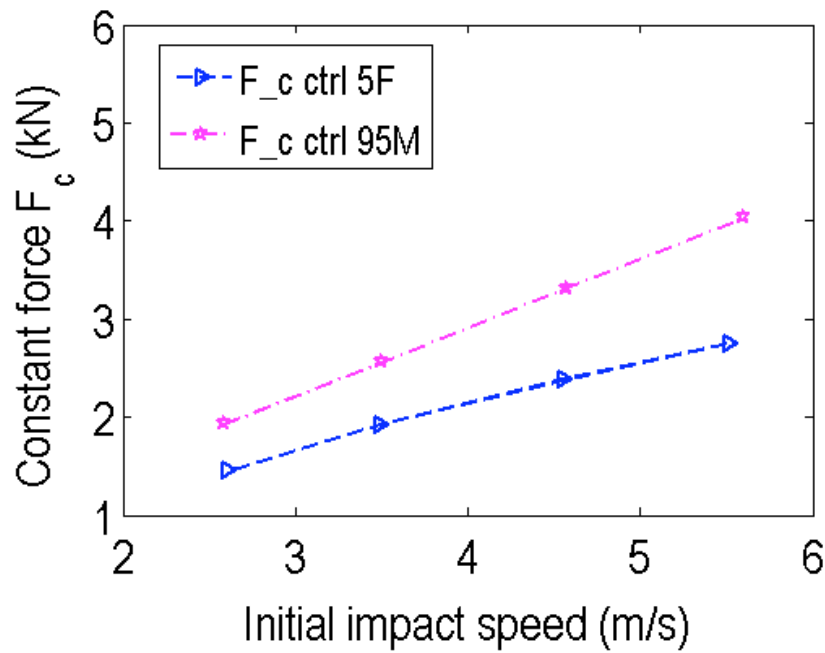
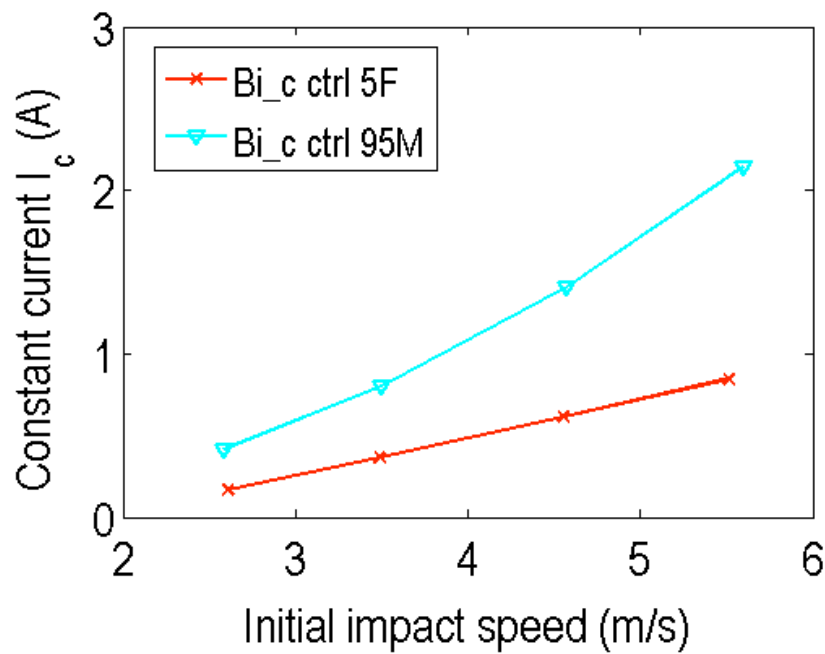


Figure 5.3: SIMULINK model file for constant current control.



(a) Reference control input for constant stroke force control



(b) Reference control input for constant Bingham number control

Figure 5.4: Reference control inputs versus initial impact speed for each control algorithm and occupant type.

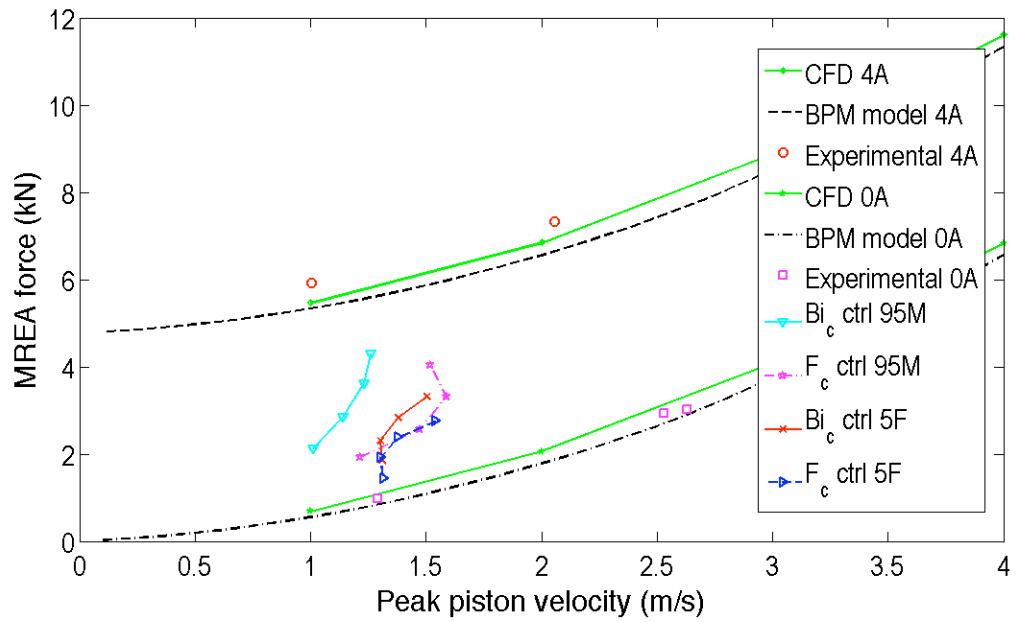


Figure 5.5: Measured MREA force capability and expected MREA peak force and peak piston velocity at each intended initial impact speed during implementation of the control algorithms.

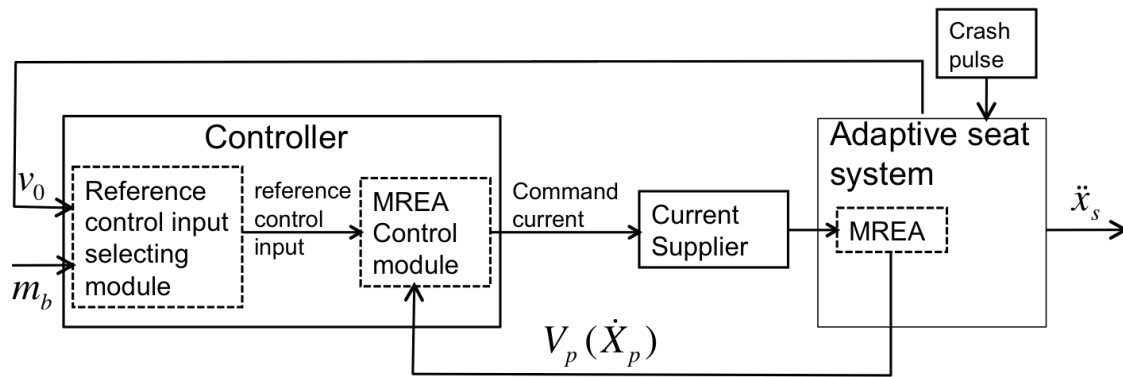


Figure 5.6: Schematic diagram of the adaptive sliding seat system with controller.

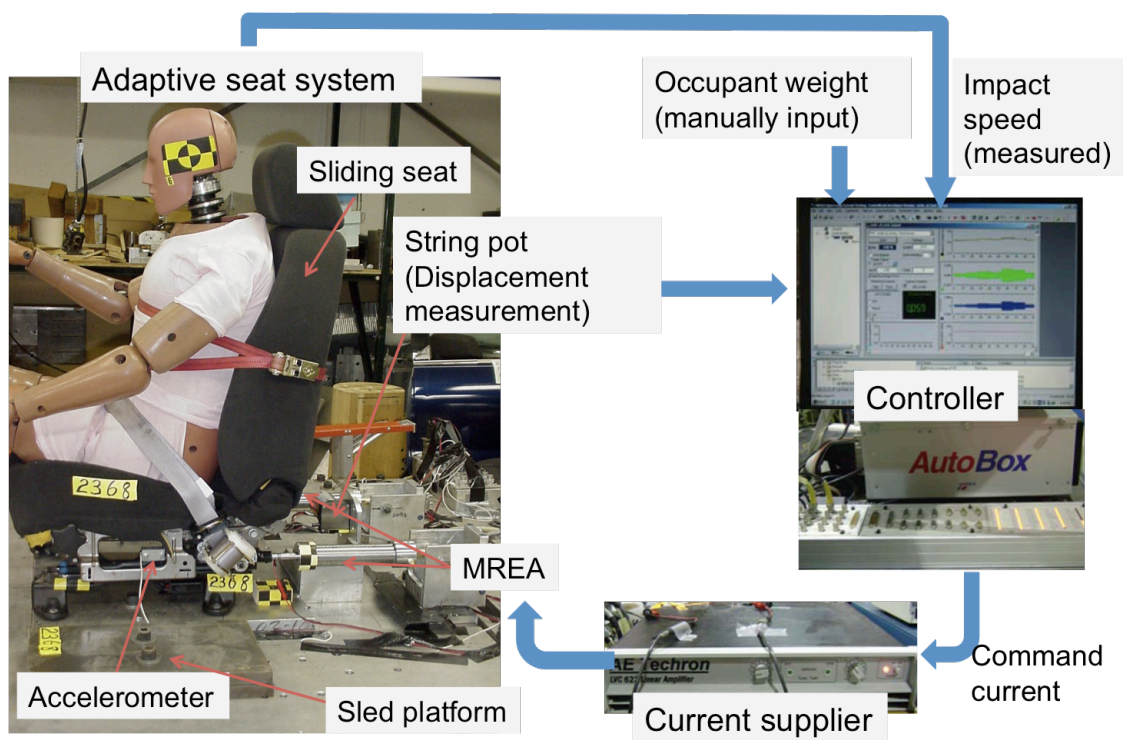


Figure 5.7: Sled test setup of the adaptive sliding seat system with controller.

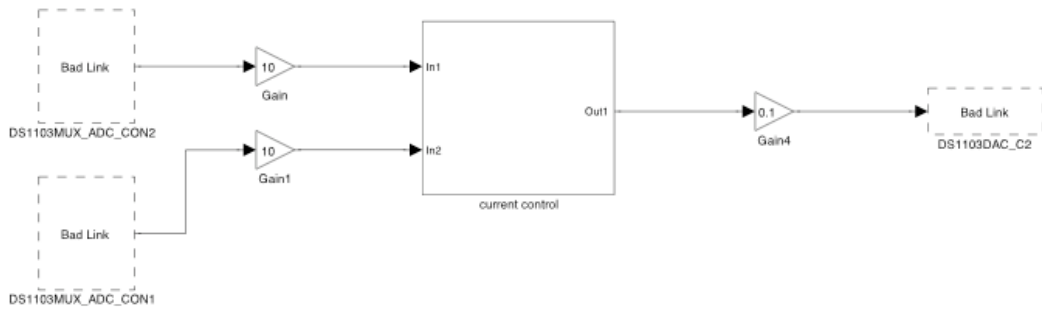


Figure 5.8(a) prototype controller (SIMULINK model file)

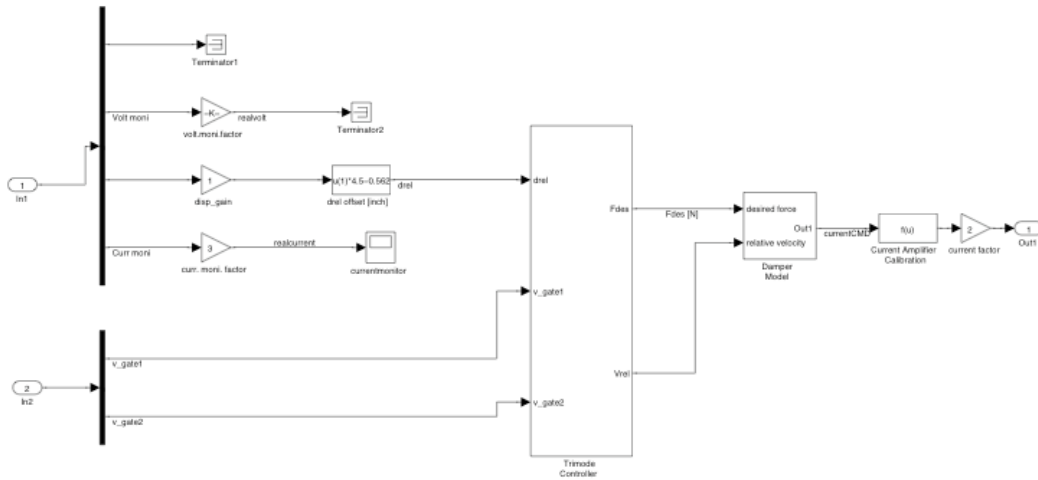


Figure 5.8(b) “current control” subsystem

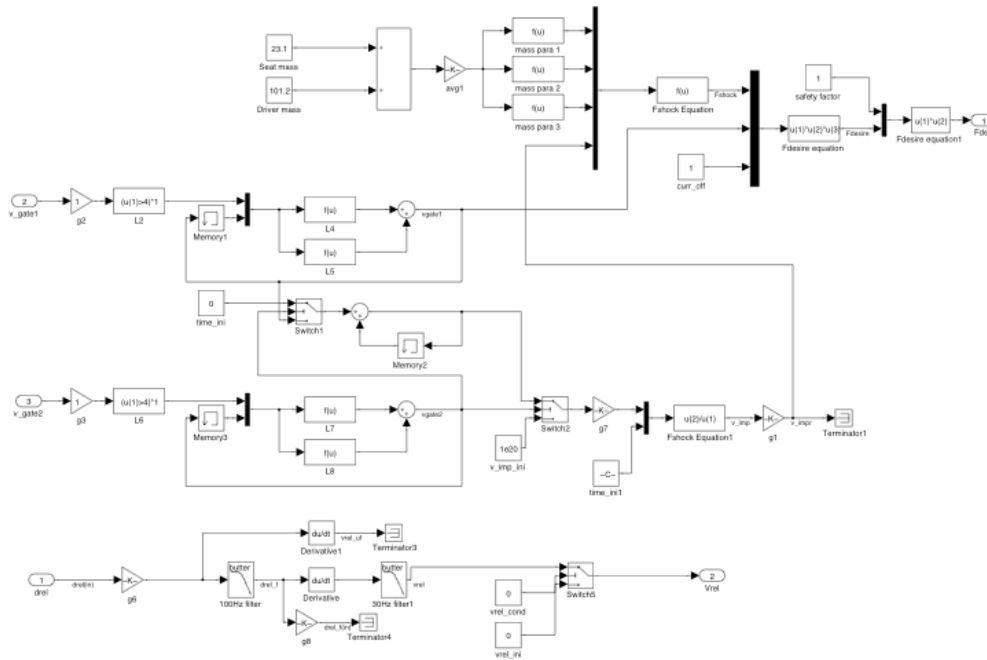


Figure 5.8(c) “Trimode controller” subsystem

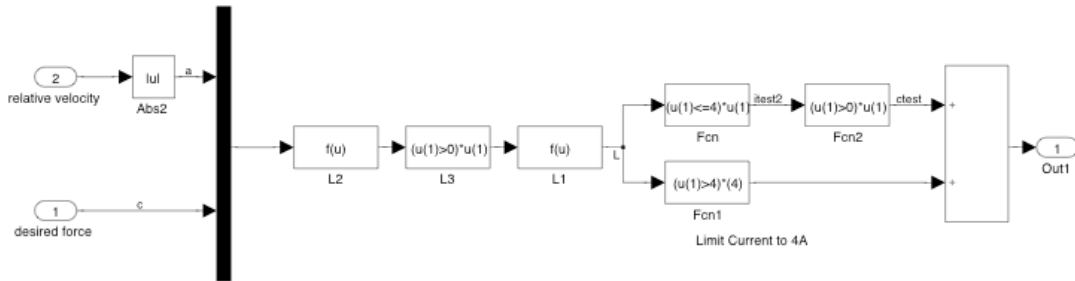


Figure 5.8(d) “Damper model” subsystem

Figure 5.8: The controller model files in SIMULINK.

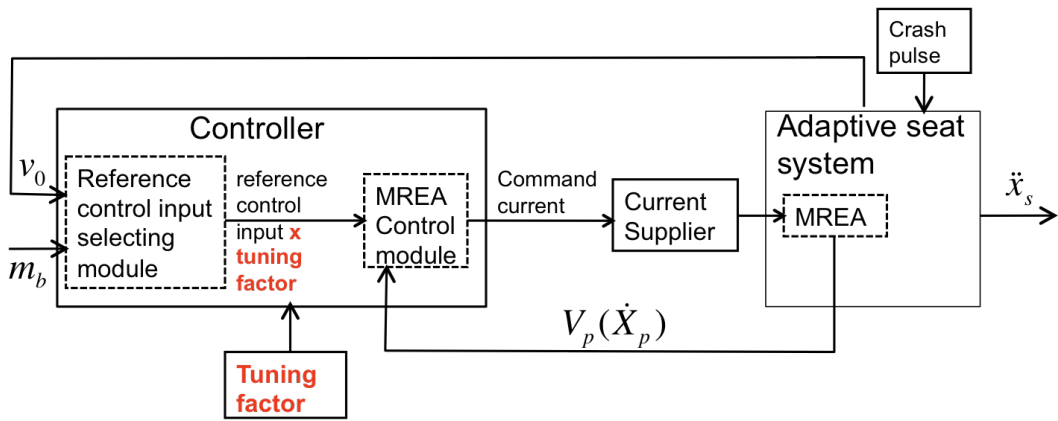
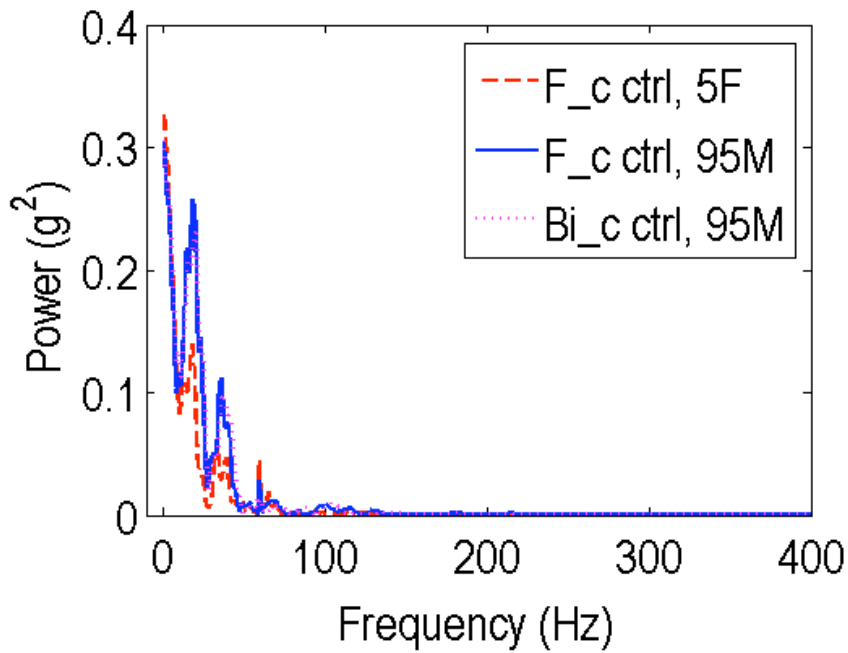
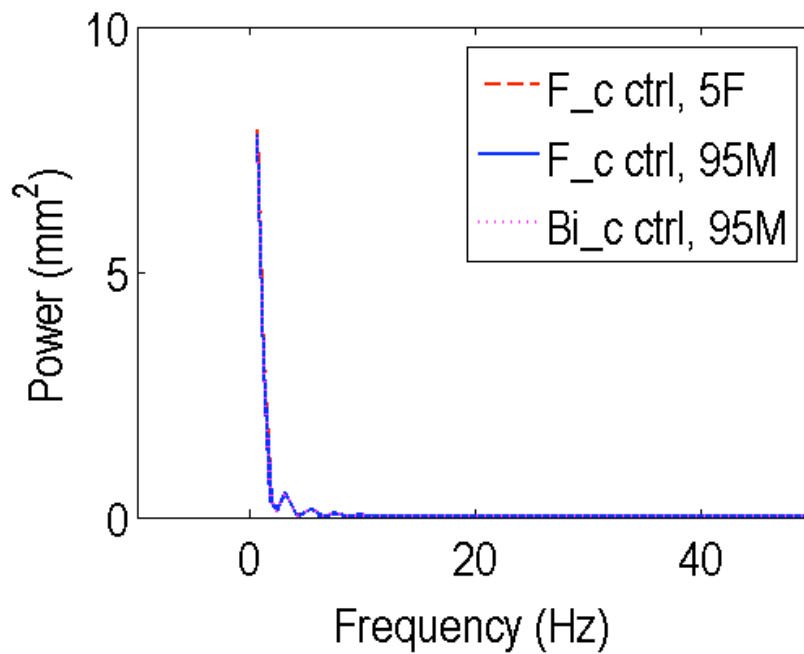


Figure 5.9: Tuning factor in the controller to find the real control input that enables the prototype AMSS system achieve the control objective.

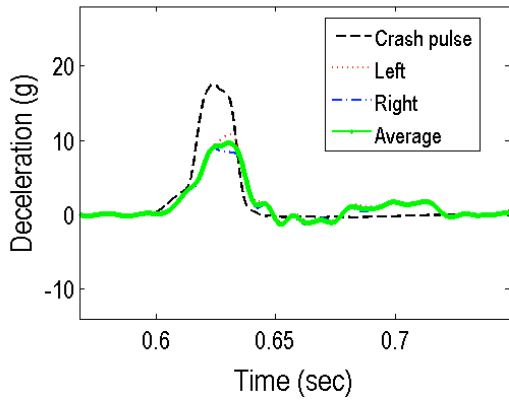


(a) power spectrum of seat deceleration

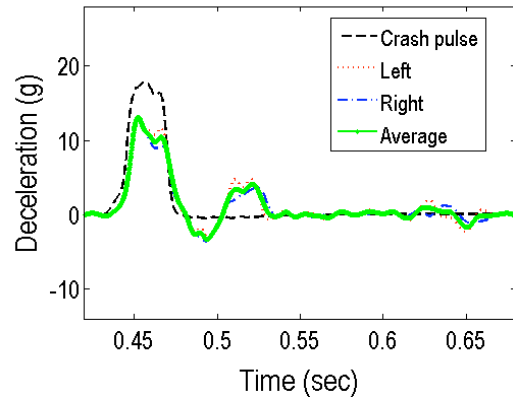


(b) power spectrum of piston displacement

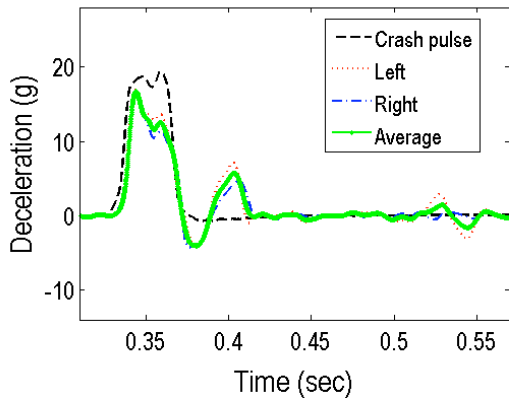
Figure 5.10: Power spectrum analysis of seat deceleration and piston displacement at nominal initial impact speed of 5.6 m/s.



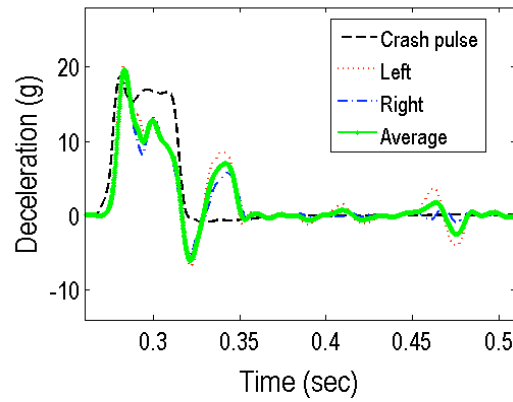
(a) 2.6 m/s



(b) 3.5 m/s

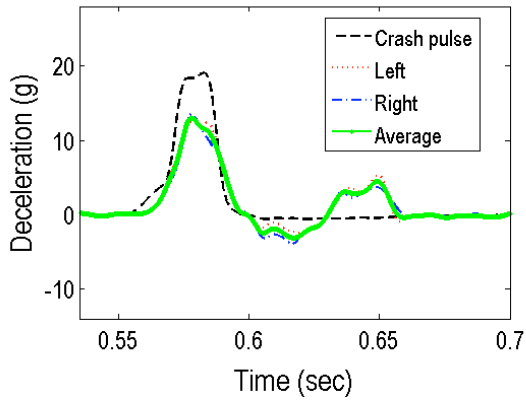


(c) 4.5 m/s

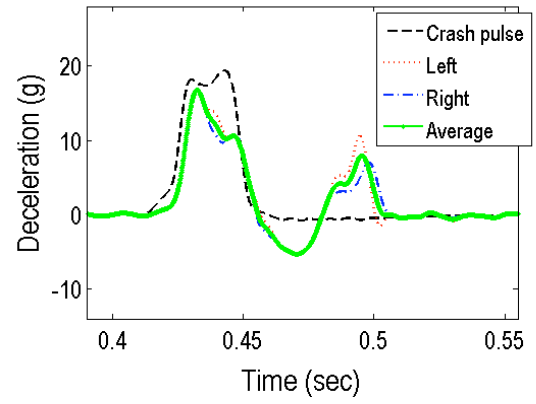


(d) 5.6 m/s

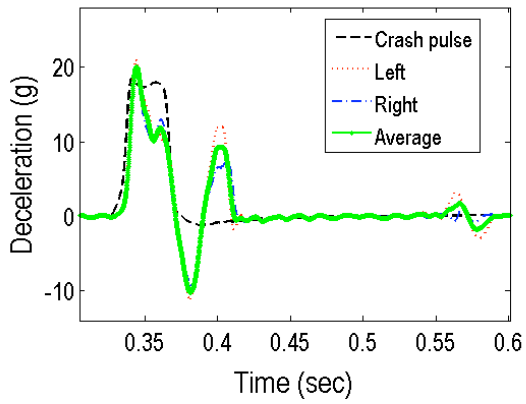
Figure 5.11: Seat decelerations under the constant stroking force (F_c) control for 5th female



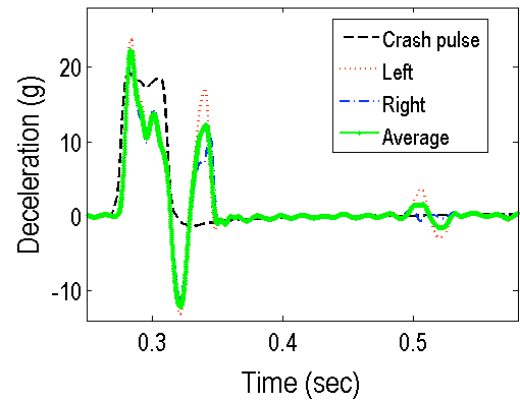
(a) 2.6 m/s



(b) 3.5 m/s

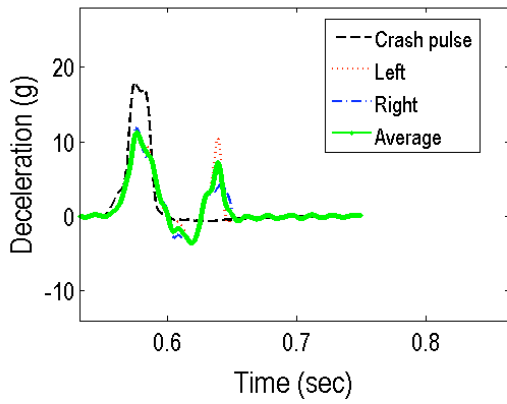


(c) 4.5 m/s

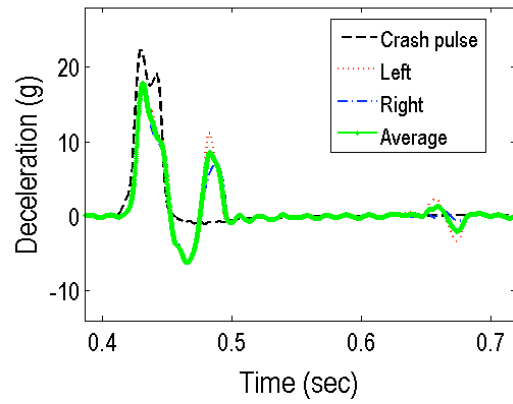


(d) 5.6 m/s

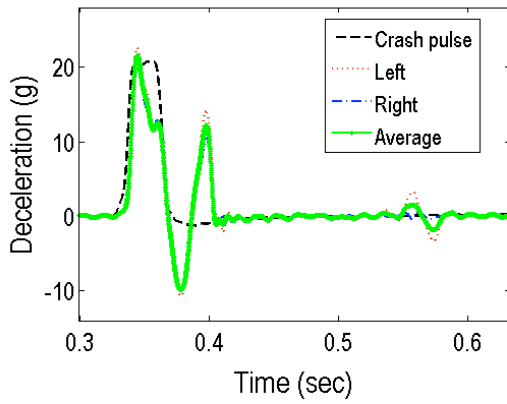
Figure 5.12: Seat decelerations under the constant stroking force (F_c) control for 95th male.



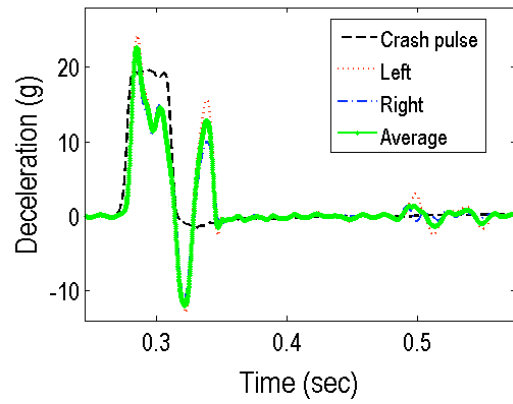
(a) 2.6 m/s



(b) 3.5 m/s



(c) 4.5 m/s



(d) 5.6 m/s

Figure 5.13: Seat decelerations under the constant Bingham number (Bi_c) control for 95th male.

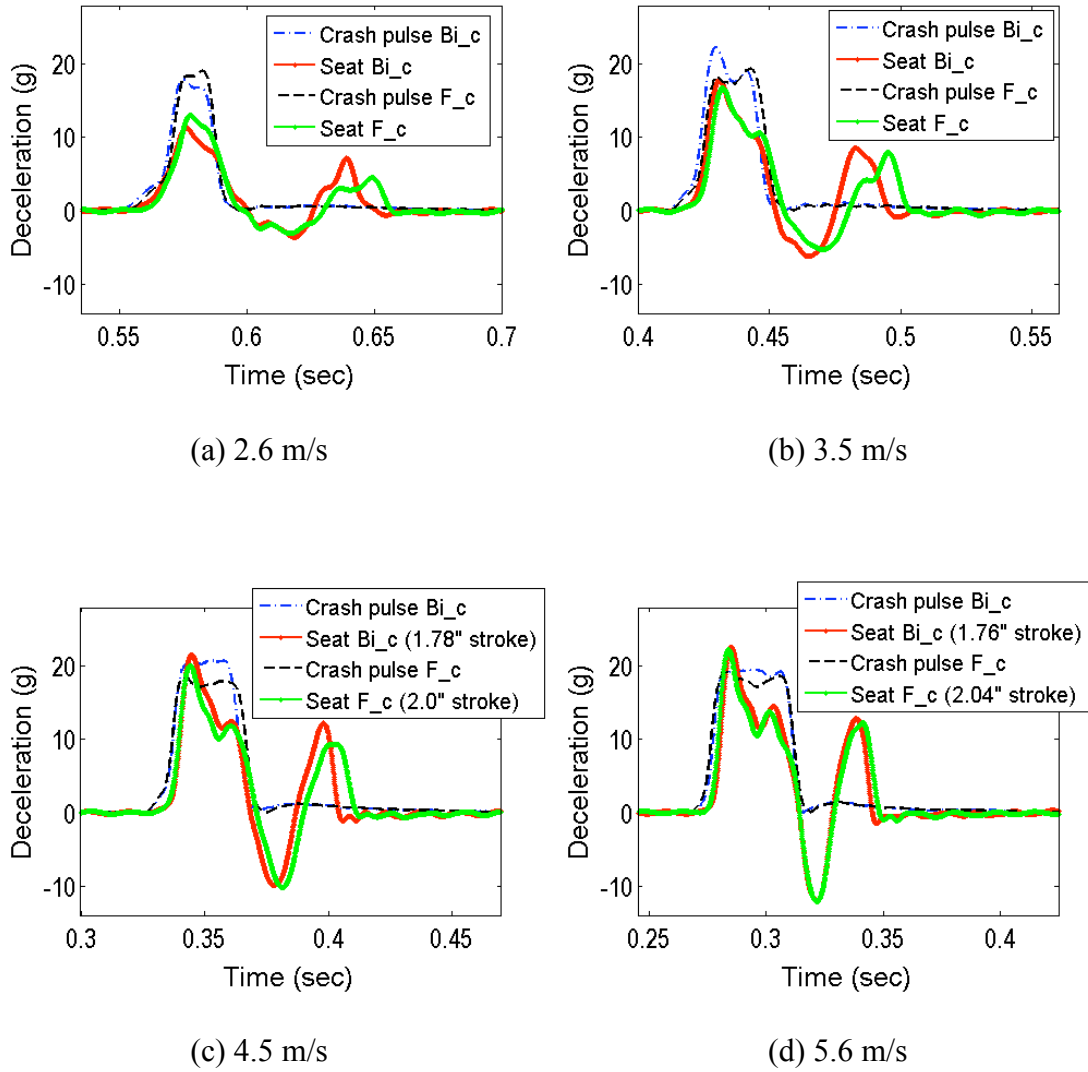
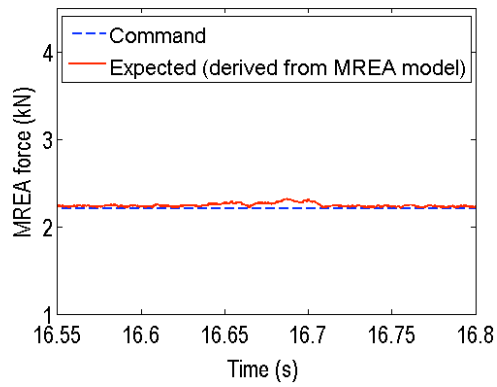
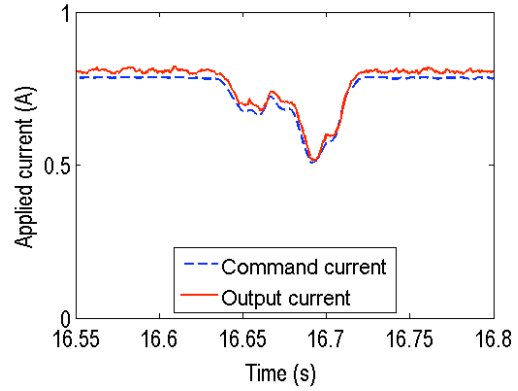


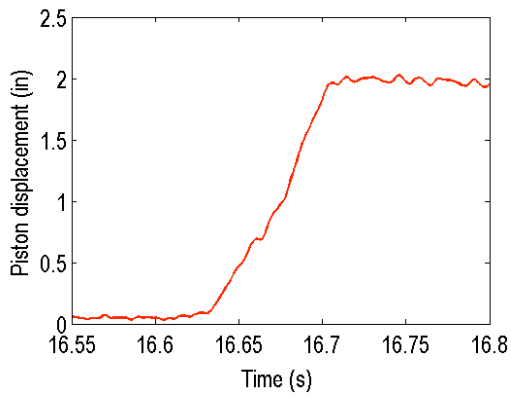
Figure 5.14: Comparison of the constant stroking force (F_c) control with the constant Bingham number control (Bi_c) at the same nominal initial impact speed for 95th male.



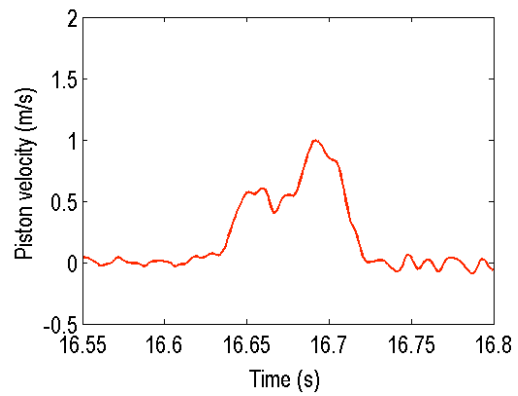
(a) MREA force



(b) Applied current



(c) Piston displacement



(d) Piston velocity

Figure 5.15: MREA dynamic response under constant stroking force control at nominal initial impact speed of 2.6 m/s for 95th male.

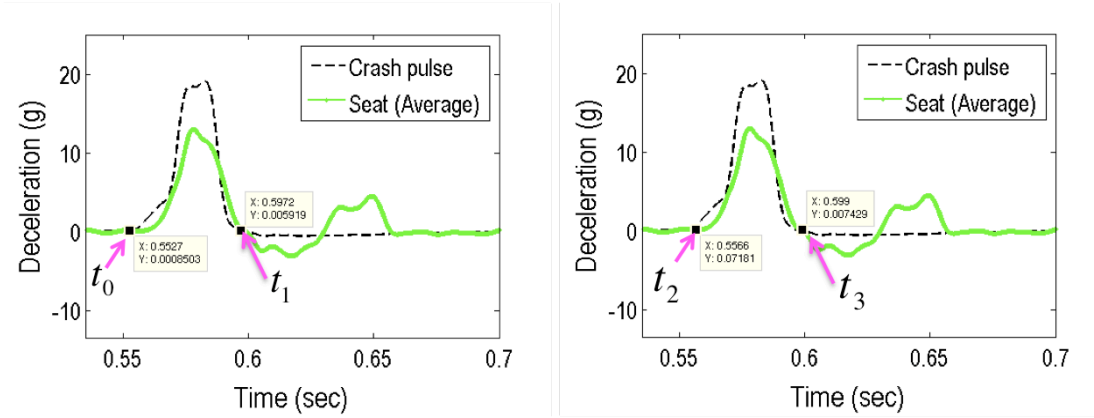
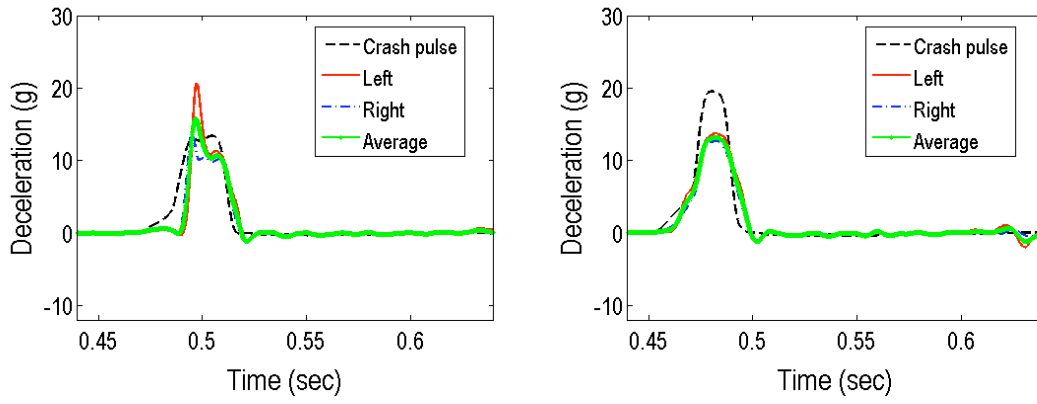


Figure 5.16: Example of sled and sliding seat impact starting time and ending time.



(a) loose fit

(b) improved fit by adding shims

Figure 5.17: Illustration of the influence of the metal-to-metal impact effect on the measured seat deceleration (i.e. large first peak appearing at the beginning moment of the seat deceleration) due to loose fit between the pin and rod eye.

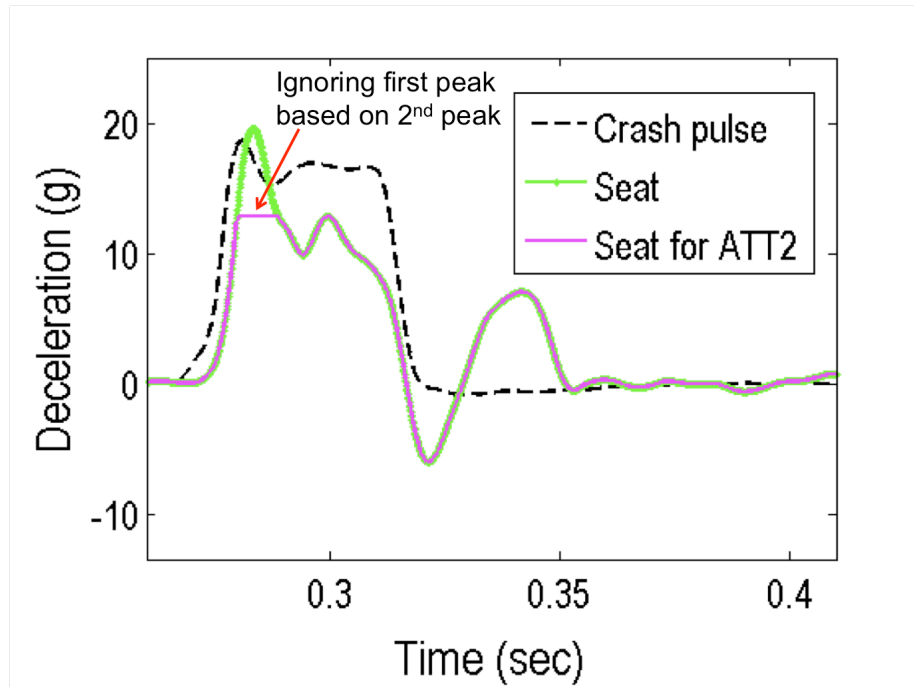


Figure 5.18: Demonstration of calculation of ATT2 (the first peak in the seat deceleration was cut based on the value of the 2nd peak and was reassigned the value of the 2nd peak).

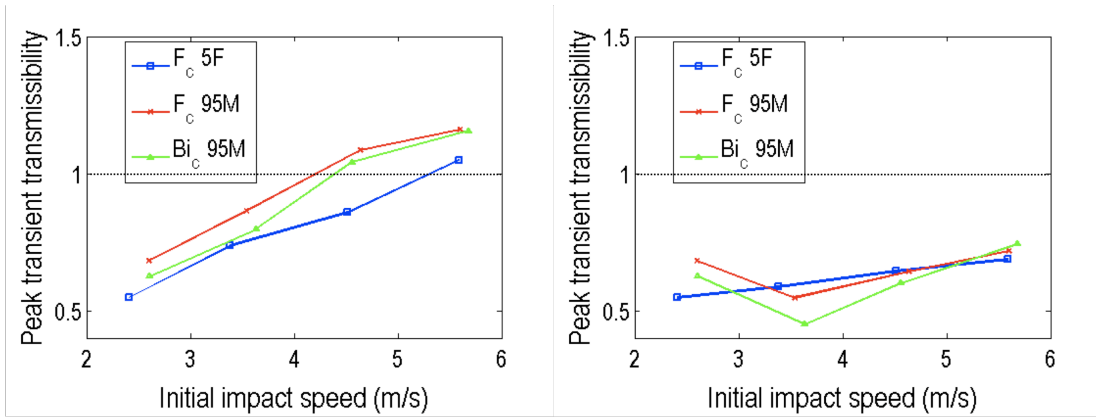


Figure 5.19: Peak transient transmissibility PTT1 and PTT2 versus initial impact speed.

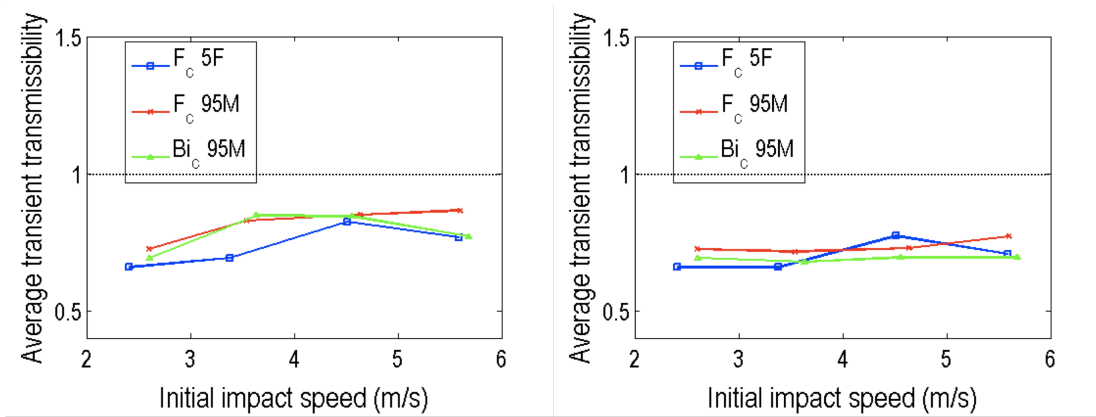


Figure 5.20: Average transient transmissibility ATT1 and ATT2 versus initial impact speed.

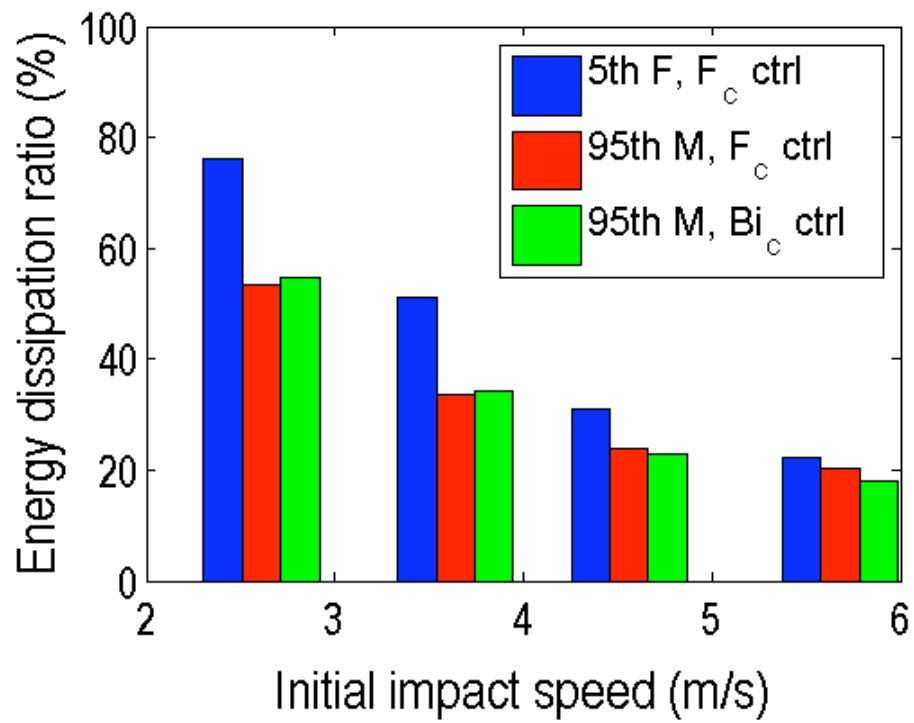
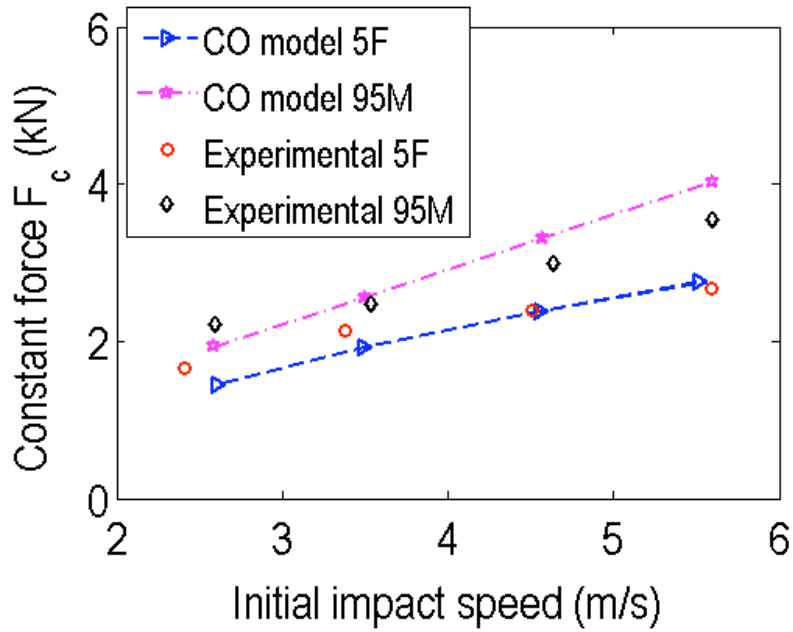
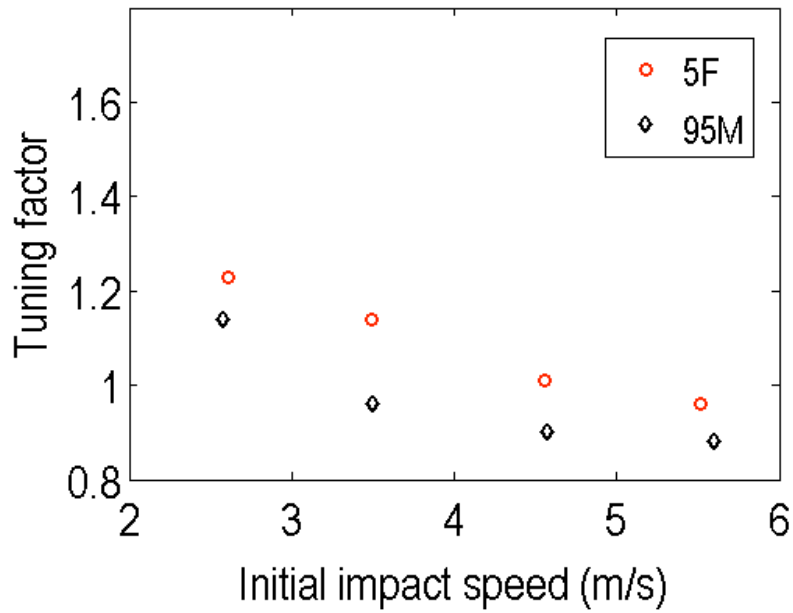


Figure 5.21: Energy dissipation ratio versus initial impact speed.

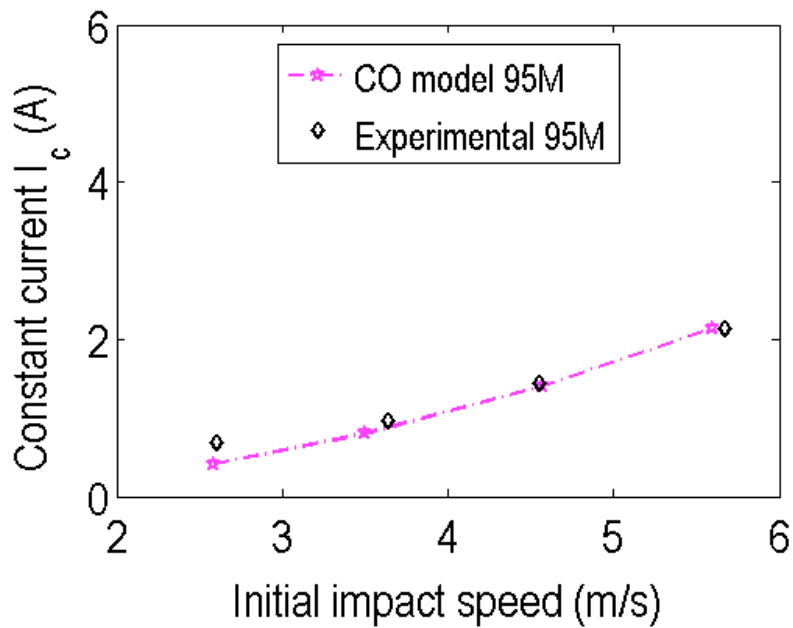


(a) constant stroking force or F_c control

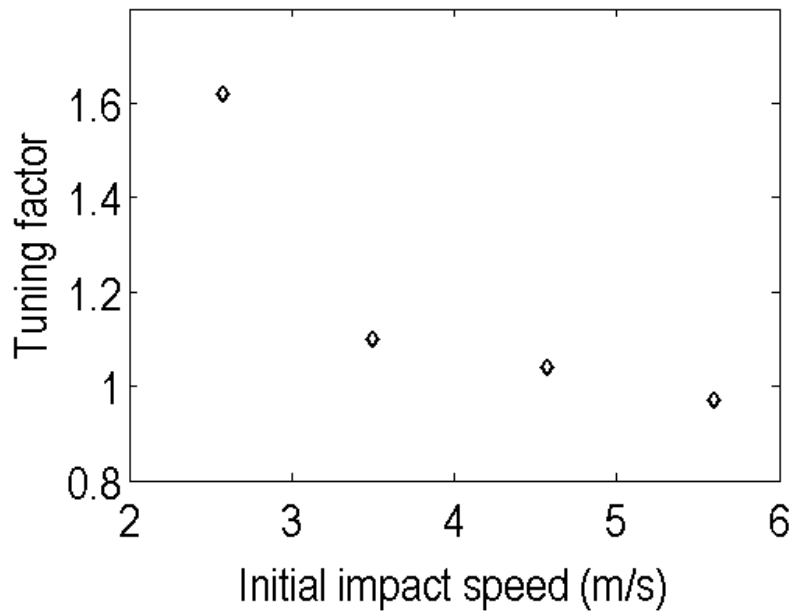


(b) tuning factor for constant stroking force or F_c control

Figure 5.22: Comparison of reference control inputs from CO model simulation with experimental control inputs from sled test as well as the tuning factor for constant stroking force or F_c control.

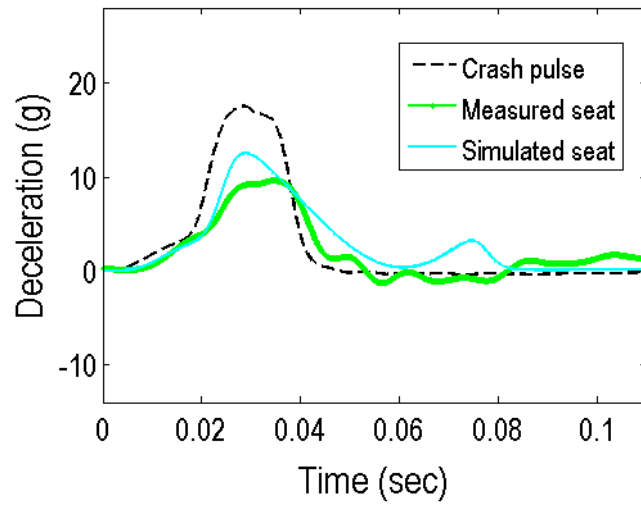


(a) constant Bingham number or Bi_c control

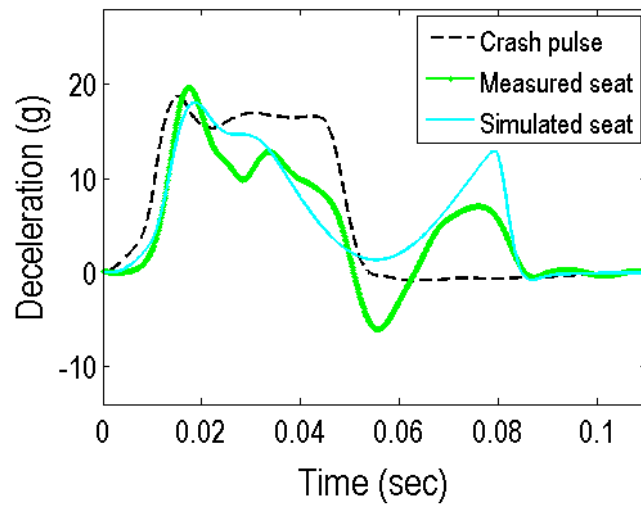


(b) tuning factor for constant Bingham number or Bi_c control

Figure 5.23: Comparison of reference control inputs from CO model simulation with experimental control inputs from sled test as well as the tuning factor for constant Bingham number or Bi_c control .

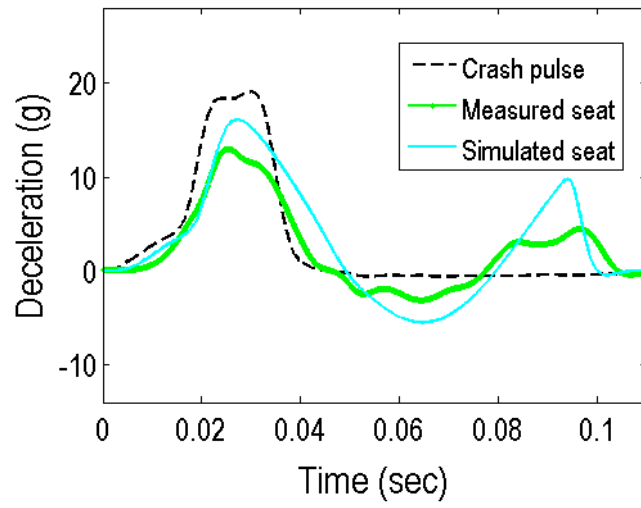


(a) 2.6 m/s

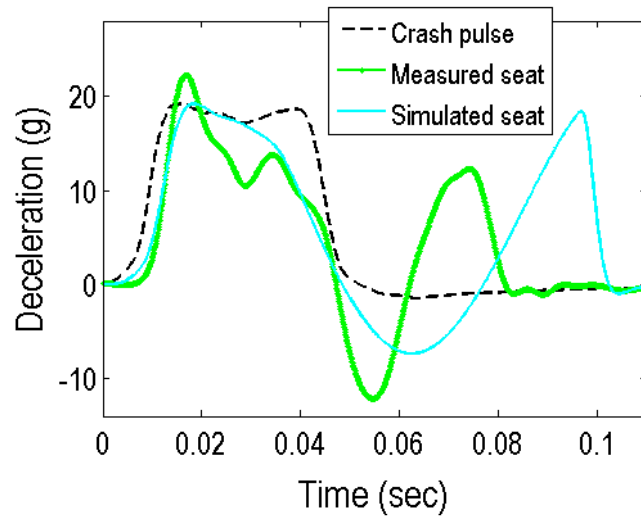


(b) 5.6 m/s

Figure 5.24: Simulated seat deceleration from CO model and comparison with measured data for 5th female under F_c control.

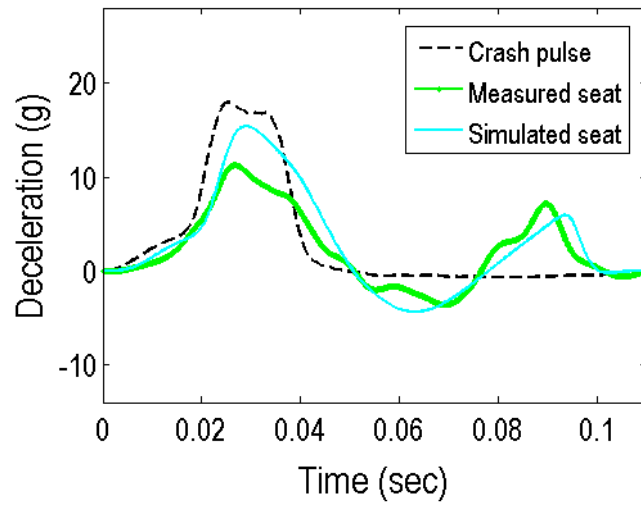


(a) 2.6 m/s

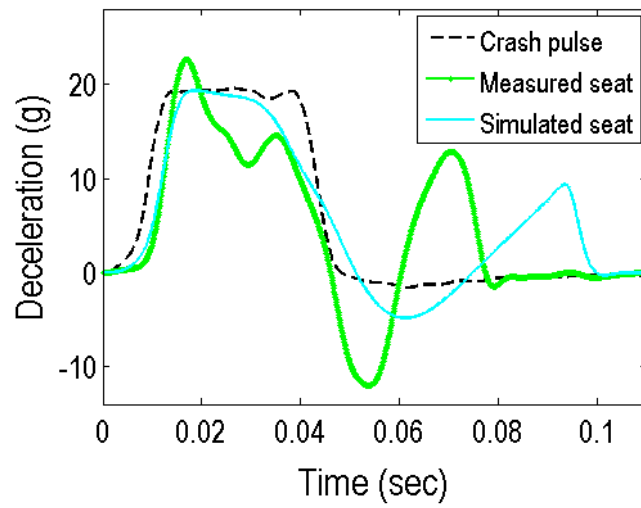


(b) 5.6 m/s

Figure 5.25: Simulated seat deceleration from CO model and comparison with measured data for 95th male under F_c control.



(a) 2.6 m/s



(b) 5.6 m/s

Figure 5.26: Simulated seat deceleration from CO model and comparison with measured data for 95th male under Bi_c control.

Chapter 6: Conclusions and Future Work

In this research, two major tasks were accomplished.

The first task focused on developing and experimentally validating an effective nonlinear MREA model (BPM model) for MREAs under high speed impact conditions. It was shown that the MREA model is capable of: 1) characterizing MREA performance for high speed operation range (0 – 5 m/s); 2) serving as an analytical model to design MREA dimensions for various MREA configurations and 3) describing MREA dynamic behavior in the time domain to enable feasible MREA control for high speed impact applications.

The first task also focused on developing and utilizing the BPM mode of an MREA for an adaptive magnetorheological sliding seat (AMSS) system, which was designed, fabricated and drop tested up to a nominal drop speed of 5 m/s. The measured MREA performance and its dynamic behavior in the time domain were well described by the BPM model.

The second task tackled the proof-of-concept investigation of an adaptive magnetorheological sliding seat (AMSS) system in a general ground transportation vehicle utilizing the controllability of MREAs to mitigate impact load imparted to the occupant in the event of a low speed frontal impact (up to 15 mph). In contrast to a traditional seat which is fixed to the vehicle floor, the seat in the AMSS system is connected to the vehicle floor via a suspension system and so is able to slide forward during a frontal impact, thereby stroking MREA(s) to dissipate all or part of the impact energy. The “adaptive” aspect of the sliding seat system implies that the

MREA in the seat system can be controlled to vary the stroking load as a function of initial impact speed and payload mass to achieve “soft-landing” (seat comes to rest after utilizing all available stroke) so as to minimize the impact load imparted to the payload. The investigation was carried out through system modeling, simulation and experimental verification.

First, the AMSS system was described using two modeling approaches. The first approach treated the seat and the occupant as a single rigid mass and the whole sliding seat system was depicted as a single-degree-of-freedom (SDOF) rigid occupant (RO) model. In the second approach, the occupant was lumped into three body parts, the head, upper torso and pelvis, and for simplicity the neck and limbs were neglected. The occupant interacted with the seat through the shoulder and lap belts, which were modeled as springs with constant stiffness. Thus, the second model was a multi-degree-of-freedom (MDOF) compliant occupant (CO) model. Two control algorithms were proposed in order to minimize the impact load of the payload based on the “soft-landing” objective, that is, to bring the payload to rest while utilizing all available MREA stroke. The first control algorithm, called constant Bingham number or Bi_c control, is essentially constant current control scheduled on impact velocity, and is suitable for implementation when piston velocity feedback is unavailable. The second control algorithm, called constant stroking load control or F_c control, is well suited for the situation when piston velocity can be measured during the impact event and used as a feedback variable. To simplify the analysis, the MREA behavior in the seat system model was characterized by a simple Bingham-plastic model. The crash pulse was assumed to be a 20 g rectangular deceleration pulse with

a duration depending on the prescribed initial impact speed. Governing equations for both models were derived: analytical solutions (control inputs) for the control algorithms in the RO model, but in the case of the CO model, numerical solutions were computed due to the complexity and nonlinearity of the CO model. Therefore, numerical techniques were developed to find the solutions for the control algorithms for the CO model.

Using the developed seat system models and control algorithms solutions, numerical simulations were conducted with assumed system and MREA parameters for initial impact speed up to 7 m/s (15.7 mph) to analyze the system response and performance. Three types of occupant were examined – 5th female, 50th male and 95th male for each initial impact speed. Transient response of the payload under each control algorithm in both models for sample cases showed that the impact load imparted to the payload was significantly mitigated compared to the case of a fixed seat. In addition, simulated transient behavior of the MREA demonstrated that the “soft-landing” control objective was successfully achieved – the payload comes to a rest while fully utilizing the 2” of available stroke – by applying the control inputs of either of the two control algorithms. The simulated peak loads of the payload and the energy dissipation ratio (defined as the ratio of dissipated energy to the payload initial kinetic energy) for various occupant types at various initial impact speeds were obtained and compared with those of the fixed seat. It was shown that for all examined occupant types (5th female to 95th male) and initial impact speeds (up to 7 m/s), the AMSS system was able to substantially mitigate the peak load transmitted to the occupant.

A prototype sliding seat system was then built. To determine the solutions (control inputs) of the control algorithms for the prototype seat system in a similar way as we did for the system model analysis, an accurate mathematical model for the prototype seat system was developed and its parameters were identified and verified experimentally. This was done by sled testing the prototype seat system under passive or uncontrolled mode in the GM R&D Center, that is, no controller was integrated into the system and the MREAs operated under pre-selected constant current level. Using the collected data and experimentally identified MREA characteristics, both the RO model and the CO model were examined to describe the prototype seat system behavior. The assumed spring stiffnesses of the shoulder and lap belts in the CO model were identified using the least squared error minimization method by minimizing the error between the predicted and measured transient seat deceleration. The other system parameter values were kept unchanged since they were obtained based on data obtained using a test dummy. It was shown that the modeling results of the CO model correlated well with the measurements during the impact period, while the RO model was not nearly as successful. Therefore, the CO model was experimentally justified as the best model to describe the prototype seat system behavior.

Utilizing the CO model of the prototype seat system, the control inputs (called reference control inputs) for the control algorithms for the prototype sliding seat system were determined using a similar numerical procedure as was adopted for the CO model in the control analysis of the AMSS system. A prototype controller was formulated using the DSPACE-MATLAB/SIMULINK real time control environment

for each control algorithm. The prototype seat system with the integrated controller was sled tested for the 5th female and 95th male for initial impact speeds up to 5.6 m/s. Due to modeling error and variations in initial impact speed and crash pulse in each test compared to the reference cases, an empirical tuning factor was used to find the real control input (called the experimental control input) that enabled the prototype seat system to achieve the “soft-landing” control objective at each tested initial impact speed in the real sled test. The experimental results demonstrated that the control algorithms were successfully implemented and were able to bring the seat to a rest at 2” stroke. Also, analysis of the transient transmissibility and the energy dissipation ratio showed that the AMSS system controlled by either of the two control algorithms can effectively reduce the impact load imparted to the seat, especially at lower initial impact speeds. Moreover, it was shown that the system performance under either control algorithm was similar. Finally the effectiveness of the CO model in predicting the control inputs was demonstrated by comparison of the reference control inputs with the experimental control inputs that used a tuning factor.

In the following sections, the significant contributions of this research are elaborated. Recommendations for future work on generic MREA modeling, design for high speed impact applications, and improvements of the AMSS system design methodology in ground vehicles are briefly discussed.

6.1 MREA Modeling and Design Under High Speed Impact Conditions

To the best knowledge of the author, this work is the first known in-depth theoretical and experimental investigation in the MREA modeling and design for MREAs under high speed (up to 6.7 m/s) impact conditions. Also, the developed

nonlinear analytical MREA model (BPM model) and the MREA design strategy for high speed impact applications were both experimentally validated. This new model has advanced the understanding of MR fluid behavior in high Reynolds number ($Re \sim 2000$) flows and facilitated the design of MREAs for these impact applications.

The BPM model took a novel approach to explain the MREA passive force-velocity squared behavior in drop tests at these speeds. Such behavior had been observed in the literature, but no experimentally validated analysis of MREA behavior under such drop tests had been developed. The BPM model integrated theory of minor losses from pipeline hydraulics into our previously established Bingham-plastic nonlinear flow model (BP model) and showed great success in describing the MREA passive force vs. velocity squared behavior because predictions agreed well with experimental data. The detailed development and analysis of the Bingham-plastic nonlinear flow model (BP model) published previously is included as appendix B for reference. The BP model extended the modeling of MREA behavior from the laminar flow range ($Re \leq 2000$) to the higher Reynolds number flow range by including transitional and turbulent flows ($Re > 2000$). Moreover, it was shown that high Reynolds number flows would greatly reduce the dynamic range of MREAs. We also constructed an effective design strategy to ensure the target MREA design would operate in the laminar flow range in order to obtain a desired dynamic range over velocity range of operation for the MREA. Later, based on the work of BP model and reported experimental MREA behaviors under high speed drop tests, the BPM model was formulated to correct the deficiency of BP model in that, in addition to turbulent flow effect, minor losses effect were also pronounced in high Reynolds

number flows and must be considered. It was shown that the BPM model was able to predict the MREA performance with prior knowledge of the fluid properties and the MREA geometric profile and dimensions, given good estimates of applicable minor loss coefficients.

Utilizing the BPM model in an inverse way, once the MREA geometric profile (usually can be determined when the basic configuration of the MREA design has been sketched out) and the fluid properties are given, the geometric dimensions of the MREA design can be obtained. The BPM model was developed in a general way and was capable of designing MREAs of any configuration. In this work, for simplicity and without loss of generality, an MREA with annular duct type MR valve was analyzed using the BPM model and an effective design strategy was proposed. Using the design strategy, an MREA was designed and the geometric dimensions of the design parameters were determined. To account for possible inaccurate estimations of empirical minor loss coefficients from published handbook values, the MREA performance (force vs. velocity relation) was also examined via CFD simulation of the flow field in the MREA using the determined geometric dimensions from the BPM model before the MREA was actually manufactured. The CFD approach (using FLOTRAN in ANSYS) proved to be effective in analyzing passive force of the MREA. It was later validated by experiment that, given good estimates of the empirical minor loss coefficients, the BPM model could well predict the MREA performance during the design stage and thus enable an effective MREA design. What's more, the CFD we adopted to predict the MREA performance was shown to be a complementary tool to facilitate MREA design. When the CFD results correlated

well with the BPM prediction, the accurate estimates of minor loss coefficients were assured. If the CFD results were not well correlated with the BPM prediction, then it would imply that estimates of the minor loss coefficients were insufficiently accurate.

Furthermore, to make MREA control in a high speed impact condition feasible, the MREA transient behavior in the time domain must be well represented by the model. To describe the MREA dynamic force (force-time history) under drop impact, an unsteady transient analysis was carried out. The results showed that inertia force only accounts for a small fraction of the total force and the dynamic force predicted by the BPM model agreed well with the measurements. Thus, we experimentally proved that the BPM model not only worked well for predicting the MREA performance during design stage but also was able to capture the MREA transient behavior during the impact period without loss of accuracy. This established a fundamental modeling basis to enable integrating MREAs in adaptive structures or systems intended for high speed impact loadings to fulfill adaptive missions via various control algorithms. Otherwise, it would be difficult if not impossible to effectively control MREAs to meet control objectives.

In a summary, several useful conclusions and findings in the MREA modeling and design are:

- (1) The BPM model can accurately predict an MREA passive force (field-off) for both low speed excitations and high speed impact conditions and is a useful tool for an effective MREA design. It can also accurately predict the field-on force for flow conditions for $Re \leq 2000$. For higher Re flows (particularly $Re > 2000$), further study is needed to understand the behavior of the MR yield stress under

high Reynolds number flows and minor loss effects in order to more accurately predict the MR field-on force.

- (2) Whenever possible, the MREA should be designed to function in laminar flows over the desired piston speed range to avoid significant reduction in MR yield force or dynamic range when high Reynolds number ($Re > 2000$) flows are induced.
- (3) The BPM model can be directly used to predict MREA dynamic force under high speed impact conditions so that control of an MREA in such situations is feasible. It can be readily integrated in the system model to facilitate control algorithm design, analysis, numerical simulation and final controller implementation in the real world.

6.2 MREA Performance Evaluation for High Reynolds Number Flows Via High Speed Drop Test

In previous reported work (Ahmadian and Norris, 2004; Browne *et al.*, 2009), MREA performance investigation under high speed impact loadings was typically done via drop test. Though we took advantage of the drop tower test facility at the GM R&D center and adopted the same experimental method to evaluate our MREA performance, we developed a more effective analysis of the experimental data to evaluate the MREA performance for high Reynolds number flows.

In the reported high speed MREA performance data by other groups, the peak MREA force was simply correlated with the nominal impact or drop speed rather than the MREA piston velocity itself. We experimentally observed that the nominal drop speed was not equal to the measured peak piston velocity. In our early work (Mao *et*

al. 2007b, 2008), we also used the nominal drop speed to correlate with the average MREA force during the impact period. However, as our understanding of the MREA behavior under high speed impact loadings advanced, we instead correlated the peak MREA force with the measured peak piston velocity to characterize the experimental MREA force vs. velocity behavior, instead of correlating MREA peak force with nominal drop speed. This approach was later justified by the transient MREA force predicted by the BPM model agreed well with the measured MREA dynamic force during the drop tests.

Also, the SSMREA in the AMSS system used the same approach for performance prediction in the design stage and performance evaluation in terms of prototype drop test data. The formula established in the MREA performance evaluation using the peak force and peak piston velocity pairs was then used to model the MREA dynamic behavior in the AMSS system for determination of control inputs using the CO model and controller implementation in the AMSS system sled test. The drop test and sled test data both supported the use of piston velocity over drop speed.

6.3 Modeling and Control Algorithm Design of an Adaptive Magnetorheological

Sliding Seat (AMSS) System

This research represents the first known theoretical and experimental investigation of utilizing adaptive controllability of MREAs into a horizontally sliding seat system to mitigate impact load imparted to a payload mass in a ground vehicle in the event of a low speed frontal impact (typically less than 15 mph). At the theoretical level, the sliding seat system was analyzed using two modeling approaches and two control algorithms were designed to bring the payload (occupant plus seat)

mass to a stop using the available stroke, while simultaneously accommodating changes in impact velocity and occupant mass ranging from a 5th percentile female to a 95th percentile male.

First, two mathematical models of the MREA integrated sliding seat system were developed and governing system equations were presented. The first approach was a rigid occupant (RO) model, which assumed that the payload mass comprised the seat and occupant mass. Second, to assess the coupling effects of a compliant occupant, the system was represented as a multi-degree-of-freedom (MDOF) compliant occupant (CO) model by incorporating a simplistic biodynamic model into the analysis, consisting of lumped mass and stiffness corresponding to pelvis, torso, and head. (Note that leg and arm masses were neglected).

The control objective for the sliding seat system was established in order to minimize the impact load transmitted to the payload by maximizing the energy dissipated by the MREA based on the generic “soft-landing” criterion (Wereley and Choi, 2008), that is, through control of the MREA during the impact event, the sliding seat can be brought to rest while fully utilizing the available stroke (here, 2”). Two simple control algorithms were formulated to achieve the control objective: (1) the constant Bingham number or Bi_c control where the only measurement needed was the initial impact speed and the occupant mass, and (2) the constant force or F_c control where initial impact speed, occupant mass and velocity feedback were required. For the rigid occupant case, analytical solutions of the control inputs to monitor the MREA as well as the system dynamic response and the MREA response during the impact period were obtained. For the CO model, an iterative numerical

technique was proposed to obtain the control inputs. Once the control inputs determined, numerical simulations can be performed to obtain the dynamic responses of seat, occupant and MREA.

To visualize the system dynamic behavior and the control process of the MREA and to foresee the superior performance of the AMSS system, numerical simulations were carried out for both rigid and compliant occupant models with assumed typical system parameter values. Three types of occupant were examined - the 5th percentile female and the 50th and 95th percentile males - for initial impact speeds of up to 7 m/s under the impact loading of a rectangular crash pulse whose magnitude was 20 *g* and duration was dependent on the prescribed initial impact speed.

The simulation results showed that the impact load imparted to the occupant was significantly reduced using the AMSS system with either control algorithm compared to a traditional fixed seat. Both control algorithms provided comparable mitigations for various occupant types over the initial impact speed range examined. It also revealed that both control algorithms were relatively easy to implement in practice. The constant Bingham number or Bi_c control is much simpler because once the initial impact speed and the occupant weight are sensed the applied current to the MREA is one-time determined and kept unchanged for the whole impact period. On the other hand, the F_c control requires additional MREA piston velocity feedback and the applied current to the MREA needs to be continuously monitored to maintain a constant stroking force. Nevertheless, the monitoring of the current was straightforward and easily accomplished.

Some of the highlights of this theoretical investigation are summarized below:

- (1) The generic “soft-landing” idea was adopted and utilized in this application context to develop two control implementations, constant Bingham number control and constant stroking load control.
- (2) The AMSS system theoretically demonstrated its potential superior performance in enhancing occupant protection in the event of low speed frontal impacts for ground vehicles.

6.4 Experimental Verification of the AMSS System and the CO Model

This experimental verification of the AMSS system is not only the first known experimental investigation of such a particular system but also the first known experimental exploration of MREA adaptive systems that was physically prototype tested with controller integrated for impact applications. As mentioned before, almost all of the studies ongoing in MREA impact applications, especially in the context of helicopter crew seat system in harsh landing, with control algorithms integrated in the system including those based on “soft-landing” optimal control criterion were limited to simulation. However, in this work, we built the prototype adaptive magnetorheological sliding seat system with an integrated controller and conducted sled tests in the laboratory. We successfully verified the feasibility of the AMSS system, the control algorithms and the effectiveness of the CO model during these experiments.

First, sled test of the prototype seat system under pre-selected constant current levels (passive mode) were carried out for nominal initial impact speeds of 2.6, 3.5, 4.5 and 5.6 m/s at the GM R&D center to study the system behavior and to establish a suitable system model. Using the passive mode test data, the stiffness of the lap belt

and the shoulder belt (K_{sb} and K_{lb}) were statistically identified and the CO model was able to adequately describe the dynamic behavior of the sliding seat during the impact period. In addition, it was found that the variation of stiffness of the lap belt and shoulder belt (K_{sb} and K_{lb}) between the mean value and respective identified value for various tested cases did not substantially affect the dynamic behavior of the seat system (while it did influence its behavior during the occupant bouncing back period).

Then the reference control inputs of the prototype seat system for each control algorithm at each initial impact speed were determined in a statistic means through numerical simulation using the CO model along with the identified constant stiffness for K_{sb} and K_{lb} as well as the collected crash pulses in the passive mode test. With these pre-determined control inputs, the prototype AMSS system with controller integrated was sled tested. For the F_c control, the 5th female and 95th male were examined. For the Bi_c control, only the 95th male was tested. To account for modeling error and small variations of initial impact speed and crash pulse in each test, empirical tuning factors were used to adjust the reference control input at each initial impact speed to obtain the control inputs for the prototype AMSS system to successfully achieve the “soft-landing” control objective in actual tests. These identified control inputs in the real world were referred to as the experimental control inputs to distinguish them from the reference control inputs designed using the CO model.

It was shown that with the experimental control inputs, the control algorithms could successfully bring the sliding seat to a rest using 2” full stroke. Therefore, the

feasibility of the conceptual AMSS system was experimentally proved and the two proposed control algorithms were verified to be able to control the AMSS system to achieve the control objective for various occupant types and various initial impact speeds. Quantitative analysis of the measured seat decelerations showed that the impact load imparted to the seat was significantly reduced, especially at lower initial impact speeds, in terms of the peak transient transmissibility (PTT2) and the average transient transmissibility (both ATT1 and ATT2) and the energy dissipation ratio. Thus, the effectiveness of the AMSS system in mitigating the impact load imparted to the payload was experimentally demonstrated. What's more, the 5th female was shown to receive better impact load mitigations than the 95th male at same initial impact speed. Besides, similar to the results obtained in the CO model simulation, the two control algorithms were turned out to offer comparable capabilities in alleviating the impact load imparted to the payload, although Bi_c control was much simpler to implement because it only used the initial impact speed and the occupant mass information, unlike the F_c control requiring piston velocity feedback.

Lastly, the effectiveness of the CO model in predicting the reference control input was illustrated by the good comparison between the reference control inputs pre-determined by the CO model and the experimental control inputs identified from the sled test. It was shown that the CO model was a relatively simple yet useful and effective analytical model to pre-determine the reference control inputs for both control algorithms.

Another important and meaningful finding was that the two control algorithms were robust to uncertainties in the variations of actual initial impact speed and crash

pulse. These algorithms were shown to be effective with only minor performance degradation if the reference control inputs pre-determined from the CO model simulation were used as the control inputs for the implemented system even when the empirical tuning factor is unavailable.

Thus, it was experimentally verified that the AMSS system with the F_c control and Bi_c control was feasible, effective and relatively easy to implement in practice. The CO model was simple yet experimentally proved to be effective and useful to facilitate control algorithm design and controller implementation.

6.5 Future Work

Though this research has successfully demonstrated the feasibility and benefits of the AMSS system in mitigating the impact load imparted to the payload while simultaneously accommodating changes of occupant mass and initial impact speed in the event of low speed front impacts for general ground vehicles, many issues remain to be addressed before this technology can be fully understood. The following section identifies some key challenges and gives suggestions to advance the state of the art in employing MREAs for 0 – 15 mph impact applications.

6.5.1 MR Yield Stress For High Reynolds Number Flows

We have shown that the BPM model can accurately characterize the MREA passive (field-off) force for flow conditions ranging from low speed laminar flows to near turbulent flows ($Re \sim 2300$). It can also successfully interpret the MREA performance for field-on cases typically for $Re < 2000$. However, for higher Reynolds number flows ($Re > 2000$), the field-on MR yield stress was observed to depart from

these predictions in some cases. The MR yield stress may be a function of Reynolds number for turbulent flows. Though it was suggested that design of an MREA's dimensions to ensure $Re < 2000$, operating MREAs with turbulent flow may not be entirely avoidable in practice due to device volume constraints, especially for high speed impact applications of MREAs. Therefore, there is a need to improve the modeling capability of the field-on force for turbulent flows.

6.5.2 Compliant Occupant Model Improvement

Though we have shown the effectiveness of the current CO model in predicting the control inputs, the CO model demonstrated its limitation in capturing the transient seat behavior when the controller integrated into the seat system as seen in Figures 5.24-5.26. This would impose estimation error of the control inputs.

Nevertheless, in this preliminary proof-of-concept study of the AMSS system, the simple CO model developed here are acceptable and have been shown to work well in implementing the control algorithms in the prototype AMSS system with the help of empirically estimated tuning factors. However, the next step should be a higher fidelity occupant model to obtain more accurate and robust prediction of control inputs for control algorithms. One possibility might be a higher order lumped parameter model of the occupant, or perhaps an FEA or MADYMO-based test dummy model.

Using a higher fidelity model, the accuracy of the estimation of the control inputs for the control algorithms proposed in this research, or control gains for new control algorithms, as well as the modeling accuracy of seat and occupant transient behaviors, would largely increase.

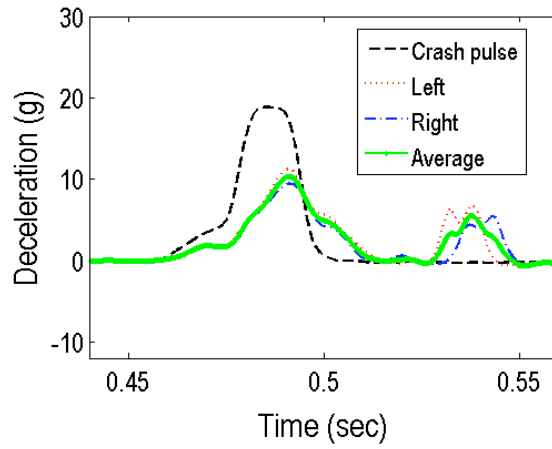
Appendix A: Measured seat deceleration and crash pulse for full stroke cases and zero (or nearly zero) stroke cases.

Note that in Figures A.1-A.6, the relatively large spikes appearing at the beginning of the impact period (first peaks) in the seat decelerations for some cases with zero strokes, especially at higher initial impact speeds, resulted from the metal-to-metal impact effect between the relatively loose fit between the pin and rod eye connection between MREA and the sliding seat. As shown in Figure A.7, when the fit is loose, the metal-to-metal impact effect cause an abnormal large spike (first peak) in the seat deceleration, which is much greater than the crash pulse and the second peak. However, by adding shims between the pin and rod eye, the large spike was minimized and there was only one peak showing up.

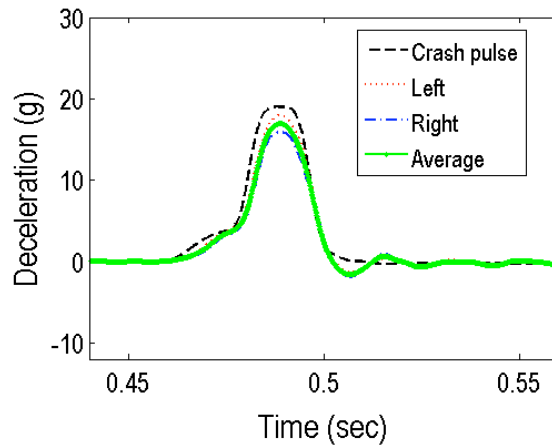
Although this metal-to-metal effect can be greatly alleviated at lower initial impact speed (i.e. 2.6 m/s) by adding shims between the pin and rod eye, it could not be avoided considering the fixture between the MREA and sled platform in the experimental setup. When the MREA force became large and no or very little stroking was enabled, this effect was pronounced more and manifested itself as the large first peak in the seat deceleration, especially at higher initial impact speed and with larger occupant mass, such as at initial impact speed of 3.5 m/s and applied current of 3.0A (with zero stroke) for the 95th male.

Nevertheless, as observed in Figure A.7, the second peak in the seat deceleration is seen to more genuinely reflect the real peak of the seat deceleration. Therefore, for the measured seat decelerations in the passive mode sled tests shown in this appendix

and in Chapter 4, as well as the measured seat decelerations in the later sled tests of the AMSS system with controller integrated in Chapter 5, the second peaks are deemed as the genuine seat deceleration peaks.

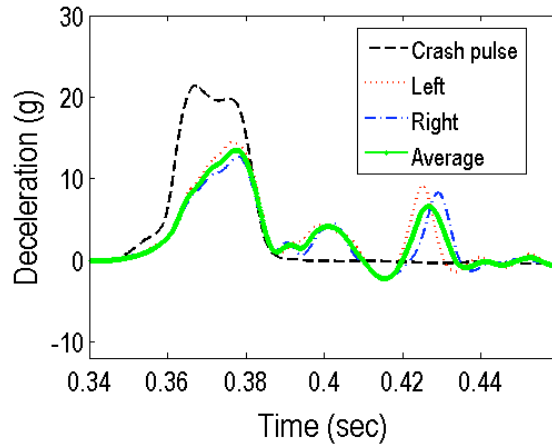


(a) full stroke case (0.0 A)

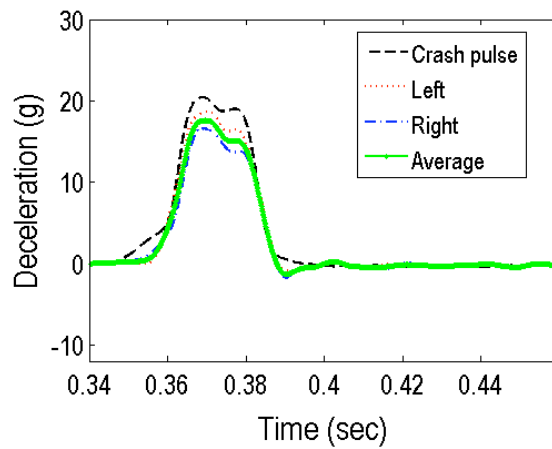


(b) zero stroke case (2.0 A)

Figure A.1: Measured seat deceleration and crash pulse at nominal initial impact speed 2.6 m/s for 5th female.

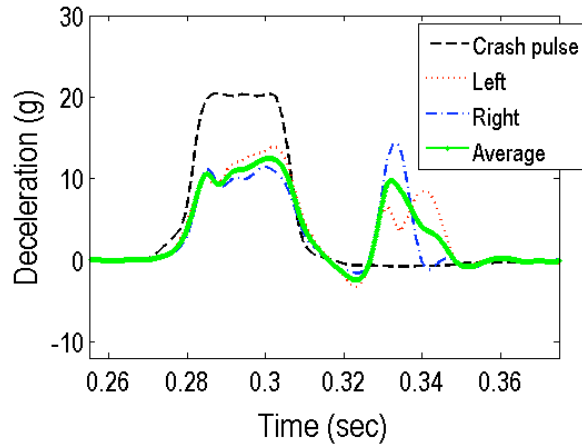


(a) full stroke case (0.0 A)

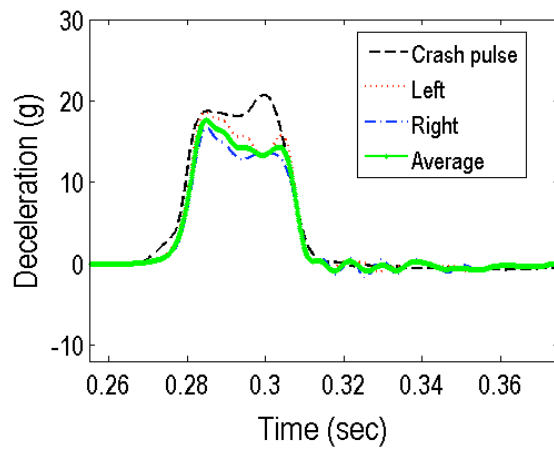


(b) zero stroke case (2.0 A)

Figure A.2: Measured seat deceleration and crash pulse at nominal initial impact speed 3.5 m/s for 5th female.

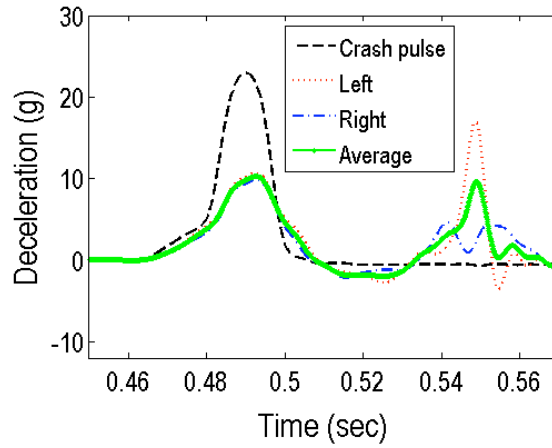


(a) full stroke case (0.5 A)

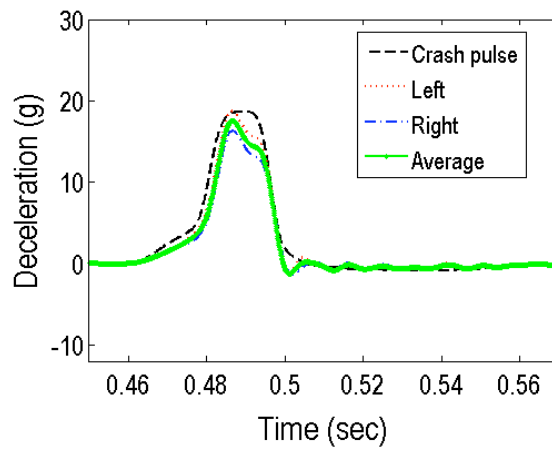


(b) zero stroke case (2.0 A)

Figure A.3: Measured seat deceleration and crash pulse at initial impact speed 4.5 m/s for 5th female.

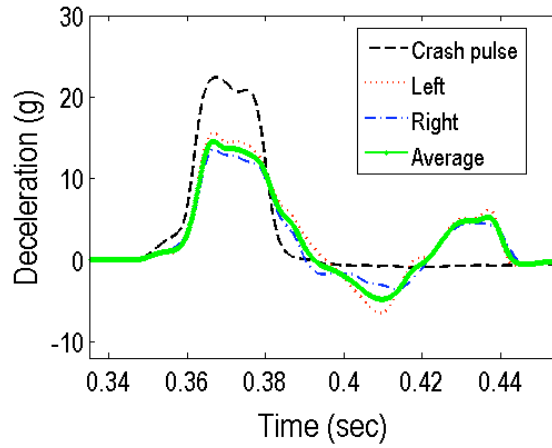


(a) full stroke case (0.5 A)

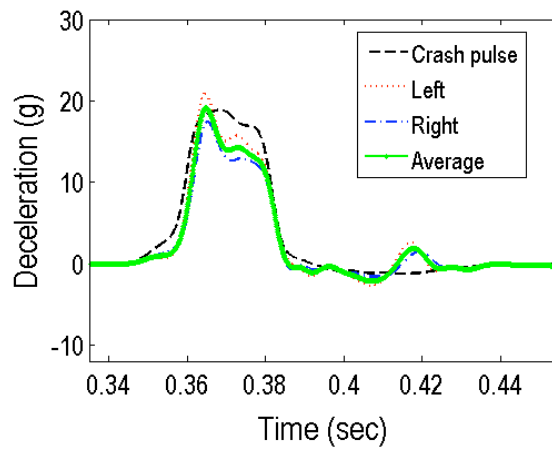


(b) zero stroke case (3.0 A)

Figure A.4: Measured seat deceleration and crash pulse at initial impact speed 2.6 m/s for 95th male.

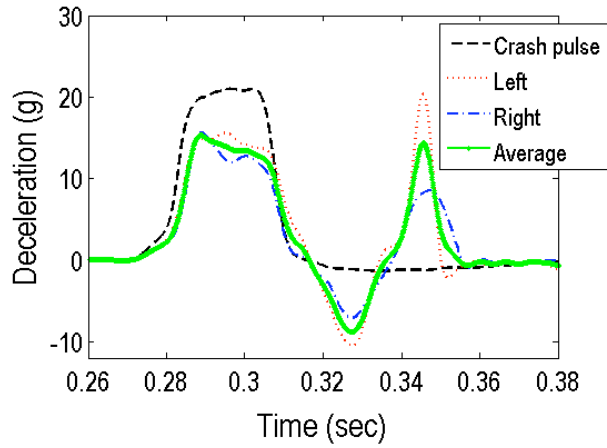


(a) full stroke case (0.8 A)

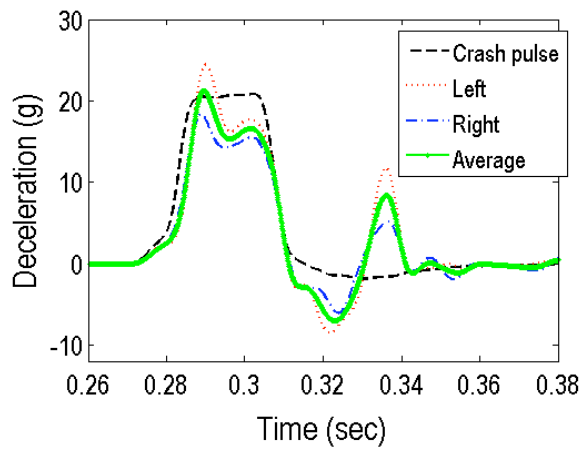


(b) zero stroke case (3.0 A)

Figure A.5: Measured seat deceleration and crash pulse at initial impact speed 3.5 m/s for 95th male.

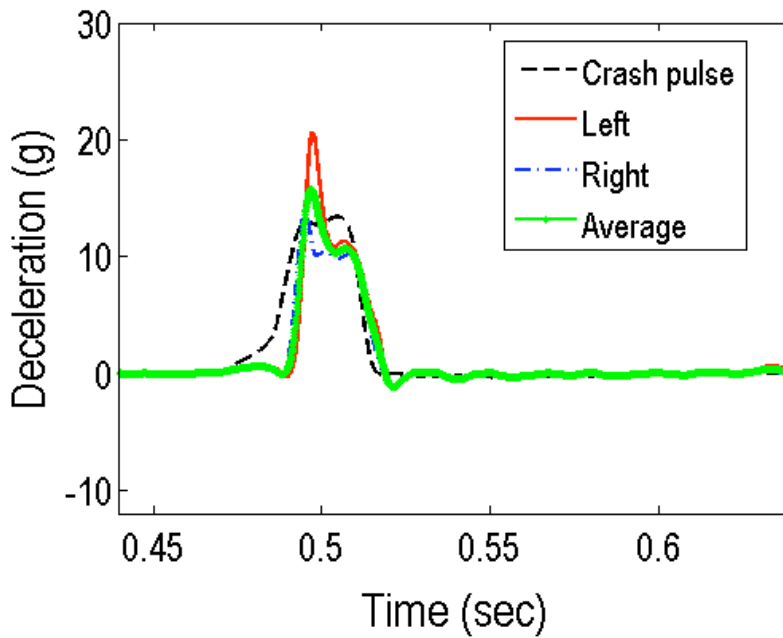


(a) full stroke case (1.0 A)

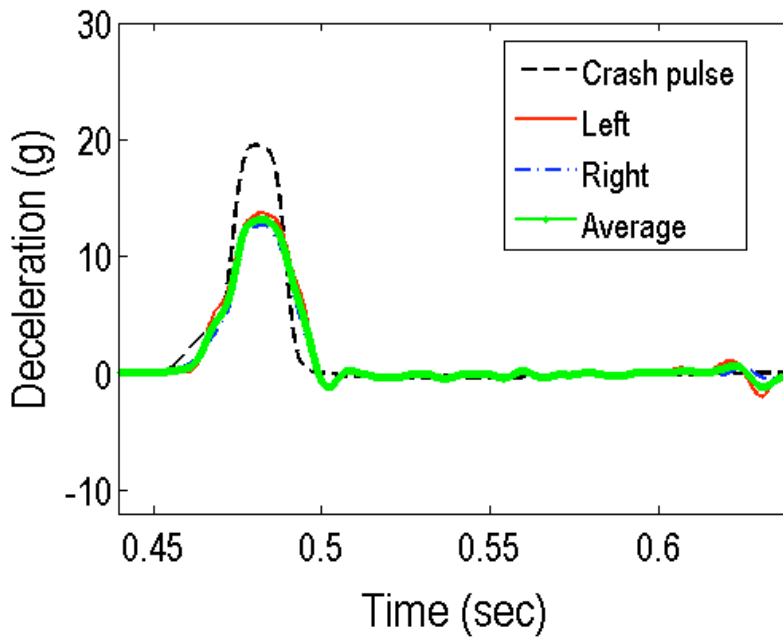


(b) zero stroke case (3.0 A)

Figure A.6: Measured seat deceleration and crash pulse at initial impact speed 4.5 m/s for 95th male.



(a) loose fit (2.6 m/s, 1.0 A)



(b) improved fit by adding shims (2.6 m/s, 1.0 A)

Figure A.7: Illustration of the influence of the metal-to-metal impact effect on the measured seat deceleration (i.e. large first peak appearing at the beginning moment of the seat deceleration) due to a loose fit between the pin and rod eye.

Appendix B: Effective design strategy for a magnetorheological damper using a nonlinear flow model*

Min Mao, Young-Tai Choi, and Norman M. Wereley

Department of Aerospace Engineering
University of Maryland, College Park, MD 20742 USA

ABSTRACT

This paper presents an effective design strategy for a magnetorheological (MR) damper using a nonlinear flow model. The MR valve inside a flow mode MR damper is approximated by a rectangular duct and its governing equation of motion is derived based on a nonlinear flow model to describe a laminar or turbulent flow behavior. Useful nondimensional variables such as, Bingham number, Reynolds number, and dynamic (controllable) range are theoretically constructed on the basis of the nonlinear model, so as to assess damping performance of the MR damper over a wide operating range of shear rates. First, the overall damping characteristics of the MR damper are evaluated through computer simulation and, second, the effects of important design parameters on damping performance of the MR damper are investigated. Finally, the effective design procedure to meet a certain performance requirement is proposed. A high force-high velocity damper is fabricated and tested, and the resulting model and design procedure are experimentally validated.

* Published in Proceedings of SPIE, 5760, pp. 446-455, 2005.

Keywords

Magnetorheological (MR) damper, nonlinear, nondimensional, turbulent, Reynolds number

B.1 Introduction

With the high increasing interest in the application of various kinds of electrorheological (ER) and magnetorheological (MR) dampers, substantial effort has been devoted to the development and discussion of theoretical models and analytical methods¹⁻¹². Generally these models are classified into two categories: (1) quasi-static or steady state models, and (2) dynamic models. Quasi-static models are usually based on Bingham plastic models or Hershel-bulkley models, and do not consider the hysteresis phenomenon in the force-velocity behavior of the ER/MR damper. Phillips¹ employed the Bingham model of ER/MR fluids and developed a nondimensional analysis as well as the corresponding equations to determine pressure drop of ER/MR fluid flowing through a rectangular duct. Gavin *et al.*² refined this analysis using an axi-symmetric model to better describe ER/MR damper quasi-static behavior. Wereley *et al.*³⁻⁵ developed similar quasi-steady models with different nondimensional variables and assumed a constant yield stress. To include shear thinning and thickening effects, Wereley *et al.*⁷ and Wang *et al.*⁸ utilized the Hershel-Bulkley model to predict the fluid flow in a rectangular duct and a circular pipe respectively. To more precisely describe practical ER/MR damper hysteretic characteristics of force-velocity relations, a variety of dynamic models were explored and reported in the literature. Stanway *et al.*⁹ derived a dynamic model by taking account of ER fluid inertia and compressibility. Spencer *et al.*¹⁰ and Yang¹¹ proposed

a phenomenological model for MR dampers based on the Bouc-Wen hysteresis model. Recently, Wereley *et al.*¹² constructed an Eyring-plastic model on the basis of an Eyring rheological model by combination of simple nonlinear functions. The Eyring-plastic model can capture practical damper responses quite well, particularly in both the pre-yield and the post-yield states.

The above models are very useful and often adequate for most commercial controllable fluid device design and analysis¹³⁻¹⁴. Particularly, the Bingham plastic quasi-static model, because of its simplicity, serves as an excellent starting point in the design of MR fluid-based devices. For most applications, the Reynolds number is small enough and laminar flow prevails so that the viscous Newtonian pressure in these quasi-static Bingham plastic analyses is developed on the basis of a linear (laminar) flow model, namely, the viscous pressure drop down the MR valve is proportional to the flow rate. However, if the induced shear rate in the MR valve is high, and under certain conditions, the viscous linear flow model may not be acceptable because of its substantial under-estimation of viscous force in the turbulent flow situation.

Therefore, this paper focuses on firstly developing a dynamic equation for flow mode MR dampers using a nonlinear flow model that can describe the fluid viscous behavior of laminar or turbulent flow depending on the flow status. The pressure drop due to MR fluid yield stress in the Bingham plastic model is left unchanged because the physics of turbulent Bingham flows are not well studied so that MR fluid behavior under turbulent flow conditions is not clear. Secondly, useful nondimensional variables such as Bingham number, Reynolds number, and dynamic range are

constructed and evaluated to assess the damping capacity of the MR damper over a wide operating range of shear rates. With this knowledge, an effective design procedure for a MR damper is proposed. A high force-high velocity MR damper is fabricated and tested, and the resulting model and design procedure are experimentally validated.

B.2 Nonlinear MR Damper Model

A schematic diagram of annular duct type MR valve in a flow-mode MR damper is presented in Fig. B.1. The damping force, F , of the MR damper can be expressed as follows:

$$F = A_p (\Delta P_\eta + \Delta P_\tau) \quad (1)$$

where

$$\Delta P_\eta = f \frac{\rho L V_d^2}{2 D_h} \text{ and } \Delta P_\tau = \frac{2 L \tau_y}{d} \quad (2)$$

Here ΔP_η is the Newtonian pressure drop, ΔP_τ is the pressure drop due to the yield stress of the MR fluid, A_p is the effective piston area, and $A_p = \pi(D_p^2 - D_r^2)/4$, where D_p is the diameter of the piston, D_r is the diameter of the piston rod. τ_y is the yield stress of an MR fluid, d is the gap of the MR valve inside the damper and D_h is the hydraulic diameter, which is used for non-circular valve path. L is the total length of the active area and $L = L_1 + L_2 + L_3$ in this configuration. f is the Darcy friction factor and is chosen depending on the magnitude of the Reynolds number of the fluid flow in the valve.

A flow mode valve in both an axi-symmetric case as well as the approximated parallel plates case was well analyzed by Atkin *et al.*¹⁸ and Kamath *et al.*¹⁹. They

showed that given Bingham fluid behavior, the error in approximating an axisymmetric valve with parallel plates is small when the ratio of gap, d , relative to their diameter, D_b , far less than one ($d/D_b \ll 1$), so that many dampers can be modeled using the parallel plates approximation. For simplicity, in this study, the annular duct in the MR valve inside the piston is approximated as a rectangular duct. As a result, the hydraulic diameter D_h is given by^{15,16}

$$D_h = 2d \quad (3)$$

The friction factor for parallel plates is given by¹⁶

$$f = \frac{96}{\text{Re}_{D_h}} \quad \text{if } \text{Re}_{D_h} \leq 2300 \quad (4a)$$

$$\frac{1}{f^{1/2}} = -1.8 \log_{10} \left[\left(\frac{\varepsilon / D_h}{3.7} \right)^{1.11} + \frac{6.9}{\text{Re}_{D_h}} \right] \quad \text{if } \text{Re}_{D_h} \geq 4000 \quad (4b)$$

where the Reynolds number is defined by

$$\text{Re}_{D_h} = \frac{2\rho V_d d}{\eta} \quad (5)$$

Here, ε is the average pipe wall roughness and assumed to be 0.01mm in this study to represent a smooth condition.

For the transition flow case, that is, a Reynolds number between 2300 and 4000, there is no corresponding defined equation to calculate the friction factor f . In this study, we will use the convex combination¹⁷ to compute f for the transition flow as follows:

$$\begin{aligned} f &= (1 - \alpha)f_{lam} + \alpha f_{turb} \\ &= (1 - \alpha) \frac{96}{2300} + \alpha \frac{1}{\left[1.8 \log_{10} \left[\left(\frac{\varepsilon / D_h}{3.7} \right)^{1.11} + \frac{6.9}{4000} \right] \right]^2} \end{aligned} \quad (6)$$

where

$$\alpha = \frac{\text{Re}_{D_b} - 2300}{4000 - 2300} \quad (7)$$

On the other hand, v_d is the average velocity of the incompressible fluid in the gap of the MR valve and can be expressed in terms of the piston velocity as follows:

$$V_d = \frac{Q}{A_d} = \frac{A_p V_p}{A_d} = \bar{A} V_p \quad (8)$$

where Q is the volumetric flow rate through the valve and here $Q = A_p V_p$, V_p is the piston velocity, A_d is the cross-sectional area of the MR valve gap, $A_d = d \cdot \pi D_b$, and D_b is the effective gap diameter. It is noted that the dimensionless number $\bar{A} = A_p / A_d$ can be used as a fluid velocity amplifying factor. If \bar{A} is large, the fluid velocity in the gap, V_d , is large even though the piston velocity, V_p , may be relatively low. Using Eq. (8), the damping force of the MR damper can be rewritten as follows:

$$F = F_\eta + F_\tau = A_p \left(f \frac{\rho L \bar{A}^2 V_p^2}{4d} + \frac{2L\tau_y}{d} \right) \quad (9)$$

It is noted that the friction factor f in Eq. (9) will be calculated as a function of the Reynolds number of the fluid flow in the valve.

The dynamic range D is defined as the ratio of the total damper force F (it corresponds to the damping force at field-on, F_{on}) to the uncontrollable force F_{uc} (it corresponds to the damping force at field-off, F_{off}) as follows:

$$D = \frac{F_{on}}{F_{off}} = 1 + \frac{F_\tau}{F_\eta} = 1 + \frac{8\tau_y}{f\rho\bar{A}^2V_p^2} \quad (10)$$

Let us define Bingham number^{4,20} as follows:

$$Bi = \frac{\tau_y d}{\eta \bar{A} V_p} \quad (11)$$

Then the relationship between the Bingham number Bi and the Reynolds number Re_{D_h} can be obtained as follows:

$$Bi = \left(\frac{2\rho d^2 \tau_y}{\eta^2} \right) \frac{1}{Re_{D_h}} \quad (12)$$

Finally, the dynamic range D can be represented in terms of the Bingham number and the Reynolds number as follows:

$$D = 1 + \frac{16}{f} \left(\frac{Bi}{Re_{D_h}} \right) \quad (13)$$

Along with the Reynolds number, the dynamic ranges are as follows:

$$D = 1 + \frac{Bi}{6} \quad \text{if } Re_{D_h} \leq 2300 \quad (14a)$$

$$D = 1 + \frac{51.84 Bi \left(\log_{10} \left[\left(\frac{\epsilon / D_h}{3.7} \right)^{1.11} + \frac{6.9}{Re_{D_h}} \right] \right)^2}{Re_{D_h}} \quad \text{if } Re_{D_h} \geq 4000 \quad (14b)$$

B.3 Computer simulation and Analysis

Based on the nonlinear MR damper model, the computer simulation is undertaken to analyze the characteristics of the MR damper.

Figure B.2 presents the field-dependent damping force vs. the piston velocity for both nonlinear and linear damper models. In the plot, “Fnon” and “Flinear” stand for the damping force calculated from the proposed nonlinear model and well-known laminar linear model respectively, their subscripts “on” and “off” corresponding to the field-on and field-off damping force. As seen in this figure, the linear (laminar) model greatly under-estimated the total damping force in both field-on and field-off

cases compared to the damping force calculated from the proposed nonlinear model. Hence, it is necessary to develop a nonlinear model to describe MR damper behavior under high fluid velocity and high shear rate.

In Fig. B.3, the solid star curve represents the boundary of minimum Bingham numbers required in order to achieve a desired dynamic range at various Reynolds numbers. In this example, the desired dynamic range is chosen to be $D=3$. The remaining three curves represent the Bingham numbers that the device can achieve with the particular gap thickness, d , specified in the legend at various Reynolds numbers. The figure demonstrates that the Bingham number required to achieve the desired dynamic range increases as the Reynolds number increases. In particular, in dominant turbulent flow over 4000 of the Reynolds number, the Bingham number required to achieve the desired dynamic range greatly increases. Figure B.4 illustrates the dynamic range at various Reynolds numbers with three different gap thicknesses. It is observed that the dynamic range D is close to 1 at higher Reynolds number. The same trend and tendency was reached through a variety of computer simulations by employing a variety of geometry size and key parameters of MR dampers.

It is conservatively concluded that it is desirable to keep the Reynolds number of the fluid flow in the valve below at least 4000 to obtain a useful dynamic range greater than 1 when designing MR dampers.

B.4 Effective Design Strategy

Based on the nonlinear model developed in this study, an effective MR damper design procedure is proposed:

1. Specify the desired dynamic range, D_{des} and the zero-field damping force, F_0 at the maximum piston velocity of interest, V_p .
2. Specify fluid properties such as τ_y , ρ , and η .
3. Calculate Bingham number from $Bi = 6(D_{des} - 1)$.
4. Determine an appropriate d from $d = \sqrt{\frac{\eta^2 \cdot Bi \cdot Re}{2\rho\tau_y}}$ so that the Reynolds number $Re \ll 4000$ (Smaller Reynolds number is recommended for a useful dynamic range greater than 1).
5. Determine \bar{A} by putting d determined from step 4 into $\bar{A} = \frac{\tau_y d}{\eta V_p Bi}$.
6. Then, depending on design restrictions to be primarily considered, follow anyone of the cases below:
 - i. If the active length L is critically constrained, determine A_p from $A_p = \frac{4dF_0}{f(\rho\bar{A}^2V_p^2)L}$ using the allowable L , then compute A_d from \bar{A} obtained from step 5.
 - ii. If the inner-diameter size of the MR damper is critically constrained, namely, A_p is restricted, then determine L from $L = \frac{4dF_0}{f(\rho\bar{A}^2V_p^2)A_p}$ using allowable A_p .
 - iii. If there is no such space limitations, choose any A_p and A_d producing the above \bar{A} and calculate L from the same equation in ii.
7. Calculate the effective diameter of the fluid path D_b from $D_b = A_d / (\pi d)$.

8. Based on the above information, given a range of interested Re ($Re \ll 4000$), plot the corresponding figures (such as d vs. Re for step 4, and so on), choose the appropriate design parameter values from these figures.

B.5 Experimental Validation

B.5.1 Damper Design

To validate the proposed nonlinear model and the design strategy, a semi-active MR damper was developed and fabricated. Design requirements are as follows: 1) the MR damper can produce maximum damping force of at least 4500N on field-on status while keeping the zero field damping force as low as possible but up to 2000N; 2) controllable force range or dynamic range is at least 2.25 at the maximum interested piston velocity of 0.9m/s; 3) the maximum inner damper diameter is 30mm.

We start the design procedure with step 1. Considering the friction force and other neglected factors during the theoretically non-dimensional analysis, we set the zero field force empirically as 1420N, and the total design damping force as 4800N, therefore the dynamic range now becomes $4800/1420=3.38$. The maximum diameter of the piston imposed on this project is 30mm and we set the shaft diameter to be 12.7mm according to a stress analysis of the piston rod.

So far, we have specified the desired dynamic range, D_{des} , the zero-field damping force, F_0 , at the maximum piston velocity of interest, V_p , and the effective piston area A_p . According to step 2, we still need to specify fluid properties such as τ_y , ρ , and η . Commercially available Lord Corporation MRF-132AD fluid was chosen for this design due to its favorable material compatibility and magnetic

properties. From the information provided by Lord Corporation, the fluid properties were finally determined as $\eta = 0.18$, $\rho = 3090 \text{ kg / m}^3$, $\tau_y = 40 \text{ kPa}$.

Continuing to step 3, we determine the required Bingham number $Bi = 6 \times (3.38 - 1) = 14.28$. With all of the above preparation, we can then proceed to step 4 to determine gap thickness and plot d versus Re (here $100 \leq Re \leq 2000$), which is shown in Fig. B.5. Again, from step 5, \bar{A} is determined (see Fig. B.6). In this case, the piston diameter was restricted to 30mm. That means the effective piston area A_p is constrained, corresponding to case (ii) of step 6. Therefore, the resulting active length L versus Re diagram is shown in Fig. B.7. Now the design task is to calculate D_b based on the design values obtained from step 1 to step 6, the corresponding result is shown in Fig. B.8.

Observing the above design plots, we can see that gap thickness, active length and \bar{A} all increase with Reynolds number increases. According to the proposed design strategy, a smaller Reynolds number is preferred, but from Fig. B.5, too small a Reynolds numbers will result in too small a gap, which may not be practical to manufacture. On the other hand, from Fig. B.7, a larger Reynolds number will require a longer active length, which will greatly increase the overall length of the damper because of requiring several magnetic coil parts. Considering all of the trade-off, we finally choose the parameters as (refer to Figs. B.5-B.8.): $Re = 195$, $d = 0.6 \text{ mm}$, $\bar{A} = 10.5$, $L = 44 \text{ mm}$, $A_d = 5.56 \text{ e} - 5 \text{ m}^2$, $D_b = 29.43 \text{ mm}$. Based on these parameters, a MR damper was fabricated at the University of Maryland.

The traditional baseline MR damper designs shown in Fig. B.1 put the magnetic circuit inside the piston head. This arrangement is often the most space efficient since

the flow must move across the piston boundary in any arrangement. During the design process such a configuration was proposed but due to the conflict of the overall length between the magnetic circuit design and the stroke, as well as a volume constraint imposed on the project, we developed an alternative configuration to meet both the performance and stroke requirements within the space restrictions. The final design is presented in Fig. B.9, where the bobbin and coil of the magnetic circuit were moved off the piston to either end of the damper. The piston rides in an inner cylinder and forces fluid through a bifold annular gap of the active area into the cavity between cylinder walls. The flow must then return through the next bifold annular gap active area back into the inner cylinder. This configuration can double the active length without increasing the total damper length and maximize the damper stroke while still satisfy other design constraints. Even though we use two bifold valves instead of one straight valve, the design meets the above specifications of the cross-sectional gap area A_v , the area ratio \bar{A} , and the effective diameter of the fluid path D_b . Alternatively, the above design dimensions determined from the effective design strategy match the dimensions in the bifold MR damper, that is, the mathematical models of the two configurations (Fig. B.1 and Fig. B.9(a)) are equivalent.

B.5.3 Damper Testing

Damper tests were performed on a hydraulically powered MTS 810 materials testing system load frame and were run at 0.5, 1, 2, 4, 6, 8, 10, and 12 Hz sinusoidal signals with applied currents of 0, 0.25, 0.5, 0.75, 1.0, 1.25, and 1.5 Amps, and the total stroke was 1 inch. Some of the data collected from the test are presented in Fig. B.10 and Fig. B.11. Figure B.10(a-b) shows the damping force vs. displacement

results at 0.0 Amps current and 1.0 Amps current with varying frequencies on each plot. The damping force vs. velocity results at 2.0 Hz and 12.0 Hz with varying applied current levels are presented in Fig. B.11(a-b). It is shown that the MR damper produces significant damping force increment from no field upon applying magnetic field at all piston velocity of interest.

Figure B.12(a) presents predicted and measured damping force vs. displacement at field-on and field-off cases, Fig. B.12(b) presents the predicted and measured damping force at various velocities on field-on and field-off status. It is observed that the predicted damping force (dash-dot lines) agrees well with the measured value (solid lines). The results justify that we do achieve the design objective using the damper parameters determined by the proposed effective design strategy, and thus the validity of the design procedure is proven.

B.6 Conclusions

A novel nondimensional nonlinear MR damper flow model was developed based on the parallel plates or rectangular duct approximation, and an effective design procedure was proposed. For verification, a high force, high velocity MR damper was designed and fabricated. The MR damper was tested on a hydraulically powered MTS 810 material testing system load frame and the data collected from the test validates the MR damper design strategy. From this study, we concluded that the design procedure proposed is quite useful and can be easily adopted to other MR damper designs.

Acknowledgment

This research was supported in part by General Motors Research and Development Center.

References

- [1] R. W. Phillips, *Engineering Applications of Fluids with a Variable Yields Stress*, Ph.D Thesis, Mechanical Engineering, University of California, Berkeley, 1969.
- [2] H. P. Gavin, R. D. Hanson and F. E. Filisko, "Electrorheological Dampers, Part I: Analysis and Design," *J. Appl. Mech.*, **63**, 678-82, 1996.
- [3] G. M. Kamath and N. M. Wereley, "A Nonlinear Viscoelastic-plastic Model for Electrorheological Fluids," *Smart Mater. Struct.*, **6** 351-9, 1996.
- [4] N. M. Wereley and L. Pang, "Nondimensional Analysis of Semi-active Electrorheological and Magnetorheological Dampers Using Approximate Parallel Plate Models," *Smart Mater. Struct.* **7**, 732-743, 1998.
- [5] W. Hu and N. M. Wereley, "Nondimensional Damping Analysis of Flow-mode Magnetorheological and Electrorheological Damper," *Proceedings of IMECE'03 ASME*, International Mechanical Engineering Congress & Exposition, Washington, D.C., USA, November 15-21, 2003.
- [6] G. Yang, B. F. Spencer, Jr., J. D. Carlson and M. K. Sain, "Large-scale MR Fluid Dampers: Modeling, and Dynamic Performance Considerations," *Engineering Structures*, **24**, 309-323, 2002.
- [7] D. Y. Lee and N. M. Wereley, "Quasi-steady Herschel-Bulkley Analysis of Electro- and Magneto-rheological Flow Mode Dampers," *Journal of Intelligent Material Systems and Structures*, **10**(10), 761-69, Oct, 2000.

- [8] X. Wang and F. Gordaninejad, "Flow Analysis of Field-controllable, Electro- and Magneto-rheological Fluids Using Herschel-Bulkley Model," *Journal of Intelligent Material Systems and Structures*, **10**(8), 601-08, Aug, 2000.
- [9] D. J. Peel, R. Stanway and W. A. Bullough, "Dynamic Modeling of an ER Vibration Damper for Vehicle Suspension Applications," *Smart Mater. Struct.*, **5**, 591-606, 1996.
- [10] B. F. Spencer, Jr, S. J. Dyke, M. K. Sain and J. D. Carlson, "Phenomenological Model for a Magnetorheological Damper," *J. Eng. Mech. Am. Soc. Civil Eng.*, **123**, 230-52, 1997.
- [11] G. Yang, *Large-scale Magnetorheological Fluid Damper for Vibration Mitigation: Modeling, Testing and Control*, Ph.D Dissertation, University of Notre Dame, IN, 2001.
- [12] L. Bitman, Y. T. Choi, S. B. Choi and N. M. Wereley, "Electrorheological Damper Analysis Using an Eyring-plastic Model," *Smart Mater. Struct.*, **14**, 237-46, 2005.
- [13] M. R. Jolly, J. W. Bender, and J. D. Carlson, "Properties and Application of Commercial Magnetorheological Fluids," *Smart Structures and Materials*, SPIE **3327**, 262-275, 1998.
- [14] S. B. Choi, Y. T. Choi, and D. W. Park, "A Sliding Mode Control of a Full-car Electrorheological Suspension System via Hardware in-the-loop Simulation," *Journal of Dynamic Systems, Measurement, and Control*, **122**, 114-122, March 2000.
- [15] F. M. White, *Fluid Mechanics*, Second Edition, McGRAW-HILL, 1986.

- [16] J. B. Franzini and E. J. Finnemore, *Fluid Mechanics with Engineering Applications*, McGraw-HILL, 1997.
- [17] J. E. Slotine and W. Li, *Applied Nonlinear Control*, Prentice-Hall, P.284, 1991.
- [18] R. J. Atkin, X. Shi, and W. A. Bullough, "Solutions of the Constitutive Equations for the Flow of an Electrorheological Fluid in Radial Configurations," *Journal of Rheology*, **35**(7), 1441-1461, 1991.
- [19] G. M. Kamath, M. K. Hurt and N. M. Wereley, "Analysis and Testing of Bingham Plastic Behavior in Semi-Active Electrorheological Fluid Dampers," *Smart Mater. Struct.*, **5**(5), 576-590, 1996.
- [20] W. Prager, *Introduction to Mechanics of Continua*, New York, Ginn and Company, P.141, 1961.

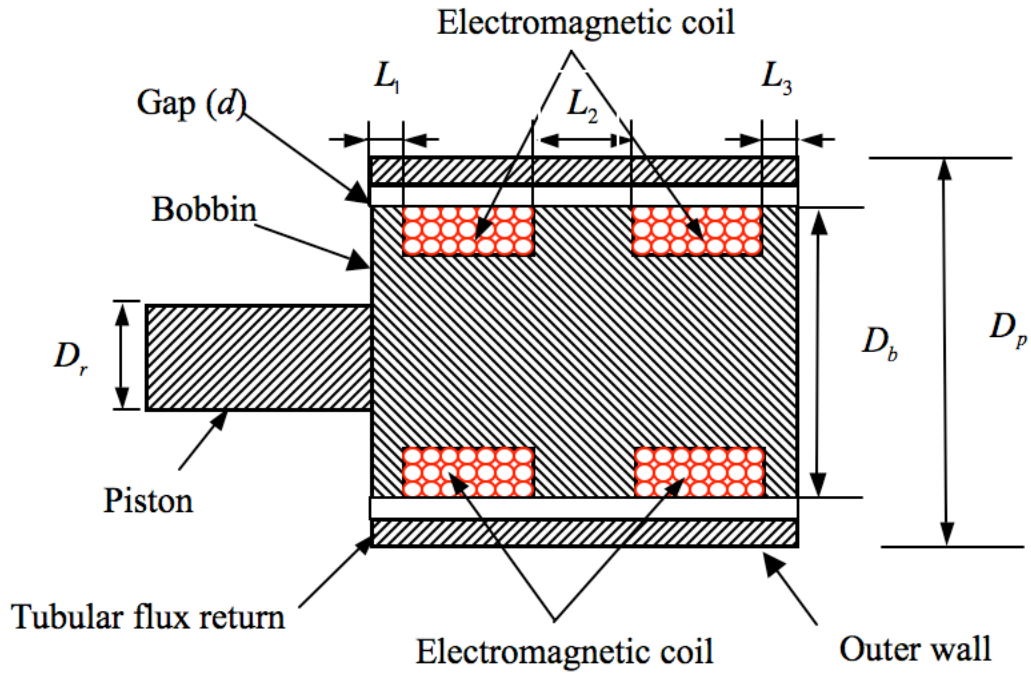


Figure B.1: Magnified fluid path in the piston head of a basic MR damper.

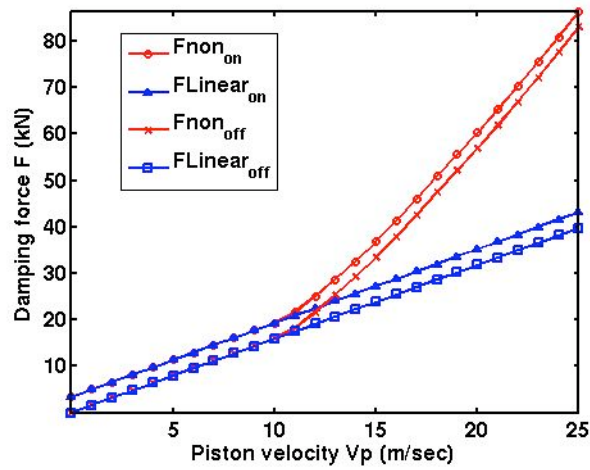


Figure B.2: Damping force vs. piston velocity.

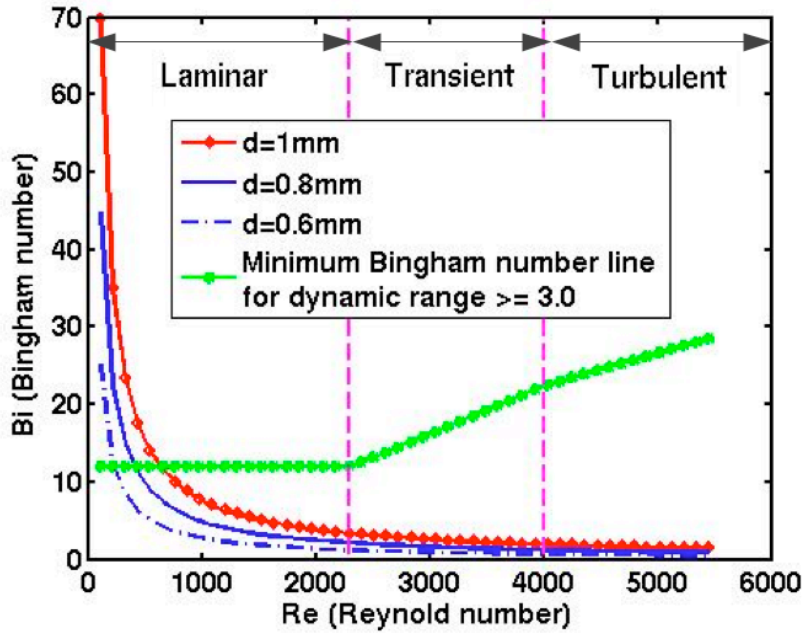


Figure B.3: Bingham number vs. Reynolds number.

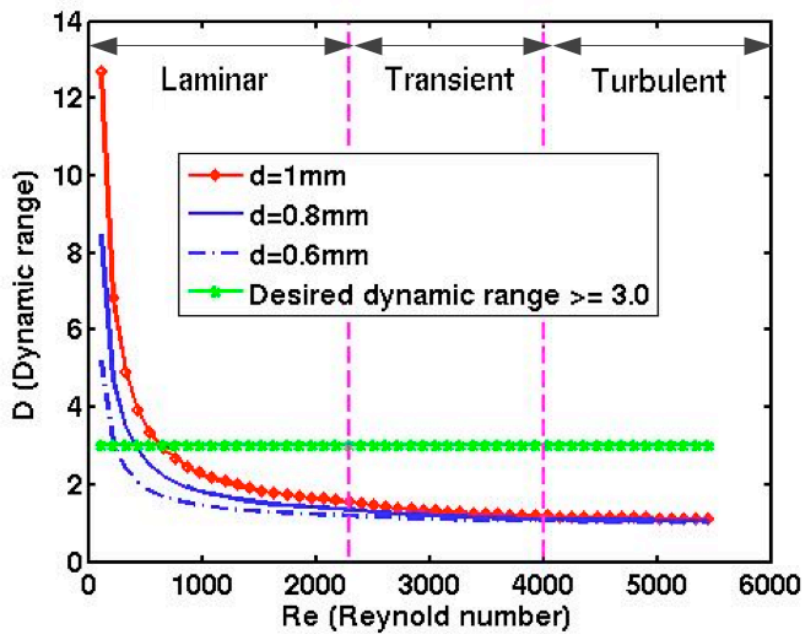


Figure B.4: Dynamic range vs. Reynolds number.

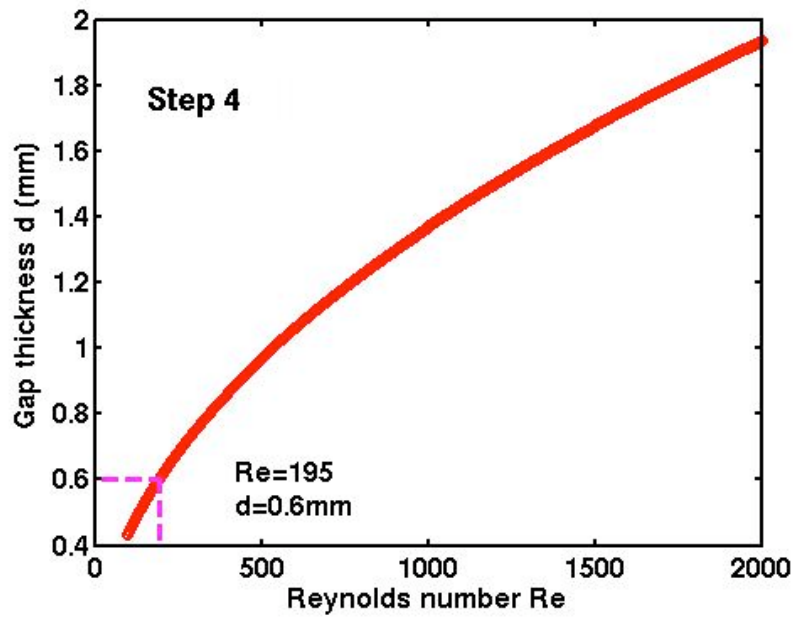


Figure B.5: Gap thickness d vs. Reynolds number.

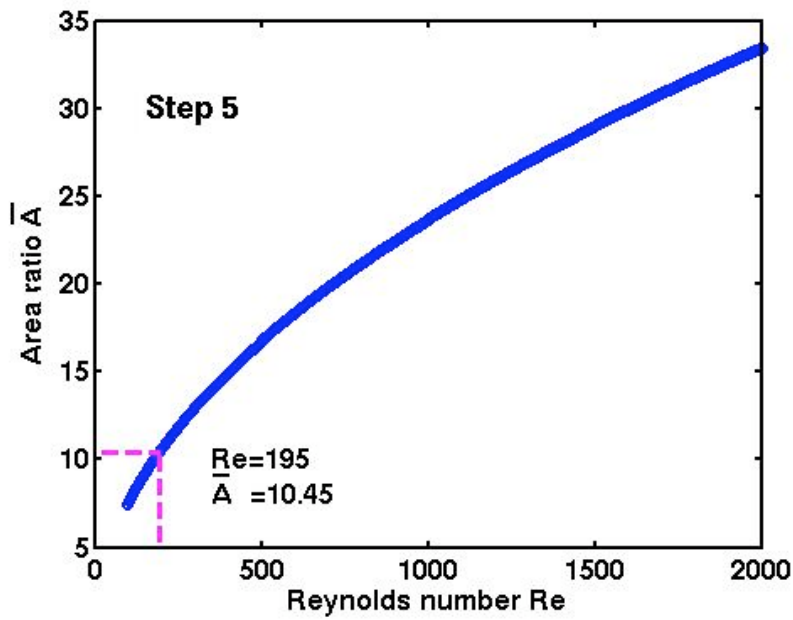


Figure B.6: Area ratio \bar{A} vs. Reynolds number.

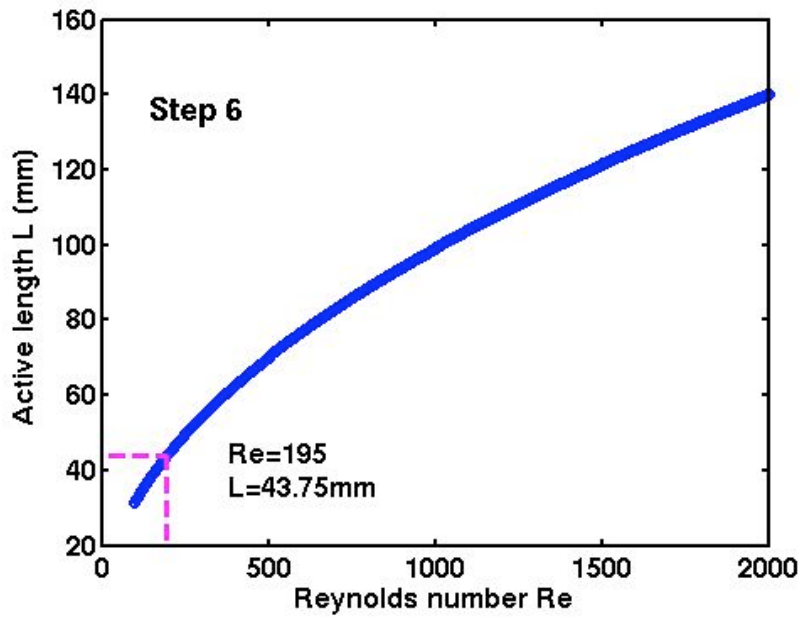


Figure B.7: Active length L vs. Reynolds number.

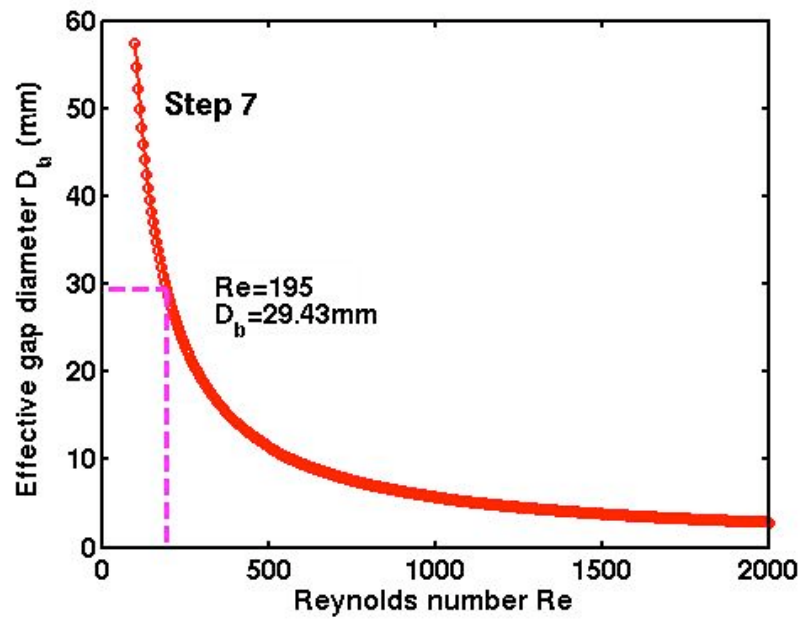
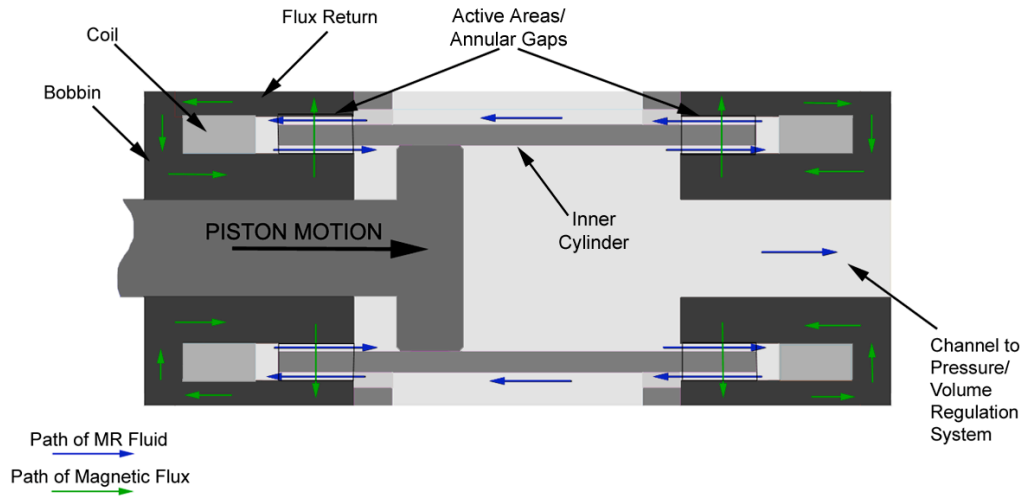
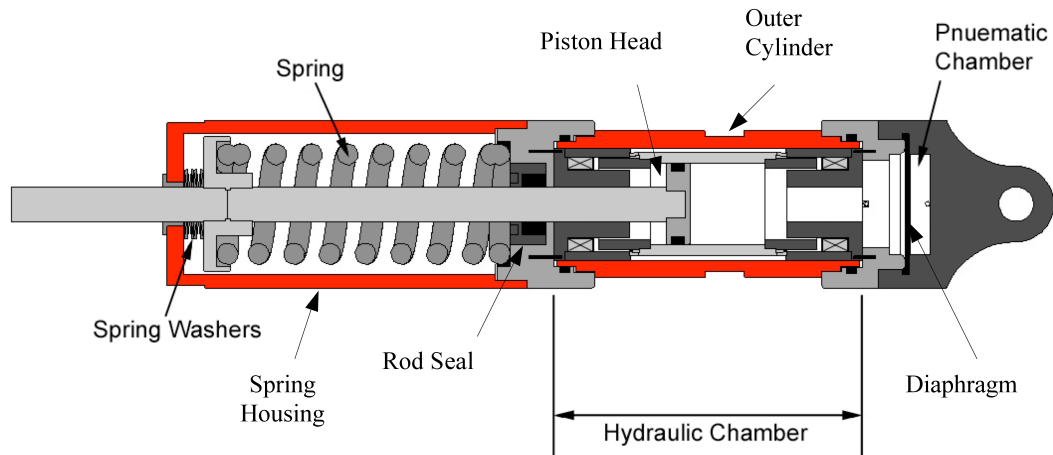


Figure B.8: Effective gap diameter D_b vs. Reynolds number.

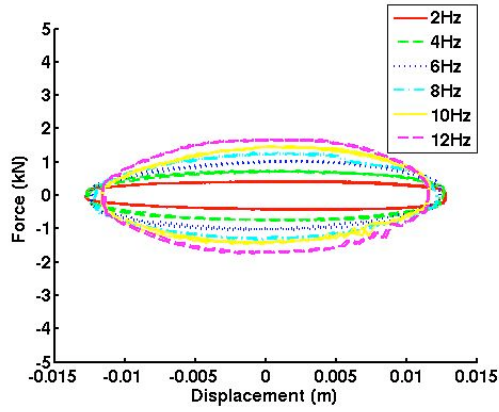


(a) Cross sectional view of the damper design showing paths of magnetic flux and MR fluid.

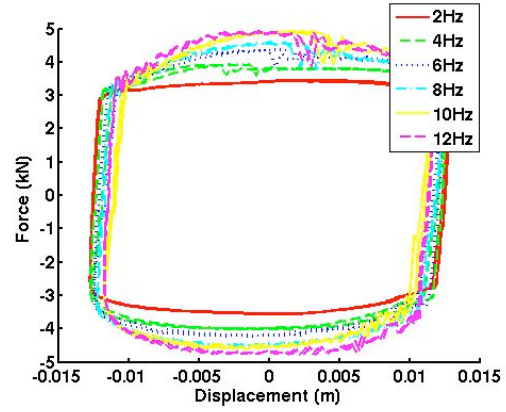


(b) Cross sectional view of complete damper with spring mechanisms in place (The spring not used for characterization tests).

Figure B.9: The example bi-fold damper design.

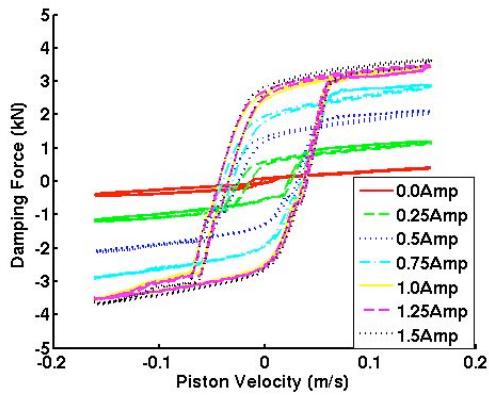


(a) 0.0 Amps Applied Current

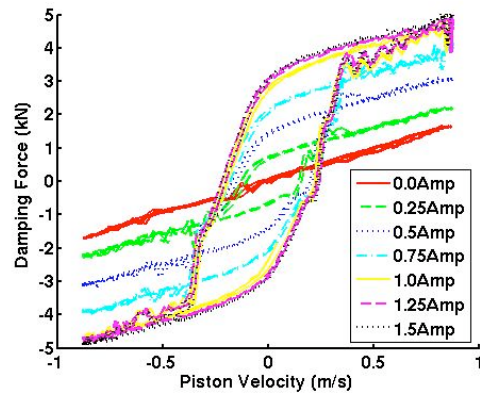


(b) 1.0 Amps Applied Current

Figure B.10: MTS force vs. displacement for sinusoidal input.

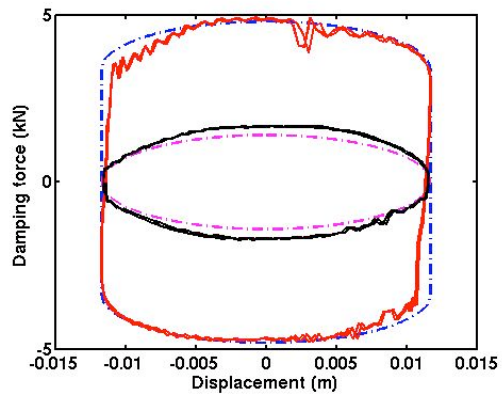


(a) 2.0 Hz

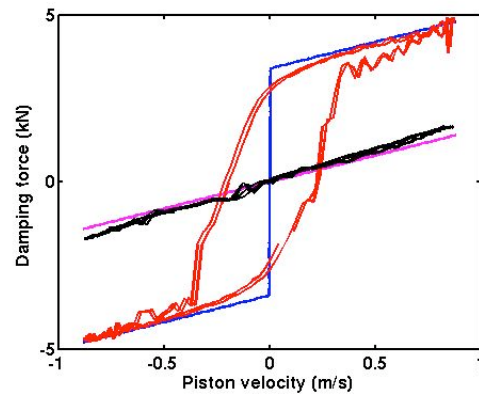


(b) 12.0 Hz

Figure B.11: MTS force vs. velocity for sinusoidal input.



(a) Damping force vs. displacement



(b) Damping force vs. velocity

Figure B.12: Predicted damping force (dash-dot lines) vs. MTS measured (solid lines).

Bibliography

- [1] Ahmadian M. and Poynor J. C., “An Evaluation of Magneto Rheological Dampers for Controlling Gun Recoil Dynamics,” *Shock and Vibration*, Vol. 8, pp. 147-155, 2001.
- [2] Ahmadian M., Appleton R. and Norris J. A., “An Analytical Study of Fire out of Battery Using Magneto Rheological Dampers,” *Shock and Vibration*, Vol. 9, pp. 129-142, 2002.
- [3] Ahmadian M. and Norris J. A., “Rheological Controllability of Double-ended MR Dampers Subjected to Impact Loading,” *Proceedings of SPIE*, Vol. 5386, pp. 185-194, 2004.
- [4] Ahmadian M. and Song X. B., “Designing an Adaptive Semiactive Magneto-rheological Seat Suspension for Heavy Truck Applications,” *Proceedings of SPIE*, Vol. 5760, pp. 247-255, San Diego, May 2005.
- [5] Batterbee D. C., Sims N. D., Stanway R. and Wolejsza Z., “Magneto-rheological Landing Gear: 1. A Design Methodology,” *Smart Materials and Structures*, Vol. 16, pp. 2429-2440, 2007.
- [6] Bitman L., Choi Y. T., Choi S. B. and Wereley N. M., “Electrorheological Damper Analysis Using an Eyring-plastic Model,” *Smart Materials and Structures*, Vol. 14, pp. 237-246, 2005.
- [7] Bois P. D., Chou C. C., Fileta B. B., Khalil T. B., King A. I., Mahmood H. F., Mertz H. J., Wismans J., Prasad P. and Belwafa J. E., *Vehicle Crashworthiness and Occupant Protection*, American Iron and Steel Institute, 2004.

- [8] Brigley M., Choi Y. T. and Wereley N. M., “Experimental and Theoretical Development of Multiple Fluid Mode Magnetorheological Isolators,” *AIAA Journal of Guidance, Control, and Dynamics*, Vol. 31, No. 3, pp. 449-459, 2008.
- [9] Browne A. L. and Johnson N. L., “Conducting Dynamic Impact Tests Using a “Free-flight” Drop Tower Facility Part 1: Theory,” ASME IMECE 2001 – Vol. 1, Paper No. IMECE 2001/AMD-25456, Nov. 2001, also in *Crashworthiness, Occupant Protection and Bio-Mechanics in Transportation Systems – 2001-*, ASME Publication AMD – Vol. 251, 2001.
- [10] Browne A. L., Namuduri C. S., Ulicny J. C. and Johnson N. L., “Seat Assemblies Including a Seat Stroking Device and Methods of Use,” US Patent 20070063566, Mar 22, 2007.
- [11] Browne A. L., McCleary J., Namuduri C. S. and Webb S., “Impact Performance of Magnetorheological Fluids,” *Journal of Intelligent Material Systems and Structures*, Vol. 20, No. 6, 723-728, 2009.
- [12] Cappon H., Ratingen M. V., Wismans J., Hell W., Lang D. and Svensson M., “Whiplash Injuries, not Only a Problem in Rear-end Impact,” The 18th International Technical Conference on the Enhanced Safety of Vehicles (ESV) Proceedings, Paper #214, Nagoya, Japan, May 19-22, 2003.
- [13] Carlson J. D., *Adaptronics and Smart Structures: Basics, Materials, Design and Applications*, Chapter 6.6 (Magnetorheological Fluid Actuators), pp. 180-195, Springer, 1999.

- [14] Carlson J. D., Matthis W. and Toscano J. R., "Smart Prosthetics Based on Magnetorheological Fluids," *Proceedings of SPIE*, Vol. 4332, pp. 308-316, 2001.
- [15] Choi S. B., Nam M. H. and Lee B. K., "Vibration Control of a MR Seat Damper for Commercial Vehicles," *Journal of Intelligent Material Systems and Structures*, Vol. 11, pp. 936-944, Dec. 2000.
- [16] Choi S. B. and Han Y. M., "MR Seat Suspension for Vibration Control of a Commercial Vehicle," *International Journal of Vehicle Design*, Vol. 31, No. 2, pp. 202-215, 2003.
- [17] Choi Y. T. and Wereley N. M., "Vibration Control of a Landing Gear System Featuring ER/MR Fluids," *AIAA Journal of Aircraft*, Vol. 40, No. 3, 2003.
- [18] Choi Y. T., Yoo J. H. and Wereley N. M., "Double Adjustable Magnetorheological Dampers for a Gun Recoil System," ASME 2005 International Mechanical Engineering Congress and Exposition (IMECE 2005), Orlando, Florida, USA, November 5-11, 2005.
- [19] Choi Y. T. and Wereley N. M., "Biodynamic Response Mitigation to Shock Loads Using Magnetorheological Helicopter Crew Seat Suspension," *AIAA Journal of Aircraft*, Vol. 42, No. 5, 2005.
- [20] Corless R. M., Gonnet G. H., Hare D. E. G., Jeffrey D. J. and Knuth D. E., "On the Lambert W function," *Advances in Computational Mathematics*, Vol. 5, pp. 329-359, 1996.
- [21] Dixon J. C., *The Shock Absorber Handbook*, Society of Automotive Engineers, February, 1999.

- [22] Dominguez A., Sedaghati R. and Stiharu I., “Modelling the Hysteresis Phenomenon of Magnetorheological Dampers,” *Smart Materials and Structures*, Vol. 13, pp. 1351-1361, 2004.
- [23] Dominguez A., Sedaghati R. and Stiharu I., “A New Dynamic Hysteresis Model for Magnetorheological Dampers,” *Smart Materials and Structures*, Vol. 15, pp. 1179-1189, 2006.
- [24] Dogruer U., Gordaninejad F. and Evrensel C. A., “A New Magneto-rheological Fluid Damper for High-mobility Multi-purpose Wheeled Vehicle (HMMWV),” *Journal of Intelligent Material Systems and Structures*, Vol. 19, No. 6, pp. 641-650, 2008.
- [25] Dong X. M., Yu M., Huang S. L., Li Z. S. and Chen W. M., “Half Car Magnetorheological Suspension System Accounting for Nonlinearity and Time Delay,” *International Journal of Modern Physics B*, Vol. 19, Nos. 7, 8 & 9, pp. 1381-1387, 2005.
- [26] Dyke S. J., Spencer Jr. B. F., Sain M. K. and Carlson J. D., “Modeling and Control of Magnetorheological Dampers for Seismic Response Reduction,” *Smart Materials and Structures*, Vol. 5, pp. 565–575, 1996a.
- [27] Dyke S. J., Spencer Jr. B. F., Sain M. K. and Carlson J. D., “Seismic Response Reduction Using Magnetorheological Dampers,” Proceedings of the IFAC World Congress, Vol. L, International Federation of Automatic Control, pp. 145–150, 1996b.

- [28] Dyke S. J., Spencer Jr. B. F., Sain M. K. and Carlson J. D., “An Experimental Study of MR Dampers for Seismic Protection,” *Smart Materials and Structures*, Vol. 5, pp. 693– 703, 1998.
- [29] Facey W. B., Rosenfeld N. C., Choi Y. T., Wereley N. M., Choi S. B. and Chen P., “Design and Testing of a Compact Magnetorheological Damper for High Impulsive Loads,” *International Journal of Modern Physics B*, Vol. 19, Nos, 7, 8 & 9, pp. 1549-1555, 2005.
- [30] Farjoud A., Vahdati N. and Fah Y. F., “MR-fluid Yield Surface Determination in Disc-type MR Rotary Brakes,” *Smart Materials and Structures*, Vol. 17, 2008.
- [31] Flores G. A. and Liu J., “In-vitro Blockage of a Simulated Vascular System Using Magnetorheological Fluids as a Cancer Therapy,” *European Cells and Materials*, Vol. 3, Suppl. 2, pp.9-11, 2002.
- [32] Franzini J. B. and Finnemore E. J., *Fluid Mechanics with Engineering Applications*, McGraw-HILL, 1997.
- [33] Gavin H. P., Hanson R. D. and Filisko F. E., “Electrorheological Dampers, Part I: Analysis and Design,” *Journal of Applied Mechanics*, Vol. 63, pp. 678-82, 1996.
- [34] Herr H. and Wilkenfeld A., “User-adaptive Control of a Magneothreological Prosthetic Knee,” *Industrial Robot: An International Journal*, Vol. 30, No. 1, pp. 42-55, 2003.

- [35] Hiemenz G. J. and Wereley N. M., "Seismic Response of Civil Structures Utilizing Semi-active MR and ER Bracing Systems," *Journal of Intelligent Material Systems and Structures*, Vol. 10, pp. 646-651, 1999.
- [36] Hiemenz G. J., Choi Y. T. and Wereley N. M., "Seismic Control of Civil Structures Utilizing Semi-Active MR Braces," *Journal of Computer-Aided Civil and Infrastructure Engineering*, Vol. 18, No. 1, pp. 31-44, 2003.
- [37] Hiemenz G. J., Hu W. and Wereley N. M., "Semi-active Magnetorheological Helicopter Crew Seat Suspension for Vibration Isolation," 48th AIAA/ASME/ASCE/AHS/ASC Structures, Structural Dynamics, and Materials Conference, Honolulu, Hawaii, April 23-26, 2007a.
- [38] Hiemenz G. J., Choi Y. T. and Wereley N. M., "Semi-Active Control of Vertical Stroking Helicopter Crew Seat for Enhanced Crashworthiness," *AIAA Journal of Aircraft*, Vol. 44, No. 3, pp. 1031-1034, 2007b.
- [39] Hong S. R., Choi S. B., Choi Y. T. and Wereley N. M., "Comparison of Damping Force Models for an Electrorheological Fluid Damper," *International Journal of Vehicle Design*, Vol. 33, No. 1A, 2003.
- [40] Hong S. R., Wang G., Hu W. and Wereley N. M., "Hydro-mechanical Analysis of a Magnetorheological Bypass Damper," Proceedings of the 10th International Conference on Electrorheological Fluids and Magnetorheological Suspensions, Lake Tahoe, USA, June 18-22, 2006.
- [41] Hu H. S., Wang J., Qian S. X. and Jiang X. Z., "Test Modeling and Parameter Identification of a Gun Magnetorheological Recoil Damper," Proceedings of the

2009 IEEE International Conference on Mechatronics and Automation, Changchun, China, August 9-12, 2009.

- [42] Hu W. and Wereley N. M., “Nondimensional Damping Analysis of Flow-mode Magnetorheological and Electrorheological Damper,” Proceedings of IMECE’03 ASME, International Mechanical Engineering Congress & Exposition, Washington, D.C., USA, November 15-21, 2003.
- [43] Hu W. and Wereley N. M., “Rate-dependent Elasto-slide Model for Single and Dual Frequency MR Lag Damper Behavior,” *International Journal of Modern Physics B*, Vol. 19, Nos. 7, 8 & 9, pp. 1527-1533, 2005a.
- [44] Hu W. and Wereley N. M., “Magnetorheological Fluid and Elastomeric Lag Damper for Helicopter Stability Augmentation,” *International Journal of Modern Physics B*, Vol. 19, Nos. 7-9, pp. 1471-1477, 2005b.
- [45] Hu W. and Wereley N. M., “Hybrid Magnetorheological Fluid-elastomeric Lag Dampers for Helicopter Stability Augmentation,” *Smart Materials and Structures*, Vol. 17, 2008.
- [46] Huang M., *Vehicle Crash Mechanics*, CRC Press, 2002.
- [47] Idelchik I. E., *Handbook of Hydraulic Resistance*, 3rd Edition, CRC Begell House, 1994.
- [48] Jansen L.M. and Dyke S.J., “Semiactive Control Strategies for MR Dampers: Comparative Study,” *Journal of Engineering Mechanics*, ASCE, Vol. 126, No. 8, pp. 795–803, 2000.
- [49] Johnson N. L. and Browne A. L., “Conducting Dynamic Impact Tests Using a “Free-Flight” Drop Tower Facility Part II: Practical Aspects,” ASME IMECE

- 2001 – Vol. 1, Paper No. IMECE 2001/AMD-25459, Nov. 2001, also in
Crashworthiness, Occupant Protection and Bio-Mechanics in Transportation
Systems – 2001-, ASME Publication AMD – Vol. 25, 2001.
- [50] Kamath G. M. and Wereley N. M., “A Nonlinear Viscoelastic-plastic Model for
Electrorheological Fluids,” *Smart Materials and Structures*, Vol. 6, pp. 351-359,
1996.
- [51] Kavlicoglu B., Gordaninejad F., Evrensel C. A., Cobanoglu N., Xin M., Heine
C., Fuchs A. and Korol, G., “A High-Torque Magneto-Rheological Fluid
Clutch,” Proceedings of SPIE Conference on Smart Materials and Structures,
San Diego, March 2002.
- [52] Kciuk M. and Turczyn R., “Properties and Application of Magnetorheological
Fluids,” *Journal of Achievements in Materials and Manufacturing Engineering*,
Vol. 18, Issue 1-2, 2006.
- [53] Lai C. Y. and Liao W. H., “Vibration Control of a Suspension System via a
Magnetorheological Fluid Damper,” *Journal of Intelligent Material Systems and
Structures*, Vol. 8, pp. 527-547, 2002.
- [54] Lampe D. and Grundmann R., “Transitional and Solid State Behavior of a
Magnetorheological Clutch,” The 7th International Conference on New
Actuators, Actuator 2000, Bremen, Germany, 2000.
- [55] Lee D. Y. and Wereley N. M., “Quasi-steady Herschel-Bulkley Analysis of
Electro- and Magneto-rheological Flow Mode Dampers,” *Journal of Intelligent
Material Systems and Structures*, Vol. 10, No. 10, pp. 761-769, Oct. 2000.

- [56] Lee U., Kim D., Hur N. and Jeon D., “Design Analysis and Experimental Evaluation of an MR Fluid Clutch,” *Journal of Intelligent Material Systems and Structures*, Vol. 10, pp. 701-707, Sept. 1999.
- [57] Liu J., Flores G. A. and Sheng R. S., “In-vitro Investigation of Blood Embolization in Cancer Treatment Using Magnetorheological Fluids,” *Journal of Magnetism and Magnetic Materials*, Vol. 225, pp. 209-217, 2001.
- [58] Mao M., Choi Y.T. and Wereley N. M., “Effective Design Strategy for a Magnetorheological Damper Using a Nonlinear Flow Model,” *Proceedings of SPIE*, Vol. 5760, pp. 446-455, 2005.
- [59] Mao M., Hu W., Choi Y.T. and Wereley, N. M., “A Magnetorheological Damper with Bifold Valves for Shock and Vibration Mitigation,” *Journal of Intelligent Material Systems and Structures*, Vol. 18, No. 12, pp. 1227-1232, 2007a.
- [60] Mao M., Hu W., Wereley N. M., Browne A. L. and Ulicny J., “Shock Load Mitigation Using Magnetorheological Energy Absorber with Bifold Valves,” *Proceedings of SPIE*, Vol. 6527, pp. 652710.1-652710.12, 2007b.
- [61] Mao M., Hu W., Choi Y. T., Wereley N. M., Browne A. L. and Ulicny J., “Performance Analysis of Magnetorheological Energy Absorbers under Impact Conditions,” *Proceedings of ASME 2008 Conference on Smart Materials, Adaptive Structures and Intelligent Systems*, Ellicott City, Maryland, Oct. 28-30, 2008.
- [62] Mao M., Hu W., Wereley N. M., Browne A. L. and Ulicny J., “A Nonlinear Analytical Model for Magnetorheological Energy Absorbers under Impact

- Conditions,” Proceedings of ASME 2009 Conference on Smart Materials, Adaptive Structures and Intelligent Systems, Oxnard, California, Sept. 21-23, 2009.
- [63] Mao M., Wereley N. M. and Browne A. L., “Adaptive Control of a Sliding Seat Using Magnetorheological Energy Absorbers,” Proceedings of ASME 2010 Conference on Smart Materials, Adaptive Structures and Intelligent Systems, Philadelphia, PA, USA, Sept. 28-Oct. 1, 2010.
- [64] Nam Y. J. and Park M. K., “Performance Evaluation of Two Different Bypass-type MR Shock Dampers,” *Journal of Intelligent Material Systems and Structures*, Vol. 18, No. 7, pp. 707-717, 2007.
- [65] Neelakantan V. A. and Washington G. N., “Modeling and Reduction of Centrifuging in Magneothreological (MR) Transmission Clutches for Automotive Applications,” *Journal of Intelligent Material Systems and Structures*, Vol. 16, pp. 703-709, Sept. 2005.
- [66] Ngatu G. T., Kothera C. S., Hu W. and Wereley N. M., “Effect of Temperature on Magnetorheological Fluid Elastomeric Lag Dampers for Helicopter Rotors,” The 50th AIAA/ASME/ASCE/AHS/ASC Structures, Structural Dynamics, and Materials Conference, Palm Springs, California, May 4-7, 2009.
- [67] Park C. and Jeon D., “Semiactive Vibration Control of a Smart Seat with an MR Fluid Damper Considering its Time Delay,” *Journal of Intelligent Material Systems and Structures*, Vol. 13, No. 7/8, pp.521-524, 2002.

- [68] Peel D. J., Stanway R. and Bullough W. A., “Dynamic Modeling of an ER Vibration Damper for Vehicle Suspension Applications,” *Smart Materials and Structures*, Vol. 5, pp. 591-606, 1996.
- [69] Phillips R. W., Engineering Applications of Fluids with a Variable Yields Stress, Ph.D Thesis, Mechanical Engineering, University of California, Berkeley, 1969.
- [70] Rabinow J., “The Magnetic Fluid Clutch.” *AIEE Transactions*, Vol. 67, pp.1308– 1315, 1948.
- [71] Rosenfeld N. C. and Wereley N. M., “Volume-constrained Optimization of Magnetorheological and Electrorheological Valves and Dampers,” *Smart Materials and Structures*, Vol. 13, pp. 1303-1313, 2004.
- [72] Snyder R. A., Kamath G. M., and Wereley N. M., “Characterization and Analysis of Magnetorheological Damper Behavior Under Sinusoidal Loading,” *AIAA Journal*, Vol. 39, No. 7, pp. 1240-1253, July 2001.
- [73] Schmitt K.-U., Muser M., Heggendorf M., Niederer P. and Walz F., “Development of a Damping Seat Slide to Reduce Whiplash Injury,” Proceedings of the Institution of the Mechanical Engineers, Vol. 217, Part D: Journal of Automobile Engineering, 2003.
- [74] Senkal D. and Gurocak H., “Spherical Brake with MR Fluid as Multi-degree of Freedom Actuator for Haptics,” *Journal of Intelligent Material Systems and Structures*, Vol. 20, No. 18, pp. 2149-2160, 2009.

- [75] Shen Y., Golnaraghi M. F. and Heppler G. R., “Semi-active Vibration Control Schemes for Suspension Systems Using Magnetorheological Dampers,” *Journal of Vibration and Control*, Vol. 12, No. 1, pp. 3-24, 2006.
- [76] Singh H., Choi Y. T. and Wereley N. M., “Optimal Control of Vertically Stroking Crew Seats Employing Magnetorheological Energy Absorbers,” Proceedings of the ASME 2009 Conference on Smart Materials, Adaptive Structures and Intelligent Systems Conference, Oxnard, California, Sept. 21-23, 2009.
- [77] Spencer Jr. B. F., Dyke S. J., and Sain M. K., “Magnetorheological Dampers: a New Approach to Seismic Protection of Structures,” Proceedings of the 35th IEEE Conference on Decision and Control, Vol. 1, pp. 676–681, 1996.
- [78] Spencer Jr. B. F., “A Comparison of Semi-active Control Strategy for the MR Damper,” Proceedings of the 1997 IASTED International Conference on Intelligent Information Systems (IIS '97), 1997a.
- [79] Spencer Jr. B. F., Dyke S. J., Sain M. K. and Carlson J. D., “Phenomenological Model for a Magnetorheological Damper,” *Journal of Engineering Mechanics*, ASCE, Vol. 123, pp. 230-52, 1997b.
- [80] Spencer Jr. B. F., Johnson E. A., and Ramallo J. C., “‘Smart’ Isolation for Seismic Control,” *JSME International Journal: Special Issue on Frontiers of Motion and Vibration Control*, Series C, Vol. 43, No. 3, pp. 704–711, 2000.
- [81] Spurk J. H. and Aksel N., *Fluid Mechanics*, Second Edition, Springer, 2008.

- [82] Stanway R., Sproston J. L., and El-Wahed A. K., "Application of Electrorheological Fluids in Vibration Control: A Survey," *Smart Materials and Structures*, Vol. 5, No. 4, pp. 464-482, 1996.
- [83] Temming J. and Zobel R., "Neck Distortion Injuries in Road Traffic Crashes (Analyses of the Volkswagen Database)," *Frontiers in Whiplash Trauma*, Yoganandan, IOS Press, pp. 118-133, 2000.
- [84] Tracy E. T., "Vehicle Crashworthiness Identifying if Vehicle Safety Defects Exist," www.vehiclesafetyfirm.com/CM/Crashworthiness/2005-vehicle-crashworthiness.pdf, 2005.
- [85] Wang D. H. and Liao W. H., "Modeling and Control of Magnetorheological Fluid Dampers Using Neural Networks," *Smart Materials and Structures*, Vol. 14, pp. 111-126, 2005.
- [86] Wang H. and Hu H. Y., "Optimal Fuzzy Control of a Semi-active Suspension of a Full-vehicle Model Using MR Dampers," *International Journal of Modern Physics B*, Vol. 19, Nos. 7, 8 & 9, pp. 1513-1519, 2005.
- [87] Wang X. and Gordaninejad F., "Flow Analysis of Field-controllable, Electro- and Magneto-rheological Fluids Using Herschel-Bulkley Model," *Journal of Intelligent Material Systems and Structures*, Vol. 10, No. 8, pp. 601-608, Aug, 2000.
- [88] Wang X. and Gordaninejad F., "Dynamic Modeling of Semi-Active ER/MR Fluid Dampers," Damping and Isolation, Proceedings of SPIE Conference on Smart Materials and Structures, Vol. 4331, Ed. Daniel J. Inman, pp. 82-91, 2001.

- [89] Wang X. J. and Gordaninejad F., “Lyapunov-based Control of a Bridge Using Magneto-rheological Fluid Dampers,” *Journal of Intelligent Material Systems and Structures*, Vol. 13, pp. 415-420, 2002.
- [90] Wereley N. M., “Nondimensional Herschel-Bulkley Analysis of Magnetorheological and Electrorheological Dampers,” *Journal of Intelligent Material Systems and Structures*, Vol. 19, No. 3, pp. 257-268, 2008.
- [91] Wereley N. M. and Choi Y. T., “Nondimensional Analysis of Magnetorheological Energy Absorbers for Drop-Induced Shock Mitigation,” The 15th International Congress on Sound and Vibration (ICSV15), Deajeon, Korea, July 6-10, 2008.
- [92] Wereley N. M., Kamath G. M. and Madhavan V., “Hysteresis Modeling of Semi-Active Magnetorheological Helicopter Dampers,” *Journal of Intelligent Material Systems and Structures*, Vol. 10, No. 8, pp. 624-633, 1999.
- [93] Wereley N. M. and Pang L., “Nondimensional Analysis of Semi-active Electrorheological and Magnetorheological Dampers Using Approximate Parallel Plate Models,” *Smart Materials and Structures*, Vol. 7, pp. 732-743, 1998.
- [94] Wereley N. M., Pang L. and Kamath G. M., “Idealized Hysteresis Modeling of Electrorheological and Magnetorheological Dampers,” *Journal of Intelligent Material Systems and Structures*, Vol. 9, No. 8, pp. 642-649, 1998.
- [95] White F. M., *Fluid Mechanics*, Second Edition, McGraw-Hill, 1986.

- [96] Yang G. Q., "Large-scale Magnetorheological Fluid Damper for Vibration Mitigation: Modeling, Testing and Control," PhD dissertation, University of Notre Dame, 2001.
- [97] Yang G. Q., Spencer Jr. B. F., Carlson J. D. and Sain M. K., "Large-scale MR Fluid Dampers: Modeling and Dynamic Performance Considerations," *Engineering Structures*, Vol. 24, Issue 3, pp. 309-323, May 2002.
- [98] Yang G. Q., Spencer Jr. B. F., Jung H. J. and Carlson J. D., "Dynamic Modeling of Large-scale Magnetorheological Damper Systems for Civil Engineering Applications," *Journal of Engineering Mechanics*, Vol. 130, No. 9, pp. 1107-1114, Sept. 2004.
- [99] Yi F., and Dyke S. J., "Structural Control Systems: Performance Assessment." Proceedings of the 2000 American Control Conference, Vol. 1, pp. 14-18, Chicago, Illinois, Sept. 2000.
- [100] Yoshioka H., Ramallo J. C., and Spencer Jr. B. F., "'Smart' Base Isolation Strategies Employing Magnetorheological Dampers," *Journal of Engineering Mechanics*, Vol. 128, No. 5, pp. 540-551, 2002.